A la recherche de la matière perdue

Philippe Di Stefano

▶ **To cite this version:**

Philippe Di Stefano. A la recherche de la matière perdue. High Energy Physics - Experiment [hep-ex]. Université Claude Bernard - Lyon I, 2007. tel-00347477

HAL Id: tel-00347477
https://theses.hal.science/tel-00347477

Submitted on 16 Dec 2008

HAL is a multi-disciplinary open access archive for the deposit and dissemination of scientific research documents, whether they are published or not. The documents may come from teaching and research institutions in France or abroad, or from public or private research centers.

L'archive ouverte pluridisciplinaire **HAL**, est destinée au dépôt et à la diffusion de documents scientifiques de niveau recherche, publiés ou non, émanant des établissements d'enseignement et de recherche français ou étrangers, des laboratoires publics ou privés.

Université Claude Bernard Lyon 1

A la recherche de la matière perdue

Habilitation à Diriger les Recherches
présentée par

Philippe Di Stefano

Soutenue le 7 décembre 2007 devant le jury composé de :

Sergio Ciliberto	examinateur
Gilles Gerbier	rapporteur
Bernard Ille	président
Franz Pröbst	rapporteur
James Rich	examinateur
Bernard Sadoulet	rapporteur
Pierre Salati	examinateur

Toute action de l'esprit est aisée si elle n'est pas soumise au réel.
Marcel Proust, Sodome et Gomorrhe [1]

Résumé des travaux

Travaux de thèse (soutenance le 24 septembre 1998)

Dans le cadre de l'expérience EDELWEISS, j'ai cherché des WIMPs, hypothétiques et discrètes particules supersymétriques, qui pourraient éclaircir l'énigme de la matière sombre. Pour cela, j'ai employé un bolomètre à ionisation, monocristal de 70 g de germanium à 20 mK, dans lequel un WIMP diffusant élastiquement sur un noyau créerait deux signaux : une impulsion de température et une charge. Afin de s'affranchir des bruits électroniques affectant nécessairement les signaux, faibles, j'ai appliqué une méthode de filtrage optimal dans l'espace des fréquences. Elle a fourni des résolutions de 1.2 keV LTMH à 122 keV d'énergie sur les deux voies. D'autre part, elle a permis de bien séparer jusqu'aux basses énergies le signal attendu (reculs nucléaires) des contaminations radioactives photoniques (reculs électroniques, plus ionisants pour une énergie identique). Ainsi, sur des étalonnages, nous avons pu rejeter 99.7 % du fond, tout en conservant 95 % du signal, au-delà de 15 keV.

Lors des 1.17 kg.jours de données prises pour chercher les WIMPs, nous avons constaté une population du fond radioactif s'immisçant dans le signal attendu. Il s'agissait vraisemblablement d'une composante électromagnétique de basse énergie, interagissant superficiellement dans le détecteur, où la charge ne peut être collectée complètement. Néanmoins, moyennant la conservation de seulement la moitié du signal, nous avons pu encore rejeter 98.5 % du fond. Ceci a permis de passer d'un taux de 40 évts/j/kg/keV à une limite supérieure (à 90 %) conservatrice sur le signal de 0.6 évts/j/kg/keV. Il s'agissait d'une amélioration de près de trois ordres de grandeur depuis la campagne précédente, et qui se rapprochait des zones prédites par la supersymétrie.

Travaux après la thèse

Au cours de mon post-doc à l'Institut-Max-Planck für Physik à Munich (décembre 1998 – septembre 2001), j'ai rejoint l'expérience de recherche de matière sombre italo-anglo-allemande CRESST. Je me suis d'abord impliqué dans le fonctionnement de l'expérience aux Laboratoires du Gran Sasso en Italie, où j'ai participé à une réduction du bruit de fond de trois ordres de grandeur. Ceci a permis d'établir de nouvelles limites pour les WIMPs de masse inférieure à 5 GeV. Je me suis ensuite engagé dans le développement de calorimètres scintillants pour la matière sombre, en optimisant les détecteurs de lumière cryogéniques et en étudiant la scintillation du $CaWO_4$ à 10 mK. Ces détecteurs peuvent fournir une palette de cibles plus vaste que celle disponible dans la technique plus éprouvée de calorimètres à ionisation.

Depuis 2001, je suis Maître de Conférence à l'Institut de Physique Nucléaire de Lyon (UCBL). Ma recherche se fait surtout dans le cadre de l'expérience de détection directe de matière sombre EDELWEISS (France-Allemagne-Russie). Dans un premier temps, j'ai participé à l'étude du blindage anti-neutrons et du système de veto contre les muons cosmiques de la nouvelle phase de l'expérience, EDELWEISS II. J'ai encadré la partie expérimentale d'une thèse sur ces sujets (L. Chabert, thèse soutenue en juillet 2004), et j'ai pris part aux tests des premiers modules scintillants du veto. Au cours d'une délégation au CNRS, je me suis ensuite impliqué dans l'installation d'EDELWEISS II au Laboratoire Souterrain de Modane. Toujours au cours de cette délégation, j'ai initié une activité de recherche et développement sur les scintillateurs cryogéniques. Depuis

l'automne 2005, je suis responsable du projet blanc ANR SciCryo (scintillation cryogénique), qui regroupe l'IAS Orsay, l'Institut Max-Planck pour la Physique à Munich et le LPCML (UCBL). J'ai co-dirigé une thèse sur la scintillation cryogénique du saphir (M. Luca, soutenue en juillet 2007) et suis co-directeur d'une thèse en cours sur la scintillation cryogénique dans EDELWEISS II (M.-A. Verdier, depuis septembre 2007). Je m'intéresse aussi à l'étude cryogénique de la rupture des matériaux, un résultat inattendu de mon post-doc en Allemagne. En décembre 2006, j'ai été un des deux lauréats du Prix Thibaud de l'Académie des Sciences, Belles-Lettres & Arts de Lyon.

Philippe DI STEFANO

Maître de Conférence

Date de naissance:	1er décembre 1971	Tél.:	04 72 44 85 05
Lieu de naissance:	Montréal, Canada	Email:	distefano@ipnl.in2p3.fr
Nationalité:	italo-canadienne	Adresse:	Institut de Physique Nucléaire de Lyon Université Claude Bernard Lyon I, 4 rue Enrico Fermi, F-69622 Villeurbanne Cedex, France

Thèmes de recherche

- **Détection directe de la matière sombre non-baryonique**
- **Scintillation cryogénique**
- **Etude cryogénique de la rupture de matériaux**

Distinctions

2006 : **Prix Thibaud**
Académie des Sciences, Belles-Lettres & Arts de Lyon

Parcours scientifique

9/2004 – 1/2006 : **Délégation au CNRS (12+6 mois)**
Institut de Physique Nucléaire de Lyon, France
- *Mise en place et démarrage de l'expérience EDELWEISS II au Laboratoire Souterrain de Modane*
- *Développement de détecteurs cryogéniques scintillants*

9/2001 → : **Maître de Conférence, expérience EDELWEISS**
Institut Universitaire Technologique B, Université Claude Bernard, Lyon
- *Enseignement d'électronique en DUT*

Institut de Physique Nucléaire de Lyon, France
- *Responsable du projet blanc ANR SciCryo sur la scintillation cryogénique (IPN Lyon, IAS Orsay, MPP Munich et LPCML Lyon)*
- *Etude par calorimétrie de fissures dans des cristaux cryogéniques*
- *Mise au point d'une acquisition rapide au standard PXI*
- *Etude du veto anti-muon pour EDELWEISS II, caractérisation des modules de veto*

12/1998 – 9/2001 : **Physicien post-doc, collaboration CRESST**
Max-Planck-Institut für Physik, Munich, Allemagne
Laboratori Nazionali del Gran Sasso, Italie
- *Implication dans le fonctionnement in situ de l'expérience*
- *Réduction du bruit de fond des détecteurs*
- *Développement de calorimètres scintillants cryogéniques*

9/1995 – 10/1998 : **Doctorant, expérience EDELWEISS**
Commissariat à l'Energie Atomique, Saclay (DAPNIA/SPP), France
- *Mise en œuvre de calorimètres cryogéniques ionisation-chaleur en Ge*
- *Programmation C++ et Java pour l'analyse hors-ligne*
- *Application aux données d'une technique de filtrage en fréquence*
- *Analyse physique des données*

Animation scientifique et vulgarisation

2007–2008 : **Membre du LOC conférence** *Dark Energy and Dark Matter* `http://cralconf.univ-lyon1.fr/2008`

2007–2008 : **Co-organisateur atelier** *CryoScint08*

2007 : **Organisateur atelier** *CryoScint07* `cryoscint07.in2p3.fr`

7/10/2007 : **Participation à une émission radio sur la matière sombre,** *Radio Pluriel*

2004– : **Membre de la commission de spécialistes, Section 29, UCBL**

Formation

1995 – 1998 : **Doctorat en physique des particules**
Commissariat à l'Energie Atomique, Saclay, France — Université Paris XI
"Recherche de matière sombre non-baryonique au moyen d'un bolomètre à ionisation dans le cadre de l'expérience EDELWEISS"

1995 : **DEA physique des gaz et des plasmas**
Université Paris XI

1992 – 1995 : **Diplôme d'ingénieur**
Ecole Centrale Paris

Publications de P. Di Stefano

Université Claude Bernard, Lyon — Institut de Physique Nucléaire de Lyon

Articles dans revues avec comité de lecture

[1] J. Åström, P. C. F. Di Stefano, F. Pröbst, L. Stodolsky, and J. Timmonen, Physical Review E (submitted), **Brittle fracture down to femto-Joules — and below**, www.arxiv.org/abs/0708.4315.

[2] S. Fiorucci et al., Astroparticle Physics **28**, 143 (2007), **Identification of backgrounds in the EDELWEISS-I dark matter search experiment**.

[3] A. Benoit et al., Nuclear Instruments and Methods in Physics Research A **577**, 558 (2007), **Measurement of the response of heat-and-ionization germanium detectors to nuclear recoils**.

[4] J. Åström et al., Physics Letters A **356**, 262 (2006), **Fracture Processes Observed with a Cryogenic Detector**, www.arxiv.org/abs/physics/0504151.

[5] V. Sanglard et al., Physical Review D **71**, 122002 (2005), **Final Results of the EDELWEISS-I Dark Matter Search with Cryogenic Heat-and-Ionization Ge Detectors**, www.arxiv.org/abs/astro-ph/0503265.

[6] A. Benoit et al., Physics Letters B **616**, 25 (2005), **Sensitivity of the EDELWEISS WIMP Search to Spin-Dependent Interactions**, www.arxiv.org/abs/astro-ph/0412061.

[7] O. Martineau et al., Nuclear Instruments and Methods in Physics Research A **530**, 426 (2004), **Calibration of the EDELWEISS cryogenic heat-and-ionization germanium detectors for dark matter search**, www.arxiv.org/abs/astro-ph/0301657.

[8] P. C. F. Di Stefano et al., Journal of Applied Physics **94**, 6887 (2003), **A Textured Si Calorimetric Light Detector**, www.arxiv.org/abs/physics/0307042.

[9] A. Benoit et al., Physics Letters B **545**, 43 (2002), **Improved Exclusion Limits from the EDELWEISS WIMP Search**, www.arxiv.org/abs/astro-ph/0206271.

[10] G. Angloher et al., Astroparticle Physics **18**, 43 (2002), **Limits on WIMP Dark Matter Using Sapphire Cryogenic Detectors**.

[11] P. C. Di Stefano, Journal of Physics G: Nuclear and Particle Physics **27**, 1959 (2001), **Expériences de détection directe de la matière sombre non baryonique**.

[12] A. Benoit et al., Physics Letters B **513**, 15 (2001), **First Results of the EDELWEISS WIMP Search Using a 320 g Heat-and-Ionization Ge Detector**, www.arxiv.org/abs/astro-ph/0106094.

[13] P. Di Stefano et al., Astroparticle Physics **14**, 329 (2001), **Background Discrimination Capabilities of a Heat and Ionization Cryogenic Detector**, www.arxiv.org/abs/astro-ph/0004308.

[14] A. Benoit et al., Physics Letters B **479**, 8 (2000), **Event categories in the EDELWEISS WIMP search experiment**, www.arxiv.org/abs/astro-ph/0002462.

Contributions à des conférences avec comité de lecture

[1] P. C. F. Di Stefano et al., Journal of Low Temperature Physics (2007), **The SciCryo project and cryogenic scintillation of Al_2O_3 for dark matter**.

[2] J. Åström et al., Nuclear Instruments and Methods in Physics Research A **559**, 754 (2006), **Fracture processes studied in CRESST**.

[3] P. C. F. Di Stefano et al., New Astronomy Reviews **49**, 251 (2005), **EDELWEISS dark matter search update**.

[4] S. Marnieros et al., Nuclear Instruments and Methods in Physics Research A **520**, 101 (2004), **Latest results from the EDELWEISS WIMP search**.

[5] O. Martineau et al., Nuclear Physics B (Proceedings Supplements) **124**, 177 (2003), **Dark matter search in the EDELWEISS experiment**.

[6] F. Proebst et al., Nuclear Physics B (Proceedings Supplements) **110**, 67 (2002), **Results of CRESST phase I**.

[7] O. Martineau et al., Nuclear Physics B (Proceedings Supplements) **110**, 70 (2002), **Dark matter search in the EDELWEISS experiment**.

[8] G. Chardin et al., Nuclear Physics B (Proceedings Supplements) **87**, 74 (2000), **Status of the EDELWEISS experiment**.

[9] M. Loidl et al., Nuclear Instruments and Methods in Physics Research A **444**, 293 (2000), **Diffusion of long-lived quasiparticles over long distances**.

[10] M. Bravin et al., **Simultaneous Measurement of Phonons and Scintillation Light for Active Background Rejection in the CRESST Experiment**, in *8th International Workshop on Low Temperature Detectors (LTD 8), Dalfsen, Netherlands., 15–20 August 1999*, 2000.

[11] O. Meier et al., Nuclear Instruments and Methods in Physics Research A **444**, 350 (2000), **Active Thermal Feedback for Massive Cryogenic Detectors**.

[12] M. Sisti et al., **The CRESST Dark Matter Experiment: Status and Perspectives**, in *8th International Workshop on Low Temperature Detectors (LTD 8), Dalfsen, Netherlands., 15–20 August 1999*, 2000.

[13] L. Bergé et al., Nuclear Physics B (Proceedings Supplements) **70**, 69 (1999), **Status of the EDELWEISS experiment**, www.arxiv.org/abs/astro-ph/9801199.

[14] D. Drain et al., Physics Reports **307**, 298 (1998), **Status of the EDELWEISS Experiment**.

Autres contributions à des conférences

[1] P. C. F. Di Stefano et al., Journal of Physics: Conference Series **39**, 70 (2006), **Status and outlook of the EDELWEISS experiment**.

[2] P. C. F. Di Stefano, **Low-Temperature Direct Dark Matter Searches**, in *Frontiers of the Universe*, edited by L. Celnikier and J. T. T. Vân, XIIIrd Rencontres de Blois, pages 85–93, Thê Giói, 2001.

[3] P. Di Stefano et al., **Development of Scintillating Calorimeters for the CRESST Experiment**, in *3rd International Workshop on the Identification of Dark Matter (IDM 2000), York, GB, 18–22 September 2000*, edited by N. J. C. Spooner and V. Kudryavtsev, World Scientific, London, 2001.

[4] P. Di Stefano et al., **The CRESST Experiment: Recent Results and Prospects**, in *Cosmology and Particle Physics (CAPP 2000), Verbier, Switzerland, 18–27 July 2000*, edited by R. Durrer, J. Garcia-Bellido, and M. Shaposhnikov, pages 381–386, American Institute of Physics, Melville, NY, 2001, www.arxiv.org/abs/hep-ex/0011064.

[5] J. Gascon et al., **The EDELWEISS Experiment: Status and Outlook**, in *International Conference on Dark Matter in Astro and Particle Physics (Dark 2000), Heidelberg, Germany, 10–16 July 2000*, 2000.

[6] J. Jochum et al., **The CRESST Dark Matter Search**, in *Fourth International Symposium on Sources and Detection of Dark Matter in the Universe (DM 2000), Marina Del Rey, USA, 23–25 February 2000*, edited by D. B. Cline, Springer-Verlag, Berlin, 2001.

[7] G. Chardin et al., **Preliminary Results of the EDELWEISS Experiment**, in *2nd International Workshop on the Identification of Dark Matter (IDM 1998), Buxton, GB, 7–11 September 1998*, edited by N. J. C. Spooner and V. Kudryavtsev, World Scientific, London, 1998.

Communications scientifiques de P. Di Stefano

1 Présentations invitées à des conférences

- *Direct Dark Matter Searches*
  Tools for Susy and the New Physics (Tools 06),
  Annecy, France, 20-26 juin 2006

- *Status and Outlook of the EDELWEISS Experiment*
  The IXth International Conference on Topics in Astroparticle and Underground Physics (TAUP 2005),
  Zaragoza, Espagne, 10-14 septembre 2005

- *New Limits from the EDELWEISS Experiment*
  The New Cosmology Confronts Observation Conference,
  Santa Barbara, Californie, 19–23 août 2002

- *Low-Temperature Direct Dark Matter Searches*
  XIIIèmes Rencontres de Blois,
  Blois, France, 17–23 juin 2001

2 Présentations à des conférences ou réunions internationales

- *SciCryo and Cryogenic Scintillation of Sapphire*
  CryoScint08, IPN Lyon, France, 23 avril 2007

- *Recherche directe de la matière sombre non-baryonique*
  Groupe de recherche sur la supersymétrie, LPSC, Grenoble, France, 7 avril 2005

- *Recent Results from the EDELWEISS Dark Matter Search*
  Sources and Detection of Dark Matter and Dark Energy in the Universe (DM2004), Marina del Rey, Californie, 18–20 février 2004

- *Update on the Lyon EDELWEISS Group*
  Réunion du réseau cryogénique européen, Naples, Italie, 29 novembre 2002

- *EDELWEISS at the LSM Underground Laboratory*
  2nd Snolab Workshop, Université Carleton, Ottawa, Canada, 21 novembre 2002

- *The CRESST Experiment: Results and Outlook*
  Session de printemps de la Deutsche Physikalische Gesellschaft (DPG), Hambourg, Allemagne, 26 mars 2001

- *Development of Scintillating Calorimeters for the CRESST II Experiment*
  Identification and Detection of Dark Matter workshop (IDM 2000), York, Angleterre, 18–22 septembre 2000

- *Status of the CRESST Experiment*
  Cosmology and Particle Physics conference (CAPP 2000), Verbier, Suisse, 17–28 juillet 2000

- *Development of Scintillating Calorimeters for the CRESST Experiment*
  Réunion du réseau cryogénique européen, Milan, Italie, 24 mars 2000

- *Status of the CRESST Experiment*
  Réunion du réseau cryogénique européen, Naples, Italie, octobre 1999

- *Surface Events in an Ionizing Calorimeter*
  Réunion du réseau cryogénique européen, Gran Sasso, Italie, avril 1998

- *Recent Results from EDELWEISS*
  Présentation à la section LSP du Groupe de Recherche sur la Supersymétrie, Laboratoire de l'Accélérateur Linéaire, Orsay, octobre 1997

- *Status of the EDELWEISS Experiment*
  Topics in Astroparticle and Underground Physics conference (TAUP 97), Gran Sasso, Italie, 7–11 septembre 1997

3 Séminaires

- *Détecteurs cryogéniques, de la matière sombre à la rupture de matériaux*
  Ecole Normale Supérieure de Lyon, France, 29 janvier 2007

- *An Update on the EDELWEISS Dark Matter Search*
  Stanford Linear Accelerator, Stanford, Californie, 24 février 2004

- *Recent Results from the EDELWEISS Dark Matter Search*
  Lawrence Berkeley Laboratories, Berkeley, Californie, 17 février 2004

- *Low-Temperature Direct Dark Matter Searches*
  Institut de Physique, Université de Zurich, Suisse, 27 novembre 2002

- *Low-Temperature Direct Dark Matter Searches*
  Queen's University, Kingston, Canada, 8 août 2002

- *Expériences cryogéniques de recherche de la matière sombre non-baryonique*
  Institut de Physique Nucléaire, Orsay, France, 8 juillet 2002

- *Recherche de matière sombre non baryonique et développement de calorimètres scintillants dans le cadre de l'expérience CRESST*
  Collège de France, Paris, France, 28 septembre 2000

- *Dark Matter Direct Detection Experiments*
  LAPP Annecy, France, 9 juin 2000

- *Expérience CRESST: Résultats Récents et Développement de Calorimètres Scintillants*
  IPN Lyon, France, 12 mai 2000

- *Résultats Récents d'EDELWEISS*
  Service de Physique des Particules, CEA Saclay, juin 1998

- *The EDELWEISS Dark Matter Search with Ionizing Calorimeters*
  Max-Planck-Institut für Physik, Munich, Allemagne, mai 1998

- *The EDELWEISS Experiment*
  Laboratoire de Physique Subatomique, Université de Montréal, 15 décembre 1997

P. Di Stefano, Maître de Conférence

1 Activités d'enseignement et responsabilités pédagogiques

1.1 GEII/IUT B — Université Claude Bernard Lyon I

Depuis septembre 2001, service complet d'enseignement (au moins 192 h équivalentes TD par an) sauf pendant 18 mois de délégation au CNRS (sept. 2004–jan. 2006). Préparation et correction de partiels. Saisie de notes et participation aux jurys.

Responsable module L2 *Basic Physics of Energy Conversion* (24 h, en anglais) (2007–2008)

Responsable pédagogique d'étudiants L1 et L2 DUT (2003–2004, 2006–2008)

TDs et TPs d'électronique, option électronique, L2 DUT (2007–2008)

TDs et TPs d'électronique, tronc commun, L2 DUT (2006–2008)

TDs et TPs d'électronique, tronc commun, L1 DUT (2001–2004, 2006–2008)

TPs de CAO électronique, L1 DUT (2006)

Suivi d'étudiants en stage, L2 DUT (2001–2004, 2006–2008)

Encadrement d'étudiants en DUETI (double diplôme) à l'étranger (2002–2004, 2006–2007)

1.2 Université Technique de Munich

Enseignement en langue allemande, environ 3 heures par semaine pendant un semestre.

TDs de physique, 3ème année d'études d'ingénieurs (2000)

TPs d'électromagnétisme, 3ème année d'études d'ingénieurs (2000)

2 Encadrement de stages scientifiques et de thèses

2.1 Institut de Physique Nucléaire de Lyon (CNRS-IN2P3/UCBL)

- Co-direction de thèse:
  - 2007–: Marc-Antoine Verdier, *Détecteurs scintillation-chaleur dans EDELWEISS II*
  - 2004–2007: Melisa Luca, *Scintillateurs cryogéniques pour la matière sombre* (soutenue 20/07/2007)
- Responsable de stage M2/DEA:
  - 2007: Marc-Antoine Verdier, *Mise en place d'un banc de mesure pour la scintillation cryogénique*
  - 2004: Melisa Luca, *Mise au point d'un dispositif expérimental pour l'étude des cristaux scintillants dans le cadre de l'expérience EDELWEISS*
- Responsable de stage M1 (TERE ou été):
  - 2006: Marc-Antoine Verdier, *Carcactérisation de l'orientation de cristaux de saphir*
  - 2004: Anne Bonnin, *Réalisation d'un banc d'essai pour les scintillateurs*
  - 2003: Samira Chermati, *Etude de cristaux scintillants à basse température*
- Participation à l'encadrement des stages et des thèses du groupe:
  - 2001–2004: Encadrement de la partie expérimentale de la thèse de Laurent Chabert, *Etude du fond neutron induit par les muons dans l'expérience EDELWEISS*

2.2 Institut Max Planck pour la Physique, Munich

Participation à l'encadrement de 2 étudiants en thèse dans le groupe de recherche (1998–2001).

Contents

1 Dark Matter and Direct Detection **7**
1.1 A decades-old enigma . . . 7
1.2 Earth, fire, water and WIMPs . . . 8
1.3 The direct detection challenge . . . 9
1.4 Direct detection experiments . . . 9
1.5A Review of direct detection . . . 13

2 The EDELWEISS and CRESST Direct Detection Experiments **15**
2.1 CRESST . . . 15
2.2 EDELWEISS . . . 15
2.3 EURECA . . . 17
2.4A Results from CRESST . . . 19
2.5A Detectors for EDELWEISS . . . 21
2.6A Results from EDELWEISS . . . 23

3 WIMPs and Neutrons **25**
3.1 Passive and active shielding for EDELWEISS II . . . 25
3.2 Light targets as complements to Ge . . . 26
3.2.1 Neutron interactions . . . 26
3.2.2 WIMP interactions . . . 28
3.3 Background reduction using coincidences and different materials . . . 29
3.4A EDELWEISS internal note on neutrons . . . 33

4 Cryogenic Scintillation **35**
4.1 Cryogenic light detectors and scintillators . . . 35
4.2 Cryogenic Scintillation of Sapphire . . . 36
4.2.1 Scintillation and trace analysis . . . 36
4.2.2 Tests from room temperature to 10 K . . . 37
4.2.3 A scintillation-phonon detector in EDELWEISS II . . . 37
4.3A Optimization of light detectors . . . 41
4.4A The SciCryo project . . . 43

5 Calorimetric Detection of Fracture **45**
5.1 The curious cracking cryogenic crystal . . . 45
5.2 Brittle fracture and earthquakes . . . 47
5.3 Towards detection of single-bond fractures . . . 49
5.4A Cryogenic fracture . . . 51
5.5A Towards single bonds . . . 53

6 Summary and outlook **55**

References **60**

Chapter 1

Dark Matter and Direct Detection

1.1 A decades-old enigma

The question of dark matter has been open since 1933. Two landmark observations had recently been made by astronomer Edwin Powell Hubble. The first, in 1924-25, was that the Universe is not limited to our Milky Way, but that there are objects "far outside the limits of the galactic system" [2, 3]. The second, in 1929, was that our Universe is not static but expanding, with a velocity proportional to distance [4, 5]. These observations were made possible by the best telescope at the time, operated at Mount Wilson in Southern California by the philanthropic Carnegie Institution. In addition to a then-record diameter of 100 inches (254 cm), it benefitted from the clear skies above nearby Los Angeles — surprising as it may seem today. Apart from Hubble, the observatory attracted a host of other talented and ambitious astronomers such as Walter Baade [6].

Mount Wilson also attracted somewhat of a maverick, Fritz Zwicky. Zwicky was born in 1898 in Varna, now part of Bulgaria, of Swiss parents, and trained as a physicist in Switzerland. In 1925 he began a long career at the California Insitute of Technology, working his way up from postdoc to assistant professor by l929 [6]. Though he had an abrasive personality that eventually isolated him from many colleagues [7], he was a polymath and made some important contributions to astronomy that were given due recognition at the time. For instance, along with W. Baade, he popularized the concept of supernovae [8] and proposed a mechanism to explain them [9] — though we now know that the mechanism he proposed, gravitational collapse to a neutron star, corresponds to a type of supernova other than the thermonuclear-driven one he observed at the time [7]. It is also interesting to note that, though the expansion of the Universe is a cornerstone of current cosmology, it was not always so: Baade and Zwicky declared in their 1934 paper [9] that *"we ourselves are by no means convinced that the universe is expanding"*[1]. Other observations and theories put forth by Zwicky, such as gravitational lensing [10], did not have much impact at the time, but now appear prescient. Still others, like the suggestion that redshifts are in fact caused by a gravitational interaction between photons and matter causing the former to lose momentum [11], are now discredited.

In 1933, Zwicky published a set of observations in a German-language Swiss physics journal, under the title *The Redshifts of Extragalactic Nebulae* [12]. This title reflects that the measurement of redshifts — the Doppler-shift in wavelength of receeding light sources such as galaxies that Hubble had used to establish the expansion of the universe — was still a fairly young science. Moreover, *extragalactic nebulae* is an acknowledgement of Hubble's recent demonstration that there is more to the universe than the Milky Way [3], and refers to what are now known as galaxies. The article itself contains contains a study of the redshifts of the galaxies making up the Coma cluster. By applying the virial theorem to the spread of radial velocities, Zwicky determined that the gravitational

[1] Anyone still unconvinced by the expansion of the Universe need only look at the proliferation of titles available at amazon.com: *The Extravagant Universe*, *The Elegant Universe*, *The Beautiful Universe*, *Endless Universe*, *The Intelligent Universe*, *The Early Universe*, *The Inflationary Universe*, *The Electric Universe*, *Strange Universe*, *The Invisible Universe*, *Magnificent Universe* .... The only limit seems to be the supply of descriptive adjectives.

density of matter in the cluster must be 400 times greater than the visible density of matter. Zwicky therefore remarked that the system must contain a large amount of *dunkle Materie*, or dark matter.

Perhaps in part because he was an outsider among astronomers, perhaps also because the relevant observational techniques took a long time to develop, Zwicky's observation generated little interest for several decades, though discrepancies between gravitational and visible masses were soon also noted in the Virgo cluster by Sinclair Smith, who mentions Zwicky's result [13]. The Smithsonian/NASA Astrophysics Data System bibliography system finds a mere two references — self-cites, at that — to Zwicky's paper in the first quarter century following 1933, but Smith's citation is not registered — a reminder not to blindly trust automated bibliometrics. The first independent citation only registers in 1960 [14]; it confirms that most of the matter in Coma does not consist of observable objects. Citations take off in the late 1970's, as observations of galactic rotation curves indicate, at smaller scales than galaxy clusters, the presence of dark matter [15]; also, undoubtedly, because cross-referencing had improved. Today, a wide range of observations with different techniques indicate the presence of dark matter from SN all the way to the CMB [7]. Modern studies of the gravitational lensing suggested by Zwicky also provide more insight. For instance, weak lensing has been used to show that, after the merger of two galaxy clusters, the gravitational potential does not follow the baryon distribution observed with X-rays; this indicates most of the mass in the system is non-baryonic and weakly interacting [16]. Moreover, microlensing demonstrates that less than 8% of our dark matter halo can be made out of massive, compact objects [17]. Structure formation [18] indicates that the dark matter is probably made up of weakly-interacting, massive particles: WIMPs. What these WIMPs actually are remains a mystery.

1.2 Earth, fire, water and WIMPs

Empedocles is said to have thought the world was made up of four elements, earth, fire, water and air, whose interactions where mediated attractively by love or repulsively by hate [19]. Modern particle physicists believe it is made up by the particles of the standard model [20]: bosons and fermions, the latter consisting of quarks and leptons. From a theoretical standpoint, the particles are all related to one another by mathematical symmetries and the $SU(3)_C \times SU(2)_L \times U(1)_Y$ group. There is overwhelming experimental evidence for almost all the members of the standard model, with the notable exception of the Higgs boson [21] which is needed to provide the masses of the particles. The Higgs boson is the main target of the Large Hadron Collider (LHC) at CERN scheduled to start hunting it in 2008. Finding the Higgs boson would not be surprising; not finding it would be worrisome.

The standard model is not totally satisfying however. For one thing, it does not include the force we are perhaps most familiar with, gravitation. Moreover, it contains a large number of parameters (29) that may seem arbitrary. For these reasons, many theorists believe the standard model is but a subset of a more complete description of nature. One of the most compelling extensions is called supersymmetry (SUSY). As its name implies, it postulates an additional symmetry, called R, linking each known boson to a new fermion, and each known fermion to a new boson. In many of these models, the lightest supersymmetric partner (LSP) is the neutralino, a combination of the spartners of the Higgs, Z and photon. If R-parity is conserved, the LSP is stable because it can not decay into a lighter, non-SUSY particle. It was pointed out in 1982 that supersymmetric particles were good candidates to be WIMPs [22]; at the time the principle suspect was the gravitino, today it is the neutralino [23].

Supersymmetry is also one of the targets of accelerator experiments like the LHC [24]. Indeed, there have already been claims in the past that SUSY has been discovered (some discussed in [25]), though they have been rapidly debunked. Despite these false alarms, SUSY remains the most credible theoretical framework for WIMP-type particles (there are other non-SUSY candidate particles such as axions, for which whatever early experimental evidence there may be [26] is still unconfirmed). SUSY provides predictions for the mass of the neutralino, which should be in the 10 GeV–1 TeV range. It also provides predictions regarding the coupling of WIMPs to matter. These can be of two types: those that depend on the spin of the target nucleus and those that do

not. The latter amount at most to some 10^{-42} cm^2, which is already quite small, equivalent to a mean free path in matter of the order of a few hundred light years, and giving a second justification to the name WIMP. Moreover, SUSY provides not a precise value for the cross-section, but a range, and the cross-sections could in fact be several orders of magnitude smaller yet (Fig. 1.3).

1.3 The direct detection challenge

There are two approaches to finding dark matter. In the indirect approach, experimenters look for the products created by annihilation of WIMPs that have been trapped gravitationally. These products can be photons from WIMPs in the center of our galaxy or in other galaxies, or neutrinos, for the WIMPs that may have accumulated in the Sun or perhaps even the Earth. In the past few years, some hints have started to appear, for instance in the gamma-ray excess at GeV energies observed by the EGRET satellite [27], or the excess at 511 keV observed by INTEGRAL [28]. However, there does not seem to be a dark matter scenario compatible with all of these observations, and they could be due to other astrophysical processes.

In the direct approach, the particles themselves are sought in an earthbound detector. Cryogenic super-conducting grains were proposed as a neutrino detector in the early 1980's [29]. It was then pointed out that such devices should also be able to detect WIMPs [30]. However, the experimental challenge is great, and theoretical uncertainties abound. In addition to the uncertainties on the cross section σ and mass m, the distribution of dark matter around us is not very well-known. It is generally assumed that the WIMPs form a spherical dark matter halo with a local mass-density of 0.3 GeV/cm^3, and a Maxwellian velocity distribution with an rms speed of 250 km/s. However, this picture is surely a simplification, and more complicated models have been proposed, based on simulations of the formations of galaxies. They could lead to a clumpy dark matter distribution [31], meaning that the interaction rate could be enhanced or reduced in proportion to the local dark matter density. However, the effect is less pronounced than with indirect detection for which the annhiliation rate varies like the square of the dark matter density. To put these interaction rates of less than one count per week and kilogram into perspective, the rate of cosmic muons at the surface of the earth is about 1 /cm^2/minute [20]. Moreover, the natural radioactivity of a typical human body, due mainly to ^{40}K and ^{14}C, amounts to about 100 disintegrations per second and per kilogram of human. Therefore, any dark matter detector will have to be deep underground and shielded from usual levels of radioactivity.

In addition to this low rate of interactions, a second experimental challenge comes from the energy distribution of the events. In addition to the ingredients of the rate calculation, this takes into account straightforward elastic-scattering kinematics that describe the efficiency with which a WIMP transfers its energy to a nucleus. It also takes into account the nuclear physics of the WIMP-nucleus interaction, by way of a form factor subject itself to theoretical uncertainties. Convoluting this with the full WIMP velocity distribution leads to a spectrum of recoil energies in the detector well approximated by a decaying exponential [32, 33] (Fig. 1.1):

$$\frac{d\mathcal{R}}{dE_R} = \frac{\mathcal{R}_0}{\eta E_0} e^{-\frac{E_R}{\eta E_0}},$$

where E_R is the recoil energy and ηE_0 its average value. This spectrum has a characteristic energy scale E_0; unfortunately it is not known *a priori* as it depends on the WIMP mass. The typical energy scale involved is of the order of a few keVs or perhaps tens of keVs, and increases as WIMP mass increases: the lighter the WIMP, the steeper the recoil spectrum; conversely, the heavier the WIMP, the flatter the spectrum. The energies involved are quite small, and this is the second experimental challenge in addition to the low rate.

1.4 Direct detection experiments

Though the detectors originally proposed for direct detection were cryogenic, such detectors have only recently begun to realize their potential in such searches. Indeed, the first searches were carried

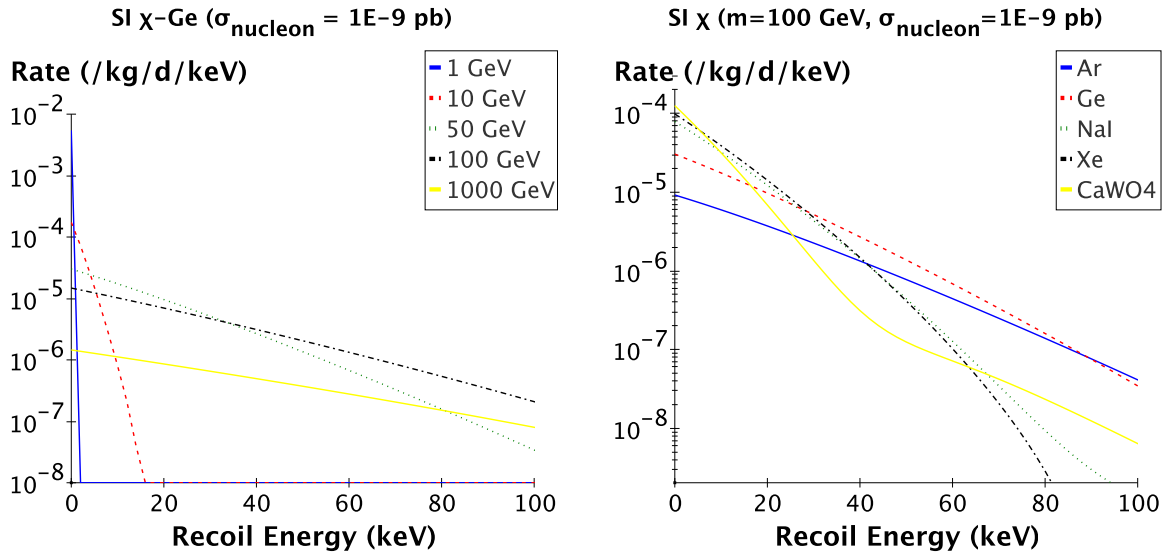

Figure 1.1: Left: the theoretical recoil energy spectra left by WIMPs on germanium, for WIMP masses between 1 GeV and 1 TeV, in the spin-independent case (shape of spectra and evolution with WIMP mass are similar in the spin-dependent case). The integrated rates are less than an event per week per kilogram of detector. Spectra fall off with an exponential-ish shape; the lighter the WIMP, the harder the fall. Right: spin-independent recoil spectra from a 100 GeV WIMP on various targets. Effect of form factor is visible for heavy targets like W and Xe.

out with existing germanium ionization detectors from double-beta decay searches [34, 35]. In these semi-conducting detectors, the nuclear recoil created by the elastic scattering of a WIMP would create electron-hole pairs read out by electrodes. These detectors where optimized for a low background in the MeV-energy region were the two electrons coming from neutrinoless double-beta decay are expected, and the data analysis was extended to the low-energy region relevant for a WIMP signal. These detectors boast good radioactive background because semi-conductors are easy to purify chemically, and can come in units of the order of kilograms. Similar experiments had the best sensitivity until the mid 1990's [36]. At that point, they were surpassed by scintillation detectors in which the nuclear recoil causes scintillation which is read by photomultipliers. A wide variety of target nuclei is available; the best sensitivities were obtained with NaI(Tl) [37]. This technique is available in larger units, of the order of 10 kg, and possesses a rough form of background discrimination based on pulse-shape analysis, though this is not effective down to the energies relevant for WIMP searches [38]. Since the turn of the millenium, cryogenic detectors in experiments such as CDMS [39], EDELWEISS [40] and CRESST [41], have been at the forefront of dark matter searches. However, rather than superconducting grains, they are calorimeters, crystals cooled to a few 10's of milliKelvin. The nuclear recoil caused by a scattering WIMP creates a slight temperature rise in the crystal which is read by a very sensitive thermometer. Basic thermodynamics imply this measures all of the deposited energy. This phonon signal provides excellent resolution and threshold. However, the strong point of the detectors is that in an appropriate crystal, the nuclear recoil can also create ionization or scintillation, and this second signal provides excellent rejection of the dominant highly ionizing radioactive background, down to keV energies. Recently-arrived competitors in the field are noble-liquid detectors that combine an ionization and scintillation measurement to identify radioactive backgrounds. This technique seems relatively straightforward to scale-up, and the XENON experiment now has the best sensitivity pending peer-review [42] (Fig. 1.3). Improving sensitivity will require doing away with the remaining background events (probably a combination of leakage from the electron-recoil band and mis-identified multiple scatters). Superheated droplet detectors like those of the PICASSO experiment are also starting to yield results [43]. More

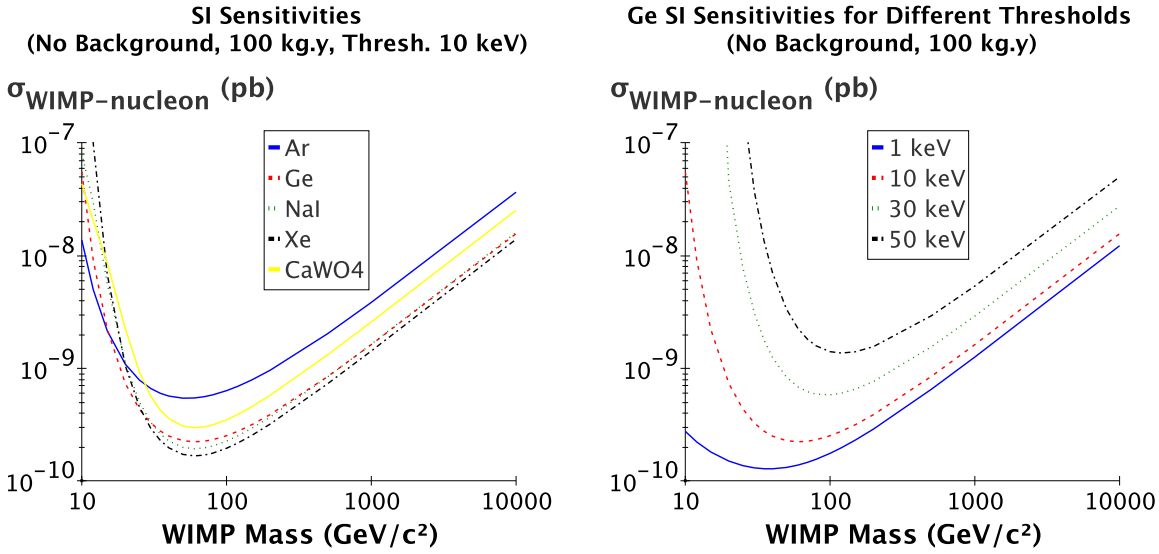

Figure 1.2: Effect of target (left) and threshold (right) on spin-independent sensitivity. In both cases, equal exposures and absence of background are assumed.

information on the all these various types of experiments is available in Ref. [44] reproduced in Sec. 1.5A.

Several factors come into play when discussing detectors. For WIMPs that couple in a spin-independent manner, heavier nuclei are favored; however their advantage is somwhat reduced by the quenching factor. The sensitivities of various heavy targets now in use are shown in Fig. 1.2, assuming no background and equal thresholds and exposures. The differences amount to a factor ≈ 3. The effect of threshold is also shown in Fig. 1.2 for germanium. This demonstrates that lower thresholds are more sensitive to light WIMPs; however for the ≈ 100 GeV WIMPs favored by theory, the difference between a 10 keV and a 30 keV threshold amounts to about a factor 3. For heavier WIMPs, since the WIMP spectrum flattens out and $E_0 \gg E_{thresh}$, sensitivitites depend on the threshold in a linear fashion.

In practice, the main factor is background and the ability to reject it. As long as there is no background, experiments run with a sensitivity that improves with the exposure MT. Once a background has been encountered, this sets the sensitivity. An experiment that can reject part of this background has a sensitivity that improves with $\sqrt{MT}$. An experiment that is able to reject all of its background is again able to improve its sensitivity with MT. The ability to reject background is crucial for a successful dark matter experiment. This has enabled experiments like CDMS [46], EDELWEISS [49] and CRESST [41] to set more stringent limits on dark matter than heavier, less-rejecting detectors.

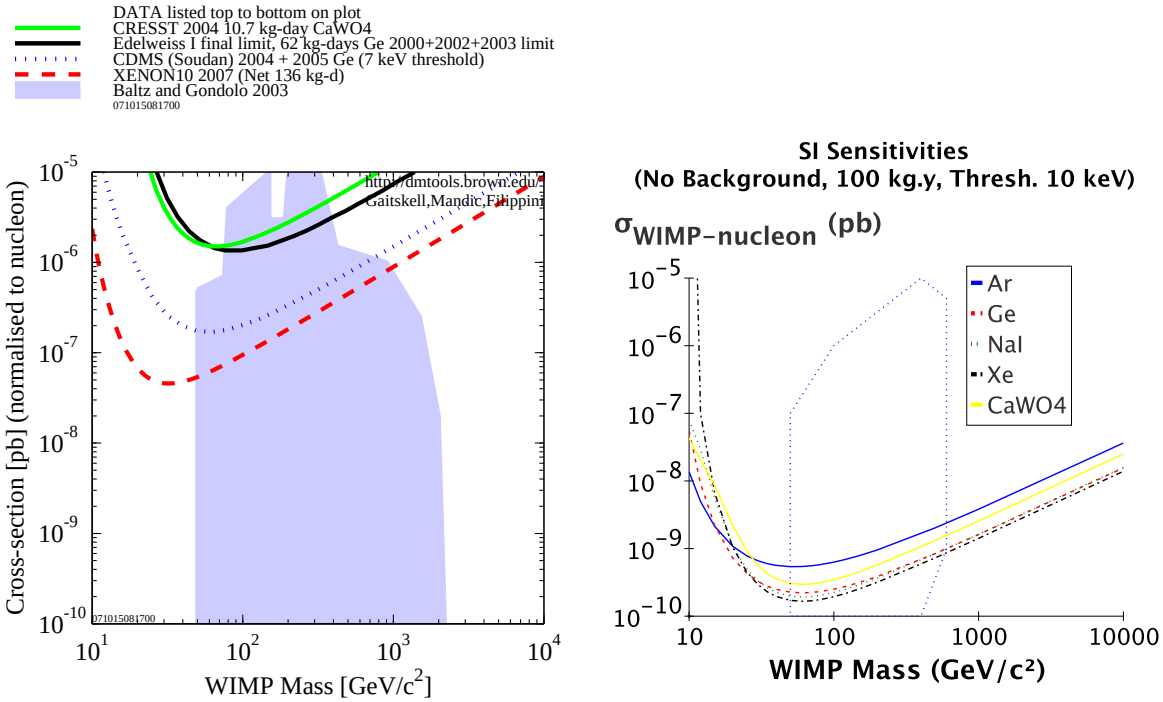

Figure 1.3: Left: current limits set by some experiments [45] (CDMS [46], CRESST [41], EDELWEISS [47] and XENON [42]). Experiments have started to enter the parameter space predicted by supersymmetric theory. Several orders of magnitude in cross-sections remain to be explored, down to between 10^{-10} pb and 10^{-15} pb depending on the supersymmetric model. Right: reaching close to 10^{-10} pb will require 100 kg-scale experiments with exposures of the order of a year and no background. Closed dotted contour is an example of SUSY predictions [48].

1.5A Review of direct detection

Ref. [44].

INSTITUTE OF PHYSICS PUBLISHING JOURNAL OF PHYSICS G: NUCLEAR AND PARTICLE PHYSICS

J. Phys. G: Nucl. Part. Phys. **27** (2001) 1959–1974 PII: S0954-3899(01)21984-7

Expériences de détection directe de la matière sombre non baryonique
Direct searches for non-baryonic dark matter

Philippe C Di Stefano

Max-Planck-Institut für Physik, Föhringer Ring 6, D-80805 München, Allemagne

E-mail: distefano@mppmu.mpg.de

Reçu le 14 Fevrier 2001, présentation définitive le 3 Juillet 2001
Publié 30 August 2001
En ligne à stacks.iop.org/JPhysG/27/1959

Résumé

La question astrophysique de la matière sombre, posée dans les années trente, attire depuis une quinzaine d'années des expériences de physique des particules hors accélérateur tentant d'y répondre par la mise en évidence de particules lourdes et interagissant faiblement. Le faible taux et la basse énergie des événements attendus rendent la tâche ardue. Les premiers détecteurs employés furent à ionisation, puis à scintillation, ceux-ci disposant d'une méthode rudimentaire pour rejeter le fond électromagnétique. Ces deux premières générations d'expériences massives sont aujourd'hui rattrapées par des nouveaux détecteurs cryogéniques associant une mesure de l'ionisation à un signal phonons, qui permettent de rejeter le fond électromagnétique très efficacement. Ces dispositifs, et de récents développements de mesure simultanée de scintillation et de phonons, pourraient donner l'avantage aux détecteurs cryogéniques.

Abstract

Since the mid-1980s, non-accelerator particle physics experiments have been searching for weakly interacting massive particles which could solve the dark matter enigma first pointed out some 70 years ago. The low event rate and energies expected pose a formidable experimental challenge. The first detectors were ionization devices, soon followed by scintillation detectors able to reject a small portion of the photon and electron radioactive backgrounds. The performance of these early generations of detectors has now been matched by new cryogenic detectors in which a simultaneous reading of phonons and charge allows a very efficient rejection of the background. These devices, along with recently developed simultaneous phonon and scintillation techniques could provide cryogenic devices with a decisive advantage.

(Some figures in this article are in colour only in the electronic version)

 © 2001 IOP Publishing Ltd Printed in the UK

1. A la recherche de la masse perdue (In search of the missing mass)

1.1. La matière sombre, de l'astrophysique à la physique des particules (Dark matter, from astrophysics to particle physics)

La question de la matière sombre semble avoir été posée pour la première fois par l'astronome helvético-bulgare de Caltech Fritz Zwicky en 1933 dans un article étudiant les décalages vers le rouge de galaxies formant divers amas [1]. En appliquant le théorème du viriel, Zwicky constate que les galaxies visibles dans l'amas Coma se meuvent comme sous l'effet d'une masse volumique au moins 400 fois plus grande que celle dite lumineuse de l'amas, estimée à partir de la masse des parties visibles des galaxies qui la composent. Il en conclut qu'il doit y avoir une importante masse de matière sombre qui explique les mouvements des galaxies. Les observations plus récentes d'émissions X d'amas de galaxies [2] mettent en évidence un plasma intra-galactique ayant une masse un ordre de grandeur au dessus de celle de l'ensemble des galaxies, mais encore un ordre de grandeur inférieur à la masse totale de l'amas nécessaire pour contenir le gaz. L'étude des amas en tant que lentilles gravitationnelles pour des sources telles que les galaxies [3] confirme que leur masse gravitationnelle est environ un ordre de grandeur plus grand que leurs masses visibles par ailleurs. Cette énigme apparaît à d'autres échelles de l'univers, depuis les courbes de rotation galactiques [4] jusqu'aux fluctuations du fond cosmologique à 3 K [5].

Ces dernières observations, avec celles des distorsions gravitationnelles à grande échelle [6, 7] et celles des supernovae [8], convergent vers un modèle d'univers plat ($\Lambda = 0.7$ et $\Omega_{matière} = 0.3$) avec une composante baryonique limitée ($\Omega_{baryons}h^2 \approx 0.02$) compatible avec les résultats de nucléosynthèse [9]. Il faut donc une composante de matière sombre non baryonique et plus particulièrement de matière froide (soit n'ayant jamais atteint l'équilibre thermique dans l'évolution de l'univers, soit étant non relativiste au moment du découplage avec le rayonnement). Une des solutions les plus plausibles consiste en des particules lourdes, interagissant faiblement, autrement dit des *weakly interacting massive particles* (WIMPs).

Indépendamment de ces considérations astrophysiques, les WIMPs apparaissent en physique des particules, dans le cadre des théories supersymétriques et de la plus légère des particules supersymétriques, la *lightest supersymmetric particle* (LSP) [10]. Dans la plupart des modèles il s'agirait du neutralino, combinaison linéaire du zino, du photino et des higgsinos. Si la R-parité est conservée, la LSP serait stable et fournirait selon certains modèles un paramètre de densité de l'ordre de $\Omega_{LSP} \approx 0.2$, intéressant du point de vue cosmologique. La masse de la LSP serait de l'ordre de quelques GeV ou TeV (la limite inférieure obtenue sur accélérateur est de 46 GeV [11]). Les interactions du neutralino avec la matière seraient comprises entre les cas limites d'un couplage indépendant du spin du noyau cible (et une section efficace sur un noyau de numéro atomique A donnant une masse réduite μ de la forme $\sigma \sim A^2(\mu^2/\mu^2_{nucléon})\sigma_{nucléon}$) et un couplage en dépendant (et une section efficace alors fonction des facteurs de spin nucléaires $\sigma \sim CJ(J+1)(\mu^2/\mu^2_{proton})\sigma_{proton}$ [12]). Les figures 1 et 2 montrent des projections de l'espace des phases d'un modèle supersymétrique dans le plan section efficace sur nucléon, masse du WIMP. Les sections efficaces qui y paraissent sont très faibles, ce qui compliquera la mise en évidence de ces particules.

Plusieurs collaborations (telles que AGAPE [13], EROS [14], MACHO [15] et OGLE [16]) cherchent la matière sombre galactique de type baryonique par l'effet de microlentille gravitationnelle [17]. Au niveau de la Voie Lactée, ces expériences montrent que des objets baryoniques pesant moins d'un dixième de masse solaire (respectivement de l'ordre d'une masse solaire) ne peuvent représenter plus de 20% de la masse du halo (respectivement 40%) [18]. Des observations optiques directes d'objets de masse solaire fourniraient d'ailleurs

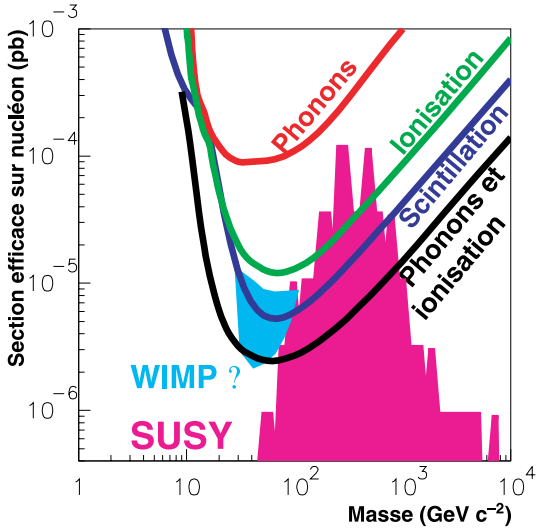

Figure 1. Prédictions supersymétriques (zone colorée [46]) et courbes d'exclusion expérimentales pour le couplage indépendant du spin (phonons [47], ionisation [29], scintillation [48, 49], WIMP hypothétique [50] et hybride phonons–ionisation [51,52]). Aux faibles masses, le seuil du détecteur est déterminant. Aux grandes masses, les courbes ont des asymptotes parallèles les unes aux autres ($\sigma \propto m$). Les calorimètres à ionisation dépassent les méthodes plus massives et éprouvées.

Figure 1. Theoretical WIMP spectra (curves) for various masses and cross section on germanium, and experimental spectrum (histogram and upper limit for a 90% confidence level). The expected spectra are exponentially decaying and are steeper when the WIMP is lighter. For a given mass, the cross section at which the theoretical spectrum is no longer compatible with the experimental one gives the limit for figure 2.

une limite inférieure à leur contribution au halo de 2% [19], mais ce résultat reste pour l'instant controversé [20]. Le modèle standard de halo de WIMPs consiste alors en une distribution à symétrie sphérique globalement au repos, avec une densité de masse $\rho \approx 0.3$ GeV cm^{-3} et des vitesses de WIMP distribuées selon une maxwellienne de vitesse quadratique moyenne 250 km s^{-1}. Le fait qu'au cours d'une année la Terre tourne autour du Soleil dans un plan différent de celui dans lequel le Soleil se déplace par rapport à la galaxie implique que la vitesse moyenne des WIMPs par rapport à la Terre subira une modulation annuelle, variant de $\approx$200 km s^{-1} en décembre à $\approx$240 km s^{-1} en juin.

1.2. Les défis de la détection directe (The direct detection challenge)

Il existe deux approches pour mettre en évidence ces particules. La détection indirecte cherche des produits d'annihilation de WIMPs piégés gravitationnellement. De grands détecteurs Čerenkov à eau, comme SuperKamiokande [21] au Japon et le projet ANTARES [22] en France, ou à glace comme AMANDA [23] dans l'Antarctique, pourraient voir les neutrinos issus de l'annihilation de WIMPs dans le Soleil; alors que des télescopes Čerenkov atmosphériques ou des satellites pourraient repérer les photons produits par l'annihilation dans des galaxies [24]. Quant à la détection directe, elle cherche à mettre en évidence les interactions des WIMPs eux-mêmes dans un détecteur (l'absorbeur). Cette technique fut proposée au milieu des années quatre-vingts [25] suite à une proposition dans le cadre de la détection de neutrinos [26].

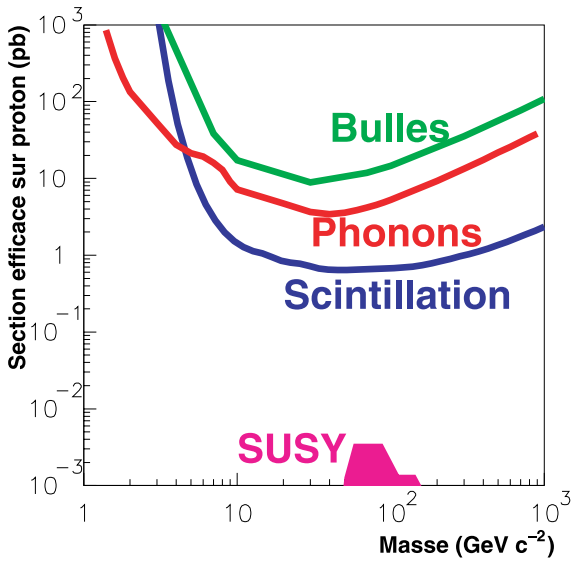

Figure 2. Prédictions supersymétriques (zone colorée [46]) et courbes d'exclusion expérimentales pour le couplage dépendant du spin (bulles [53, 54], scintillation [48, 49] et phonons [55]). Les détecteurs à ionisation sont absents à cause du manque de spin dans le germanium naturel ou enrichi en ^{76}Ge. Contrairement au couplage indépendant du spin, ces sections efficaces ne bénéficient pas d'un facteur d'amplification $\sim A^2$.

Figure 2. Supersymmetric predictions (coloured region [46]) and experimental limits for spin-independent cross-sections (phonons [47], ionization [29], scintillation [48,49], WIMP claim [50], hybrid phonon-ionization [51,52]). For light WIMPs, detector threshold is critical. For heavy ones, the limits have parallel asymptotes (σ proportional to m). Ionization calorimeters now give better results than heavier and older methods.

Les faibles interactions des WIMPs avec la matière posent un important défi expérimental. Le spectre d'événements attendus (figure 3), en coups par jour par kilogramme de détecteur et par keV d'énergie de recul, décroît exponentiellement en première approximation[1] [28]:

$$\frac{\mathrm{d}\mathcal{R}}{\mathrm{d}E_R} = \frac{\mathcal{R}_0}{\eta E_0} \exp\left(-\frac{E_R}{\eta E_0}\right)$$

où E_R est l'énergie de recul déposée dans le détecteur par un WIMP et ηE_0 sa valeur moyenne. Pour un WIMP de masse $m \approx 10$ GeV et de vitesse caractéristique $v \approx 10^{-3}c$, cette valeur moyenne est donnée par l'énergie cinétique, $E_0 = \frac{1}{2}mv^2 \approx 5$ keV, et par $\eta = 2mM/(m+M)^2$, un facteur cinétique traduisant l'énergie transmise au noyau cible de masse M. Le spectre intégré sur toutes les énergies de recul, $\mathcal{R}_0 = 2nv\sigma/(\sqrt{\pi}M)$, vaut tout au plus de l'ordre de quelques événements par jour et par kilogramme de détecteur, la densité numérique de WIMPs étant $n = \rho/m$. Le spectre est d'autant plus piqué à basses énergies que le WIMP est léger. La forme du spectre et ses valeurs impliquent les critères suivants pour un détecteur: un fond radioactif aussi faible que possible, un seuil bas et une masse importante. Il convient de leur ajouter la possibilité de varier les noyaux cibles afin d'étudier

[1] Un traitement rigoureux ferait intervenir un facteur de forme traduisant une perte de cohérence pour des noyaux lourds par un amortissement du spectre [27] et tiendrait compte de la variation annuelle de la vitesse de la Terre par rapport au halo.

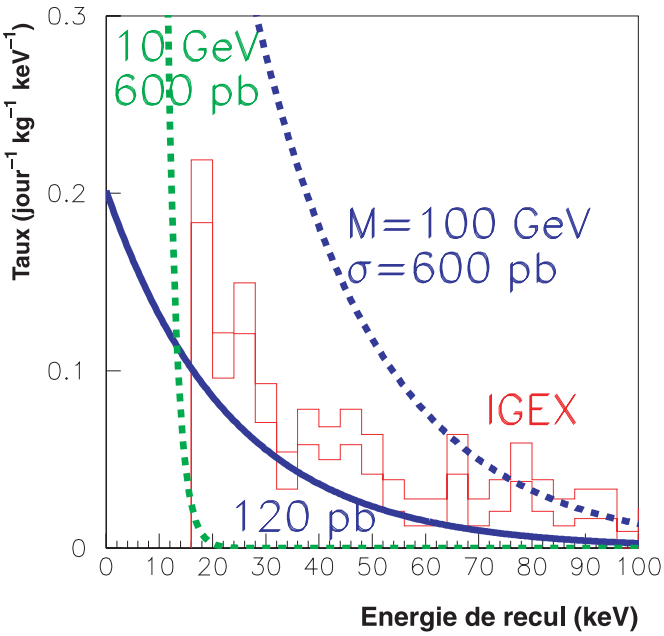

Figure 3. Spectres théoriques de WIMPs (courbes) pour divers masses et couplages sur le germanium et le spectre expérimental (l'histogramme et sa limite supérieure pour un intervalle de confiance de 90%). Les spectres attendus sont exponentiellement décroissants et d'autant plus piqués à basse énergie que le WIMP est léger. Pour une masse donnée, la section efficace à partir de laquelle le spectre théorique dépasse celui expérimental fournit la limite de la figure 1. Les données expérimentales proviennent d'IGEX [29].

Figure 3. Supersymmetric predictions (coloured region [46]) and experimental limits for spin-dependent cross sections (bubbles [53,54], scintillation [48,49], phonons [55]). Ionization detectors are absent because of the lack of spin in natural germanium or germanium enriched in ^{76}Ge. Unlike in the spin-independent case, these cross sections do not benefit from an amplification factor proportional to A^2.

les divers couplages d'une particule éventuelle. Une autre caractéristique de ce signal serait sa modulation saisonnière du fait de la variation annuelle de la vitesse de la Terre par rapport au halo. L'effet, de l'ordre de 5% sur le spectre intégré, demanderait beaucoup de données pour être discernable.

La première exigence entraîne que la plupart des expériences de détection directe soient enfouies profondément sous terre où le flux de muons cosmiques décroît rapidement avec la profondeur mesurée en mètres d'eau équivalents (MWE, voir le tableau 1) [30], et que toutes ces expériences utilisent un important blindage pour les protéger des divers fonds radioactifs. Le blindage lui-même peut être une source de contaminations, donc un métal particulièrement prisé est le plomb d'origine archéologique [31]. Ce dernier, s'il a été produit dans de bonnes conditions, a depuis longtemps été séparé de l'uranium avec lequel il se trouve dans la nature. Or l'isotope ^{238}U génère du ^{210}Pb qui a une demi-vie de 22 ans et est très radioactif. Le plomb archéologique a donc eu le temps de s'appauvrir en ce dernier isotope gênant.

Le fait que photons et électrons représentent une composante importante du bruit de fond conduit à s'intéresser à leurs interactions dans un détecteur. Ces particules y créent des reculs d'électrons, alors que le bruit de fond neutronique et le signal attendu de WIMPs causent des

Tableau 1. Quelques sites souterrains et leurs profondeurs en mètres d'eau équivalents (MWE).
Table 1. Some underground sites and their depth in metres water-equivalent (MWE).

Site	Lieu	Profondeur (MWE)	Expériences
Nokogiriyama	Japon	15	Tokyo LiF
Stanford	Californie, USA	20	CDMS
Rustrel	Vaucluse, France	1500	SIMPLE
Soudan	Minnesota, USA	2100	CDMS II
Canfranc	Pyrénées, Espagne	2500	IGEX, NaI Canfranc ROSEBUD, COSME
Kamioka	Japon	2700	ELEGANTS
Boulby	Grande Bretagne	3500	UKDMC
Gran Sasso	Abruzzes, Italie	3500	Heidelberg–Moscou, DAMA Milano $\beta\beta$, CRESST
Modane	Alpes, France	4500	NaI Saclay, EDELWEISS

reculs nucléaires. Or l'énergie de recul déposée par une particule incidente dans un cristal peut se répartir sous trois formes (de l'ionisation, de la scintillation et des phonons) dans des proportions dépendant de la nature du recul. Pour cela il sera utile de définir des facteurs dits de quenching, rapports de l'ionisation (ou de la scintillation) créée par un recul nucléaire sur l'ionisation (respectivement sur la scintillation) créée par un recul électronique de même énergie. Ces facteurs serviront à convertir les énergies étalonnées en keV équivalent électrons (keV EE) par des sources photons en des énergies en keV recul, nécessaires pour l'analyse des spectres en terme de WIMPs.

2. Détecteurs semi-conducteurs à ionisation (Semiconductor ionization detectors)

La première génération d'expériences emploie des détecteurs solides à ionisation [32]. Cette technique était déjà en place quand l'idée de la détection directe survint. Il s'agit de cristaux semi-conducteurs, de masse généralement comprise entre quelques centaines de grammes et quelques kilogrammes, maintenus à 77 K par de l'azote liquide. Une particule incidente y crée un recul de noyau ou d'électron, libérant des paires électrons–trous. Un recul d'électrons utilise 3 eV pour créer une paire électron–trou dans le germanium, le surplus par rapport au gap de 0.7 V passant directement en chaleur. Une polarisation de l'ordre du kilovolt peut être appliquée au dispositif pour capter les charges à l'aide d'électrodes implantées sur le cristal.

Les deux premières expériences, américaines, publièrent leurs premiers résultats en 1987 [33] et en 1988 [34] avec des détecteurs de germanium pesant respectivement 715 et 900 g. Les résultats obtenus trahissaient des contaminations photoniques à basse énergie, mais suffisaient déjà à exclure quelques modèles de matière sombre de l'époque, tels le cosmion et le neutrino de Dirac massif [35, 36]. Depuis, les meilleurs résultats absolus ont longtemps été ceux des détecteurs en germanium de l'expérience Heidelberg–Moscou [37, 38] située au Gran Sasso. Optimisés pour la recherche d'un signal de double β vers 2 MeV, les détecteurs de 2.8 kg enrichis en ^{76}Ge ont un seuil relativement élevé de 9 keV EE

et une résolution de 2.4 keV largeur totale à mi-hauteur (LTMH) à 500 keV EE. Depuis peu, l'expérience à ionisation la plus performante est celle de double β de l'*International Germanium Experiment* (IGEX) [29], située dans le tunnel pyrénéen du Canfranc, avec un détecteur d'environ 2 kg enrichi au ^{76}Ge donnant un seuil de 4 keV EE et un taux moyen d'environ 0.07 événements jour^{-1} kg^{-1} keV^{-1} EE entre 10 et 20 keV EE. Une expérience plus petite dans le même site, COSME (avec 234 g de germanium naturel), possède un seuil un peu plus faible (2.5 keV EE) et contraint un peu mieux les WIMPs légers malgré un fond plus élevé [39]. Notons enfin une expérience plus récente du groupe de Heidelberg, Heidelberg Dark Matter Search (HDMS) [40]. Elle comporte deux détecteurs à ionisation en germanium disposés de façon concentrique. En principe, le bruit de fond radioactif du détecteur interne se trouve réduit, d'une part car ce détecteur est entouré de germanium pur et d'autre part car les coïncidences entre les deux détecteurs causées par les interactions Compton de photons peuvent être rejetées. Malgré tout, les premières mesures révèlent un fond un peu plus élevé que celui de Heidelberg–Moscou, sans doute parce que le détecteur interne est fait en germanium non enrichi qui a eu peu de temps pour récupérer de son activation cosmique au niveau du sol lors de sa fabrication, ce qui le laisse avec des contaminations dans la masse plus difficiles à rejeter par coïncidences avec le détecteur externe. En dépit de ceci, les premières limites améliorent celles de Heidelberg–Moscou pour les faibles masses de WIMP, grâce encore une fois au seuil de 2 keV EE.

Les spectres obtenus, étalonnés avec des sources de photons, se convertissent de keV EE en keV de recul, avec le facteur de quenching mesuré sur faisceau [41, 42] ou par d'autres méthodes [43,44]. Les valeurs du facteur de quenching, de l'ordre de 0.25 pour le germanium (0.4 pour le silicium) et croissantes avec l'énergie, concordent avec les prédictions théoriques remontant aux années soixante [45].

Le spectre expérimental peut alors être comparé aux spectres théoriques des WIMPs (figure 3). Le spectre théorique étant proportionnel à la section efficace, pour une masse de WIMP donnée, il y aura une section efficace limite au-delà de laquelle le spectre attendu dépassera le spectre obtenu pour un critère statistique donné. Les sections efficaces plus grandes seront donc exclues pour cette masse. Il est donc possible de construire une courbe d'exclusion dans le plan section efficace–masse (figure 1). Les sections efficaces sont normalisées à celles du nucléon afin de permettre la comparaison des résultats provenant de diverses cibles.

Les détecteurs à ionisation, qui bénéficient d'une grande pureté chimique, de masses moyennes et de conditions d'opérations relativement standard, pâtissent toutefois de l'absence de méthode de rejet du bruit de fond (hormis les coïncidences entre détecteurs) et sont restreints à deux noyaux cibles, le germanium et le silicium. Parmi les évolutions possibles de ces détecteurs, le très ambitieux projet *Germanium in Liquid Nitrogen Undergound Setup* (GENIUS) [56] vise une sensibilité accrue grâce à 100 kg de germanium baignant directement dans de l'azote liquide dont la haute pureté en fait un excellent blindage basse radioactivité malgré sa faible densité.

3. Expériences à scintillation (Scintillation detectors)

Pour pouvoir bénéficier d'un plus grand choix de noyaux cibles, des détecteurs à scintillation ont ensuite été mis en œuvre. Un cristal scintillant de masse comprise entre un et une dizaine de kilogrammes constitue l'absorbeur et le recul créé par la particule incidente libère des photons. Ceux-ci peuvent s'échapper du cristal et peuvent être dirigés par des guides de lumière en quartz ou en silice vers des photomultiplicateurs qui fournissent alors un signal pouvant atteindre dix photoélectrons par keV déposé pour des configurations usuelles. Le

Tableau 2. Expériences de scintillation. Les performances en termes de fond (présentées sans PSD ici) et de maîtrise des systématiques sont déterminantes (voir le texte).

Table 2. Scintillation experiments. Background (shown here without PSD) and understanding of systematics are essential (see text).

Expérience	Masse active (kg)	Exposition (kg jour)	Fond (jour^{-1} kg^{-1} keV^{-1} EE)	Intervalle (keV EE)	Référence
UK Dark Matter Collaboration (UKDMC)	6	1 000	≈2	4–25	[49]
NaI Saclay	10	805	≈2	5–20	[57]
NaI Canfranc	32	4 600	≈15	9–17	[58]
Dark Matter Experiment (DAMA)	115	58 000	≈2	2–10	[50]
Electron Gamma-Ray Neutrino Spectrometer (ELEGANTS)	662	242 000	≈8	10–20	[59]

scintillateur peut être soit intrinsèque ($PbWO_4$, $CaWO_4$, ...) soit dopé (NaI(Tl), CsI(Tl), ...), ces derniers émettant en général plus de lumière à température ambiante. Plusieurs groupes à travers le monde utilisent cette technique de détection (tableau 2). Si ces détecteurs ont des résolutions typiques médiocres (de l'ordre de 12 keV EE LTMH à une énergie de 47 keV EE) par rapport aux dispositifs à ionisation, ils se rattrapent grâce à leurs masses plus importantes et à la grande section efficace cohérente de l'iode ($A = 127$). De plus, l'étude de la dispersion des temps caractéristiques de scintillation (*pulse shape discrimination* ou PSD) permet dans une certaine mesure de distinguer reculs d'électrons (le bruit de fond électromagnétique) et reculs de noyaux (le signal attendu et le fond neutronique), comme le montre la figure 4. Cette technique d'analyse, de type statistique, exige de grands échantillons et de faibles erreurs systématiques, car la différence entre les deux populations est petite devant leurs largeurs respectives. D'autre part, cette différence diminue fortement aux basses énergies, si bien que dans le cas du couplage indépendant du spin, où les plus faibles énergies de recul contraignent le plus (compte tenu des facteurs de quenching de l'iode, ≈8%, et du sodium, ≈25% [57,60]), le PSD n'apporte quasiment rien, même s'il permet de gagner un demi ordre de grandeur dans le cas du couplage dépendant du spin [57]. Les meilleures limites obtenues, améliorant celles des expériences à ionisation, sont celles de 1996 de *Dark Matter* (DAMA) [60] et de 2000 de *UK Dark Matter Collaboration* (UKDMC) [49] (figure 1).

Du fait de leurs masses et expositions importantes, les données acquises avec des détecteurs de type NaI peuvent se prêter aussi à une analyse en termes d'une éventuelle modulation annuelle [59, 61]. Ainsi l'expérience DAMA annonce-t-elle une modulation imputable à un WIMP d'une cinquantaine de GeV. Les premières données présentées en 1997 [62] posaient quelques problèmes d'interprétation (dont une modulation présente dans seulement un tiers des cristaux) [63]. Depuis, la collaboration persiste avec des données plus récentes [50] et une polémique à la hauteur de l'enjeu s'est développée autour des interrogations expérimentales (par exemple, le spectre de fond après soustraction de l'éventuel signal WIMP semble

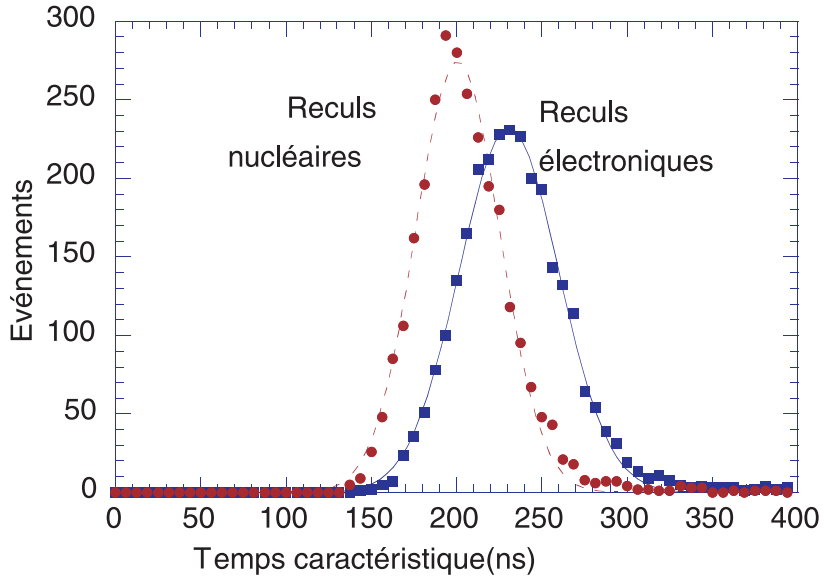

Figure 4. La différence de temps de scintillation entre reculs nucléaires et reculs électroniques, entre 12 et 14 keV EE (soit entre 150 et 175 keV en reculs d'iode), d'après [57]. La séparation entre les deux populations est nettement moins bonne que celle obtenue par d'autres méthodes (voir la figure 5).

Figure 4. Difference in scintillation times between nuclear recoils and electronic recoils, between 12 and 14 keV ee (i.e. between 150 and 175 keV recoil on iodine), from [57]. The separation between the two populations is much worse that that obtained from other methods (figure 5).

incompatible avec un fond d'électrons à dominante Compton) [64–66]. Notons aussi que la compatibilité entre ce résultat et la théorie ne fait pas l'unanimité; se reporter aux [67, 68] pour des avis divergents.

Une autre énigme concernant les détecteurs à NaI est la présence d'une troisième population d'événements à basse énergie, plus rapides que les reculs nucléaires, dans deux expériences indépendantes, NaI Saclay [57] et UKDMC [69]. La compréhension de ces événements paraît capitale et une interprétation possible [70, 71] consisterait dans la contamination de la surface des cristaux par du radon.

4. Expériences cryogéniques à phonons (Cryogenic experiments with phonons)

La troisième génération d'expériences est celle des calorimètres (ou bolomètres). Au sens large, il s'agit de mesurer l'élévation de température causée par une interaction dans le détecteur et les précurseurs exploitant la variation de la susceptibilité magnétique de sels en fonction de la température remontent au moins à l'époque de Zwicky [72]. Plus récemment, la technique découle des expériences à grains supraconducteurs initialement envisagées pour les neutrinos astrophysiques [26] puis pour les WIMPs [25]. Il s'agissait de mettre en évidence la diffusion élastique de la particule incidente sur un noyau dans une bille de quelques micromètres refroidie à la limite de la supraconductivité, grâce à l'élévation de température engendrant une variation macroscopique du flux magnétique. La collaboration germano-suisse ORPHEUS [73] poursuit

l'application de cette technique à la matière sombre, malgré quelques obstacles techniques comme l'hétérogénéité des grains [74].

Vers la même époque que la suggestion d'utiliser des billes supraconductrices pour chercher les WIMPs, la technique de calorimétrie, au sens dans lequel elle est entendue ici, commençait à obtenir des résultats probants dans l'étude des rayons X [75]. Elle fut proposée pour diverses problématiques: l'étude des neutrinos provenant d'accélérateurs [76], la désintégration double β [77] (domaine dans lequel elle est d'actualité) et la question des neutrinos solaires [78]. La difficulté de réaliser des calorimètres massifs était reconnue [79] et dans le cadre de la matière sombre cette technique a mis plus de temps à mûrir que celles de l'ionisation et de la scintillation. La technique exploite le fait que, fuites et mesures mises à part, toutes les formes d'énergie dans un cristal diélectrique devraient se dégrader en phonons. A basse température, la lecture des phonons libérés par le recul imparti à un cristal par une particule incidente doit donc fournir un signal beaucoup plus sensible que les techniques vues précédemment, d'où d'excellents seuils et résolutions. La mesure se fait au moyen d'une thermistance en contact thermique avec le cristal et dont la variation de résistance fournit le signal.

4.1. Calorimètres standards (Standard calorimeters)

Le signal thermique sera une élévation de température proportionnelle à l'énergie déposée dans l'absorbeur divisée par la capacité calorifique de ce dernier: $\Delta T \propto E/C_{absorbeur}$ [80]. La chaleur spécifique d'un cristal diélectrique variant comme le cube de la température, pour maximiser le signal, il convient de réduire la température autant que possible. En pratique, les calorimètres opèrent à des températures voisines de 10 mK, où l'élévation relative de température reste faible (de l'ordre d'un millième) mais exploitable. Les thermistances les plus courantes sont de type *neutron transmutation doped* (NTD). Il s'agit de morceaux de germanium rapprochés de la transition entre l'état isolant et l'état conducteur par une irradiation neutronique qui finit par transformer des noyaux de germanium en gallium (un accepteur d'électrons), arsenic et sélénium (tous les deux donneurs). Pour éviter une capacité calorifique supplémentaire qui réduirait le signal, les NTDs sont en général de très faible volume, avec des dimensions caractéristiques de l'ordre du millimètre.

Au moins trois collaborations emploient de tels dispositifs: le groupe japonais de Tokyo [81], l'expérience franco-espagnole *Rare Object Search Employing Bolometers UndergrounD* (ROSEBUD) [82] et l'expérience de recherche de double β de Milan (Mi$\beta\beta$) [83]. L'expérience de Tokyo a pour l'instant déployé huit détecteurs de 21 g de fluorure de lithium. Pénalisés par le fait d'être en site surfacique et par des problèmes de microphonie, le seuil effectif est d'au moins 14 keV et le taux relativement élevé. La présence de ^{19}F en fait des détecteurs orientés vers les couplages dépendant du spin et les particules légères. ROSEBUD utilise des absorbeurs en saphir pesant 50 g au Canfranc et développe des cristaux pesant jusqu'à un kilogramme [84]. Les petits détecteurs ont un excellent seuil de 500 eV et une résolution de 120 eV LTMH à 1.2 keV. La composition du saphir ($A_{Al} = 27$, $A_O = 16$) oriente encore une fois ces détecteurs surtout vers des WIMPs légers ou des couplages dépendant du spin (celui de l'aluminium valant $\frac{5}{2}$). Enfin, la collaboration italienne emploie des cristaux de dioxyde de tellure de 340 g. Leur seuil vaut 10 keV. Dans des mesures indépendantes, les groupes français et italien ont mesuré un facteur de quenching pour les phonons se confondant avec l'unité [85, 86]. Ce résultat s'obtient en implantant (volontairement ou non) un isotope radioactif sous la surface d'un calorimètre en face d'un second calorimètre. Quand une décomposition radioactive a lieu (de ^{210}Po par exemple), le recul nucléaire (^{206}Pb dans ce cas) et la particule (de type α alors) émise peuvent se répartir parmi les deux détecteurs; l'énergie de recul nucléaire, connue *a priori*,

peut alors être comparée à celle obtenue par l'étalonnage en reculs électroniques établi avec une source de photons.

Ces calorimètres thermiques présentent un inconvénient de taille, puisque le signal thermique est inversement proportionnel à la masse de l'absorbeur, alors que la recherche de WIMPs exige des absorbeurs massifs. Pour cette raison, il est avantageux de lire les phonons avec un senseur avant qu'ils se soient thermalisés dans l'absorbeur [87]. Le signal est alors de la forme $\epsilon E/C_{senseur}$, où la capacité calorifique qui intervient maintenant est celle du senseur et le terme ϵ représente la fraction de phonons thermalisés dans le senseur plutôt que dans l'absorbeur. Cette fraction croît avec la qualité de l'interface absorbeur–senseur et en particulier sa surface. Un senseur athermique disposera donc d'une grande surface de contact et d'une capacité calorifique faible. L'expérience italo-anglo-allemande *Cryogenic Rare Event Search with Superconducting Thermometers* (CRESST) utilise des couches minces de tungstène en phase α, d'environ 1 cm $\times$ 1 cm $\times$ 2000 Å. Vers 15 mK, ces couches passent abruptement de l'état supraconducteur à l'état normal sur une plage de l'ordre d'un millikelvin. Avec ses couches évaporées sur des cristaux de saphir de 262 g, les performances sont excellentes aussi bien en termes de seuil (500 eV) que de résolution (LTMH 230 eV à 1 keV) [88]. L'expérience CRESST a récemment réduit son fond de trois ordres de grandeur en constatant qu'il était dû à la propagation de fissures dans le saphir aux points de contact du détecteur avec son environnement [89]. Elle détient maintenant les meilleures limites calorimétriques pour le couplage dépendant du spin [55].

4.2. Calorimètres hybrides (Hybrid calorimeters)

Les calorimètres standards possèdent d'excellents seuils et résolutions, mais sont quelque peu limités du fait de leurs faibles masses individuelles dépassant rarement quelques centaines de grammes. Associer une seconde mesure simultanée à celle des phonons permet de surmonter ce handicap. La technique hybride la plus avancée à ce jour est celle de l'ionisation et de la chaleur. Le dispositif consiste en un calorimètre, dont l'absorbeur est un semi-conducteur. Comme dans les détecteurs à ionisation, deux surfaces sont implantées pour collectionner les charges libérées, avec toutefois une polarisation relativement faible, de l'ordre du volt. Un groupe anglais avait développé cette technique sur 0.25 g de silicium [90] vers la même époque qu'un groupe américain travaillant sur 60 g de germanium [43]. Les perspectives d'agrandir les dispositifs semblant faibles, seule l'équipe américaine, devenue depuis *Cryogenic Dark Matter Search* (CDMS), poursuivit son développement jusqu'au bout. Aujourd'hui, l'expérience française Expérience pour Detecter les WIMPs en SIte Souterrain (EDELWEISS) emploie aussi cette technique avec succès [91]. La double mesure ionisation–chaleur permet une excellente identification des reculs nucléaires et des reculs électroniques, comme le montre l'étalonnage de la figure 5. En utilisant comme variable le rapport de l'ionisation sur l'énergie de recul pour rejeter les reculs électroniques, dans le cas idéal des étalonnages, la sensibilité de ce type de dispositif est de la forme [92]

$$\text{sensibilité (événements kg}^{-1}\text{ jour}^{-1}) = (\text{facteur de séparation}) \times \left(\frac{\text{fond (événements kg}^{-1}\text{ jour}^{-1})}{\text{exposition (kg jour)}}\right)^{1/2}.$$

Or, pour ce type de détecteur, le facteur de séparation vaut $\approx 10^{-1}$ [91] alors que dans le cas analogue des scintillateurs avec PSD, il vaut ≈ 1 [57]. Donc dans ce cas idéal, à fond et à durée d'acquisition égaux, un calorimètre à ionisation sera aussi sensible qu'un détecteur à scintillation 100 fois plus massif.

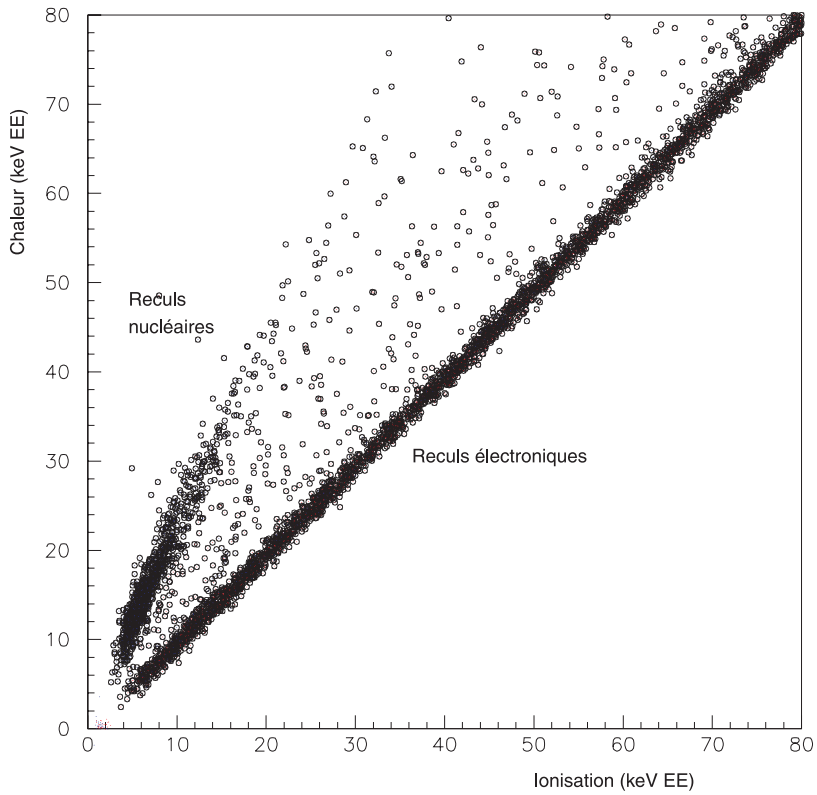

Figure 5. L'étalonnage d'un détecteur ionisation–chaleur en germanium [91]. La population de reculs nucléaires, peu ionisants, se distingue nettement des reculs électroniques, plus ionisants.

Figure 5. Calibration of an ionization-heat germanium detector [91]. The weakly ionizing nuclear recoil population is clearly separated from the highly ionizing electron recoils.

En pratique, pour chercher les WIMPs, ce résultat ne peut s'appliquer tel quel, car les étalonnages ne représentent pas correctement le fond. En effet, deux populations viennent s'ajouter aux reculs d'électrons et aux reculs de noyaux normaux [93]. Il s'agit d'événements interagissant dans la superficie du détecteur et dont la charge n'est pas correctement collectionnée. De ce fait, les reculs électroniques surfaciques dus à des photons ou électrons de basse énergie manquent de charge et viennent polluer la zone où les reculs nucléaires sont attendus. Les reculs nucléaires surfaciques pourraient d'ailleurs expliquer le problème des événements anormaux dans le NaI [94]. Il n'est pas possible d'augmenter sensiblement la polarisation au-delà de quelques volts afin de mieux collecter les charges, d'une part car les diodes utilisées deviendraient passantes et d'autre part à cause de l'effet Neganov–Luke [95–97]. Celui-ci, analogue au chauffage Joule mais dans un semi-conducteur, fait que le produit de la charge créée et de la polarisation appliquée vient s'ajouter à l'énergie déposée pour créer le signal thermique. Le signal thermique et le signal de charge sont donc d'autant plus corrélés que la polarisation est grande et il convient de choisir une polarisation qui minimise cet effet tout en optimisant la collecte de charge.

Malgré ces problèmes surfaciques, les capacités de rejet de ce type de détecteur restent très bonnes. Avec une exposition de 10.6 kg jour dans trois détecteurs germanium de 100 g (seuil 10 keV), l'expérience CDMS [51] améliore la limite de 4 T jour de DAMA [48] sur toutes les masses de WIMPs et contredit le prétendu WIMP (figure 1). Toutefois, les résultats de CDMS sont obtenus dans le site de Stanford fortement exposé aux rayons cosmiques (table 1) qui induisent des neutrons en quantité mal connue. En comparant le nombre de reculs nucléaires dans les détecteurs en germanium avec celui dans d'autres en silicium et en considérant le nombre de diffusions nucléaires multiples dans les détecteurs en germanium, CDMS effectue alors une soustraction du fond neutron pour améliorer son résultat d'un facteur $\approx$2. L'expérience EDELWEISS obtient une limite proche de celle de CDMS grâce à 4.53 kg jour de données dans un détecteur de 320 g de germanium avec un seuil plus élevé que CDMS (30 keV), mais sans soustraction de fond neutronique puisque déjà en site profond [52]. CDMS et EDELWEISS devraient bientôt pouvoir améliorer ces limites, d'une part car CDMS II s'installe dans un site mieux protégé et d'autre part car le résultat d'EDELWEISS devrait s'améliorer avec plus d'exposition (aucun événement recul observé).

Pour avoir accès à un plus vaste choix de noyaux cibles et pour éviter les problèmes d'événements surfaciques, une seconde mesure calorimétrique hybride envisagée est celle de la scintillation et des phonons, proposée il y a une douzaine d'années [98]. L'expérience CRESST a récemment démontré la faisabilité d'utiliser un calorimètre principal dont l'absorbeur, un cristal scintillant, fournit un signal phonons ainsi que des photons. Un second calorimètre, très sensible, mesure cette lumière pour donner le signal dit photons. L'expérience de démonstration [99], réalisée avec un cristal scintillant de 6 g de $CaWO_4$, a démontré un facteur de rejet au moins aussi bon que celui des détecteurs ionisation–phonons, d'autant plus que la technique ne pâtit pas de problèmes découlant d'événements superficiels. Un nouveau dispositif comprenant un cristal scintillant de 300 g est en cours de préparation. Cette technique est aussi étudiée par ROSEBUD.

5. Autres techniques (Other techniques)

Un développement prometteur reprend le concept des chambres à bulles, sous forme de gouttelettes surchauffées métastables (taille caractéristique 10–100 μm) d'un réfrigérant (par exemple du fréon) dans une matrice. Une particule incidente déposant une concentration suffisante d'énergie ($\mathrm{d}E/\mathrm{d}x > 200$ keV $\mu\mathrm{m}^{-1}$) vaporisera des gouttelettes, les transformant en bulles de diamètre voisin du millimètre. L'événement sera caractérisé par sa signature acoustique ou visuelle. La technique est développée en parallèle au Canada par l'expérience *Project In CAnada to Search for Supersymmetric Objects* (PICASSO) [54] et en France par *Superheated Instrument for Massive Particle Searches* (SIMPLE) [53]. En jouant sur des pressions et températures voisines de celles ambiantes, ces détecteurs peuvent être rendus insensibles aux photons et aux électrons. Les détecteurs fournissent jusqu'ici des spectres intégrés à partir d'un seuil donné. Il semblerait possible d'obtenir des spectres différentiels par soustraction des spectres intégrés de détecteurs ayant des seuils différents et une statistique suffisante. D'autre part, pour l'instant, les numéros atomiques engagés sont faibles tout comme les masses actives (typiquement une dizaine de grammes) ce qui n'empêche pas PICASSO et SIMPLE d'avoir de bonnes limites dépendantes du spin grâce à la présence de fluor. Cette technique relativement bon marché devrait d'ailleurs s'appliquer à des composés plus favorables pour les couplages indépendants du spin (tels que $CBrF_3$ ou CIF_3) et fournir des modules de masse active de quelques centaines de grammes.

Enfin, plusieurs projets, comme ZEPLIN II [100], étudient l'ionisation et la scintillation dans le système diphasique du xénon. Dans la phase liquide, l'interaction d'une particule

créera de la scintillation lue par des photomultiplicateurs et de l'ionisation qui, par électroluminescence dans la phase gazeuse, fournira un second signal lumineux. Outre l'avantage de rejeter du bruit de fond électromagnétique, cette technique devrait aboutir rapidement à des masses importantes de détecteurs (30 kg envisagés), avec des seuils toutefois élevés (de l'ordre d'une cinquantaine de keV en recul nucléaire).

6. Conclusion et perspectives (Conclusions and perspectives)

Après trois quarts de siècle, la question de la matière sombre reste encore ouverte. Les expérimentateurs s'y intéressent depuis une quinzaine d'années. Les détecteurs utilisant la technologie déjà existante de l'ionisation dans un semi-conducteur ont pu restreindre les hypothèses. Les détecteurs à scintillation en NaI, plus massifs et capables de rejeter une faible portion du bruit de fond, ont repoussé les limites vers l'espace des phases prédit par la supersymétrie. Une évolution des détecteurs initialement pressentis, les nouveaux détecteurs calorimétriques à ionisation en Ge, rejettent bien plus efficacement le bruit de fond, et fournissent maintenant les meilleures limites, tout en gardant une bonne marge de progression. Même si les actuels résultats expérimentaux contradictoires entre NaI et Ge sur un éventuel WIMP peuvent sans doute être réconciliés par des aménagements à la théorie des couplages WIMP–matière, il semble plus prudent d'attendre de nouvelles données indépendantes pour trancher. Elles pourraient provenir de dispositifs calorimétriques à scintillation employant d'autres noyaux cibles tels que $CaWO_4$. Cette technologie pourrait jouer un role complémentaire à l'ionisation–chaleur dans la résolution de l'énigme de la matière sombre.

Remerciements (Acknowledgments)

L'auteur remercie G Chardin, P Magnier, J Rich, L Stodolsky et un arbitre anonyme pour leurs commentaires sur le manuscrit, G Gerbier pour ses discussions sur le PSD, E García, G Nollez et S Scopel pour les informations sur les courbes d'exclusion, P Gondolo et K Olive pour les modèles supersymétriques, L Baudis, J I Collar, V Kudryavtsev, P de Marcillac, S Pirro, F Pröbst, R Schnee ainsi que les autres membres des diverses expériences qui ont bien voulu répondre aux demandes de renseignements. Les archives du California Institute of Technology ont fournit des renseignements biographiques sur F Zwicky. Ce travail a été financé en partie par le réseau européen TMR pour les détecteurs cryogéniques ERB-FMRX-CT98-0167.

Références (References)

[1] Zwicky F 1933 *Helv. Phys. Acta* **6** 110
[2] Sarazin C 1986 *Rev. Mod. Phys.* **58**
[3] Böhringer H *et al* 2000 *Astron. Astrophys.* **353** 124
(Böhringer H *et al* 1999 *Preprint* astro-ph/9910363)
[4] Ashman K M 1992 *Pub. Astron. Soc. Pacific* **104** 1109
[5] de Bernardis P *et al* 2001 *Preprint* astro-ph/0105296
[6] Waerbeke L V *et al* 2000 *Astron. Astrophys.* **358** 30
(Waerbeke L V *et al* 2000 *Preprint* astro-ph/0002500)
[7] Wittman D M *et al* 2000 *Nature* **405** 143
[8] Burrows A 2000 *Nature* **403** 727
[9] Burles S *et al* 2001 *Astrophys. J.* **552** L1
(Burles S *et al* 2000 *Preprint* astro-ph/0010171)
[10] Jungman G *et al* 1996 *Phys. Rep.* **267** 195
[11] Ellis J *et al* 2000 *Phys. Rev.* D **62** 075010
(Ellis J *et al* 2000 *Preprint* hep-ph/0004169)

[12] Tovey D R *et al* 2000 *Phys. Lett.* B **488** 17
(Tovey D R *et al* 2000 *Preprint* hep-ph/0005041)
[13] Ansari R *et al* 1997 *Astron. Astrophys.* **324** 843
[14] Aubourg E *et al* 1993 *Nature* **365** 623
[15] Alcock C *et al* 1993 *Nature* **365** 621
[16] Udalski A *et al* 1993 *Acta Astron.* **43** 289
[17] Paczynski B 1986 *Astrophys. J.* **304** 1
[18] Lasserre T *et al* 2000 *Astron. Astrophys.* **355** L39
(Lasserre T *et al* 2000 *Preprint* astro-ph/0002253)
[19] Oppenheimer B R *et al* 2001 *Science* **292** 698
[20] Gibson B K *et al* 2001 *Science* **292** 2211a
(Gibson B K *et al* 2001 *Preprints* astro-ph/0104255, astro-ph/0104210, astro-ph/0106269)
[21] Desai S 2001 *4th Int. Symp. on Sources and Detection of Dark Matter in the Universe (Marina Del Rey)* éd D B Cline
[22] Montanet F 2000 *Nucl. Phys.* B *(Proc. Suppl.)* **87** 436
[23] Edsjö J *et al* 2001 *3rd Int. Workshop on the Identification of Dark Matter (York)* éd N J C Spooner et V Kudryavtsev
[24] Salati P 2000 *Nucl. Phys.* B *(Proc. Suppl.)* **87** 366
[25] Goodman M W et Witten E 1985 *Phys. Rev.* D **31** 3059
[26] Drukier A et Stodolsky L 1984 *Phys. Rev.* D **30** 2295
(Drukier A et Stodolsky L 1982 *Preprint* MPI-PAE/PTh 26/82)
[27] Rich J 1996 *Astropart. Phys.* **4** 387
[28] Smith P et Lewin J 1990 *Phys. Rep.* **187** 203
[29] Morales A *et al* 2000 *Phys. Lett.* B **489** 268
(Morales A *et al* 2000 *Preprint* hep-ex/0002053)
[30] Groom D *et al* 2000 *Eur. Phys. J.* C **15** 150
[31] L'Hour M 1987 *Rev. Archéol. Ouest* **4** 113
[32] Knoll G F 1989 *Radiation Detection and Measurement* 2ième édn (New York: Wiley)
[33] Ahlen S *et al* 1987 *Phys. Lett.* B **195** 603
[34] Caldwell D O *et al* 1988 *Phys. Rev. Lett.* **61** 510
[35] Steigman G *et al* 1978 *Astron. J.* **83** 1050
[36] Spergel D N et Press W H 1985 *Astrophys. J.* **294** 663
[37] Beck M *et al* 1994 *Phys. Lett.* B **336** 141
[38] Baudis L *et al* 1998 *Phys. Rev.* D **59** 022001
[39] Morales A *et al* 2001 *Preprint* hep-ex/0101037
[40] Baudis L *et al* 2001 *Phys. Rev.* D **63** 022001
(Baudis L *et al* 2000 *Preprint* astro-ph/0008339)
[41] Chasman C *et al* 1965 *Phys. Rev. Lett.* **15** 245
[42] Gerbier G *et al* 1990 *Phys. Rev.* D **42** 3211
[43] Shutt T *et al* 1992 *Phys. Rev. Lett.* **69** 3425
[44] Di Stefano P *et al* 2001 *Astropart. Phys.* **14** 329
(Di Stefano P *et al* 2000 *Preprint* astro-ph/0004308)
[45] Lindhard J *et al* 1963 *Mat.-fys. Medd. Kong. Danske Vidensk. Selskab* **33** 1
[46] Gondolo P *Communication privée*
[47] Pirro S *et al* 2001 *4th Int. Symp. on Sources and Detection of Dark Matter in the Universe (Marina Del Rey)* éd D B Cline
[48] Bernabei R *et al* 1996 *Phys. Lett.* B **389** 757
[49] Spooner N J C *et al* 2000 *Phys. Lett.* B **473** 330
[50] Bernabei R *et al* 2000 *Phys. Lett.* B **480** 23
[51] Abusaidi R *et al* 2000 *Phys. Rev. Lett.* **84** 5699
(Abusaidi R *et al* 2000 *Preprint* astro-ph/0002471)
[52] Benoit A *et al* 2001 *Preprint* astro-ph/0106094
[53] Collar J I *et al* 2000 *Phys. Rev. Lett.* **85** 3083
(Collar J I *et al* 2000 *Preprint* astro-ph/0001511)
[54] Boukhira N *et al* 2000 *Astropart. Phys.* **14** 227
[55] Bucci C *et al* 2001 *Preprint* MPI-PhE/2001-02
[56] Baudis L *et al* 2001 *4th Int. Symp. on Sources and Detection of Dark Matter in the Universe (Marina Del Rey)* éd D B Cline

(Baudis L *et al* 2000 *Preprint* astro-ph/0005568)
[57] Gerbier G *et al* 1999 *Astropart. Phys.* **11** 287
[58] Sarsa M *et al* 1997 *Phys. Rev.* D **56** 1856
[59] Fushimi K *et al* 1999 *Astropart. Phys.* **12** 185
[60] Bernabei R *et al* 1996 *Phys. Lett.* B **389** 757
[61] Sarsa M *et al* 1996 *Phys. Lett.* B **386** 458
[62] Bernabei R *et al* 1999 *Nucl. Phys.* B *(Proc. Suppl.)* **70** 79
[63] Gerbier G *et al Preprint* astro-ph/9710181
[64] Gerbier G *et al Preprint* astro-ph/9902194
[65] Gaitskell R J 2000 http://cdms.berkeley.edu/gaitskell
[66] Bernabei R *et al* 2000 *Eur. Phys. J.* C **18** 283
[67] Bottino A *et al* 2000 *Astropart. Phys.* **13** 215
[68] Ellis J *et al* 2001 *Phys. Rev.* D **63** 065016
(Ellis J *et al* 2000 *Preprint* hep-ph/0007113)
[69] Liubarsky I *et al* 2000 *Nucl. Phys.* B *(Proc. Suppl.)* **87** 64
[70] Smith N J T *et al* 2000 *Phys. Lett.* B **485** 9
[71] Cooper S *et al* 2000 *Phys. Lett.* B **490** 6
[72] Simon F 1935 *Nature* **135** 763
[73] van den Brandt B *et al* 2000 *Nucl. Phys.* B *(Proc. Suppl.)* **87** 117
[74] Frank M *et al* 1990 *Nucl. Instrum. Methods* A **287** 583
[75] Moseley S H *et al* 1984 *J. Appl. Phys.* **56** 1257
[76] Niinikoski T O et Udo F 1974 *CERN NP Internal Report* 74–6
[77] Fiorini E et Niinikoski T O 1984 *Nucl. Instrum. Methods* A **224** 83
[78] Cabrera B *et al* 1985 *Phys. Rev. Lett.* **55** 25
[79] Sadoulet B 1987 *Low Temperature Detectors for Neutrinos and Dark Matter (Ringberg Castle)* éd K Pretzl *et al*
[80] Booth N E *et al* 1996 *Annu. Rev. Nucl. Part. Sci.* **46** 471
[81] Ootani W *et al* 1999 *Phys. Lett.* B **461** 371
[82] Cebrián S *et al* 2001 *Astropart. Phys.* **15** 79
(Cebrián S *et al* 2000 *Preprint* astro-ph/0004292)
[83] Pirro S *et al* 2000 *Nucl. Instrum. Methods* A **444** 71
[84] Pécourt S *et al* 1999 *Nucl. Instrum. Methods* A **438** 333
[85] Zhou J *et al* 1994 *Nucl. Instrum. Methods* A **349** 225
[86] Alessandrello A *et al* 1997 *Phys. Lett.* B **408** 465
[87] Pröbst F *et al* 1995 *J. Low Temp. Phys.* **100** 69
[88] Sisti M *et al* 2001 *Nucl. Instrum. Methods* A **466** 499
[89] Di Stefano P *et al* 2001 *Cosmology and Particle Physics 2000 (Verbier)* éd R Durrer *et al*
(Di Stefano P *et al* 2000 *Preprint* hep-ex/ 0011064)
[90] Spooner N J *et al* 1991 *Phys. Lett.* B **273** 333
[91] Bergé L *et al* 1999 *Nucl. Phys.* B *(Proc. Suppl.)* **70** 69
(Bergé L *et al* 1998 *Preprint* astro-ph/9801199)
[92] Gaitskell R J *et al* 1996 *Nucl. Phys.* B *(Proc. Suppl.)* **51** 279
[93] Benoit A *et al* 2000 *Phys. Lett.* B **479** 8
(Benoit A *et al* 2000 *Preprint* astro-ph/0002462)
[94] Chardin G *et al* 2001 *4th Int. Symp. on Sources and Detection of Dark Matter in the Universe (Marina Del Rey)* éd D B Cline
[95] Neganov B S et Trofimov V N 1985 *Otkrytiya Izobreteniya* **146** 215
[96] Luke P *et al* 1990 *Nucl. Instrum. Methods* A **289** 406
[97] Neganov B S *et al* 1993 *J. Low Temp. Phys.* **93** 417
[98] Chaminade J P *et al* 1989 *XXIVième Rencontres de Moriond (Les Arcs)* éd O Fackler et J Tran Thanh Van
(Chaminade J P *et al* 1989 *Preprint* LAPP-EXP-89–04)
[99] Meunier P *et al* 1999 *Appl. Phys. Lett.* **75** 1335
(Meunier P *et al* 1999 *Preprint* physics/9906017)
[100] Cline D B 2000 *Nucl. Phys.* B *(Proc. Suppl.)* **87** 114
(Cline D B 2000 *Preprint* astro-ph/0001243)

Chapter 2

The EDELWEISS and CRESST Direct Detection Experiments

2.1 CRESST

Between 1998 and 2001, I worked on the first phase of the *Cryogenic Rare Event Search with Superconducting Thermometers* (CRESST) experiment. I was heavily involved in the experiment itself in the Gran Sasso underground laboratories (LNGS) during the first two years, and I worked on detector development at the Max-Planck-Institut für Physik (MPP) in Munich the last year. We deployed up to four 262 g Al_2O_3 detectors in a low-radioactivity cryostat at LNGS. The detectors had only a phonon signal, readout thanks to tungsten transition-edge sensors (TES) and a SQUID amplifier. These provided the detectors with excellent thresholds and energy resolutions (down to 133 eV on the 1.5 keV Al line when active thermal feedback was used [50]). A system of heater pulses was used to monitor the stability of the detectors, to linearize the sensor response, and to establish trigger efficiency. Once we understood and eliminated the dominant background emanating from fractures in the sapphire absorbers (Chap. 5), the experiment showed a low background of 0.73 ± 0.22 /kg/keV/day in the 15–25 keV range. This yielded the most sensitive limits for low-mass WIMPs weighing less than 5 GeV [51] (Sec. 2.4A).

Shortly before my arrival, the MPP group had demonstrated the feasability of scintillation-phonon dark matter detectors using their TES technology [52]. As background rejection is paramount for dark-matter detectors, development of $CaWO_4$ scintillation-phonon devices became a priority for CRESST, and I switched to this subject during the last year of my postdoc. My work is described in Chap. 4. The CRESST experiment has gone on to obtain excellent sensitivities with this type of detector [41].

2.2 EDELWEISS

I carried out my PhD on the EDELWEISS (*Expérience pour Détecter les WIMPs en Site Souterrain*) experiment [53] in the DAPNIA/SPP group at CEA Saclay, and then rejoined the experiment, this time at IPN Lyon, after my post-doc. During my PhD, I tested a 70 g ionization-phonon detector; it demonstrated excellent background rejection capabilities despite some misidentified surface events [54] (Sec. 2.5A). Three years later, EDELWEISS was deploying scaled-up 320 g germanium devices in the Modane underground laboratory (LSM). The detectors had a cylindrical geometry; a basic form of radial sensitivity was achieved through the use of two concentric electrodes; this allowed identification of events on the cylindrical surfaces of the detectors where the electrical charge collection field may not have been very homogenous and where surface events from the sides of the detectors could appear. An important feature of these detectors was the use of a 60 nm amorphous layer of Ge or Si below the charge collection electrodes first implemented by the CDMS experiment [55, 56]; this greatly reduced the number of surface events.

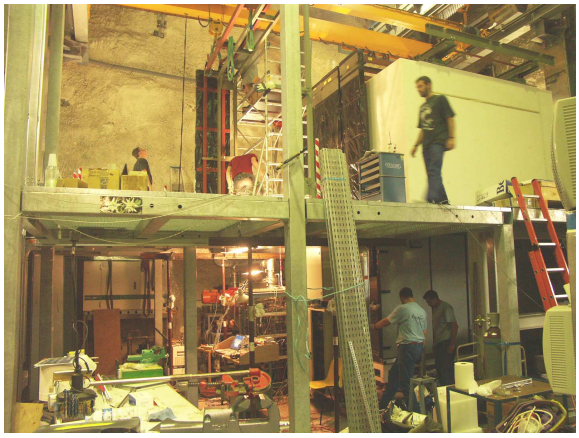

Figure 2.1: Installation of EDELWEISS II in the Modane underground laboratory. The 30 ton mobile white PE shielding is visible, partially covered by the black muon veto modules.

In 2001, we published the first limits from EDELWEISS using a single 320 g detector; in 4.5 kg.d, no events were observed; this gave us among the best spin-dependent sensitivities [57]. We later deployed up to three detectors at LSM; in 7.4 kg days, no events were observed for WIMPs lighter than 1 TeV; combining these data with the previous ones provided us with the best sensitivity to WIMPs in the world [49] (Sec. 2.6A). In particular, our sensitivity bested that of the previous leaders, the CDMS experiment located in a shallow underground site at Stanford [58]. Our data also started to constrain WIMP parameter space. In a further exposure bringing the total to 62 kg.d [47], our sensitivity remained unchanged statistically because events started to appear in the detectors. The distribution of the ionization-over-energy ratio of these events is smeared between the distributions expected for well-collected highly-ionizing particles and well-collected nuclear recoils, so some of these events are undoubtedly misidentified surface background. Morevover, some coincidences were observed between the detectors, and the remaining events are probably neutron background. At this point our sensitivity was leapfrogged by that of the CMDS experiment, now in the deep Soudan site [46].

As this first phase of EDELWEISS was now limited by background, we proceeded to dismantle the experiment and over the course of two years, installed the next phase, EDELWEISS II at LSM. This phase aims to gain two orders of magnitude in sensitivity, down to 10^{-8} pb. It consists of a novel reversed cryostat, designed by CRTBT Grenoble, cooled by three pulse tubes and a dilution unit, and using a reliquifier to reduce He consumption. The cryostat is manufactured out of materials screened for low radioactivity. It can accomodate up to 120 detectors. The cryostat is shielded from external γ particles by 30 tons of lead, with an inner archaeological lead layer. Around it are 30 tons of polyethylene (PE) to moderate the fast neutron background. The PE itself is enclosed in plastic scintillators that tag the rare but non-negligeable muons that cross the experiment and can create neutrons by interacting in the Pb shielding. All of this is located in a class-100 cleanroom to reduce radioactive contaminations. Installation of EDELWEISS II was spearheaded by D. Drain of IPN Lyon; I contributed to the effort during an 18-month leave from teaching I obtained (Fig. 2.1). Further information on the EDELWEISS II setup is available in Ref. [59].

Once the cryostat was commissioned, I participated in detector installation (Fig. 2.2) and tests of electronics and data-acquisition. Data taking has now started in the new experiment. Improvements in sensitivity will come not only from this cleaner environment, and a larger mass of detectors (about 10 kg are now installed, with capacity for ≈ 36 kg), but also from improvements to the detectors themselves, in particular with respect to the surface events. One approach is to obtain sensitivity along the vertical axis of the cylindrical detectors, by measuring the athermal component of the particle pulses using large-area NbSi thin-films [60]. As of this writing, results are encouraging

Figure 2.2: Installation of detectors in the low-background EDELWEISS II cryostat. The housings of ten standard Ge-NTD detectors are visible, as is a Ge-NbSi detector above them, and a SciCryo-IAS Al_2O_3 detector of smaller diameter below them (Sec. 4.2.3).

though the energy resolution is not yet optimal. Two 200 g and two 400 g Ge devices are currently deployed in EDELWEISS II. The other approach to obtain this axial-position sensitivity is via the charge signal. The shape of the ionization signal pulse is one possibility, though its effectiveness below 50 keV has not yet been demonstrated [61]. Another promising possibility is to use several patterned electrodes on each face of the detector; the distribution of the collected charge by each electrode allows clear identification of surface events. Detectors of this type will soon be added to those already underground in EDELWEISS II.

2.3 EURECA

To conclude this chapter, it is worth noting that EDELWEISS and CRESST have a common future, the *European Underground Rare Event Calorimetric Array* (EURECA) [62]. In addition to the two experiments I have worked on, this project will bring together other groups such as CERN and the ROSEBUD collaboration. The aim is to build a cryogenic direct detection experiment, with a mass between several hundred kilograms and a ton, and a sensitivity of 10^{-10} pb, able to sweep a good portion of SUSY parameter space. A similar project, SuperCDMS, is proposed in North-America [63]. In the case of EURECA, the choice of detector technology (ionization-phonon or scintillation-phonon) will depend to a great extent on the results of the 10 kg phases of EDELWEISS and CRESST.

2.4A Results from CRESST

Ref. [51].

ELSEVIER

Astroparticle Physics 18 (2002) 43–55

Astroparticle Physics

www.elsevier.com/locate/astropart

Limits on WIMP dark matter using sapphire cryogenic detectors

G. Angloher [a], M. Bruckmayer [b], C. Bucci [c], M. Bühler [d], S. Cooper [a], C. Cozzini [b], P. DiStefano [b], F. von Feilitzsch [d], T. Frank [b], D. Hauff [b], Th. Jagemann [d], J. Jochum [d], V. Jörgens [c], R. Keeling [a], H. Kraus [a], M. Loidl [b,1], J. Marchese [a], O. Meier [b], U. Nagel [d,2], F. Pröbst [b,*], Y. Ramachers [a], A. Rulofs [b], J. Schnagl [d], W. Seidel [b], I. Sergeyev [b,3], M. Sisti [b,4], M. Stark [d], S. Uchaikin [b], L. Stodolsky [b], H. Wulandari [d], L. Zerle [b]

[a] *Department of Physics, University of Oxford, Oxford OX1 3RH, UK*
[b] *Max-Planck-Institut für Physik, Föhringer Ring 6, D-80805 Munich, Germany*
[c] *Laboratori Nazionali del Gran Sasso, I-67010 Assergi, Italy*
[d] *Physik Department, Technische Universität München, D-85747 Munich, Germany*

Received 27 September 2001; accepted 21 November 2001

Abstract

Data taken by CRESST with a cryogenic detector system based on 262 g sapphire crystals has been used to place limits on WIMP dark matter in the Galactic Halo. The experiment was especially sensitive for low-mass WIMPs with spin-dependent cross sections and improves on existing limits in this region. © 2002 Elsevier Science B.V. All rights reserved.

1. Introduction

The goal of the CRESST [5] experiment is to detect WIMP dark matter particles via the energy they deposit when elastically scattering on nuclei. We have developed very sensitive massive cryogenic detectors for this purpose and installed them in a low-background facility in the Gran Sasso Underground Laboratory (LNGS). This paper

* Corresponding author. Tel.: +49-89-3235-4270.
E-mail address: proebst@mppmu.mpg.de (F. Pröbst).
[1] Present Address: CEA Saclay, DSM/DAPNIA, 91191 Giff-sur-Yvette Cedex, France.
[2] Permanent Address: National Institute of Chemical Physics and Biophysics, EE-12618 Tallinn, Estonia.
[3] Permanent Address: Joint Institute for Nuclear Research, Dubna, 141980, Russia.
[4] Present Address: INFN—Sezione di Milano, Piazza della Scienza 3, I-20126 Milano, Italy.

[5] Cryogenic Rare Event Search with Superconducting Thermometers.

0927-6505/02/$ - see front matter © 2002 Elsevier Science B.V. All rights reserved.
PII: S0927-6505(02)00111-1

describes our low-background facility in LNGS and Phase I of the project, which used 262 g sapphire cryogenic calorimeters, and presents the resulting dark matter limits.

2. Low-background facility

Since our detectors operate at ~15 mK, the central part of the CRESST low-background facility is the cryostat. The design of this cryostat had to combine the requirements of low temperatures with those of low background. Earlier cryostats in this field were conventional dilution refrigerators with some of the materials selected for low radioactivity. However, due to cryogenic requirements, some non-radiopure materials such as stainless steel cannot be completely avoided. Therefore we chose the design shown in Fig. 1, in which the experimental volume is housed in a

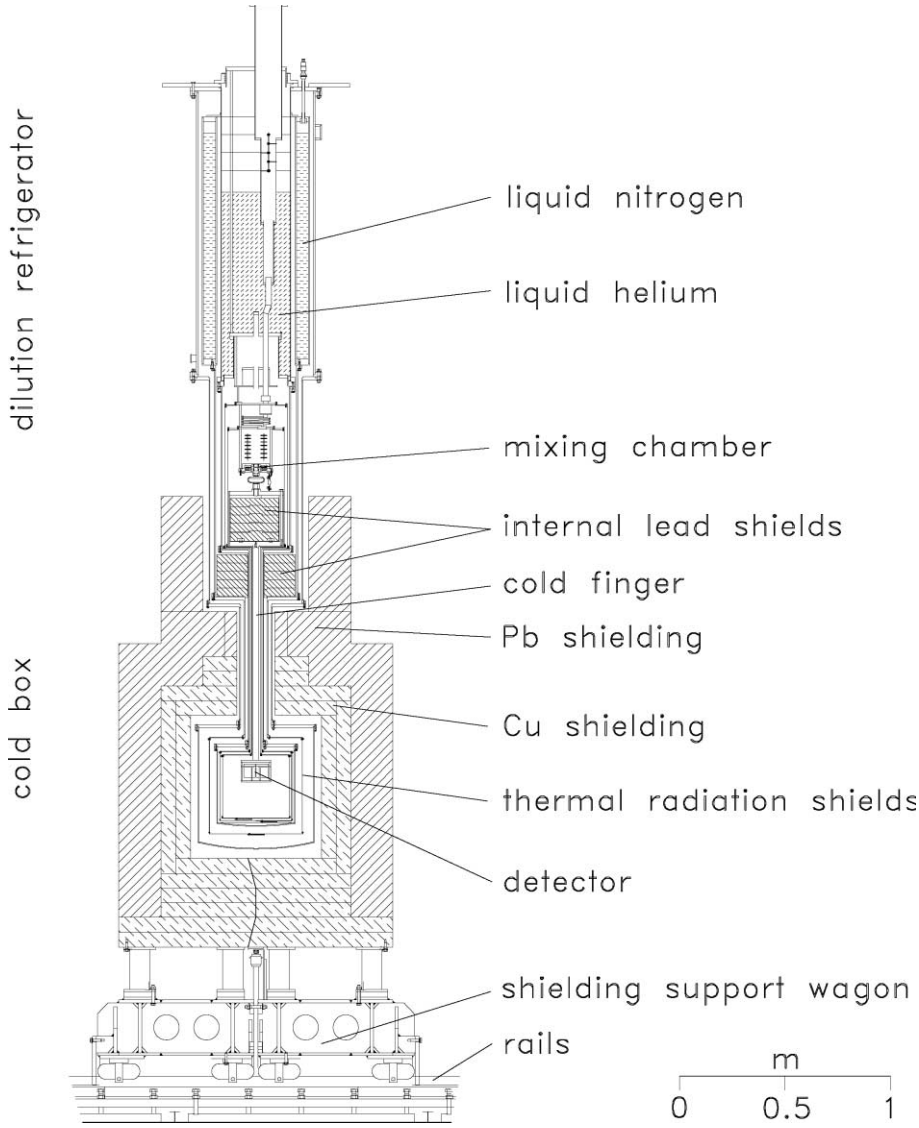

Fig. 1. Layout of dilution refrigerator and cold box.

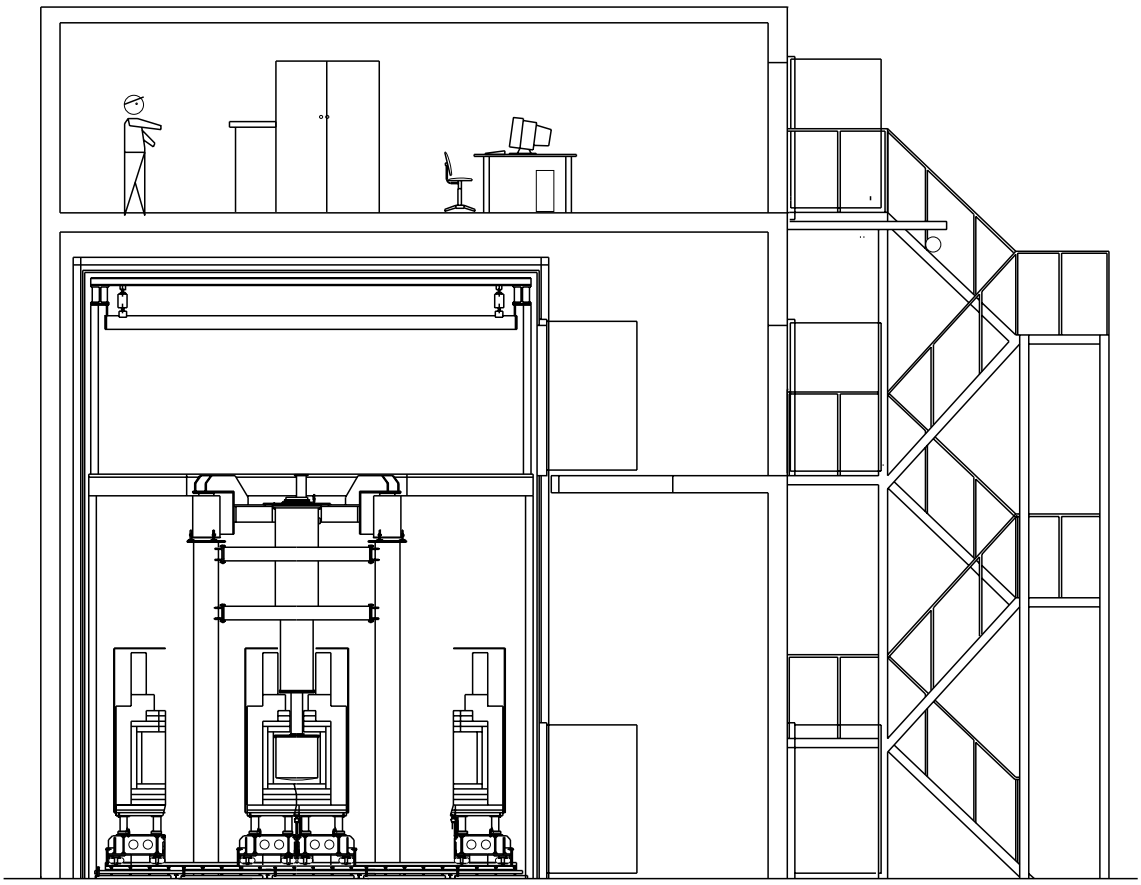

Fig. 2. Cross section of CRESST building in Hall B of LNGS. The external shielding is shown in both its open and closed positions.

"cold box", well separated from the dilution refrigerator. The experimental volume can hold up to 100 kg of target mass. The cold box was made of low-background copper, with high-purity lead used for the vacuum seals. It was surrounded by shielding consisting of 14 cm of low-background copper and 20 cm of lead. Special consideration was given to the space between the dilution refrigerator and the cold box. The separation was chosen large enough so that the "neck" of the external shielding, together with the internal shields, eliminated any direct line of sight from the outside world into the cold box. The low temperature of the dilution refrigerator was transferred to the cold box by a 1.5 m long cold finger protected by thermal radiation shields, all of low-background copper. A 20 cm thick lead shield inside a copper can was placed between the mixing chamber and the cold finger, with the low temperature transmitted here by the copper can. This internal shield, combined with another one surrounding the cold finger, served to block any line of sight for radiation coming from the dilution refrigerator into the experimental volume.

To avoid activation of the copper by cosmic rays we minimized the amount of time that the copper of the shielding and the cold box spent above ground. After electrolytic production the copper was stored in the cellar of a beer brewery near Munich, which shielded it from cosmic rays by more than 10 m water equivalent, reducing the hadronic component of the cosmic rays by a factor of about 500. Each piece was only brought out

of the brewery cellar for the few days needed for its machining, and then returned to the cellar. The total above-ground exposure of the copper was about 10 weeks.

It is not sufficient to use high-purity materials. Their surfaces must also be kept clean during use, and we have taken care to design our facilities in Gran Sasso to make this possible. The Faraday cage surrounding the experiment (Fig. 2) was chosen large enough so that all work on the low-background components of the experiment could be performed inside the cage. The cage was divided into two levels. The lower level was equipped as a clean room with a measured clean room class of 100 to protect the low-background components. Entrance to the clean room was through a changing room external to the Faraday cage (not shown in Fig. 2). The external lead and copper shields were in two closely fitting halves, each supported on a "wagon" on rails, so that the shielding could be opened without handling the individual pieces. The entire shielding was enclosed in a gas-tight radon box that is flushed with boil-off N_2 gas and maintained at a small overpressure. In its retracted position (shown in Fig. 2) the shielding was outside the dilution refrigerator support structure but still inside the clean room and sufficient room was then available to disassemble the cold box.

The upper level of the Faraday cage was outside the clean room and allowed access to the top of the cryostat for servicing and to the electronics. To save on floor space in Gran Sasso, the counting room and a laminar-flow work space for handling the detectors were placed on top of the Faraday cage. All of this equipment was inside a building in Hall B.

The original installation used a prototype cold box, not made of radiopure materials. The purpose of the prototype was to test the cryogenic functioning of the design and to provide a well-shielded environment for completing the development of the 262 g detectors. At the end of 1998 the prototype cold box was replaced by a radiopure version of the same design. After machining, the new cold box was cleaned by electropolishing and subsequent rinsing with high-purity water. The pieces were then brought to Gran Sasso in gas-tight transport containers made of PE and flushed with nitrogen.

3. Detectors used in Phase I

3.1. Sapphire cryogenic calorimeters

The detectors we have developed [1,2] consist of a dielectric crystal in which the particle interaction takes place, and a small superconducting film evaporated onto the surface, serving as a thermometer. The detector is operated within the superconducting-to-normal transition of the thermometer, where a small temperature rise ΔT of the thermometer leads to a relatively large rise ΔR of its resistance. The ΔT induced by a particle in the energy range of interest for dark matter is much smaller than the width of the transition, so that there is an approximately linear relation between ΔT and ΔR.

We have found [3] that the energy deposited by the particle does not thermalize in the dielectric crystal. Instead, to good approximation, the high frequency phonons created by an event spread throughout the crystal and reflect at the surfaces until they are directly absorbed in the superconducting film. Thus the energy resolution is only moderately dependent on the size of the crystal, and scaling up to large detectors is feasible.

This technique can be applied to a variety of materials. The detectors employed in Phase I of the CRESST experiment in Gran Sasso used 262 g sapphire (Al_2O_3) absorbers and tungsten (W) thermometers operating near 15 mK. The 262 g sapphire detectors were developed by scaling up a 32 g sapphire detector [2]. Due to optimized design, and because of the non-thermalization of the phonons, this scaling-up was achieved without significant loss in sensitivity.

Fig. 3 shows a 262 g sapphire detector mounted in its copper holder. The $4.0 \times 4.0 \times 4.1$ cm^3 crystal rested thermally insulated on supports attached to the holder. In the original design, these supports were sapphire balls. Some of the supports were fixed and others were on pins loaded with plastic springs.

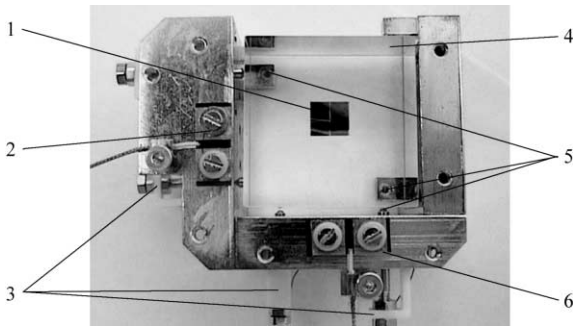

Fig. 3. Photograph of a 262 g sapphire detector. The transparent sapphire crystal (4) is in the center. The other visible components are (1) tungsten thermometer, (2) holder pads with screw contacts for connecting to the heater circuit, (3) plastic springs, (5) sapphire balls, (6) holder pads with screw contacts for connecting to the SQUID read-out circuit.

A succession of detectors were installed with varying thermometer geometry and electrical connections. Detector #8 (numbered in order of fabrication), which was used for dark matter limits presented here, had a W thermometer of size 3 mm × 5 mm. The electrical and thermal connections to the detector are shown in Fig. 4. Thermal contact between the holder and the detector was provided by gold wires of 25 μm diameter bonded to the Cu holder and to a gold contact pad in the middle of the W thermometer. The copper holder was thermally connected via the cold finger to the mixing chamber of the dilution refrigerator, which was stabilized to a temperature of 6 mK. The electrical connection to the detector was made by superconducting Al wires bonded to Al pads on each end of the thermometer and to isolated contact pads on the holder. To avoid radioactive solder joints, the superconducting wires from the holder pads to the external readout circuit were screwed to the contact pads. The resistance of the thermometer (∼0.1 Ω) was measured by passing a constant current I_0 through the readout circuit in which the thermometer was in parallel with a small (∼0.05 Ω) resistor and the input coil of a dc-SQUID (Fig. 5). A rise in the thermometer resistance was then measured via the current rise through the SQUID input coil.

In a separate circuit, a heater to control the temperature of the detector was provided by a ∼5 mm long 25 μm diameter gold wire which was bonded to the gold pad in the center of the W thermometer and two very small Al contact pads on the sapphire crystal to either side of the thermometer. External connections to the two small Al pads were used to apply a controlled voltage across this gold wire. To avoid interaction between the heater circuit and the readout circuit, the place where they connect—the bond spot of the gold wire—was made as small as possible and its long axis was perpendicular to the direction of current

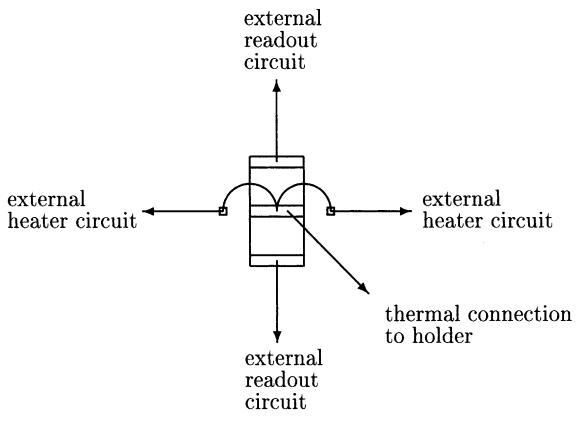

Fig. 4. Thermal and electrical connections to thermometer.

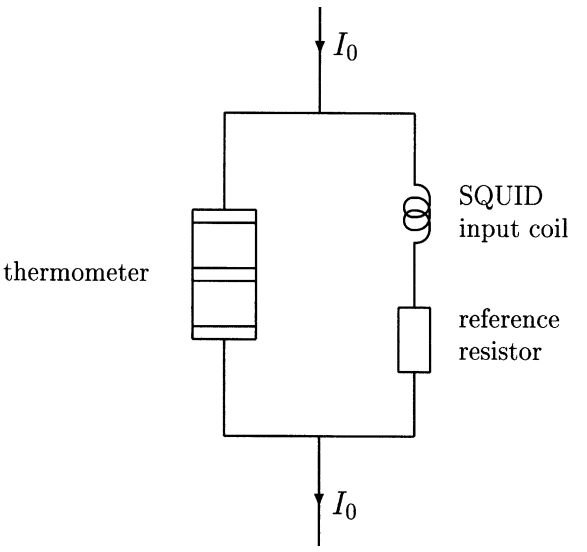

Fig. 5. Readout circuit to measure the resistance of the thermometer.

flow in the thermometer. The thermometer temperature was kept constant between pulses using the baseline of the SQUID output voltage as the temperature indicator and regulating the voltage to the heater under computer control using a proportional integral algorithm. The heater was additionally used to inject short heat pulses for monitoring the long term stability of the energy calibration and for measuring the trigger efficiency close to threshold.

For the data-acquisition system, the output voltage of the SQUID electronics was split into two branches. One was shaped and ac-coupled to a trigger unit and the other passed through an anti-aliasing filter and was dc-coupled to a 16-bit transient recorder. The time base of the transient recorder was chosen to be 40 μs, which provided about 20 samples in the rise time of the pulse. The record length of 1024 time bins included a "pre-trigger" region of 256 bins, to record the baseline before the event, and a "post-trigger" region which contained the pulse. A typical recorded pulse is shown in Fig. 6. The transient recorder data for each triggered event were written to disk for off-line analysis. After each trigger there was a dead time of ~25 ms to allow time for the readout and the next pre-trigger region. Pulses arriving in another detector within half of the post-trigger period of the detector which triggered first were also recorded, including the time delay with respect to the first trigger.

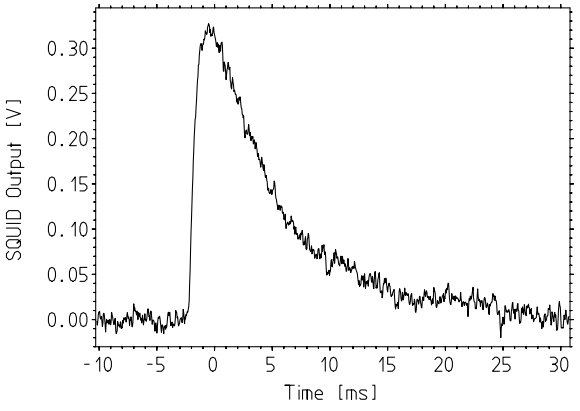

Fig. 6. Typical measured pulse of about 6 keV.

3.2. Data taken in Gran Sasso

The sensitivity and size of the 262 g detectors meant that they could only be meaningfully tested in a low-background environment. This was first done in our setup in Gran Sasso using the prototype cold box of normal copper. Using active thermal feedback, an energy resolution of 133 eV (FWHM) was achieved for 1.5 keV X-rays [4]. This active feedback was not used in our dark matter run, and without it the resolution at 1.5 keV was more typically 230–330 eV [5].

During 1999, a first series of measurements with four 262 g detectors under low-background conditions was performed in the new radiopure cold box. The measured background was much higher than expected. It was time-dependent and not Poissonian, indicating that it was not caused by radioactivity. The origin of this background was investigated in a series of runs and finally identified as the spontaneous formation of microscopic cracks in the sapphire crystal at the points where it was supported by sapphire balls. Due to the extremely small contact area of the balls, an excessive pressure resulted from the force needed to tightly hold the crystal. In the spring of 2000 the balls were replaced by plastic stubs with a larger contact area (3 mm diameter) and the spurious background completely disappeared. The use of these stubs did not lead to a noticeable loss of sensitivity, despite their larger contact area.

To study the background and obtain dark matter limits, several runs were performed in 2000, with the longest one lasting about three months. The high reliability, long-term stability and uptime during these runs demonstrated convincingly the suitability of such a system for dark matter searches.

In October 2000 the shaping of the trigger signal was optimized and a lower trigger threshold was obtained. A week of data were taken under these conditions, with a few short interruptions to re-fill the cryostat with liquid helium. Due to the lower threshold, the dark matter limits obtained from these data are better than those from the previous longer runs, and it is these data which we discuss further. The data consist of a 10 h calibration run with an external ^{57}Co source, the dark

matter run without source (138.8 h of which 0.6 was dead time following triggers) and finally another calibration run. The data from detector #8, which had the lowest threshold, was used to set our dark matter limits. A second detector was used to eliminate coincident events.

3.3. Detector monitoring and calibration

The performance of each detector was monitored by injecting heater pulses into the small heater wire bonded to the W thermometer. These were produced by a voltage pulse from a pulser module, with the shape adjusted to create a detector response similar to that caused by a particle interaction. A pulse was sent every 30 s throughout both dark matter and calibration runs. The height of the pulses was varied to cover the whole dynamic range, with more pulses in the low energy region. This method provided a monitor of the stability of the detectors, an extrapolation of the energy calibration over the whole dynamic range, and a measure of their trigger efficiency as a function of deposited energy. To calibrate the energy scale a ^{57}Co source (122 and 136 keV γ lines) was inserted inside the shielding via a removable plug, illuminating the cold box from below. Data were taken with this source along with the heater pulses. Comparison of the pulse heights from the source and heater pulses provided an absolute calibration of the heater pulses in terms of equivalent γ energy.

The amplitude of each pulse was determined by fitting it with a template. This avoids the bias of picking the highest point of suitably filtered pulses, which is systematically pulled by noise fluctuations to larger values. The absence of any bias is important for a precise definition of the threshold. It was therefore checked by fitting randomly-sampled baseline noise taken throughout the data-taking period. The resulting distribution peaked with no significant bias at (-0.0019 ± 0.003) keV.

The first step in the energy calibration used the heater pulses. A separate heater pulse template for each pulser voltage was made by averaging many measured pulses from that voltage, and this template used to fit the amplitude of each heater pulse. The stability of detector #8 during the dark matter run can be seen in Fig. 7 where the amplitude for heater pulses is shown as a function of time. To interpolate between pulser voltages, the amplitudes for heater pulses were plotted as a function of pulser voltage and fit with a polynomial function. Similarly a template was made for pulses in the 122 keV γ line of the calibration source to fit the amplitude of those pulses. This was compared to the heater pulse amplitudes to determine the scale factor between pulser voltage and γ energy. The resulting detector response as a function of γ energy is shown in Fig. 8.

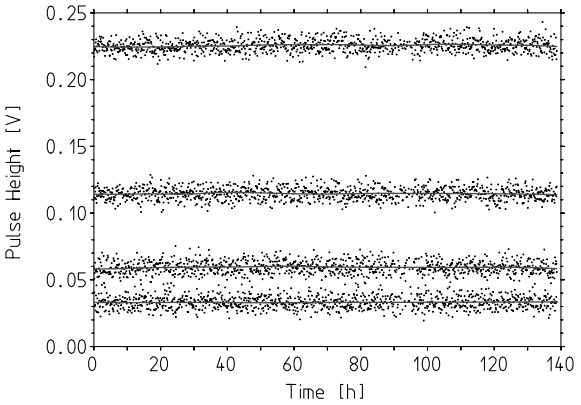

Fig. 7. The measured pulse height of detector #8 as a function of time during the dark matter run for the heater pulses of energy 0.58, 1.04, 2.04, and 4.08 keV. The detector is seen to be stable to within the resolution. The fitted lines were used to calculate the response function at the time of event pulses as shown in Fig. 8.

For the dark matter data, the response function determined above was used to convert each event's pulse shape to energy in each time bin of the transient recorder record. A template was made from similarly-converted calibration-source pulses around the Compton edge (30–35 keV). This template could be used to fit the pulse height, but it was found that an optimal filter gave a slightly better resolution. The optimal filter was calculated using the template and randomly sampled baseline noise. A comparison to the template fit showed that the optimal filter did not introduce an energy bias. The resulting spectrum for the dark matter run is shown as the upper histogram in Fig. 9.

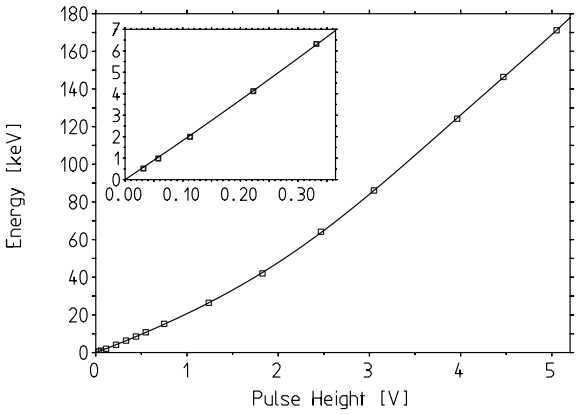

Fig. 8. The pulse heights for detector #8 for each injected heater pulse energy calculated from the lines in Fig. 7 are shown as points. The curve is the fitted polynomial which was used as the response function. The inset is an enlargement of the low energy region.

The reliability of the energy calibration method to low energy was later checked with a dedicated run where a low-activity ^{57}Co source was mounted inside the cryostat directly facing the crystals. Besides the 122 and 136 keV γ lines, this source gave a 14.4 keV γ line and a 6.4 keV Fe X-ray line. The source was chosen to be very weak to reduce the chance of contamination, with the result that the one week run gave low statistics in the 14.4 and 6.4 keV lines. After applying the standard calibration method of extrapolation from the 122 keV line as described above, the measured energies for the 14.4 and 6.4 keV lines were $15.16^{+0.09}_{-0.09}$ keV and $6.70^{+0.07}_{-0.05}$ keV, respectively, with the fit errors corresponding to 90% CL. Our calibration procedure puts the 14.4 and the 6.4 keV lines 5.3% and 5.4% too high. Since it is the lower energies which most affect our dark matter limits, this tendency to shift events up in energy puts our limits on the conservative side.

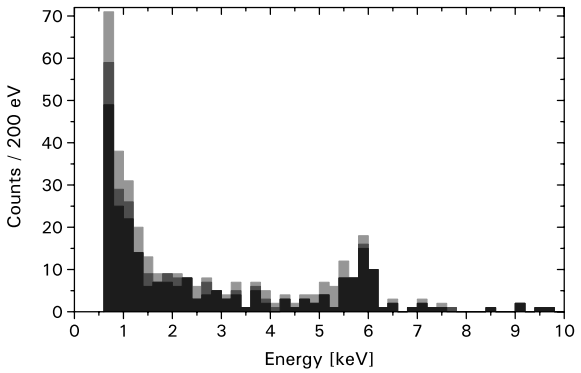

Fig. 9. Energy spectrum of events in detector #8 in the dark matter run (without source) in 200 eV bins. The upper histogram shows the uncut data, the middle histogram the data after coincident events were rejected, and the lower histogram after the pulse shape cut.

4. Limits on WIMP dark matter

4.1. Energy spectrum from dark matter run

The individual detectors varied in their response, with detector #8 having a lower threshold and thus giving the best dark matter limits. The trigger efficiency of this detector was measured to be 100% down to an energy of 580 eV throughout the dark matter run. A software threshold of 600 eV was used to avoid reliance on the detailed behaviour of the trigger efficiency at very low energies. Detector #8 had 446 events from the software threshold to 120 keV. The uncut spectrum is shown as the upper histogram in Fig. 9.

Events in coincidence in two or more detectors cannot be due to WIMP interactions, and so can be discarded. The distribution of the time differences between events showed a clear coincidence peak with a full width at half maximum of about 0.4 ms and long tails extending to about 4 ms for very low detected energies. The coincidence cut was set at ± 4 ms, removing 76 events (17% of the total events) and introducing negligible dead time.

The pulse shape of the remaining 370 events was then examined. Some of the events were spurious, induced by mechanical vibration or electronic noise, with an abnormal pulse shape. Particle interactions could also produce distorted shapes when the energy deposit was high and beyond the detector's dynamic range. To judge the correctness of the pulse shape, each event was fitted with the template and the r.m.s. deviation calculated. A cut on this deviation was chosen to be conservative and have a retention efficiency of essentially 100% at all energies for good events. Its efficiency was tested

with heater pulses, resulting in only 1 out of 1032 of the 580 eV heater pulses being discarded. A second test with the calibration source showed that only 0.22% of the events were discarded. After the pulse shape cut 320 events remain. These are shown as the lower histogram in Fig. 9.

To investigate the significance of the coincidence rate in more detail, the order of the cuts was reversed. Applying the pulse shape cut first removed 59 events. The coincidence cut then removed 67 events. Thus nine events were both in coincidence and had bad pulse shapes and could be due to a common external source such as a microphonic disturbance from the cryostat. The energy of these nine events was below 6 keV in both detectors. The remaining 67 coincident events appear to be good pulses and could be due to a photon or neutron scattering depositing energy in two crystals. These 67 coincident events are 17% of the total events with good pulse shape. Considering that only two detectors were active in this run and only one out of six faces was facing the other crystal, this coincidence rate of 17% is consistent with the solid angle for detecting coincidence and thus with all events being background. This shows that the coincidence cut could be very useful in eliminating background in a larger segmented detector.

The final spectrum for detector #8 is shown again in Fig. 10. In the energy range from 15 to 25 keV there are 11 counts which translate into a background of (0.73 ± 0.22) counts/kg/keV/day. The background drops to about 0.3 counts/kg/keV/day at 100 keV.

The spectrum shows a peak at about 5.9 keV with (7.0 ± 1.2) counts/day. The position of the peak suggests a contamination with ^{55}Fe in the vicinity of the crystal. ^{55}Fe emits Mn X-rays at 5.9 keV with no γ's and was used as a source for characterizing the performance of the detectors. The spectra measured with other detectors were very similar, with nearly the same count rates in both the peak and the continuous part of the spectrum. However the peak is wider than expected, 572 ± 90 eV FWHM compared to the 200 ± 50 eV of the 6.4 keV line from the internal calibration source, so that it may be due to more than a single X-ray line.

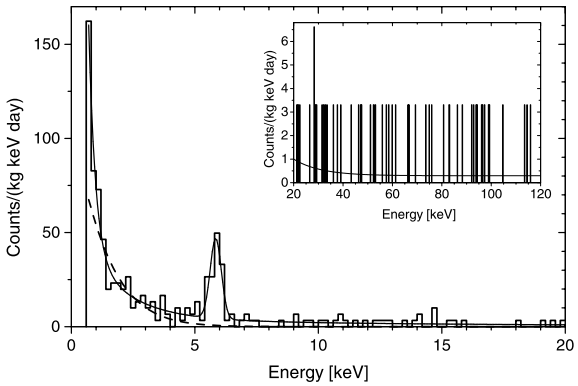

Fig. 10. Energy spectrum of detector #8 during the dark matter run (1.51 kg day) in 200 eV bins. The inset shows the spectrum at higher energies. The solid curve is an empirical fit to the experimental spectrum which was used in extracting dark matter limits. For illustration a 5 GeV WIMP excluded at 90% CL is shown as the dashed curve.

4.2. Extraction of limits

The extraction of upper limits for the WIMP scattering cross section as a function of WIMP mass involves comparing the measured energy spectrum to that expected for nuclear recoils caused by elastic WIMP scattering.

The recoil spectrum expected from WIMP scattering on the nuclei of the detector was calculated using the formulae from Ref. [6] for a truncated Maxwell velocity distribution in an isothermal WIMP–halo model. The parameters are summarized in Table 1. For the spin-dependent interaction the only contribution is from the ^{27}Al nuclei, which have spin of 5/2 and 100% natural isotopic abundance. The WIMP–nucleus scattering cross section σ_0 remains as a free parameter which scales with the number of expected events.

Table 1
List of parameters used for calculating WIMP recoil spectra

Parameter name	Value
WIMP Maxwellian velocity parameter v_0	220 km/s
Escape velocity	650 km/s
Earth's relative velocity	230 km/s
WIMP local halo density	0.3 GeV/cm^3

The WIMP–nucleus scattering cross section at finite momentum transfers q is parameterized as

$$\frac{\mathrm{d}\sigma}{\mathrm{d}q^2}(q) = \frac{\sigma_0}{q_{\max}^2} F^2(q), \tag{1}$$

where σ_0 is the total point like isotropic scattering cross section, $q_{\max}$ is the largest momentum transfer and $F(q)$ is the form factor. For the spin independent interaction we have used the Helm form factor [9]

$$F(q) = \frac{3j_1(qR_0)}{qR_0} \exp[-(qs)^2/2], \tag{2}$$

where j_1 is the spherical Bessel function of index 1, $R_0 = \sqrt{R^2 - 5s^2}$, $s = 1$ fm and $R = 1.2A^{1/3}$ fm (A is the atomic number) as suggested in Ref. [10]. For small nuclei the effect of the form factor is small, for ^{27}Al reducing the cross section by only a factor of 0.712 at a recoil energy of 100 keV, so that details of the form factor have negligible effect on the resulting exclusion plot. For spin-dependent interactions we have used the form factor of Ref. [11] explicitly calculated for the ^{27}Al nucleus.

The theoretical WIMP recoil spectrum must be convoluted with the experimental resolution. The width of the 5.9 keV peak in Fig. 10 is $\Delta E = 572 \pm 90$ eV (FWHM), whereas the resolution of the peak at 6.4 keV from the internal calibration source is 200 ± 50 eV, in agreement with the energy resolution of the heater pulses. At the 122 keV peak of the calibration source the resolution degrades to about 5 keV. To be conservative we chose the larger value for the resolution at 6 keV and used an energy-dependent resolution formula which interpolates between 6 and 122 keV values: $\Delta E = ((0.519\ \mathrm{keV})^2 + (0.0408\ E)^2)^{1/2}$. A comparison with the limits obtained using the smaller resolution at 6 keV showed negligible change. The recoil spectrum was convolved with a Gaussian curve with that full width at half maximum. We assumed that electron and nuclear recoils have the same fraction of their energy going into phonons (i.e. a quenching factor of 1). An experimental proof of this plausible assumption does not yet exist for our sapphire detectors; however, quenching factors close to 1 have been measured with other cryogenic detectors [12].

There is no standard procedure for extracting upper limits in a case like this where the signal shape is a broad smooth spectrum on top of an unknown background spectrum of similar shape. To be free of assumptions on the background shape, one intuitively wants to rule out WIMP cross sections σ_0 where the WIMP recoil spectrum alone is above the data. The problem is how to do this in a statistically correct manner to obtain a limit at a given confidence level (here 90%). Below we describe three different approaches and compare their results.

The optimal interval method has been used by other groups [13–16]. This method uses the fact that for a given WIMP mass, some energy intervals (typically close to the threshold) are more effective than others for constraining the existence of a WIMP signal in the data. The optimal interval method tries all possible energy intervals and chooses for each WIMP mass the one which gives the most stringent limit on σ_0. In each interval the total number of detected events is simply compared to the integral of the WIMP spectrum to find the σ_0 that is excluded to 90% CL, with no consideration given to whether the shapes agree within the interval. We applied this method, using a variable-width energy interval with a smallest width of 1.2 keV (twice our energy resolution). The result is shown as the dashed line in Fig. 11. The expected WIMP spectrum is always largest at the lowest recoil energy and falls more steeply for lower mass WIMPs. Therefore at low WIMP masses the optimal interval starts at threshold and is limited by the 1.2 keV minimal width, which is quite large for very low WIMP masses. The downward jump near 10 GeV in the optimal interval limits is due to the optimal interval shifting from below the 5.9 keV peak to above it. For WIMP masses above 10 GeV the optimal interval can be selected as a small section of a wide region with low statistics, which can result in a large selection bias. For example for WIMP masses between 30 and 1000 GeV the relatively small interval from 22.6 to 26.4 keV with no counts is selected. To test the selection bias we have used two simple alternative methods.

In the fit method we fit the spectrum with an empirical function B as shown in Fig. 10. using a

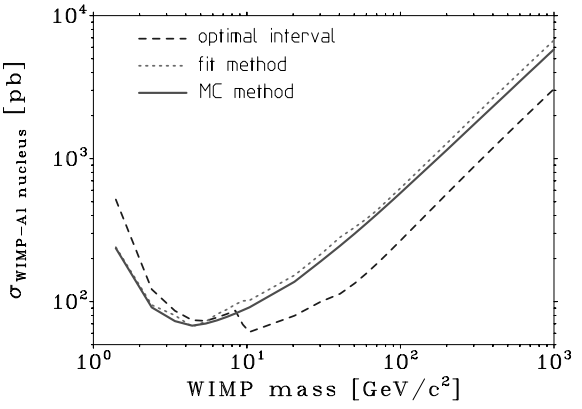

Fig. 11. Comparison of the different methods described in the text to extract 90% CL exclusion limits for the WIMP-^{27}Al spin-dependent σ_0 limit. The MC method was selected to extract the limits shown in Figs. 12 and 13.

maximum likelihood method with Poissonian statistics in each bin. The function is the sum of three falling exponentials, a constant term, and a Gaussian curve for the peak near 5.9 keV. The maximum likelihood $\mathscr{L}$ of the best fit B_0 is called $\mathscr{L}_0$. Without a WIMP contribution the function B_0 just describes the background. Then a WIMP signal S is added and the background function is redefined to $B' = B_0 - S$, or if that is negative then $B' = 0$. With this redefinition we avoid in any sense subtracting the background, and are only using it as a way to calculate the likelihood. For a small enough σ_0, for which S is below the function B_0 in each bin, the likelihood is unchanged. With increasing σ_0, when S starts to exceed the function B_0 in some energy bin, B' becomes limited at 0 and the likelihood $\mathscr{L}$ starts to decrease. The σ_0 excluded at 90% CL is obtained when $\ln \mathscr{L} = \ln \mathscr{L}_0 - 1.28^2/2$ is reached. (1.28σ gives the two-sided 80% CL of a Gaussian distribution; the factor of 2 is because we use likelihood rather than χ^2.)

The Monte Carlo (MC) method starts from the same empirical fit of the data and uses this fit function B_0 as the Poisson mean in each bin to generate a large number of synthetic MC spectra. To determine the 90% CL upper limit the same functional form B is fit to each synthetic data set and the σ_0 is found for which $S = B$ in one energy bin for that data set. Those σ_0 values are then ordered and the 90% CL upper limit is that σ_0 which is above 90% of the values determined from all the synthetic data sets. Finally, the adequacy of the fit function B_0 to describe the real data was tested by comparing the likelihood of B_0 for the data with the likelihoods of the fits to the synthetic data sets. The likelihood of B_0 is near the middle of the distribution, with 53% of the synthetic likelihood values being larger, indicating a very adequate choice of fit function.

The results of all three methods are compared in Fig. 11. At low WIMP masses the optimal interval method yields weaker limits due to the restriction to a 1.2 keV minimal width. For WIMP masses above 10 GeV the optimal interval gives the strongest limits, demonstrating the effect of the selection bias. The difference between MC and fit method is small and we have chosen the MC method to present our limits.

Fig. 12 shows our 90% CL upper limits on the σ_0 for spin-dependent WIMP interactions on Al. In order to compare our results to those of experiments using other target nuclei, we have converted our WIMP–nucleus cross sections to WIMP–proton cross sections [18]. This conversion introduces some dependence on the model for the

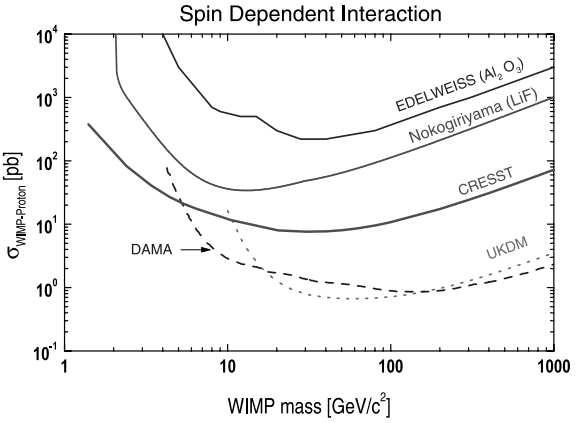

Fig. 12. Equivalent WIMP–proton cross section limits (90% CL) for a spin-dependent interaction as a function of the WIMP mass from a 1.51 kg day exposure of a 262 g sapphire detector. For comparison we show limits from the EDELWEISS dark matter search with cryogenic sapphire detectors [16], from the experiment at the Nokogiriyama site with cryogenic LiF detectors [17], and from DAMA [19] and UKDMC [20] with NaI detectors.

nuclear physics of the target nuclei and the SUSY composition of the WIMP.

The 'conventional' conversion procedure relied on the odd-group model [21,22] in which the only contribution to the WIMP–nucleus interaction for a nucleus with an unpaired proton or neutron comes from the protons or neutrons, respectively. Then, when converted to the cross section on the unpaired nucleon (proton for Al, Na, I), the WIMP-model dependence conveniently cancelled. In the notation of Ref. [22] the WIMP–proton cross section is then obtained from the WIMP–nucleus cross section σ_0 by

$$\sigma_{\mathrm{WIMP\text{–}p}} = \sigma_0 \frac{\mu_\mathrm{p}^2}{\mu_\mathrm{A}^2} \frac{\lambda_\mathrm{p}^2 J_\mathrm{p}(J_\mathrm{p}+1)}{\lambda_\mathrm{A}^2 J_\mathrm{A}(J_\mathrm{A}+1)} \tag{3}$$

The reduced mass μ_A is given by $\mu_\mathrm{A} = m_\mathrm{A} m_\chi/(m_\mathrm{A}+m_\chi)$ for WIMP mass m_χ and target nucleus mass m_A. The values for the $\lambda^2 J(J+1)$ factors are given in Ref. [22] as 0.750 for the proton and 0.087 for ^{27}Al. These values and Eq. (3) were used to obtain the CRESST WIMP–p limits given in Fig. 12. In the odd group model a comparison to n-type nuclei like ^{73}Ge becomes very problematic because the WIMP-model dependence does not cancel (see e.g. the discussion in Ref. [7, Table 4]). Therefore in Fig. 12 we only compare our results to those of other p-type nuclei. As can be seen in Fig. 12, we improve existing limits for low-mass WIMPs. This is due to our low threshold, and was the goal of the first phase of CRESST.

According to shell model calculations (see Ref. [7,8,23]) and references therein; for ^{27}Al, (see Ref. [11]) strict p- or n-type nuclei do not exist and in general both protons and neutrons contribute and can even interfere in the cross section. Using the spin factor from Ref. [11] would shift the whole CRESST exclusion curve down by a factor of 1/1.9 to lower cross sections, if one neglects the neutron part for the spin factor as described in [23].

For the spin-independent interaction both Al and O nuclei contribute. The spin-independent (scalar) interaction is dominated by the strange and heavy quark content of the proton and neutron, which are usually assumed to be equal, leading to an A^2 dependence of the cross section [24]. We assumed this dependence in calculating the expected recoil spectrum used to extract our spin-independent cross section limits, which are shown as the equivalent WIMP–p cross section in Fig. 13. The scalar channel is not very favourable for a target with light nuclei like sapphire, containing aluminium and oxygen, due to the crucial A^2 coherence factor. However we still succeed in improving the limits for WIMP masses below 5 GeV.

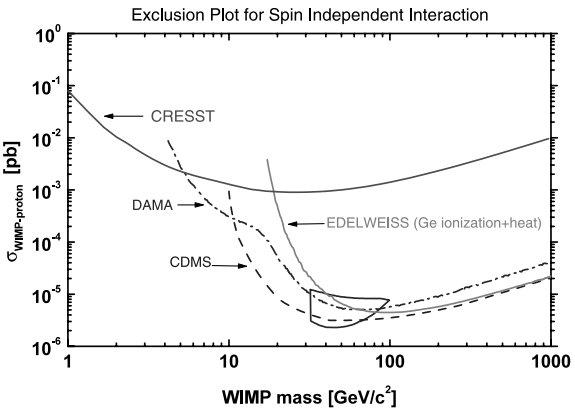

Fig. 13. Equivalent WIMP–nucleon cross section limits (90% CL) for a spin-independent interaction as a function of the WIMP mass from a 1.51 kg day exposure of a 262 g sapphire detector. For comparison limits are shown from CDMS with cryogenic detectors and statistical subtraction of the neutron background [25], EDELWEISS with a heat and ionization Ge detector [26], and UKDMC [20] and DAMA [19] with NaI detectors, together with the allowed region at 3σ CL from the DAMA annual modulation data [27].

5. Conclusions

The CRESST installation in Gran Sasso and our cryogenic detectors with superconducting phase transition thermometers and SQUID readout have been demonstrated to meet the needs of a dark matter search in terms of low radioactive background and long-term stable cryogenic operation, with one run lasting for three months.

Phase I of the experiment used 262 g sapphire crystals as the target medium and was designed to provide a low energy threshold for nuclear recoils and thus good sensitivity for low-mass WIMPs. The best WIMP limits were obtained from a 138 h

run during which one of the detectors was 100% efficient above a software threshold of 600 eV. The background level was below 1 count/kg/keV/day above 20 keV, falling to about 0.3 at 100 keV. Events in coincidence in two detectors made up a significant fraction of the background, so that a coincidence cut could be a powerful tool in reducing the background in a larger segmented detector. Dark matter limits were obtained without the need for background subtraction or large efficiency corrections. Data from the best detector yielded limits on both spin-dependent and spin-independent WIMP interactions which are more stringent than previously available limits for WIMP masses below 5 GeV.

The second phase of the experiment is now being prepared. This will use cryogenic scintillators [28,29], with simultaneous measurement of the phonon and scintillation light to reduce the background from local radioactivity and provide improved sensitivity for high-mass WIMPs.

Acknowledgements

This work was supported by the DFG SFB 375 "Particle Astrophysics", the EU Network "Cryogenic Detectors" (contract ERBFMRXCT980-167), BMBF, PPARC, and two EU Marie Curie Fellowships.

References

[1] W. Seidel, G. Forster, et al., Phys. Lett. B 236 (1990) 483; M. Frank, D. Dummer, et al., Nucl. Instrum. Meth. A 345 (1994) 367;
P. Ferger et al., Phys. Lett. B 323 (1994) 95.
[2] P. Colling, A. Nucciotti, C. Bucci, et al., Nucl. Instrum. Meth. A 354 (1995) 408.
[3] F. Pröbst, M. Frank, et al., J. Low Temp. Phys. 100 (1995) 69.
[4] O. Meier et al., Proc. LTD-8, Nucl. Instrum. Meth. A 444 (2000) 350.
[5] M. Sisti, O. Meier, et al., Nucl. Instrum. Meth. A 466 (2001) 499.
[6] F. Donato, N. Fornengo, S. Scopel, Astropart. Phys. 9 (1998) 247.
[7] J.D. Lewin, P.F. Smith, Astropart. Phys. 6 (1996) 87.
[8] G. Jungman, M. Kamionkowski, K. Griest, Phys. Rep. 267 (1996) 195.
[9] R.H. Helm, Phys. Rev. 104 (1956) 1466.
[10] J. Engel, Phys. Lett. B 264 (1991) 114.
[11] J. Engel et al., Phys. Rev. C 52 (1995) 2216.
[12] A. Alessandrello et al., Phys. Lett. B 384 (1996) 316.
[13] HDMS, L. Baudis et al., Phys. Rev. D 59 (1999) 022001.
[14] IGEX, A. Morales et al., Phys. Lett. B 489 (2000) 268.
[15] ROSEBUD, S. Cebrian et al., Astropart. Phys. 15 (2001) 79.
[16] EDELWEISS, A. de Bellefon et al., Astropart. Phys. 6 (1996) 35.
[17] W. Ootani et al., Phys. Lett. B 461 (1999) 371.
[18] CRESST, W. Seidel et al., Proc. LTD-5, J. Low Temp. Phys. 93 (1993) 797.
[19] DAMA, R. Bernabei et al., Phys. Lett. B 389 (1996) 757.
[20] UKDMC, N. Spooner et al., Phys. Lett. B 473 (2000) 330.
[21] J. Engel, P. Vogel, Phys. Rev. D 40 (1989) 3132.
[22] J. Ellis, R.A. Flores, Phys. Lett. B 263 (1991) 259.
[23] D.R. Tovey et al., Phys. Lett. B 488 (2000) 17.
[24] J. Engel, S. Pittel, P. Vogel, Int. J. Mod. Phys. E 1 (1992) 1.
[25] CDMS, R. Abusaidi et al., Phys. Rev. Lett. 84 (2000) 5699.
[26] EDELWEISS, A. Benoit et al., astrp-ph/0106094, 6 June 2001.
[27] DAMA, R. Bernabei et al., Phys. Lett. B 480 (2000) 23.
[28] P. Meunier et al., Appl. Phys. Lett. 75 (1999) 1335.
[29] CRESST, M. Bravin et al., Astropart. Phys. 12 (1999) 107.

2.5A Detectors for EDELWEISS

Ref. [54].

ELSEVIER

Astroparticle Physics 14 (2001) 329–337

Astroparticle Physics

www.elsevier.nl/locate/astropart

Background discrimination capabilities of a heat and ionization germanium cryogenic detector

EDELWEISS Collaboration

P. Di Stefano [a,*], L. Bergé [b], B. Chambon [c], M. Chapellier [d], J. Chaumont [b], G. Chardin [a], P. Charvin [a,e], M. De Jésus [c], D. Drain [c], L. Dumoulin [b], P. Forget [d], P. Garoche [f], J. Gascon [c], C. Goldbach [g], D. L'Hôte [d], J. Mallet [a], J. Mangin [h], S. Marnieros [b], L. Miramonti [a], L. Mosca [a], X-F. Navick [a], G. Nollez [g], P. Pari [d], S. Pécourt [c], E. Simon [c], L. Stab [i], J-P. Torre [j], R. Tourbot [d], D. Yvon [a]

[a] *CEA, Centre d'Etudes Nucléaires de Saclay, DSM/DAPNIA, F-91191 Gif-sur-Yvette Cedex, France*
[b] *CSNSM, IN2P3-CNRS, Université Paris XI, bât. 108, F-91405 Orsay Cedex, France*
[c] *IPN Lyon and UCBL, IN2P3-CNRS, 43 Bd. du 11 novembre 1918, F-69622 Villeurbanne Cedex, France*
[d] *CEA, Centre d'Etudes Nucléaires de Saclay, DSM/DRECAM, F-91191 Gif-sur-Yvette Cedex, France*
[e] *Laboratoire Souterrain de Modane, CEA-CNRS, 90 rue Polset, F-73500 Modane, France*
[f] *Laboratoire de Physique des Solides, Université Paris XI, F-91405 Orsay Cedex, France*
[g] *Institut d'Astrophysique de Paris, INSU-CNRS, 98 bis Bd. Arago, F-75014 Paris, France*
[h] *LPUB, Université de Bourgogne, F-21078 Dijon, France*
[i] *Institut de Physique Nucléaire, Université Paris XI, F-91405 Orsay Cedex, France*
[j] *Service d'Aéronomie, BP 3, F-91371 Verrières le Buisson Cedex, France*

Received 21 March 2000

Abstract

The discrimination capabilities of a 70 g heat and ionization Ge bolometer are studied. This first prototype has been used by the EDELWEISS dark matter experiment, installed in the Laboratoire Souterrain de Modane, for direct detection of WIMPs. Gamma and neutron calibrations demonstrate that this type of detector is able to reject more than 99.6% of the background while retaining 95% of the signal, provided that the background events distribution is not biased towards the surface of the Ge crystal. However, the 1.17 kg day of data taken in a relatively important radioactive environment show an extra population slightly overlapping the signal. This background is likely due to interactions of low energy photons or electrons near the surface of the crystal, and is somewhat reduced by applying a higher charge-collecting inverse bias voltage (−6 V instead of −2 V) to the Ge diode. Despite this contamination, more than 98% of the background can be rejected while retaining 50% of the signal. This yields a conservative upper limit of 0.7 event $\mathrm{day}^{-1}\,\mathrm{kg}^{-1}\,\mathrm{keV}_{\mathrm{recoil}}^{-1}$ at 90% confidence level in the 15–45 keV recoil energy interval; the present sensitivity appears to be limited by the fast ambient neutrons. Upgrades in progress on the installation are summarized. © 2001 Elsevier Science B.V. All rights reserved.

* Corresponding author. Address: Max-Planck-Institut für Physik, Föhringer Ring 6, D-80805 Munich, Germany.
E-mail address: distefano@mppmu.mpg.de (P. Di Stefano).

0927-6505/01/$ - see front matter © 2001 Elsevier Science B.V. All rights reserved.
PII: S0927-6505(00)00127-4

PACS: 95.35.+d
Keywords: Dark matter; WIMP; Cryogenic detector

1. Introduction

The search for dark matter is one of the major challenges of contemporary physics. Despite extensive scans for massive compact halo objects (MACHOs) initiated by several groups [1–3], it appears at present that the local density of dark matter can hardly be composed of baryonic matter essentially. Indeed, recent results from these experiments indicate that a significant fraction of the MACHOs observed in the direction of the small magellanic cloud (SMC) are probably due to deflectors internal to the SMC, further reducing the possible amount of dark matter in the form of MACHOs in the halo itself [4].

The coincidence of the electroweak interaction scale (SUSY theory) with that required for weakly interacting massive particles (WIMPs) to contribute significantly to the solution of the dark matter problem is a further motivation for attacking the WIMPs direct detection challenge. In addition, these hypothetical particles represent an attractive solution to the problem of galaxy formation. Experimental efforts are underway to detect these particles, either indirectly, by searching for products of their annihilation in the core of the Sun or of the Earth, or directly, by detecting the interactions of the WIMPs themselves in ordinary matter, as first suggested in the mid 1980s [5,6].

The sensitivity of present experiments appears to be limited by the radioactive background rate of the detectors [7] and by the systematics of the rejection scheme using statistical identification methods based on pulse shape discrimination (PSD) techniques in NaI crystals [8–13]. The motivation for the development of cryogenic detectors is the possibility, when the heat measurement is coupled with a measurement of ionization [14–17] (or of scintillation [18]), to discriminate much more reliably the main source of radioactive background, producing electron recoils, from the nuclear recoils expected from WIMP interactions. Indeed, WIMPs scatter off nuclei, which ionize (or produce scintillation) less efficiently than electron recoils for a given energy deposit in the absorber.

In the following, we present the discrimination capabilities of this new generation of detectors in the Expérience pour Détecter les WIMPs en Site Souterrain (EDELWEISS) underground experiment and we show that a 70 g high-purity Ge crystal can already reach sensitivity levels typical of the best existing experiments despite its small mass and a relatively high radioactivity level in the detector environment. The present limitations of these detectors are then explored and the first attempts to counteract them are discussed.

2. The EDELWEISS experiment

The EDELWEISS cryogenic experiment operates in the Laboratoire Souterrain de Modane (LSM), an underground laboratory off the Fréjus highway tunnel beneath the French-Italian Alps. The 4600 mwe of rock reduce the muon flux to one part in two million of its surface value, i.e., to about 4.5 muons $m^{-2}\,day^{-1}$. The fast ambient neutron flux is measured to be 4×10^{-6} $cm^{-2}\,s^{-1}$ [19].

The cryogenic setup and shielding are presented in Ref. [20]. In particular, the dilution refrigerator has a cooling power of 100 μW at 100 mK, a useful volume for bolometer installation of about one liter and can reach temperatures as low as 10 mK. The optimized readout electronics are described in Ref. [21]. The results presented here concern a prototype germanium detector of only moderate radioactive cleanliness, without near Roman lead shielding, radon removal or ambient neutron moderator.

2.1. The cryogenic detector

The absorber of the detector consists in a 70 g germanium monocrystal of high purity ($n_D - n_A \cong$

5×10^9 cm^{-3}). The crystal shape is a disc 8 mm thick and 48 mm in diameter with bevelled edges.

Both charge and heat signals resulting from a particle interaction are measured by this detector. Charge collection is achieved by an electric field applied between two electrodes realized by boron implantation on one face of the monocrystal and by phosphorus implantation on the other. The applied bias voltages are of the order of a few volts. The p–i–n structure has been chosen to decrease, as much as possible, the injection of carriers in the detector volume and to allow large bias voltages. The doses of implanted ions are two orders of magnitude above the insulator–metal transition. The implantation energies have been chosen in order to reduce the thickness of the non-metallic implanted region and to ensure that the metallic layer reaches the detector surface. Recrystallization in the implanted region has been achieved by a fast thermal annealing and its quality checked by ellipsometry and by SIMS. [1] In addition, sheet resistances have been measured on this last detector to verify the metallic behavior at very low temperatures [22,23]. Several improvements of the detector design result from a study of the trap ionization and neutralization mechanisms in the bulk of the detector. The very low density of ionized traps we reached allows a noticeable improvement of the ionization channel time stability and energy resolution [23–28]. In order to minimize edge effects and to maximize charge collection, the thickness of the monocrystal has been reduced to 4 mm along its contour to increase the field strength, thereby reducing trapping and recombination.

The heat measurement is based on the variation, according to the Mott–Efrös–Schklovskii law, of the resistivity of a neutron transmutation doped (NTD) germanium. This thermal sensor is glued to one face of the detector. The size of this NTD is $2 \times 1 \times 0.8$ mm^3. The heat sink consists of three copper wires 50 μm in diameter and about 2 cm length. The operating temperature of the NTD sensor is about 20 mK for a mixing chamber temperature around 10 mK.

The whole detector lies on sapphire balls to ensure a good thermal decoupling from the detector holder made of low radioactivity copper and brass. A detailed description of the detector manufacturing and performances is given in Refs. [22–28].

2.2. Off-line data analysis

The small size of the heat and ionization signals (typically a temperature increase of $\approx 10^{-6}$ K, and of the order of a thousand electron–hole pairs) exposes them to various electronic noises, which may be fundamental or instrumental (Fig. 1). Therefore, analysis of the data has been performed off-line using various methods including the optimal filtering technique in Fourier space [29]. This involves a least square fit in frequency space between the actual event and a model event (obtained by averaging away the noise on several real events) while inversely weighting each frequency by the standard deviation of the noise at that frequency.

Neglecting pileup and assuming pulse shapes independent of pulse amplitude, each event s can be represented as the sum of a scaled and shifted model m and of a random noise n, $s(t) = Am(t - t_s) + n(t)$. Further assuming the noise to be gaussian in frequency space, we can construct a χ^2

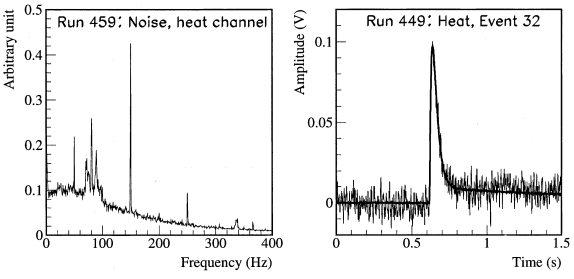

Fig. 1. Left: a noise spectrum of the heat channel. Overall shape is that of thermodynamical noise level of the NTD, squashed by low-pass filter. Two types of peaks are visible: narrow electromagnetic ones essentially due to the odd harmonics of the electrical supply, and wider ones due to microphonics. Right: result of optimal filter fit on a heat event (≈60 keV).

[1] Second Ionisation Mass Spectroscopy. These electrode characterizations have been done with a previous detector by J.-P. Ponpon of the PHASE Laboratory (Strasbourg, France).

as the weighted difference between signal and scaled and shifted model [29]:

$$\chi^2 = \sum_{\omega} \frac{|N(\omega)|^2}{\sigma_\omega^2} = \sum_{\omega} \frac{|S(\omega) - A\mathrm{e}^{-\mathrm{i}\omega t_s} M(\omega)|^2}{\sigma_\omega^2},$$

where σ_ω is the standard deviation of the noise at frequency $\omega/2\pi$ and capital letters represent the Fourier transform of their lowercase counterparts. Minimization with respect to A and t_s yields an estimate of these two parameters. Parseval's identity allows us to simply maximize over time shifts the scalar product $A = \sum_t f(t - t_s)s(t)$, where the function f can be calculated from its Fourier transform once for all events [30]

$$F(\omega) = \mathrm{e}^{-\mathrm{i}\omega t_s} \frac{M(\omega)}{\sigma_\omega^2} \Big/ \sum_{\omega} \frac{|M(\omega)|^2}{\sigma_\omega^2}.$$

Calculating the χ^2 to judge the quality of the fit is however more tractable in frequency space, and this remains computationally feasible thanks to fast Fourier transforms.

With respect to time fit techniques, this method selectively filters out noisy frequencies and thus is advantageous in the many cases of non-white noise spectra (Fig. 1). Like straightforward time fit techniques however, it is ill-suited to data presenting pileups, though given current masses of bolometers this is not yet a problem when looking for WIMPs.

3. In situ detector calibrations

3.1. Energy normalization and recoil energy determination

The heat signal results from the sum of the heat deposited by the incident particle and of the heat generated by the charge carriers during their drift (the so-called Luke-Neganov effect [31]). This last term is given by the product of the bias voltage by the collected charge. Thus as bias voltage increases, the fraction of the heat signal directly correlated to the ionization signal increases, hampering separation of the electron recoils from the nuclear recoils. In practice, although bias voltages up to -12 V have been used, most of the data have been accumulated under bias voltages of -2 and -6 V. There is in fact an additional electric field to that applied; it is caused by the 0.7 eV gap in Ge which creates a -0.7 V reverse field in the p–i–n diode. However, only the applied field ultimately counts for the Luke-Neganov effect: the energy equal to the additional field times the collected charge is indeed released when the charges are collected, but merely compensates the energy used to create the pairs in the first place [32].

Moreover, it is a standard procedure to normalize heat (phonon) energies (keV heat) to equivalent electron energies (keV e.e). Volume electron recoils (with almost complete charge collection) are used to calibrate the charge and phonon channels. For such a volume electron recoil of a given energy (e.g. 122 keV for a ^{57}Co calibration), both charge and phonon amplitudes (E_{ch} and E_{ph}, respectively) are normalized to the deposited energy. In order to reconstruct this energy deposited in the detector, or recoil energy E_{rec}, from these quantities, the following formula [31,33] is applied:

$$E_{\mathrm{rec}} = E_{\mathrm{ph}} \left(1 + \frac{eV}{\epsilon_\gamma}\right) - E_{\mathrm{ch}} \frac{eV}{\epsilon_\gamma},$$

where V is the bias voltage for charge collection (V), e, the elementary charge and ϵ_γ, the average energy per electron–hole pair (eV) for an electron recoil. The recoil energy resolution becomes thus bias-dependent, as shown in Fig. 6. In the absence of Luke-Neganov effect ($V = 0$) $E_{\mathrm{rec}} = E_{\mathrm{ph}}$; for a photon interaction where all the charge is collected (volume electron recoil), $E_{\mathrm{rec}} = E_{\mathrm{ph}} = E_{\mathrm{ch}}$.

It is shown in Refs. [33,34], how the ϵ_γ parameter can be measured using, in X- and γ-ray line calibrations, the small fractions of events which exhibits an incomplete charge collection. The measured value is close to the standard value $\epsilon_\gamma \cong 3$ eV for the 77 K germanium diode detectors [35].

3.2. Electron recoil thresholds and resolutions

Electron recoil energy resolutions and thresholds have been studied using a ^{57}Co source which provides essentially photoelectric interactions

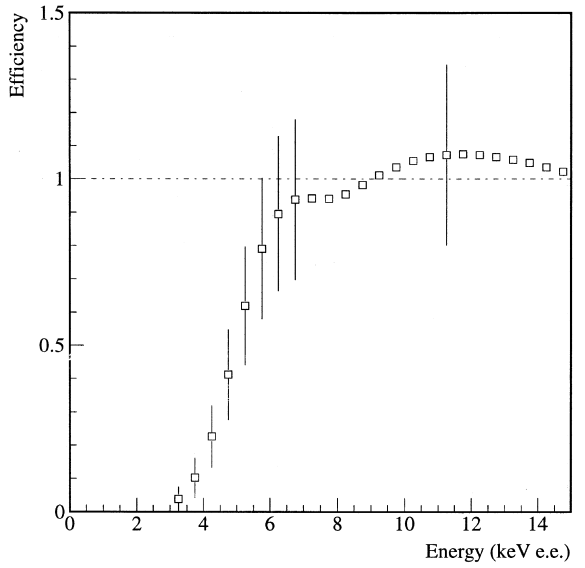

Fig. 2. The threshold efficiency of the ionization channel, determined by comparing the data of ^{60}Co calibrations with a Monte-Carlo simulation.

from its main peak at 122 keV. The ionization signal being roughly 1000 times faster than the heat signal, the former has usually been used as trigger for the acquisitions with an effective threshold at 4 keV equivalent electron (e.e.) on the charge channel. Threshold efficiency has been studied by comparing a ^{60}Co calibration with a Monte-Carlo simulation. It is found to rise rapidly to 100% by 6 keV [36] (Fig. 2).

The heat and ionization channels exhibit energy FWHM resolution of $\approx$1 and $\approx$1.2 keV e.e. at 122 keV. According to the $E_{\rm rec}$ expression of Section 3.1, the corresponding resolutions on the recoil energy are $\approx$1.8 keV at -2 V and $\approx$3.8 keV at -6 V.

3.3. Signal and background calibrations

The detector has been calibrated with both neutron and gamma sources in order to check its power of separation between nuclear recoil (“signal”) and electron recoil (background) events. High energy photons provide Compton interactions throughout the crystal rather than biased towards its surface.

A ^{252}Cf neutron source, of about 2.5μCi activity, has been used for this calibration at two different values of the reverse bias voltage (-2 and -6 V). The branching ratio for neutron emission in the decay of the ^{252}Cf isotope is about 12% and the average kinetic energy of the emitted neutrons is around 2 MeV. The ^{252}Cf isotope is also a gamma source with a branching ratio of about 60%, and about 80% of these gammas have energy less than 1 MeV. So, in principle, this source alone is sufficient to obtain simultaneously both neutron and gamma calibrations. In order to improve the statistics without too long an exposure of the detector to the neutron source and the associated risk of neutron activation, we use also a ^{60}Co source to mimick the background noise of electron recoils. Results are presented in Fig. 3 for both polarization voltages, showing a remarkably good separation between gamma and neutron recoil events down to low energy. While most electron recoil events appear well behaved, and neatly line up along the main diagonal in the heat-ionization plane, approximately 5% suffer from incomplete charge collection.

The recoil energy $E_{\rm rec}$ is derived according to Section 3.1. Merging the data obtained at the two bias voltages yields the quenching factor $(E_{\rm ch}/E_{\rm rec})$ versus $E_{\rm rec}$ in Fig. 4. The curve 4 keV/$E_{\rm rec}$, which represents the threshold (at 4 keV e.e.), is also given. A “neutron line” (the quenching factor for nuclear recoils) can be parameterized using the measured spreads and mean values of the charge over recoil ratio, calculated in discrete recoil energy intervals above 20 keV (under 20 keV, a

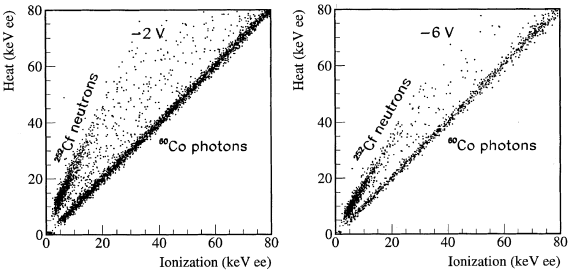

Fig. 3. Heat-ionization planes of ^{60}Co and ^{252}Cf calibrations at two bias voltages. Over the 0–80 keV e.e. energy interval, 5% of the events from ^{60}Co are ionization deficient at -2 V and 3% at -6 V.

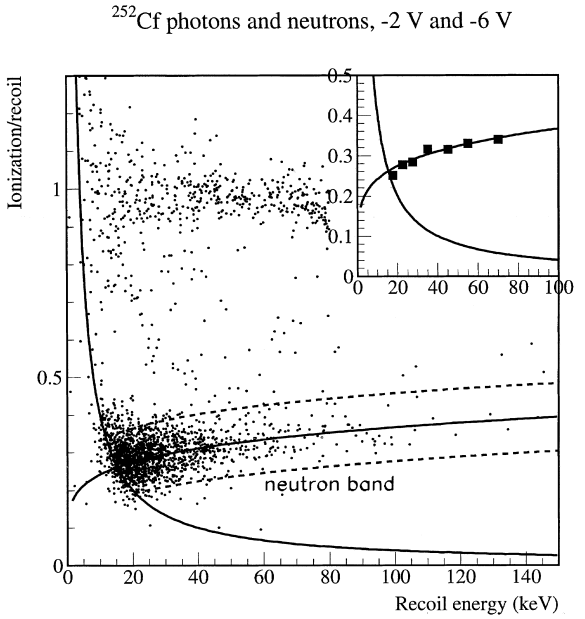

Fig. 4. The quenching factor, or ionization over recoil energy ratio, as a function of the recoil energy. To improve the statistics, the ^{252}Cf data collected at -2 and -6 V are merged. A neutron zone which contains 95% of the nuclear recoils is represented. The inset shows the agreement with the CDMS results [14] ((■) the extension of which is the order of the error bar).

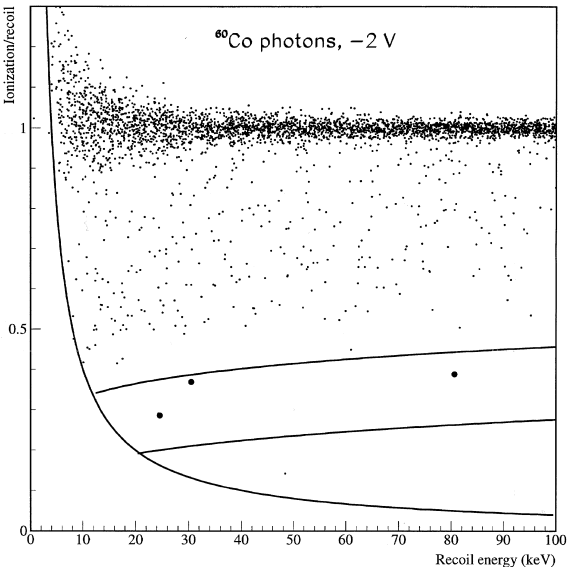

Fig. 5. Separation of signal from background based upon ^{60}Co photon calibration at -2 V bias voltage. 3229 events are found over the 15–100 keV recoil energy interval but only 3 remain in the 95% acceptance nuclear recoil band.

threshold bias is clearly visible). We obtain $E_{ch}/E_{rec} = (0.16 \pm 0.07)\ E_{rec}^{0.18\pm0.1}$, a result in agreement (within error limits) with those of the Heidelberg–Moscow collaboration [37], parameterized in [7] by $E_{ch} = 0.14E_{rec}^{1.19}$, and in turn in agreement with the Lindhard theory [38] and most of the previous experiments (see Ref. [37] and references therein). The comparison with the results of the CDMS experiment [14], shown in Fig. 4 inset, shows a very good agreement.

A neutron zone of known acceptance can be constructed by adjusting a power law of the recoil energy to the points at $+n\sigma$, $-m\sigma$ above and below the mean charge over recoil ratio. For a given background, the choice of the n and m values is a matter of optimizing the signal-to-noise ratio. In Fig. 4, the 95% acceptance neutron zone ($\pm 2\sigma$) is shown as an example. This neutron calibration induces a slight bias in the determination of the quenching factor: the non-negligible number of multiple diffusions in the crystal leads to a merging of the quenching factor values at different energies. The width of the nuclear recoil band is overestimated accordingly for WIMPs for which it should by single interactions only.

We now turn our attention to the separation capabilities of the detector based on the two types of calibration just discussed. In Fig. 5, we apply the neutron zone method to the data of the ^{60}Co calibration taken at -2 V. In the 15–100 keV recoil energy interval, three events (out of 3229) are found within the 95%-acceptance nuclear recoil band: $(99.90 \pm 0.05)\%$ of photon background is rejected. At -6 V, we find a rejection of $(99.6 \pm 0.2)\%$. These results are very promising; however, it must be kept in mind that they have been obtained from calibrations and that operational values may differ as we will see later.

4. A realistic case of data taking

Following the benchmarks just discussed, 0.65 kg day and 1.17 kg day of data were taken at the bias voltages of -2 and -6 V, respectively. Both

spectra show a rate of roughly ≈35–40 event $kg^{-1}\,day^{-1}\,keV_{recoil}^{-1}$ in the 15–45 keV recoil energy interval, below the 46.5 keV peak due to ^{210}Pb contamination. The recoil energy versus ionization plots of the data (Fig. 6) show a large number of off-axis events. This population, interpreted as incomplete charge collection of electron surface events, is discussed in Ref. [34] together with another population which appears at recoil energies of the order of 80–100 keV and is attributed to surface nuclear recoils.

Given the large number of events with incomplete charge collection, we only retain the $(0\sigma, -2\sigma)$ neutron zones as discussed in Section 3 (Fig. 7). This improves the signal-to-noise ratio and halves the acceptance to 0.475. The samples recorded respectively at −2 and −6 V bias contain six events (respectively seven events) in the 15–45 keV recoil range. We assume they are nuclear recoils, and use them to derive a conservative upper limits on a signal. For the respective exposures and acceptance, they yield upper limits at the 90% confidence level of 1.1 event $kg^{-1}\,day^{-1}\,keV_{recoil}^{-1}$ at −2 V, and 0.7 event $kg^{-1}\,day^{-1}\,keV_{recoil}^{-1}$ at −6 V. It will appear below that a large fraction of the events observed in the nuclear recoil band can probably be attributed to neutron interactions inside the detector. One can thus only set a lower limit of 98% for the rejection factor of the electron recoil background.

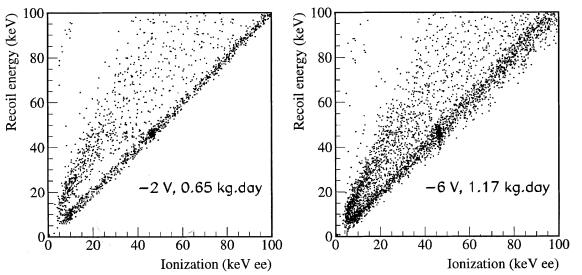

Fig. 6. Data at −2 and −6 V. Deriving recoil energies from the heat signal by the subtraction of charge times bias voltage causes the recoil energy resolution to become bias dependant, as can be seen on the 46.5 keV peak of ^{210}Pb.

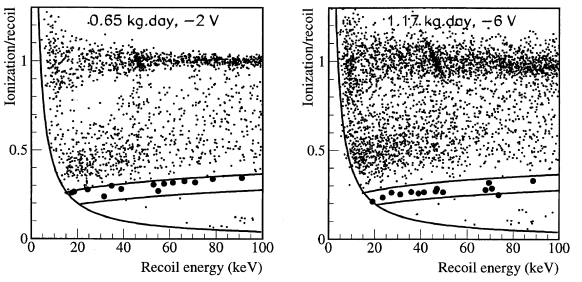

Fig. 7. Neutron zones and data at −2 and −6 V. We only retain the $(0\sigma, -2\sigma)$ neutron zones (47.5% acceptance) where 14 and 15 events (●●●) subsist, respectively over the 15–100 keV recoil energy range.

When we compare the mean ionization over recoil energy ratio of the off-axis events (electron surface events) at both bias voltages (0.46 ± 0.01 at −2 V and 0.539 ± 0.006 at −6 V), we find that the higher bias voltage brings the off-axis events significantly closer to the well-collected events.

We have also run the detector using a heat trigger. Because the ionization signal is roughly 1000 times faster than the heat signal, it is not always possible to correlate the pulse with the charge pulse. Nonetheless, this trigger mode has brought to light a distinct second type of thermal event, one with a rise time dominated by electronics and practically never correlated with an ionization event. For these two reasons, we attribute these events to interactions in the heat sensor itself. The energy spectrum of these events is compatible with a small amount of tritium activity in the NTD thermometer.

The events surviving in the neutron zone are not sufficiently separated from the population of electron surface events to be attributed with certainty to nuclear recoil events, induced in the Ge detector by ambient neutrons (the observed rate being much higher than what would be expected from WIMPs [7–10]). The flux and energy spectrum of the fast ambient neutrons originating for the most part from internal radioactivity in the surrounding rock have been measured in the LSM by our collaboration using conventional scintillation detectors. The flux was found to be $4.0 \pm 0.1\ 10^{-6}$ $cm^{-2}\,s^{-1}$ (statistical error only) [19]. A Monte-Carlo simulation was then performed to predict the expected number of neutron-induced nuclear recoils in our 70 g Ge detector. It uses the GEANT Monte-Carlo simulation [39] in conjunction with a package specially developed [40] to handle low

Table 1
Measured number of events and simulated number of ambient neutron events in the nuclear recoil band (47.5% acceptance) over 15–100 keV recoil energy[a]

Bias voltage (V)	Exposure (kg day)	Measured recoil number	Simulated neutron number
−2	0.65	14 ± 4	7 ± 2
−6	1.17	15 ± 4	12 ± 3

[a] The error bars on the simulated neutron numbers result from the experimental error on the measured neutron flux.

energy neutrons (from a few eV to a few MeV). The expected and measured number of recoils in the nuclear recoil band (47.5% acceptance) over the recoil energy interval 15–100 keV are given in Table 1.

By inspection of Table 1, it appears that at the −6 V polarization a large fraction, and possibly all the events observed in the nuclear recoil region can be attributed to neutron interaction inside the detector. At −2 V, however, the separation between nuclear recoils and electron surface events is, as already noted, slightly less favorable, and accordingly the simulation indicates a pollution of the nuclear recoil band by surface events.

5. Conclusion and outlook

Our prototype heat and ionization bolometer provides an excellent separation of the calibrated background and signal down to an energy of 4 keV e.e. However, data taken during background runs contain an important population of off-axis events (electron surface events) essentially not seen during the calibrations. Despite this, the rejection capabilities of the detector remain satisfactory, still reducing the number of electron recoil events by nearly two orders of magnitude. Sensitivity limits on WIMPs [16,17] obtained with this prototype are only a factor of 10 higher than the best existing limits obtained with longer-established techniques [7–10] despite the small mass (70 g) of our detector and the relatively high radioactivity level in the detector environment. Moreover, the present sensitivity of the experiment appears to be limited, principally for the runs with a −6 V bias voltage, not by the gamma background or by parasitic electron surface events, but by the ambient neutrons in the underground laboratory. Given the systematic uncertainties in the Monte-Carlo neutron simulations, a background subtraction is not attempted, but, clearly, shielding against neutrons is required.

A new generation of detectors is being tested in the LSM with new implantation schemes for the electrodes and a rigorous selection procedure of the crystal holder material [41]. Several improvements have been undertaken in the detector environment: nitrogen flushing for radon removal, improved passive protection against gamma radioactivity (including close Roman lead shielding) and 30 cm removable paraffin shielding against neutrons. In an initial test run, two 70 g prototypes show background levels before rejection of ≈ 2 event $\mathrm{keV}^{-1}\,\mathrm{kg}^{-1}\,\mathrm{day}^{-1}$ below 50 keV, a factor of 10 improvement over previous data, with a comparable progression for electron surface events. The number of events remaining in the neutron zone is now extremely limited and could be due to residual neutron interactions inside the present shielding. Assuming a good performance of the neutron shielding and that the energy resolution and background rejection are the same as those reported here, a few months of data taking with these detector should allow a test of the entire parameter region claimed by the DAMA experiment [8–10], and the entrance into the relevant supersymmetry parameter space.

Acknowledgements

The support of the technical staff of the Laboratorie Souterrain de Modane and of the participating laboratories is gratefully acknowledged. We thank J.P. Passerieux, A. Le Coguie and B. Cahan for the quality of their contribution to the drawing and realization of electronic components.

This work has been partially funded by the EEC-Network program under contract ERB-FMRXCT980167.

References

[1] C. Alcock, et al. (MACHO Collaboration), Nature 365 (1993) 621.
[2] E. Aubourg, et al. (EROS Collaboration), Nature 365 (1993) 623.
[3] B. Paczynski, et al., Bull. Am. Astron. Soc. 187 (1995) 1407.
[4] C. Alcock, et al. (EROS and MACHO Collaborations), Ap. J. 499 (1998) L9.
[5] A. Drukier, L. Stodolsky, Phys. Rev. D 30 (1984) 2295.
[6] M.W. Goodman, E. Witten, Phys. Rev. D 31 (1985) 3059.
[7] L. Baudis, et al., Phys. Rev. D 59 (1999) 022001.
[8] R. Bernabei, et al., Phys. Lett. B 389 (1996) 757.
[9] R. Bernabei, et al., Phys. Lett. B 424 (1998) 195.
[10] R. Bernabei, et al., Phys. Lett. B 450 (1999) 448.
[11] P.F. Smith, et al., Phys. Lett. B 379 (1996) 299.
[12] P.F. Smith, et al., Phys. Rep. 307 (1998) 275.
[13] G. Gerbier, et al., Astropart. Phys. 11 (1999) 287.
[14] T. Shutt, et al., Phys. Rev. Lett. 69 (1992) 3425.
[15] R.W. Schnee, et al., Phys. Rep. 307 (1998) 283.
[16] D. Drain, et al., Phys. Rep. 307 (1998) 297.
[17] L. Bergé, et al., Nucl. Phys. B 70 (1999) 69.
[18] P. Meunier, et al., Appl. Phys. Lett. 75 (1999) 1335.
[19] V. Chazal, et al., Astropart. Phys. 9 (1998) 163.
[20] A. de Bellefon, et al., Astropart. Phys. 6 (1996) 35.
[21] D. Yvon, et al., Nucl. Instr. Meth. Phys. Res. A 368 (1996) 778.
[22] D. L'Hote, et al., Nucl. Instr. Meth. Phys. Rev A 370 (1996) 193.
[23] X.-F. Navick, Thèse Doctorat, No 97/PA07/7146, Université Paris VII, 1997, unpublished.
[24] X.-F. Navick, et al., Nucl. Instr. Meth. Phys. Res. A 442 (2000) 267.
[25] X.-F. Navick, et al., Nucl. Instr. Meth. Phys. Res. A 370 (1996) 213.
[26] X.-F. Navick, et al., in: S. Cooper (Ed.), Proceedings of the Seventh International Workshop on Low Temperature Detectors, Munich, Germany, 1997, p. 244.
[27] D. L'Hôte, et al., Czechoslovak J. Phys. 46-S5 (1996) 2903.
[28] D. L'Hôte, et al., J. Appl. Phys. 87 (2000) 1507.
[29] S.H. Moseley, J.C. Mather, D. Mc Cammon, J. Appl. Phys. 56 (1984) 1257.
[30] A.E. Szymkowiak, R.L. Kelley, S.H. Moseley, C.K. Stahle, J. Low Temp. Phys. 93 (1993) 281.
[31] P.N. Luke, J. Appl. Phys. 64 (1988) 6858.
[32] T. Shutt, et al., Phys. Rev. Lett. 69 (1992) 3531.
[33] P. Di Stefano, Thèse de Doctorat, Université Paris XI Orsay, 1998, unpublished.
[34] A. Benoit, et al., Phys. Lett. B, 479 (2000) 8.
[35] G.E. Knoll, Radiation Detection and Measurement, Wiley, New York, 1989.
[36] L. Miramonti, Thèse de Doctorat, Université Paris XI Orsay, 1999, unpublished.
[37] L. Baudis, et al., Nucl. Instr. Meth. Phys. Res. A 418 (1998) 348.
[38] J. Lindhard, V. Nielsen, M. Scharff, P.V. Thomsen, Mat. Fyz. Medd. Dan. Vid. Selsk. 33 (1963) 1.
[39] GEANT Detector Description and Simulation Tool, CERN Program Library, W5103, CERN, 1993.
[40] H. de Kerret, B. Lefièvre, Report, Collège de France, LPC 88 01, 1988, unpublished.
[41] X.-F. Navick, et al., Nucl. Instr. Meth. Phys. Res. A 444 (2000) 361.

2.6A Results from EDELWEISS

Ref. [49].

ELSEVIER

Physics Letters B 545 (2002) 43–49

PHYSICS LETTERS B

www.elsevier.com/locate/npe

Improved exclusion limits from the EDELWEISS WIMP search

EDELWEISS Collaboration

A. Benoit [a], L. Bergé [b], A. Broniatowski [b], L. Chabert [c], B. Chambon [c], M. Chapellier [d], G. Chardin [e], P. Charvin [e,f], M. De Jésus [c], P. Di Stefano [c], D. Drain [c], L. Dumoulin [b], J. Gascon [c], G. Gerbier [e], E. Gerlic [c], C. Goldbach [g], M. Goyot [c], M. Gros [e], J.P. Hadjout [c], S. Hervé [e], A. Juillard [b], A. de Lesquen [e], M. Loidl [e], J. Mallet [e], S. Marnieros [b], O. Martineau [c], N. Mirabolfathi [b], L. Mosca [e,f], X.-F. Navick [e], G. Nollez [g], P. Pari [d], C. Riccio [e,f], V. Sanglard [c], M. Stern [c], L. Vagneron [c]

[a] *Centre de Recherche sur les Très Basses Températures, SPM-CNRS, BP 166, 38042 Grenoble, France*
[b] *Centre de Spectroscopie Nucléaire et de Spectroscopie de Masse, IN2P3-CNRS, Université Paris XI, bat 108, 91405 Orsay, France*
[c] *Institut de Physique Nucléaire de Lyon-UCBL, IN2P3-CNRS, 4 rue Enrico Fermi, 69622 Villeurbanne Cedex, France*
[d] *CEA, Centre d'Études Nucléaires de Saclay, DSM/DRECAM, 91191 Gif-sur-Yvette Cedex, France*
[e] *CEA, Centre d'Études Nucléaires de Saclay, DSM/DAPNIA, 91191 Gif-sur-Yvette Cedex, France*
[f] *Laboratoire Souterrain de Modane, CEA-CNRS, 90 rue Polset, 73500 Modane, France*
[g] *Institut d'Astrophysique de Paris, INSU-CNRS, 98 bis Bd Arago, 75014 Paris, France*

Received 18 June 2002; accepted 2 July 2002

Editor: L. Montanet

Abstract

The EDELWEISS experiment has improved its sensitivity for the direct search for WIMP dark matter. In the recoil energy range relevant for WIMP masses below 10 TeV/c^2, no nuclear recoils were observed in the fiducial volume of a heat-and-ionization cryogenic Ge detector operated in the low-background environment of the Laboratoire Souterrain de Modane in the Fréjus Tunnel, during an effective exposure of 7.4 kg d. This result is combined with the previous EDELWEISS data to derive a limit on the cross-section for spin-independent interaction of WIMPs and nucleons as a function of WIMP mass, using standard nuclear physics and astrophysical assumptions. This limit excludes at more than 99.8% CL a WIMP candidate with a mass of 44 GeV/c^2 and a cross-section of 5.4×10^{-6} pb, as reported by the DAMA Collaboration. A first sample of supersymmetric models are also excluded at 90% CL.
© 2002 Elsevier Science B.V. All rights reserved.

PACS: 95.35.+d; 14.80.Ly; 98.80.Es; 29.40.Wk

Keywords: Dark matter; WIMPs; Supersymmetry; Germanium detectors; Bolometers

E-mail address: gascon@ipnl.in2p3.fr (J. Gascon).

0370-2693/02/$ – see front matter © 2002 Elsevier Science B.V. All rights reserved.
PII: S0370-2693(02)02238-4

1. Introduction

The experimental efforts in the search for Cold Dark Matter in the form of Weakly Interacting Massive Particles (WIMPs) are steadily increasing (see, e.g., Ref. [1] for a review). In direct searches, the experimental signature of the WIMPs from the galactic halo is the observation of nuclear recoils induced by their scattering. Current experimental sensitivities for the interaction rate of WIMPs are of the order of 1 per kilogram detector material and per day for the various experiments at the forefront of this search [2–8].

The experiment DAMA [3] has reported an annual modulation signal in NaI detectors. This represents a challenge to other detecting methods to reach equivalent sensitivities, a standard procedure to compare different experiments having been laid out in Ref. [9]. Two experiments [4,8], both using cryogenic heat-and-ionization germanium detectors, were able to exclude at more than 90% CL the central value deduced by DAMA from its annual modulation signal for the WIMP mass and its nucleon scattering cross-section ($M_W = 52$ GeV$/c^2$ and $\sigma_n = 7.2 \times 10^{-6}$ pb, respectively). The CDMS experiment [4] was the first to report a limit excluding this value. However, the operation of the detectors in a shallow site, with only 16 meters of water equivalent (m.w.e.) protection from cosmic rays, leads to a sizable background of nuclear recoils from neutron scattering that requires a delicate procedure of background subtraction [7]. The EDELWEISS experiment [8], located in a 4800 m.w.e. deep underground site, was also able to reject that value without requiring any background subtraction. However, the energy resolution in that experiment restricted the sensitivity to nuclear recoils above 30 keV and the accumulated run time was not sufficient to extend the sensitivity to the central value obtained by DAMA [3] when their annual modulation signal is combined with their exclusion limit from pulse shape discrimination in NaI [2] ($M_W = 44$ GeV$/c^2$ and $\sigma_n = 5.4 \times 10^{-6}$ pb). Beyond this, an important step in these searches would be to reach out to the Supersymmetric model calculations predicting the largest σ_n values.

Following the results obtained by EDELWEISS using a heat-and-ionization cryogenic Ge detector [8], three new detectors were put in operation. The aim was to improve our understanding of the performance of such detectors, and to extend the sensitivity to lower cross-sections. This Letter presents the improved cross-section limit achieved using a detector with improved charge collection and energy resolution.

2. Experimental setup

The experiment is located in the Laboratoire Souterrain de Modane in the Fréjus Tunnel under the French–Italian Alps, under a 4800 m.w.e. rock overburden. The experimental setup is described in [8]; only the relevant modifications are discussed here.

Three new 320 g cryogenic Ge detectors [10], each 70 mm in diameter and 20 mm in height, are operated simultaneously. Each one is equipped with a segmented electrode defining two regions, a central part and a guard ring. To improve their reliability, all electrical contacts with the electrodes are ultrasound-bonded instead of glued as in Ref. [8].

Two of the detectors, labeled GeAl9 and GeAl10, are very similar to the one used in the year 2000 runs (Ref. [8]), labeled GeAl6. The third detector, GGA1, differs by the presence of a 60 nm hydrogenated amorphous Ge layer deposited under the 70 nm Al electrodes and on all exposed surfaces. This modification was done to test whether an amorphous layer can improve charge collection properties, as suggested by [12]. Bias voltage values between 2 and 4 V are used.

The size of the NTD heat sensors and the thermalization of the detectors are improved for a better sensitivity, in light of the previous experience with GeAl6. As a result, it was possible to operate the detector at a reduced temperature of 17 mK (regulated to within 10 μK).

The data acquisition system has been upgraded to a design with fully numerical data flow and trigger. The signals from the 3 heat and 6 ionization channels are continuously digitized at respective rates of 2 and 200 ksample/s and sent to the data acquisition PC via an optical link. The ionization data are then filtered on-line using an Infinite Impulse Response (IIR) high-pass elliptic filter of 4th order, in order to remove most of the microphonics noise, below a frequency of 1200 Hz. The trigger is defined by requiring a

minimum threshold on the absolute value of any of the filtered ionization channels.

3. Detector calibration

The heat and ionization responses to γ rays were calibrated using ^{57}Co and ^{60}Co sources. In 2000 [8], the performance of the detector GeAl6 was partly limited by a poor baseline resolution on both ionization and heat channels. While resolutions at 122 keV of the new detectors remained close to those of GeAl6, the baseline resolutions were somewhat improved. The ionization baseline resolutions are all below 1.5 keV FWHM, and are 1.3, 0.5 and 0.4 keV for the heat channels in GGA1, GeAl9 and GeAl10, respectively. The resulting improvement is illustrated in Fig. 1, showing the low-energy spectra recorded in the three detectors in the low-background physics run. Here, the energy corresponds to the average of the ionization and heat signals, weighted by the square of their respective resolutions. The 8.98 and 10.37 keV lines from the decay of the cosmic-ray induced long-lived isotopes ^{65}Zn and ^{68}Ge [13] are clearly resolved in GeAl9 and GeAl10, with a resolution of 0.6 keV FWHM. The resolution in GGA1 is only 1.2 keV FWHM, but the two-peaked structure can again be observed. The degraded resolution of GGA1 relative to the two other detectors is due to a reduced NTD sensor volume (1.6 vs. 5.6 mm^3), and an increased sensitivity to microphonics of the center electrode ionization channel.

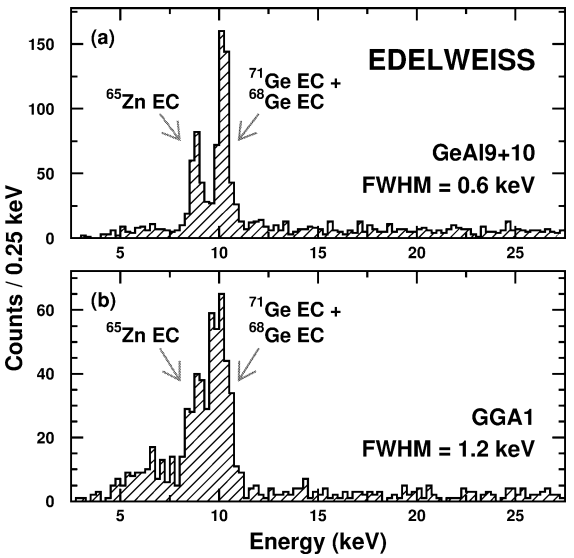

Fig. 1. Energy pulse height spectra for low-energy gammas (sum of the ionization and heat channels, weighted by their resolution squared) in the fiducial volume of the EDELWEISS detector, for the low-background physics runs: (a) sum of the distributions of the detectors GeAl9 and GeAl10; (b) distribution in the detector GGA1. The arrows indicate the peaks at 8.98 and 10.37 keV, corresponding to the de-excitation of the cosmogenic activation of ^{65}Zn and ^{68}Ge in the detector, and the ^{71}Ge activation that follows neutron calibrations.

The threshold level of the ionization trigger was measured using two different techniques. The first one consists in extracting, as in Ref. [8], the threshold value corresponding to an efficiency of 50% from a fit to the low-energy part of the Compton plateau recorded with a ^{60}Co γ-ray source. The second technique was made possible by the simultaneous operation of the three detectors with a ^{252}Cf neutron source. Neutron scattering induces a large number of coincidence events where at least two detectors are hit. The efficiency curve as a function of ionization energy in one detector is given by the ratio of the ionisation energy distributions obtained with and without that detector appearing in the trigger pattern, the reference population being all events where at least one other detector took part in the trigger. Both Compton and coincidence techniques give consistent ionization threshold measurements within 0.2 keV. For GGA1, the values corresponding to an efficiency of 50% are 3.7 ± 0.2 and 3.5 ± 0.1 keV, respectively. This represents a significant improvement compared to the performance of GeAl6, where the corresponding values varied between 5.7 and 11 keV during the run and restricted the analysis to nuclear recoils above 30 keV. With a 50% efficiency reached at 4 keV, the nuclear recoil selection described below reaches its full efficiency within less than 1% for recoil energies above 20 keV.

The study of the distribution of the quenching factors Q (the ratio of the ionization signal to the recoil energy, calculated as in [8]) recorded in the presence of a γ-ray source revealed problems with the charge collection in GeAl9 and GeAl10. Fig. 2 shows the Q distribution for recoils between 20 and 200 keV recorded with ^{57,60}Co sources, for the different detectors. GeAl9 and GeAl10 have been added together, since they display a very similar

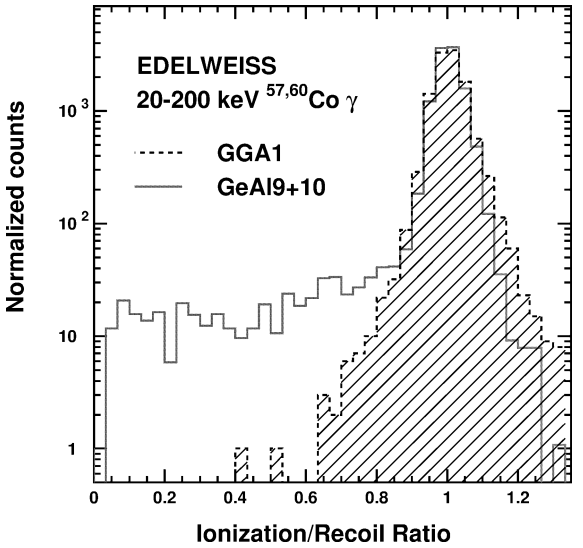

Fig. 2. Distribution of the ratio of the ionization pulse height to the recoil energy (quenching factor Q) obtained by exposing the detectors to ^{57}Co and ^{60}Co γ-ray sources. The ratio is normalized to 1 for electron recoils using the photopeaks of the ^{57}Co source. Shaded histogram: detector GGA1. Line histogram: sum of the detector GeAl9 and GeAl10, normalized to the same number of entries of GGA1.

behavior. The distributions are normalized to the number of entries in GGA1. The distribution for GGA1 is centered on 1, as expected by construction for electron recoils. The distribution for GeAl9 and GeAl10 show a narrower peak centered at 1, as expected from the better heat resolution. However, a relatively flat tail of events with Q values ranging from 0 to 1 is observed. While 1.3 and 2.2% of events have Q values below 0.5 in GeAl9 and GeAl10, this fraction is approximately 0.01% in GGA1. The tail amplitudes do not depend on the recoil energy range. On the basis of the ^{57,60}Co calibration runs it can be expected—and later experimentally verified—that these will produce fake nuclear recoil events ($Q \sim 0.3$, see below) at a rate of a few events per kg d in GeAl9 and GeAl10. It was therefore decided that only the GGA1 data would be used for deriving a limit on WIMP interactions.

Although the suppression of charge collection problems in GGA1 may indicate that the amorphous layer helps prevent them, as suggested by [12], more thorough tests are needed before reaching any firm conclusion.

4. Fiducial volume and acceptance

As in Ref. [8], a fiducial volume is defined in order to exclude events occurring in the outer perimeter of the detector as it is more exposed to external sources of radioactivity and to charge collection problems. The selection cut is the same: more than 75% of the total charge must be collected on the center electrode. Here also, two methods are used to measure the fraction of the total detector volume thus defined. The first one uses the data collected with the ^{252}Cf source: the fraction of nuclear recoil candidates passing the fiducial cut is compared with the results of a Monte Carlo simulation of the neutron interactions in the detector. The second method exploits the uniformity of the ^{65}Zn and ^{68}Ge decays within the detector volume. The fraction of the total intensity of the 8.98 and 10.37 keV peaks selected by the fiducial acceptance is then equal to the fiducial volume fraction. The two methods give identical results for GGA1 ($57 \pm 3\%$) and agree within 3% for the other two detectors.

The acceptance for nuclear recoils is defined both in terms of ranges in Q and recoil energies. The neutron calibration of the three detectors confirms the parametrization used in Ref. [8], namely, the center of the band is given by $0.16(E_R)^{0.18}$, where E_R is the recoil energy in keV, and its width is equal to that predicted from the propagation of the heat and ionization resolutions added in quadrature with a constant rms spread of ~ 0.035. Again, the width of the band is set to $\pm 1.645\sigma$. It was verified on the neutron data that this selection does correspond to an efficiency of 90%.

The lower bound of the recoil energy range for the selection of nuclear recoil is set to 20 keV, based on the same arguments as in Ref. [8]: the efficiency to nuclear recoils should be as uniform as possible within the band, and it should exclude regions where the γ-ray rejection, estimated by propagating the experimental heat and ionization resolutions, is expected to be worse than 99.9%.

Given that a background of events with improper charge collection has appeared in GeAl9 and GeAl10, and that it has a flat distribution in both Q and recoil energy, one could expect a similar behavior, albeit at a lower level, in GGA1. Therefore, some care must be taken in the definition of the upper bound of the recoil energy range of WIMP candidates. The natural choice

is to calculate, using the prescription of Ref. [9], the upper bound corresponding to 95% of all WIMP-induced recoils above 20 keV. Using the standard halo and nuclear form factor parameters,[1] this bound depends on the mass of the WIMP and varies from 33 keV at 20 GeV/c^2 to 86 keV at 100 GeV/c^2 and saturates slightly above 110 keV at masses above 10 TeV/c^2.

Within the fiducial volume (57% of 318.5 g), the acceptance for nuclear recoils from WIMP interactions thus corresponds to 90% (width in Q) times 95% of all recoils above 20 keV (mass-dependent recoil energy range).

5. Results and discussion

The low-background physics data consists of all physics runs recorded over a period from February to May 2002. The physics data-taking period started a few months after the installation of the detectors in the Laboratoire Souterrain de Modane, after a period of optimization of resolution, calibration and of long exposure to an intense ^{60}Co source while all electrodes were shorted. The running conditions were kept as homogeneous as possible, until the run was interrupted by an accidental warm-up of the detector. In addition to a constant monitoring of the data, the homogeneity of the running conditions was checked with ∼ weekly ^{57}Co calibrations and two neutron calibrations. The total physics run time at low background corresponds to 54 days, of which 2.0% are lost due to the regular shorting of the electrodes to prevent the accumulation of space charge, 3.9% are lost due to the dead-time of the data acquisition and 6.2% are lost in a few hour-long episodes where the microphonics noise reached unacceptable levels, as attested by a strong deterioration of the baseline resolutions. The total exposure is thus 15.1 kg d, of which 8.6 is in the center fiducial volume. The exposure corrected for the acceptance of the nuclear recoil band is 7.4 kg d.

The data recorded in the fiducial volume of GGA1 are shown in Fig. 3. The ionization-to-recoil energy ratios are plotted as a function of the recoil energy. Only events triggered by GGA1 alone and with an ionization energy above 3.5 keV (hyperbolic dashed line) are shown. The 99.9% acceptance band for photons shown as a dotted line is the result of a simple propagation of the average heat and ionization resolution, assuming a Gaussian dispersion. The population of events around $Q \sim 0.5$ associated with low-energy β and γ surface events, so prominent in our previous data of Ref. [11] and less so in Ref. [8], is only represented here by 4 to possibly 5 events. The correct interpretation of these events would require a significant increase in exposure, given the low level of background reached with the present detector. The same is true for the interpretation of the three events below $Q = 0.7$ and with recoil energies between 119 and 182 keV.

The event at 119 keV and $Q = 0.3$ is lying at -1.646σ of the centre of the nuclear recoil band. Given the uncertainty in the experimental determina-

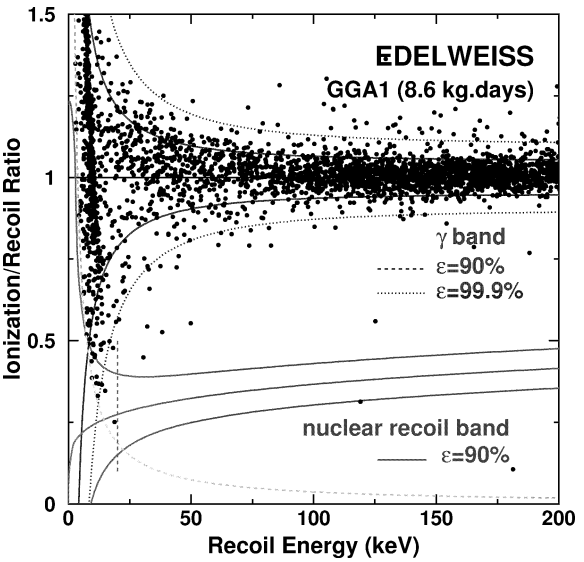

Fig. 3. Distribution of the quenching factor (ratio of the ionization signal to the recoil energy) as a function of the recoil energy from the data collected in the center fiducial volume of the 320 g EDELWEISS detector GGA1. The exposure of the fiducial volume corresponds to 8.6 kg d. Also plotted as full lines are the $\pm 1.645\sigma$ bands (90% efficiency) for photons and for nuclear recoils. The 99.9% efficiency region for photons is also shown (dotted line). The hyperbolic dashed curve corresponds to 3.5 keV ionization energy and the vertical dashed line to 20 keV recoil energy.

[1] The halo parameters are a local WIMP density of 0.3 GeV/c^2/cm^3, a rms velocity of 270 km/s, an escape velocity of 650 km/s and an Earth-halo relative velocity of 230 km/s. The Helm parametrization of the nuclear form factor is used with the recommended values of $a = 0.52$ fm, $s = 0.9$ fm and $c = 1.23A^{1/3} - 0.6$ fm. See Ref. [9] for details.

tion of σ, we conservatively choose to consider this event as a nuclear recoil, entering in the acceptance for WIMP masses above 10 TeV/c^2. For lower WIMP masses, no events are in the nuclear recoil band.

The absence of events in the defined acceptance is interpreted in terms of upper limits at 90% CL on WIMP-nucleon scattering cross sections for $M_W < 10$ TeV/c^2 following the prescriptions of Ref. [9] with the standard halo and nuclear models described above.

The limit as a function of WIMP mass is shown in Fig. 4, where it is compared with the previous result obtained with an effective exposure of 4.3 kg d of the GeAl6 detector [8]. The limit resulting from the combination of the two measurements, corresponding to an effective exposure of 11.7 kg d is also shown. The 3σ contour corresponding to the annual modulation effect of DAMA NaI1-4 [3] is shown: the black circle marks the central value of that measurement at $M_W = 52$ GeV/c^2 and $\sigma_n = 7.2 \times 10^{-6}$ pb. The present combined results are incompatible with the interpretation of the modulation effect in terms of a WIMP behaving according to the standard phenomenological model of Ref. [9]. While 9.8 nuclear recoils should have been observed between 20 and 64 keV, none are observed. The Poisson probability of such a fluctuation is 0.006%. The black triangle on Fig. 4 at $M_W = 44$ GeV/c^2 and $\sigma_n = 5.4 \times 10^{-6}$ pb corresponds to the most likely value quoted by DAMA when they combine their modulation results with their limit achieved using pulse shape discrimination in NaI [2]. It is also incompatible with the present EDELWEISS results, the Poisson probability of observing no events from a prediction of 6.2 events being 0.2%. The only remaining part of the 3σ NaI1-4 DAMA zone corresponds to neutralino masses below the limit of 45 GeV/c^2 obtained at LEP [14]. Clearly, the standard prescriptions of Ref. [9] fail at reconciling the EDELWEISS and DAMA experimental results.

In Fig. 5 the combined EDELWEISS limit is compared to those obtained by other direct WIMP

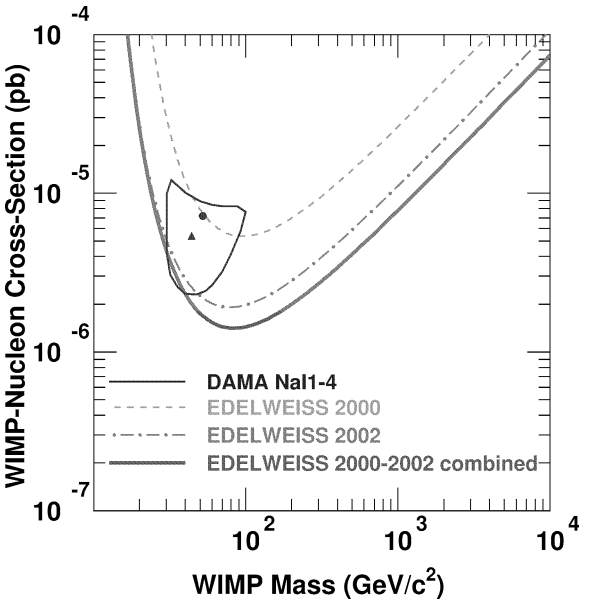

Fig. 4. Spin-independent exclusion limits (dark solid curve) obtained by combining our 2000 data from Ref. [8] with the present data, for a total exposure of 11.7 kg d. Dashed curve: previous EDELWEISS data [8] re-analyzed using the new definition of the upper bound of the recoil energy range (acceptance of 95%). Dash-dotted curve: present 2002 data. Closed contour: allowed region at 3σ CL from the DAMA1-4 annual modulation data [3]. The full circle and triangle within this contour are defined in the text.

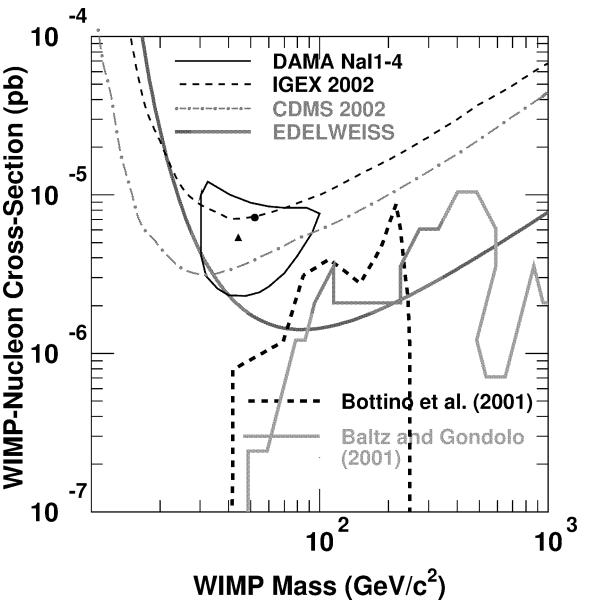

Fig. 5. Combined EDELWEISS spin-independent exclusion limits (dark solid curve) compared with published limits from other experiments and theoretical calculations. Dashed curve: Ge diode limit from IGEX [6]. Dash-dotted curve: CDMS limit with statistical subtraction of the neutron background [7]. Closed contour: allowed region at 3σ CL from the DAMA1-4 annual modulation data [3]. Two regions spanned by some of the supersymmetric model calculations of Refs. [15,16] are also shown.

searches. The EDELWEISS sensitivity for spin-independent WIMP-nucleon interaction is the best achieved so far by any dark matter search for masses above 35 GeV/c^2. Furthermore, the EDELWEISS data start to probe some of the supersymmetric models predicting the highest interaction rates. Fig. 5 shows as an example the range of masses and cross-sections allowed in the calculations of Refs. [15,16], where relaxed conditions of unification at the GUT scale yield higher upper bounds for σ_n (for comparison, see, e.g., Ref. [17]).

6. Conclusion

The EDELWEISS Collaboration has searched for nuclear recoils due to the scattering of WIMP dark matter using a 320 g heat-and-ionization Ge detector operated in a low-background environment in the Laboratoire Souterrain de Modane. After a combination with our previous data [8], the achieved sensitivity is so far the best for all direct searches for WIMP masses above 35 GeV/c^2. The limit obtained on WIMP-nucleon interaction cross-sections as a function of WIMP mass is based on the absence of events in the recoil energy range relevant for WIMP masses below 10 TeV/c^2 and does not rely on any background subtraction. The combined EDELWEISS result is incompatible at more than 99.8% CL with a WIMP of mass 44 GeV/c^2 and a nucleon scattering cross-section of 5.4×10^{-6} pb reported by the experiment DAMA [3] based on the same standard nuclear physics and astrophysical assumptions. Furthermore, the EDELWEISS experiment excludes a first sample of supersymmetric models predicting the highest WIMP-nucleon interaction rates [15,16].

Acknowledgements

The help of the staff of the Laboratoire Souterrain de Modane and of the participating laboratories is gratefully acknowledged. This work has been partially funded by the EEC Network program under contract ERBFMRXCT980167.

References

[1] L. Bergström, Rep. Prog. Phys. 63 (2000) 793;
A. Morales, Nucl. Phys. Proc. Suppl. 110 (2002) 39, astro-ph/0112550;
J. Ellis, astro-ph/0204059.
[2] R. Bernabei, et al., Phys. Lett. B 389 (1996) 757.
[3] R. Bernabei, et al., Phys. Lett. B 480 (2000) 23.
[4] R. Abusaidi, et al., Phys. Rev. Lett. 84 (2000) 5699.
[5] L. Baudis, et al., Phys. Rev. D 63 (2001) 022001.
[6] A. Morales, et al., Phys. Lett. B 532 (2002) 8.
[7] D. Abrams, et al., astro-ph/0203500, submitted to Phys. Rev. D.
[8] A. Benoit, et al., Phys. Lett. B 513 (2001) 8, astro-ph/0106094.
[9] J.D. Lewin, P.F. Smith, Astropart. Phys. 6 (1996) 87.
[10] X.F. Navick, et al., Nucl. Instrum. Methods A 444 (2000) 361.
[11] P. Di Stefano, et al., Astropart. Phys. 14 (2001) 329, astro-ph/0004308;
A. Benoit, et al., Phys. Lett. B 479 (2000) 8, astro-ph/0002462.
[12] P.N. Luke, C.S. Rossington, M.F. Wesela, IEEE Trans. Nucl. Sci. 41 (1994) 1074, LBNL-33980;
T. Shutt, et al., Nucl. Instrum. Methods A 444 (2000) 340.
[13] M.C. Lederer, V.S. Shirley, Table of Isotopes, VIIth Edition, Wiley, New York, 1978.
[14] I. Laktineh, Proceedings of the XXXVII Rencontres de Moriond, Les Arcs, France, 2002, hep-ex/0205088.
[15] A. Bottino, F. Donato, N. Fornengo, S. Scopel, Phys. Rev. D 63 (2001) 125003.
[16] E.A. Baltz, P. Gondolo, Phys. Rev. Lett. 86 (2001) 5004.
[17] J. Ellis, A. Ferstl, K.A. Olive, Phys. Lett. B 481 (2001) 304.

Chapter 3

WIMPs and Neutrons

Ionization-phonon and scintillation-phonon cryogenic detectors have excellent rejection of the dominant radioactive background. This background comes mainly from photons, and these particles can be identified because for a given amount of energy they deposit in the detector, they create much more ionization than a WIMP would. However, neutrons, like WIMPs, can elastically scatter off nuclei and therefore the ionization or scintillation yield of the interaction is not sufficient to distinguish between neutrons and WIMPs. Neutrons thus make up a difficult background for this type of detector. The first measure to take is to reduce the neutron background as much as possible, through passive and active shielding. The second measure is to identify those neutrons that do infiltrate the experiment.

3.1 Passive and active shielding for EDELWEISS II

The neutrons that are problematic for an experiment like EDELWEISS are those that deposit energies in the Ge detectors similar to those deposited by WIMPs, typically up to 100 keV. The kinematics of elastic scattering imply that the guilty neutrons have energies in the 400 keV–4 MeV range. These neutrons have several origins at the Modane underground laboratory. The flux of neutrons in the 1–10 MeV energy range has been measured to be $1.6 \times 10^{-6}\mathrm{cm}^{-1}\mathrm{s}^{-1}$ [64, 65]. The main contribution is from α-n reactions in the rock; their average energy is ≈ 3.5 MeV. In EDELWEISS II, these neutrons are dealt with by 50 cm of polyethylene (PE) moderator around the experiment; this moderates the energies of the fast neutrons and reduces their contribution to events in the detectors by three orders of magnitude down to 5×10^{-4} evts/d/kg above a 10 keV threshold. One of my first tasks in EDELWEISS II was to find a supplier for the PE moderator; eventually, the half of it consisting of large slabs was purchased locally, while the other half that follows a complicated geometry with many cutouts (for pumping lines for instance) was assembled from Czech LEGO-style bricks [66]. The bricks came from a special batch without the boron the supplier usually mixes into the PE.

Other neutrons, the subject of L. Chabert's PhD thesis at UCBL defended in 2004 [67], are induced by the rare cosmic muons that make it through the ≈ 1.5 km of rock above the experiment and spallate on a heavy element like iron or lead close to the experiment. This creates a cascade of fast neutrons. If the spallation happens in the 30 tons of Pb shielding right around the experiment, this can lead to a rate of 10^{-2} evts/d/kg above a 10 keV threshold in the detectors. To deal with such neutrons, EDELWEISS II is surrounded by 140 m^2 of plastic scintillators that tag passage of muons. These scintillator modules, each 5 cm thick, 2–3 m^2 in size, and complete with their photomultipliers, were recovered from the KARMEN neutrino experiment [68] when the Karlsruhe group joined EDELWEISS. Along with L. Chabert, I carried out feasibility tests on these scintillator modules, verifying the uniformity of their response in Lyon. We also assembled and installed a simple muon telescope (two modules separated by Pb bricks) underground at LSM to verify their performance and threshold settings (Fig. 3.1). The 250 days of data demonstrated it would be possible to tag the majority of muons while maintaining a reasonable count rate [67]. We measured

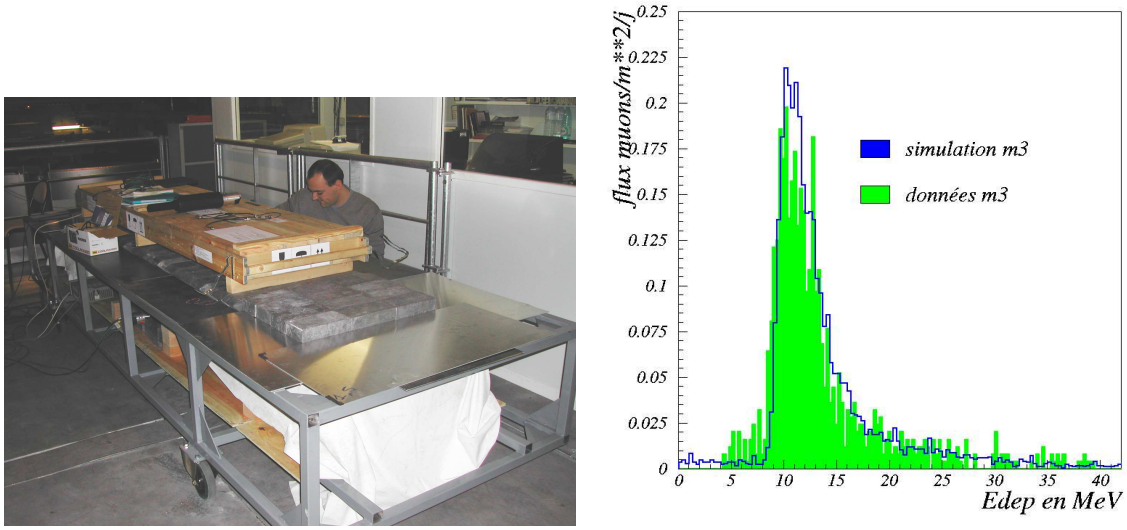

Figure 3.1: Left: muon telescope at LSM along with then-PhD student L. Chabert, in December 2002. Telescope consists of two large plastic scintillators shielded from light, the upper in a wooden box, the lower wrapped in plastic, and seperated by Pb bricks. Right: muon spectrum in telescope, and fit to simulations [67].

a rate of 4.44 ± 0.34 muons per day through a horizontal surface of unit area, in agreement with earlier measurements [69].

A remaining source of neutrons is muon spallation on the heavy elements in the rock right around the experiment. Early simulations show their rate should be quite low, and there may be a possibility of tagging either the muons that go through the rock or other products of the muon interaction with the existing muon veto.

3.2 Light targets as complements to Ge

Despite the efforts undertaken to shield the experiment, some neutrons may still infiltrate it. Their effect may be reduced because the setup is segmented, making it possible to tag neutrons by their coincidences between detectors. Moreover, using other targets in addition to Ge may also provide useful information on the neutron background. This approach has already been used by the CDMS experiment in its initial, shallow, site, exposed to a strong neutron background, as Si ionization-phonon detectors were mixed in with the Ge ones [58]. Indeed, the collaboration has pursued this approach even in its new, deeper site [46]. We have compared responses to neutrons and to WIMPs of Ge, Si, but also of LiF and Al_2O_3, two light targets that could be suitable for scintillation-phonon detectors. Such detectors would use scintillation, rather than ionization, to discriminate between interacting particles of various nature. Physical properties of these materials are given in Tab. 3.1. The following discussion is detailed in Sec. 3.4A.

3.2.1 Neutron interactions

Mean free paths for neutrons in the 400 keV–4 MeV energy range, calculated from the densities in Tab. 3.1 and publicly available cross-sections, appear in Fig. 3.2. The dominant cross-sections are elastic at these energies. Mean free paths are of the order of 8 cm for Si and Ge, but only of about half as long for LiF and Al_2O_3. Therefore, neutrons are more likely to interact in a given volume of LiF or Al_2O_3 than Si or Ge; moreover, a given neutron interaction will leave a larger signal in

Material	Element	Mass number A	Mass density ρ (g/cm^3)	Nuclei per unit volume δ (/cm^3)	Unpaired nucleons per unit volume δ' (/cm^3)
LiF			2.6		
	Li	6.9		6.1×10^{22}	6.6×10^{22}
	F	19		6.1×10^{22}	6.1×10^{22}
Al_2O_3			4.0		
	O	16		6.9×10^{22}	0
	Al	27		4.6×10^{22}	4.6×10^{22}
Si		28.1	2.3	5.0×10^{22}	2.3×10^{21}
Ge		72.6	5.3	4.4×10^{22}	3.1×10^{21}

Table 3.1: Some physical properties of LiF, Al_2O_3, Si and Ge. Despite having nearly the lowest mass density, LiF has the most nuclei per unit volume. Given that LiF and Al_2O_3 are naturally rich in elements with odd mass-numbers, both have at least an order of magnitude more unpaired nucleons per unit volume than either Si or Ge.

the former detectors than in the latter because of elastic scattering kinematics.

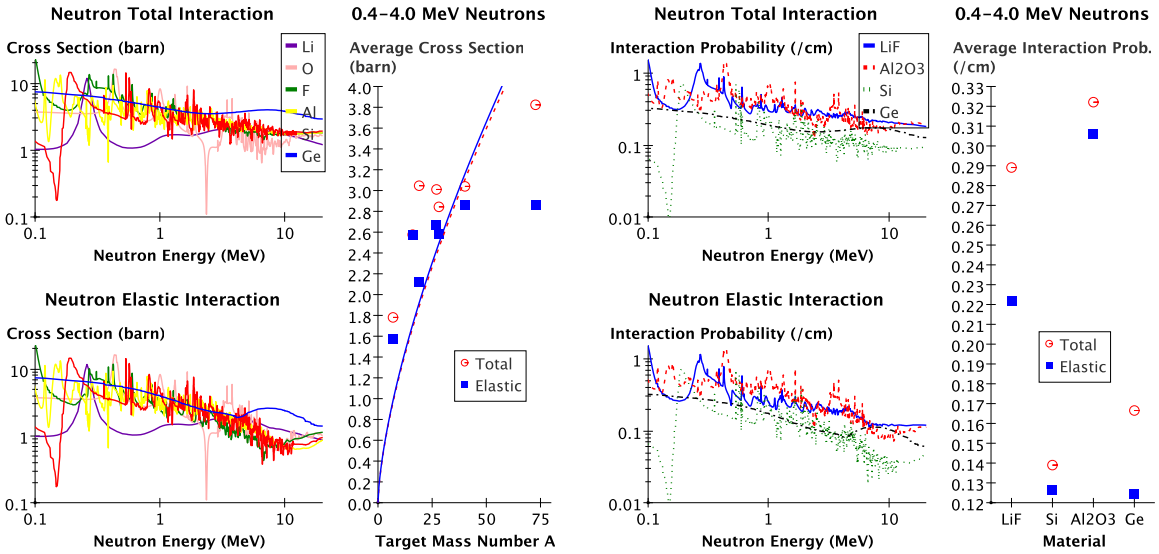

Figure 3.2: Left: neutron cross sections, total and elastic, as a function of neutron energy, for various targets. Many resonances are visible. Averaged over 0.4–4 MeV energies, cross sections increase with target mass number A. Right: interaction probability Σ $(\delta\sigma) = 1/\lambda$, for various materials. LiF and Al_2O_3 have significantly shorter mfps λ than Si and Ge.

A more detailed study requires a Monte Carlo simulation of the EDELWEISS II setup at Modane. Such simulations have been carried out by M. De Jésus of IPN Lyon, using the GEANT3 package. The simulation starts with the spectrum of neutrons in the underground laboratory at Modane, and propagates the particles through the experiment, polyethylene moderator and Pb shielding in particular, all the way to the detectors, where energy spectra and coincidences are reconstructed (Fig. 3.3). The integral over all energies of the spectra of Fig. 3.3 reflect the interaction probabilities of the various materials; indeed the numerical values are in qualitative agreement: per unit volume, Si sees slightly fewer interactions than Ge, while LiF and Al_2O_3 see significantly more than Ge. Slopes of the spectra also agree qualititatively with the elastic scattering kinematics: energy transfer becomes more efficient as one moves from Ge to Si, Al_2O_3 and LiF. Overall, LiF and Al_2O_3 are

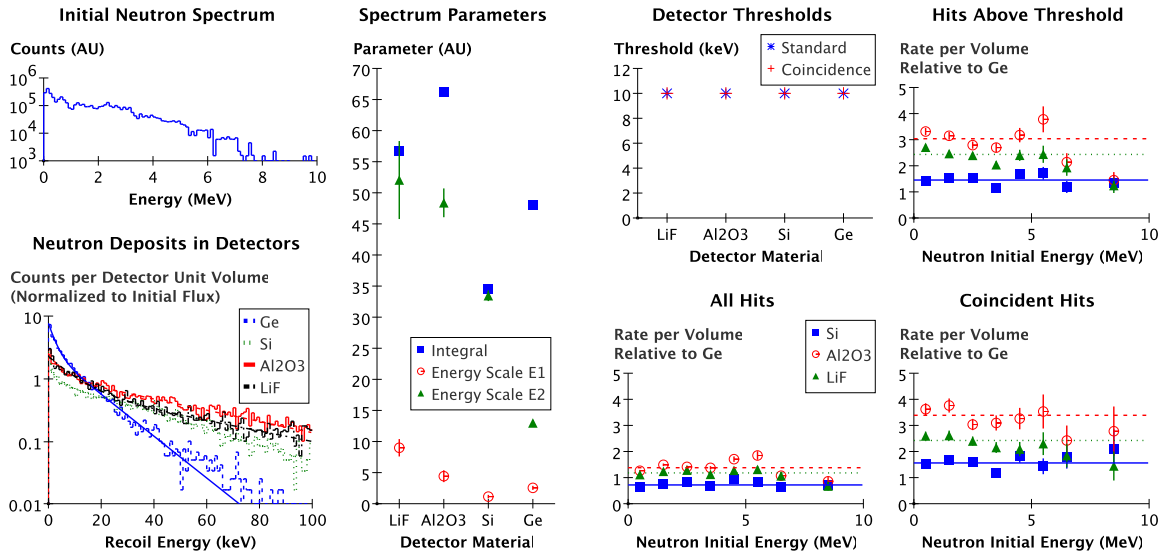

Figure 3.3: Neutron simulations of the EDELWEISS II experiment. Top left: initial neutron spectrum of the LSM. Bottom left: recoil spectra per detector, per unit volume. Integrals of spectra are qualitatively compatible with total interaction probablity $1/\lambda$ of Fig. 3.2, favorizing LiF and Al_2O_3 over Ge and especially Si. Slopes show effects of scattering kinematics, further favorizing the light targets. Right, rates per detector as a function of neutron initial energy. When thresholds are taken into account (10 keV for all detectors, for single hits as well as for coincidences), kinematics strongly enhance the advantage of Al_2O_3 and LiF relative to Ge and Si, in particular in the case of coincidences. Over most of the initial neutron energies, these numbers vary little.

significantly more sensitive to neutrons than are Ge and Si.

3.2.2 WIMP interactions

In typical supersymmetric models, the WIMP interaction is dominated by the spin-independent component [24]. Its cross section is proportional to the square of the WIMP-nucleus reduced mass μ as well as to the square of the target atomic number, A, and depends on one unknown parameter, $f_{nucleon}$, the effective coupling to a nucleon [23]: $\sigma = \frac{4}{\pi}\mu^2 A^2 {f_{nucleon}}^2$. This cross-section increases strongly with target mass, favouring Ge over lighter nuclei. The cross-section depends much more strongly on target mass number than material densities do (Tab. 3.1); therefore the strong advantage of Ge is maintained. Targets with odd numbers of protons and/or neutrons can also interact with WIMPs in a spin-dependent fashion. The cross section depends on the spin content of the target nucleus; this puts Si at a disadvantage and favours LiF and Al_2O_3.

The spectrum of recoil energies left by WIMPs in a detector per unit mass and time is obtained by folding in the astrophysical parameters (the galactic velocity distribution and local mass densities of WIMPs, galactic speed of earthbound detector) with the particle physics parameters (the cross section σ and nuclear form factor F) and the elastic scattering kinematics, as described for instance in [33]. The spectrum falls off roughly like an exponential and can be expressed as:

$$\frac{dR}{dE} = \frac{1}{\sqrt{\pi}} \frac{\sigma n_0}{v_0 \mu^2} F^2(E) \int_{v_{min}}^{v_{max}} \frac{f(v)}{v} dv \tag{3.1}$$

where $v_{min} = \sqrt{\frac{EM}{2\mu^2}}$ is the minimum WIMP speed that can deposit an energy E, and v_{max} is the maximum WIMP velocity given galactic evaporation. We assume a local dark matter density of $\rho_0 = \mathcal{M} n_0 = 0.3$ GeV/c^2, a Maxwellian WIMP galactic velocity distribution with a typical speed

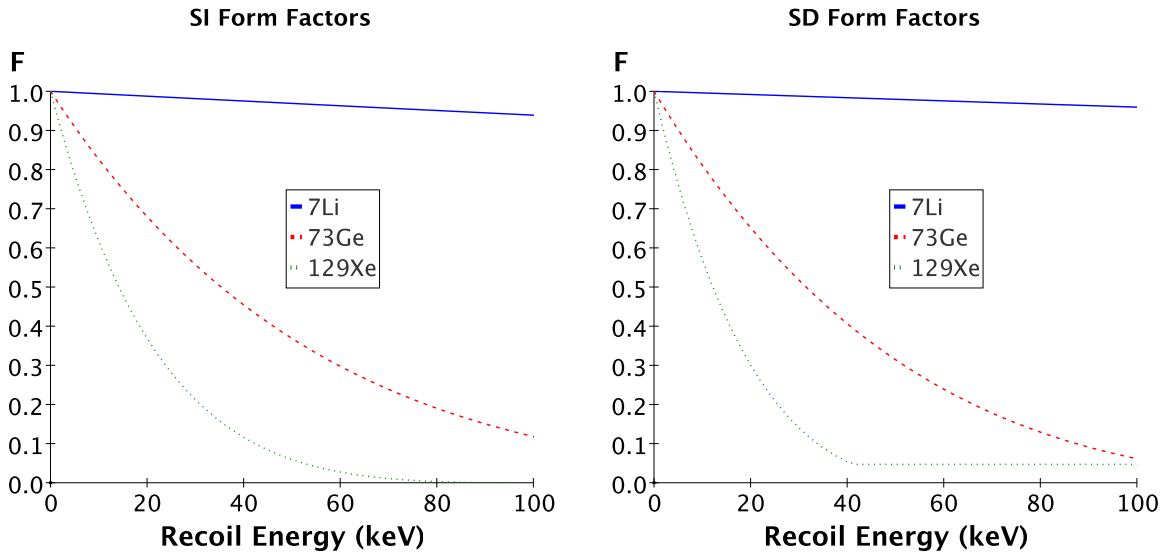

Figure 3.4: Spin-independent (SI) and spin-dependent (SD) nuclear form factors on some nuclei. Shows loss of coherance on heavy nuclei, offsetting some of the gain from the increased cross section in the SI case.

of 220 km/s and an escape velocity of 650 km/s, a speed of the Earth in the galaxy of 235 km/s, and a Helm-type nuclear form-factor with the parameters suggested in Sec. 4 of Ref. [33]. For the spin-independent interaction, the form-factor describes the loss of coherence from a value of 1 at zero momentum transfer as the wavelength of the WIMP decreases compared to the typical size of the target. The form-factor thus somewhat reduces the advantage heavy targets (Ge) have over their lighter counterparts (Li and O), as shown in Fig. 3.4. The slope of the spectrum depends on the WIMP mass; its shape may be hard to distinguish from that of the spectrum caused by the neutron background especially for low statistics (Fig. 3.3).

In Fig. 3.5, we numerically integrate Eq. 3.1 over recoil energies to obtain interaction rates per unit mass and time in the detectors above a given threshold, for spin-dependent, spin-independent and total interactions. Ge is the most effective WIMP detector considered except for the lightest WIMPs when LiF, Al_2O_3 and Si have a low enough threshold. For heavier WIMPs, LiF and Al_2O_3 are at least an order of magnitude less sensitive than Ge; Si is about five times less sensitive than Ge.

3.3 Background reduction using coincidences and different materials

Once neutrons have slipped into the experiment, there remain ways to identify them. This can be done by a combination of exploiting coincidences between detectors and relative rates between different types of detectors. Fig. 3.6 shows that LiF and Al_2O_3 have neutron and WIMP properties othogonal to those of Ge.

The mean free path of 0.4–4 MeV neutrons in matter is of the order of a few cm; that of WIMPs is at least several light years. A closely packed, segmented experiment with units of typical size a few cm would therefore see coincidences between detectors when a neutron passes through, but should only see a single interactions from WIMPs. The simplest approach here is to use this property to veto those neutrons. Simulations show that in the EDELWEISS II geometry completely filled with Ge detectors of threshold 10 keV, only about 44% of events from neutrons are expected to escape a coincident cut. This number can be lowered to 41% by considering the top and bottom Ge layers

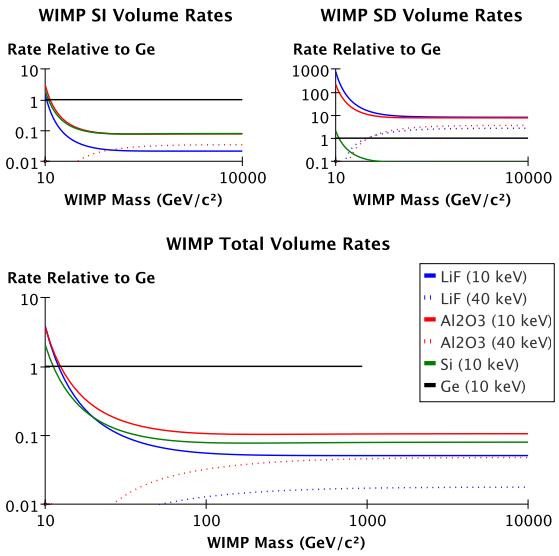

Figure 3.5: Interaction rates of WIMPs per unit volume of various detectors as a function of WIMP mass, for 10 keV and 40 keV thresholds, relative to Ge (10 keV threshold). Top left: spin-independent rates. Cross section proportional to A^2 ensures Ge dominates other materials by at least an order of magnitude. Top right: spin dependent rates. LiF and Al_2O_3 dominate thanks to their abundance of spin-rich isotopes. Si is at a great disadvantage because its rare isotope with spin has very little of it. Bottom: the spin-independent contribution dominates the combination of both interactions in typical supersymmetric scenarios.

just as a veto around the middle detectors, though this comes with a loss of 20% of fiducial volume for WIMPs. Replacing the top and bottom layers of detectors by Si, Al_2O_3 and LiF lowers the ratio of uncoincident to coincident neutrons in the middle Ge layers to respectively 38%, 34% and 37%, as Fig. 3.7 shows. In practice, the sacrifice of 20% of the fiducial volume in favour of a 23% better identification of neutrons is only beneficial if statistics are sufficient. However, simulations show that the break-even point is reached fairly quickly, after only about 2 uncoincident neutron events in the Ge detectors. Coincidences can also be used to subtract neutron background (Fig. 3.7), with a gain of up to 25% in the error on a WIMP signal.

More complicated background reduction scenarios are possible. However, this already indicates that LiF and Al_2O_3 should be superior to Si as complements to Ge — provided they can be made to function as cryogenic scintillation-phonon detectors with decent thresholds.

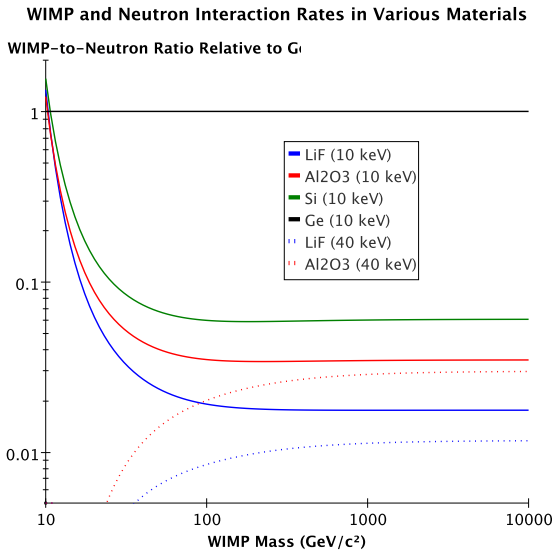

Figure 3.6: The ratio of number of neutron events over number of WIMP events above the threshold in a given detector, divided by the same ratio in a Ge detector (with a 10 keV threshold). For most WIMP masses, Si and especially Al_2O_3 and LiF have neutron and WIMP properties that are orthogonal to those of Ge.

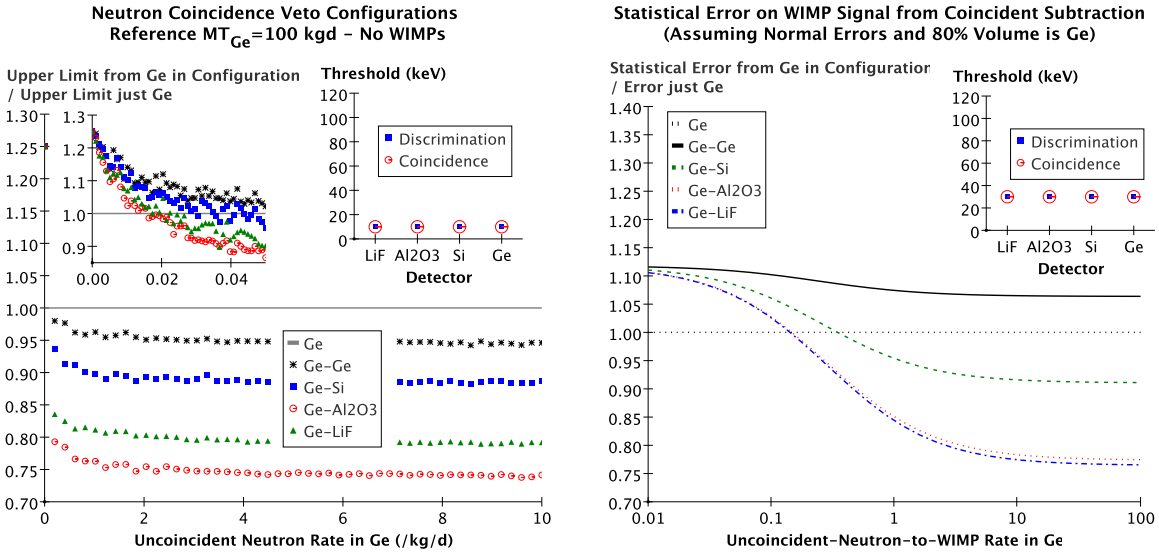

Figure 3.7: Left: simulations showing effect of vetoing the neutron background on the upper limit that can be placed on a null WIMP signal. The reference scenario is that all detectors are Ge; in this case, only 44% of neutron interactions are not coincident. Using the top and bottom layers of detectors as neutron-coincidence vetos yields a relative gain in the upper limit of 5% given sufficient statistics. Replacing top and bottom layers by Si, LiF or Al_2O_3 yields an improvement in the upper limit on the WIMP rate of up to 25 %. Sacrificing 20% of Ge fiducial volume costs at most 25% of the limit; moreover, the break-even point is reached quickly, after only 2 uncoincident neutrons in Ge for the Ge-Al_2O_3 scenario. Right: error on a WIMP signal for similar detector configurations, assuming normal errors, as a function of neutron-to-WIMP rate. Coincidences have been used to subtract neutron background. Error can be reduced by 25%, but can also be increased.

3.4A EDELWEISS internal note on neutrons

Ref. [70].

November 22, 2007

EDELWEISS Internal Note
EDELWEISS II, neutrons, WIMPs and light targets
PRELIMINARY

P. Di Stefano

Analysis of cross sections and simulations show that LiF and Al_2O_3 are more sensitive to neutrons than Ge and Si are, by virtue of their shorter mean free path and also their elastic scattering kinematics. On the other hand, these light targets are about an order of magnitude less sensitive to WIMPs than Ge is. Replacing a fifth of the Ge detectors by light targets in an EDELWEISS II-type configuration can improve the upper limit on a null WIMP signal by up to 25%. The error on a WIMP signal can also be reduced by up to 25%.

Sec. I discusses neutrons interactions in the various types of targets; Sec. II deals with WIMP interactions; Sec. III discusses some methods to reduce the neutron background. Physical properties of the targets are given in Tab. I and II.

Material	Element	Mass number A	Mass density ρ (g/cm^3)	Nuclei per unit volume δ (/cm^3)	Unpaired nucleons per unit volume δ' (/cm^3)
LiF		$\frac{6.9+19}{2} = 12.9$	2.6	$(2 \times 6.1 = 12.2) \times 10^{22}$	$(6.6 + 6.1 = 12.7) \times 10^{22}$
	Li	6.9		6.1×10^{22}	6.6×10^{22}
	F	19		6.1×10^{22}	6.1×10^{22}
Al_2O_3		$\frac{2\times27+3\times16}{5} = 20.4$	4.0	$(5 \times 2.3 = 11.5) \times 10^{22}$	$(2 \times 2.3 = 4.6) \times 10^{22}$
	O	16		6.9×10^{22}	0
	Al	27		4.6×10^{22}	4.6×10^{22}
Si		28.1	2.3	5.0×10^{22}	2.3×10^{21}
Ge		72.6	5.3	4.4×10^{22}	3.1×10^{21}

TABLE I: Some physical properties of LiF, Al_2O_3, Si and Ge. Despite having the lowest mass density, LiF has the most nuclei per unit volume. Given that LiF and Al_2O_3 are naturally rich in elements with odd mass-numbers (Tab. II), both have at least an order of magnitude more unpaired nucleons per unit volume than either Si or Ge.

Z	Element	6	7	16	18	19	27	28	29	30	70	72	73	74	76
3	Li	7.5 (p,n)	92.5 (p)												
8	O			99.8	0.2										
9	F					100 (p)									
13	Al						100 (p)								
14	Si							92.2	4.7 (n)	3.1					
32	Ge										21.2	27.7	7.7 (n)	35.9	7.5

TABLE II: Natural isotope abundances relevant to LiF, Al_2O_3, Si and Ge, in % of number of atoms [1]. For nuclei with odd A or N, type of free nucleon is given in parenthesis.

I. NEUTRON SIMULATIONS

A. Data sets

Simulations were carried out by M. de Jésus using GEANT3. Ge cross sections were modified to account for forward-scattering. Four simulations were carried out; in all, the 8 middle detector layers (12 detectors each) are all Ge; the top and bottom layers are Al_2O_3, Si, Ge or LiF according to the simulation. The LSM neutron background spectrum is propagated through the experiment and to the detectors. Run is `2005_05_31`, files are `edw2saph.hbook`,`edw2si.hbook`, `edw2ge.hbook` and `edw2lif.hbook` respectively.

Cross section data from KAERI have also been used.

B. Data analysis

Two tuples, 200 and 700, are present in most runs.

1. Tuple 200

Eini (MeV) Energy of neutron at source.

Er (keV) Recoil energy of nucleus.

2. Tuple 700

Ecini (GeV) Energy of neutron at source

Gekin (GeV) Energy of neutron just before an interaction.

Erec (MeV) Recoil energy of nucleus after a single interaction.

In the following, only 700 has been used.

The simulation takes into account all processes for Ge, but only elastic processes for the other targets. Therefore, in this analysis, only the elastic interactions are considered; ie in tuple 700, only interactions of type 13 have been retained.

3. Events and thresholds

An event is defined as any number of neutron interactions in a single detector volume; a neutron interacting in several detectors counts for as many coincident events as there are affected detectors.

The discrimination threshold is defined as the threshold above which an interaction in a detector can be identified as a neutron.

The coincidence threshold is defined as the threshold above which events above the discrimination threshold in another detector can be detected as coincidences. It is inferior or equal to the discrimination threshold.

C. Results

1. *Cross Sections and Mean Free Paths*

See Fig. 1 and Tab. III and Tab. IV.

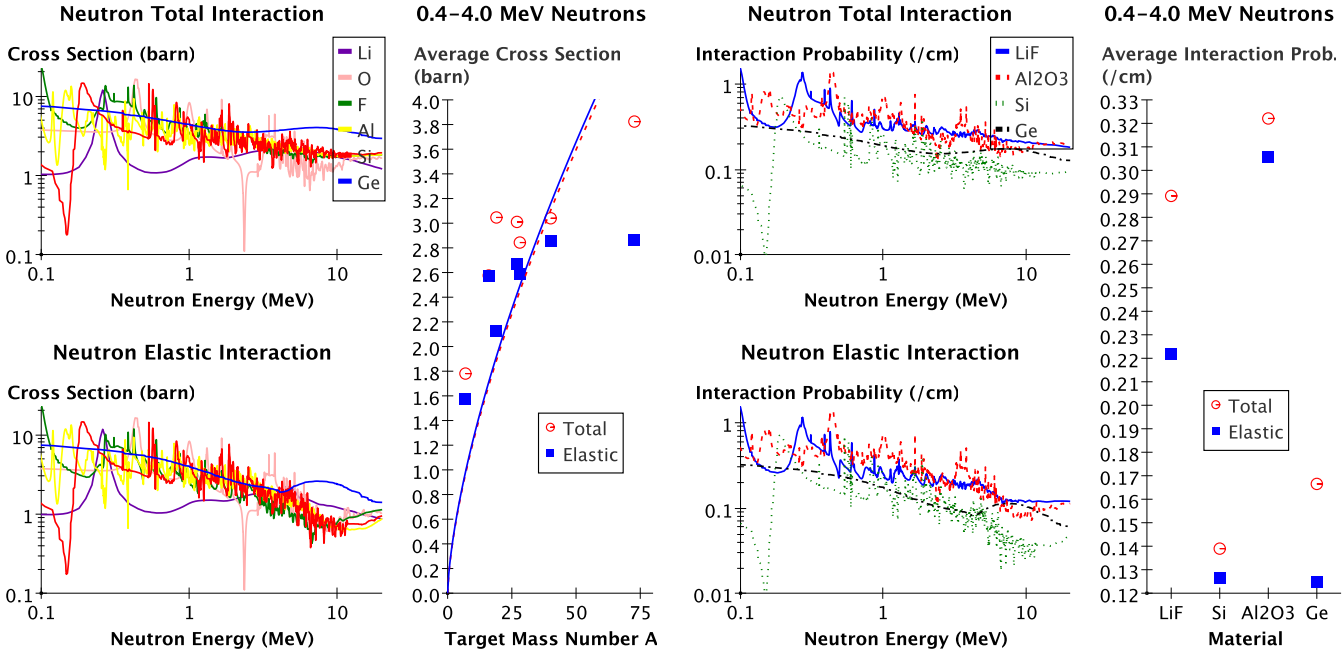

FIG. 1: Left: neutron cross sections, total and elastic, as a function of neutron energy, for various targets. Many resonances are visible. Averaged over 0.4–4 MeV energies, cross sections increase with target mass number A, but fit to canonical $A^{2/3}$ is poor. Right: interaction probability $\Sigma\ (\delta\sigma) = 1/\lambda$, for various materials. LiF and Al_2O_3 have significantly shorter mfps λ than Si and Ge.

Element	Neutron kinematic	Emin MeV	Emax MeV	SigTot barn	SigElas barn	SigTot Ge units	SigElas Ge units
Li	0.220	0.4	4	1.78	1.58	0.47	0.55
O	0.111	0.4	4	2.58	2.57	0.67	0.90
F	0.095	0.4	4	3.05	2.12	0.80	0.74
Al	0.069	0.4	4	3.01	2.67	0.79	0.93
Si	0.066	0.4	4	2.84	2.59	0.74	0.90
Ca	0.047	0.4	4	3.04	2.86	0.79	1.00
Ge	0.027	0.4	4	3.82	2.86	1.00	1.00

TABLE III: Neutron cross sections from JENDL and ENDF (Recap_CrossSections.java — Element_Cross_Sections.tex).

Material	Emin MeV	Emax MeV	MFP tot cm	MFP elas cm	MFP tot Ge units	MFP elas Ge units	IntProb tot /cm	IntProb elas /cm	IntProb tot Ge units	IntProb elas Ge units
LiF	0.4	4	3.46	4.51	0.58	0.56	0.29	0.22	1.74	1.78
Al2O3	0.4	4	3.10	3.27	0.52	0.41	0.32	0.31	1.93	2.45
Si	0.4	4	7.20	7.91	1.20	0.99	0.14	0.13	0.83	1.01
Ge	0.4	4	6.01	8.03	1.00	1.00	0.17	0.12	1.00	1.00

TABLE IV: Neutron interaction probabilities (IP) and mean free paths (MFP) (Recap_MeanFreePaths.java — Material_Mean_Free_Paths.tex).

2. *Simulation*

See Fig 4 and Tab. V, Tab. IX, Tab. X.

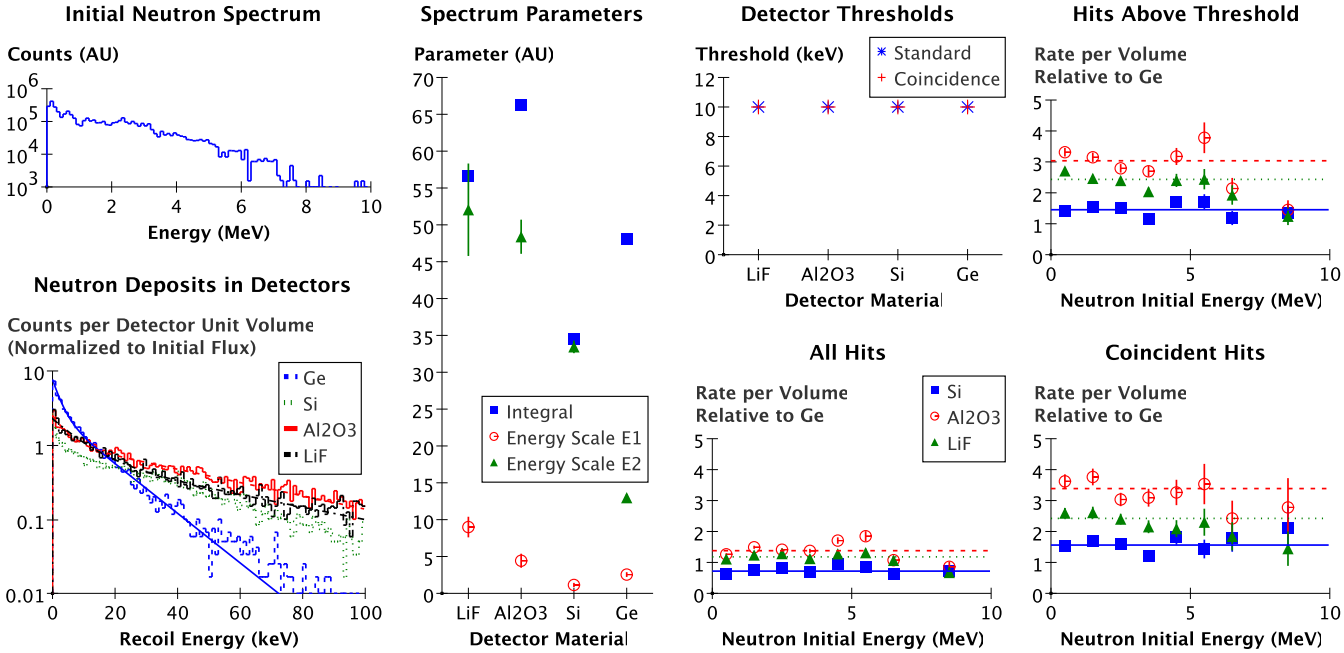

FIG. 2: Neutron simulations of the EDELWEISS II experiment. Top left: initial neutron spectrum of the LSM. Bottom left: recoil spectra per detector, per unit volume. Integrals of spectra are qualitatively compatible with total interaction probablity $1/\lambda$ of Tab. IV, favorizing LiF and Al_2O_3 over Ge and especially Si. Slopes show effects of scattering kinematics, favorizing the light targets further. Right, rates per detector as a function of neutron initial energy. When thresholds are taken into account (10 keV for all detectors, for single hits as well as for coincidences), kinematics strongly enhance the advantage of Al_2O_3 and LiF relative to Ge and Si, in particular in the case of coincidences. Over most of the initial neutron energies, these numbers vary little.

Simulation	Detector	Num. of Det.	Initial Neutrons	Thresh. (keV)	Coinc. Thresh. (keV)	Events Total	Events Threshold	Events Uncoinc	Events Coinc	Rate per Detector Total	Rate per Detector Threshold	Rate per Detector Uncoinc	Rate per Detector Coinc
Ge	Ge	120	5.0×10^6	10	10	28738 ± 170	10039 ± 100	4432 ± 67	5607 ± 75	47.9 ± 0.28	16.73 ± 0.17	7.39 ± 0.11	9.34 ± 0.12
Ge	Top+Bottom	24	5.0×10^6	10	10	5763 ± 76	2005 ± 45	1102 ± 33	903 ± 30	48.02 ± 0.63	16.71 ± 0.37	9.18 ± 0.28	7.52 ± 0.25
Ge	Middle	96	5.0×10^6	10	10	22975 ± 152	8034 ± 90	3330 ± 58	4704 ± 69	47.86 ± 0.32	16.74 ± 0.19	6.94 ± 0.12	9.8 ± 0.14
Ge	Total	120	5.0×10^6	-10	-10	28738 ± 170	10039 ± 100	4432 ± 67	5607 ± 75	47.9 ± 0.28	16.73 ± 0.17	7.39 ± 0.11	9.34 ± 0.12
Simulation	Detector	Num. of Det.	Initial Neutrons	Thresh. (keV)	Coinc. Thresh. (keV)	Events Total	Events Threshold	Events Uncoinc	Events Coinc	Rate per Detector Total	Rate per Detector Threshold	Rate per Detector Uncoinc	Rate per Detector Coinc
Ge-Si	Ge	96	5.0×10^6	10	10	23588 ± 154	8115 ± 90	3111 ± 56	5004 ± 71	49.14 ± 0.32	16.91 ± 0.19	6.48 ± 0.12	10.42 ± 0.15
Ge-Si	Si	24	5.0×10^6	10	10	4143 ± 64	2914 ± 54	1504 ± 39	1410 ± 38	34.52 ± 0.54	24.28 ± 0.45	12.53 ± 0.32	11.75 ± 0.31
Ge-Si	Top+Bottom	24	5.0×10^6	10	10	4143 ± 64	2914 ± 54	1504 ± 39	1410 ± 38	34.52 ± 0.54	24.28 ± 0.45	12.53 ± 0.32	11.75 ± 0.31
Ge-Si	Middle	96	5.0×10^6	10	10	23588 ± 154	8115 ± 90	3111 ± 56	5004 ± 71	49.14 ± 0.32	16.91 ± 0.19	6.48 ± 0.12	10.42 ± 0.15
Ge-Si	Total	120	5.0×10^6	-10	-10	27731 ± 167	11029 ± 105	4615 ± 68	6414 ± 80	46.22 ± 0.28	18.38 ± 0.18	7.69 ± 0.11	10.69 ± 0.13
Simulation	Detector	Num. of Det.	Initial Neutrons	Thresh. (keV)	Coinc. Thresh. (keV)	Events Total	Events Threshold	Events Uncoinc	Events Coinc	Rate per Detector Total	Rate per Detector Threshold	Rate per Detector Uncoinc	Rate per Detector Coinc
Ge-Al2O3	Ge	96	5.0×10^6	10	10	23125 ± 152	7718 ± 88	2593 ± 51	5125 ± 72	48.18 ± 0.32	16.08 ± 0.18	5.4 ± 0.11	10.68 ± 0.15
Ge-Al2O3	Al2O3	24	5.0×10^6	10	10	7949 ± 89	6088 ± 78	3029 ± 55	3059 ± 55	66.24 ± 0.74	50.73 ± 0.65	25.24 ± 0.46	25.49 ± 0.46
Ge-Al2O3	Top+Bottom	24	5.0×10^6	10	10	7949 ± 89	6088 ± 78	3029 ± 55	3059 ± 55	66.24 ± 0.74	50.73 ± 0.65	25.24 ± 0.46	25.49 ± 0.46
Ge-Al2O3	Middle	96	5.0×10^6	10	10	23125 ± 152	7718 ± 88	2593 ± 51	5125 ± 72	48.18 ± 0.32	16.08 ± 0.18	5.4 ± 0.11	10.68 ± 0.15
Ge-Al2O3	Total	120	5.0×10^6	-10	-10	31074 ± 176	13806 ± 117	5622 ± 75	8184 ± 90	51.79 ± 0.29	23.01 ± 0.2	9.37 ± 0.12	13.64 ± 0.15
Simulation	Detector	Num. of Det.	Initial Neutrons	Thresh. (keV)	Coinc. Thresh. (keV)	Events Total	Events Threshold	Events Uncoinc	Events Coinc	Rate per Detector Total	Rate per Detector Threshold	Rate per Detector Uncoinc	Rate per Detector Coinc
Ge-LiF	Ge	96	5.0×10^6	10	10	23351 ± 153	7485 ± 87	2775 ± 53	4710 ± 69	48.65 ± 0.32	15.59 ± 0.18	5.78 ± 0.11	9.81 ± 0.14
Ge-LiF	LiF	24	5.0×10^6	10	10	6798 ± 82	4881 ± 70	2693 ± 52	2188 ± 47	56.65 ± 0.69	40.68 ± 0.58	22.44 ± 0.43	18.23 ± 0.39
Ge-LiF	Top+Bottom	24	5.0×10^6	10	10	6798 ± 82	4881 ± 70	2693 ± 52	2188 ± 47	56.65 ± 0.69	40.68 ± 0.58	22.44 ± 0.43	18.23 ± 0.39
Ge-LiF	Middle	96	5.0×10^6	10	10	23351 ± 153	7485 ± 87	2775 ± 53	4710 ± 69	48.65 ± 0.32	15.59 ± 0.18	5.78 ± 0.11	9.81 ± 0.14
Ge-LiF	Total	120	5.0×10^6	-10	-10	30149 ± 174	12366 ± 111	5468 ± 74	6898 ± 83	50.25 ± 0.29	20.61 ± 0.19	9.11 ± 0.12	11.5 ± 0.14

TABLE V: Simulation numbers normalized to incident flux (Simulation_Analysis_EDII.java — Ge_counts.tex, Ge-Si_counts.tex ...). Normalization is 10^6/ incident neutrons. An event is defined as any number of neutron interactions in a single detector volume; a neutron interacting in several detectors counts for as many coincident events. All thresholds here are 10 keV.

Simulation	Detector	Num. of Det.	Initial Neutrons	Thresh. (keV)	Coinc. Thresh. (keV)	Events Total	Events Threshold	Events Uncoinc	Events Coinc	Rate per Detector Total	Rate per Detector Threshold	Rate per Detector Uncoinc	Rate per Detector Coinc
Ge	Ge	120	5.0×10^6	30	30	28738 ± 170	2382 ± 49	1818 ± 43	564 ± 24	47.9 ± 0.28	3.97 ± 0.08	3.03 ± 0.07	0.94 ± 0.04
Ge	Top+Bottom	24	5.0×10^6	30	30	5763 ± 76	487 ± 22	405 ± 20	82 ± 9	48.02 ± 0.63	4.06 ± 0.18	3.38 ± 0.17	0.68 ± 0.08
Ge	Middle	96	5.0×10^6	30	30	22975 ± 152	1895 ± 44	1413 ± 38	482 ± 22	47.86 ± 0.32	3.95 ± 0.09	2.94 ± 0.08	1 ± 0.05
Ge	Total	120	5.0×10^6	-10	-10	28738 ± 170	2382 ± 49	1818 ± 43	564 ± 24	47.9 ± 0.28	3.97 ± 0.08	3.03 ± 0.07	0.94 ± 0.04
Simulation	Detector	Num. of Det.	Initial Neutrons	Thresh. (keV)	Coinc. Thresh. (keV)	Events Total	Events Threshold	Events Uncoinc	Events Coinc	Rate per Detector Total	Rate per Detector Threshold	Rate per Detector Uncoinc	Rate per Detector Coinc
Ge-Si	Ge	96	5.0×10^6	30	30	23588 ± 154	1961 ± 44	1324 ± 36	637 ± 25	49.14 ± 0.32	4.09 ± 0.09	2.76 ± 0.08	1.33 ± 0.05
Ge-Si	Si	24	5.0×10^6	30	30	4143 ± 64	1710 ± 41	1323 ± 36	387 ± 20	34.52 ± 0.54	14.25 ± 0.34	11.02 ± 0.3	3.22 ± 0.16
Ge-Si	Top+Bottom	24	5.0×10^6	30	30	4143 ± 64	1710 ± 41	1323 ± 36	387 ± 20	34.52 ± 0.54	14.25 ± 0.34	11.02 ± 0.3	3.22 ± 0.16
Ge-Si	Middle	96	5.0×10^6	30	30	23588 ± 154	1961 ± 44	1324 ± 36	637 ± 25	49.14 ± 0.32	4.09 ± 0.09	2.76 ± 0.08	1.33 ± 0.05
Ge-Si	Total	120	5.0×10^6	-10	-10	27731 ± 167	3671 ± 61	2647 ± 51	1024 ± 32	46.22 ± 0.28	6.12 ± 0.1	4.41 ± 0.09	1.71 ± 0.05
Simulation	Detector	Num. of Det.	Initial Neutrons	Thresh. (keV)	Coinc. Thresh. (keV)	Events Total	Events Threshold	Events Uncoinc	Events Coinc	Rate per Detector Total	Rate per Detector Threshold	Rate per Detector Uncoinc	Rate per Detector Coinc
Ge-Al2O3	Ge	96	5.0×10^6	30	30	23125 ± 152	1804 ± 42	1117 ± 33	687 ± 26	48.18 ± 0.32	3.76 ± 0.09	2.33 ± 0.07	1.43 ± 0.05
Ge-Al2O3	Al2O3	24	5.0×10^6	30	30	7949 ± 89	4204 ± 65	2958 ± 54	1246 ± 35	66.24 ± 0.74	35.03 ± 0.54	24.65 ± 0.45	10.38 ± 0.29
Ge-Al2O3	Top+Bottom	24	5.0×10^6	30	30	7949 ± 89	4204 ± 65	2958 ± 54	1246 ± 35	66.24 ± 0.74	35.03 ± 0.54	24.65 ± 0.45	10.38 ± 0.29
Ge-Al2O3	Middle	96	5.0×10^6	30	30	23125 ± 152	1804 ± 42	1117 ± 33	687 ± 26	48.18 ± 0.32	3.76 ± 0.09	2.33 ± 0.07	1.43 ± 0.05
Ge-Al2O3	Total	120	5.0×10^6	-10	-10	31074 ± 176	6008 ± 78	4075 ± 64	1933 ± 44	51.79 ± 0.29	10.01 ± 0.13	6.79 ± 0.11	3.22 ± 0.07
Simulation	Detector	Num. of Det.	Initial Neutrons	Thresh. (keV)	Coinc. Thresh. (keV)	Events Total	Events Threshold	Events Uncoinc	Events Coinc	Rate per Detector Total	Rate per Detector Threshold	Rate per Detector Uncoinc	Rate per Detector Coinc
Ge-LiF	Ge	96	5.0×10^6	30	30	23351 ± 153	1817 ± 43	1113 ± 33	704 ± 27	48.65 ± 0.32	3.79 ± 0.09	2.32 ± 0.07	1.47 ± 0.06
Ge-LiF	LiF	24	5.0×10^6	30	30	6798 ± 82	3190 ± 56	2389 ± 49	801 ± 28	56.65 ± 0.69	26.58 ± 0.47	19.91 ± 0.41	6.68 ± 0.24
Ge-LiF	Top+Bottom	24	5.0×10^6	30	30	6798 ± 82	3190 ± 56	2389 ± 49	801 ± 28	56.65 ± 0.69	26.58 ± 0.47	19.91 ± 0.41	6.68 ± 0.24
Ge-LiF	Middle	96	5.0×10^6	30	30	23351 ± 153	1817 ± 43	1113 ± 33	704 ± 27	48.65 ± 0.32	3.79 ± 0.09	2.32 ± 0.07	1.47 ± 0.06
Ge-LiF	Total	120	5.0×10^6	-10	-10	30149 ± 174	5007 ± 71	3502 ± 59	1505 ± 39	50.25 ± 0.29	8.34 ± 0.12	5.84 ± 0.1	2.51 ± 0.06

TABLE VI: Same as Tab. V, but with all thresholds set to 30 keV. Rise in threshold means relatively more neutrons are seen in the light targets like Al_2O_3 and LiF than in Ge, because of kinematics.

Simulation	Detector	Num. of Det.	Initial Neutrons	Thresh. (keV)	Coinc. Thresh. (keV)	Events Total	Events Threshold	Events Uncoinc	Events Coinc	Rate per Detector Total	Rate per Detector Threshold	Rate per Detector Uncoinc	Rate per Detector Coinc
Ge	Ge	120	5.0×10^6	30	10	28738 ± 170	2382 ± 49	1129 ± 34	1253 ± 35	47.9 ± 0.28	3.97 ± 0.08	1.88 ± 0.06	2.09 ± 0.06
Ge	Top+Bottom	24	5.0×10^6	30	10	5763 ± 76	487 ± 22	284 ± 17	203 ± 14	48.02 ± 0.63	4.06 ± 0.18	2.37 ± 0.14	1.69 ± 0.12
Ge	Middle	96	5.0×10^6	30	10	22975 ± 152	1895 ± 44	845 ± 29	1050 ± 32	47.86 ± 0.32	3.95 ± 0.09	1.76 ± 0.06	2.19 ± 0.07
Ge	Total	120	5.0×10^6	-10	-10	28738 ± 170	2382 ± 49	1129 ± 34	1253 ± 35	47.9 ± 0.28	3.97 ± 0.08	1.88 ± 0.06	2.09 ± 0.06
Simulation	Detector	Num. of Det.	Initial Neutrons	Thresh. (keV)	Coinc. Thresh. (keV)	Events Total	Events Threshold	Events Uncoinc	Events Coinc	Rate per Detector Total	Rate per Detector Threshold	Rate per Detector Uncoinc	Rate per Detector Coinc
Ge-Si	Ge	96	5.0×10^6	30	10	23588 ± 154	1961 ± 44	822 ± 29	1139 ± 34	49.14 ± 0.32	4.09 ± 0.09	1.71 ± 0.06	2.37 ± 0.07
Ge-Si	Si	24	5.0×10^6	30	10	4143 ± 64	1710 ± 41	876 ± 30	834 ± 29	34.52 ± 0.54	14.25 ± 0.34	7.3 ± 0.25	6.95 ± 0.24
Ge-Si	Top+Bottom	24	5.0×10^6	30	10	4143 ± 64	1710 ± 41	876 ± 30	834 ± 29	34.52 ± 0.54	14.25 ± 0.34	7.3 ± 0.25	6.95 ± 0.24
Ge-Si	Middle	96	5.0×10^6	30	10	23588 ± 154	1961 ± 44	822 ± 29	1139 ± 34	49.14 ± 0.32	4.09 ± 0.09	1.71 ± 0.06	2.37 ± 0.07
Ge-Si	Total	120	5.0×10^6	-10	-10	27731 ± 167	3671 ± 61	1698 ± 41	1973 ± 44	46.22 ± 0.28	6.12 ± 0.1	2.83 ± 0.07	3.29 ± 0.07
Simulation	Detector	Num. of Det.	Initial Neutrons	Thresh. (keV)	Coinc. Thresh. (keV)	Events Total	Events Threshold	Events Uncoinc	Events Coinc	Rate per Detector Total	Rate per Detector Threshold	Rate per Detector Uncoinc	Rate per Detector Coinc
Ge-Al2O3	Ge	96	5.0×10^6	30	10	23125 ± 152	1804 ± 42	699 ± 26	1105 ± 33	48.18 ± 0.32	3.76 ± 0.09	1.46 ± 0.06	2.3 ± 0.07
Ge-Al2O3	Al2O3	24	5.0×10^6	30	10	7949 ± 89	4204 ± 65	2065 ± 45	2139 ± 46	66.24 ± 0.74	35.03 ± 0.54	17.21 ± 0.38	17.82 ± 0.39
Ge-Al2O3	Top+Bottom	24	5.0×10^6	30	10	7949 ± 89	4204 ± 65	2065 ± 45	2139 ± 46	66.24 ± 0.74	35.03 ± 0.54	17.21 ± 0.38	17.82 ± 0.39
Ge-Al2O3	Middle	96	5.0×10^6	30	10	23125 ± 152	1804 ± 42	699 ± 26	1105 ± 33	48.18 ± 0.32	3.76 ± 0.09	1.46 ± 0.06	2.3 ± 0.07
Ge-Al2O3	Total	120	5.0×10^6	-10	-10	31074 ± 176	6008 ± 78	2764 ± 53	3244 ± 57	51.79 ± 0.29	10.01 ± 0.13	4.61 ± 0.09	5.41 ± 0.09
Simulation	Detector	Num. of Det.	Initial Neutrons	Thresh. (keV)	Coinc. Thresh. (keV)	Events Total	Events Threshold	Events Uncoinc	Events Coinc	Rate per Detector Total	Rate per Detector Threshold	Rate per Detector Uncoinc	Rate per Detector Coinc
Ge-LiF	Ge	96	5.0×10^6	30	10	23351 ± 153	1817 ± 43	714 ± 27	1103 ± 33	48.65 ± 0.32	3.79 ± 0.09	1.49 ± 0.06	2.3 ± 0.07
Ge-LiF	LiF	24	5.0×10^6	30	10	6798 ± 82	3190 ± 56	1713 ± 41	1477 ± 38	56.65 ± 0.69	26.58 ± 0.47	14.28 ± 0.34	12.31 ± 0.32
Ge-LiF	Top+Bottom	24	5.0×10^6	30	10	6798 ± 82	3190 ± 56	1713 ± 41	1477 ± 38	56.65 ± 0.69	26.58 ± 0.47	14.28 ± 0.34	12.31 ± 0.32
Ge-LiF	Middle	96	5.0×10^6	30	10	23351 ± 153	1817 ± 43	714 ± 27	1103 ± 33	48.65 ± 0.32	3.79 ± 0.09	1.49 ± 0.06	2.3 ± 0.07
Ge-LiF	Total	120	5.0×10^6	-10	-10	30149 ± 174	5007 ± 71	2427 ± 49	2580 ± 51	50.25 ± 0.29	8.34 ± 0.12	4.04 ± 0.08	4.3 ± 0.08

TABLE VII: Same as Tab. V, but with all discrimination thresholds set to 30 keV and all coincidence thresholds set to 10 keV.

Simulation	Detector	Num. of Det.	Initial Neutrons	Thresh. (keV)	Coinc. Thresh. (keV)	Events Total	Events Threshold	Events Uncoinc	Events Coinc	Rate per Detector Total	Rate per Detector Threshold	Rate per Detector Uncoinc	Rate per Detector Coinc
Ge	Ge	120	5.0×10^6	30	30	28738 ± 170	2382 ± 49	1818 ± 43	564 ± 24	47.9 ± 0.28	3.97 ± 0.08	3.03 ± 0.07	0.94 ± 0.04
Ge	Top+Bottom	24	5.0×10^6	30	30	5763 ± 76	487 ± 22	405 ± 20	82 ± 9	48.02 ± 0.63	4.06 ± 0.18	3.38 ± 0.17	0.68 ± 0.08
Ge	Middle	96	5.0×10^6	30	30	22975 ± 152	1895 ± 44	1413 ± 38	482 ± 22	47.86 ± 0.32	3.95 ± 0.09	2.94 ± 0.08	1 ± 0.05
Ge	Total	120	5.0×10^6	-10	-10	28738 ± 170	2382 ± 49	1818 ± 43	564 ± 24	47.9 ± 0.28	3.97 ± 0.08	3.03 ± 0.07	0.94 ± 0.04
Simulation	Detector	Num. of Det.	Initial Neutrons	Thresh. (keV)	Coinc. Thresh. (keV)	Events Total	Events Threshold	Events Uncoinc	Events Coinc	Rate per Detector Total	Rate per Detector Threshold	Rate per Detector Uncoinc	Rate per Detector Coinc
Ge-Si	Ge	96	5.0×10^6	30	30	23588 ± 154	1961 ± 44	1324 ± 36	637 ± 25	49.14 ± 0.32	4.09 ± 0.09	2.76 ± 0.08	1.33 ± 0.05
Ge-Si	Si	24	5.0×10^6	30	30	4143 ± 64	1710 ± 41	1323 ± 36	387 ± 20	34.52 ± 0.54	14.25 ± 0.34	11.02 ± 0.3	3.22 ± 0.16
Ge-Si	Top+Bottom	24	5.0×10^6	30	30	4143 ± 64	1710 ± 41	1323 ± 36	387 ± 20	34.52 ± 0.54	14.25 ± 0.34	11.02 ± 0.3	3.22 ± 0.16
Ge-Si	Middle	96	5.0×10^6	30	30	23588 ± 154	1961 ± 44	1324 ± 36	637 ± 25	49.14 ± 0.32	4.09 ± 0.09	2.76 ± 0.08	1.33 ± 0.05
Ge-Si	Total	120	5.0×10^6	-10	-10	27731 ± 167	3671 ± 61	2647 ± 51	1024 ± 32	46.22 ± 0.28	6.12 ± 0.1	4.41 ± 0.09	1.71 ± 0.05
Simulation	Detector	Num. of Det.	Initial Neutrons	Thresh. (keV)	Coinc. Thresh. (keV)	Events Total	Events Threshold	Events Uncoinc	Events Coinc	Rate per Detector Total	Rate per Detector Threshold	Rate per Detector Uncoinc	Rate per Detector Coinc
Ge-Al2O3	Ge	96	5.0×10^6	30	30	23125 ± 152	1804 ± 42	1267 ± 36	537 ± 23	48.18 ± 0.32	3.76 ± 0.09	2.64 ± 0.07	1.12 ± 0.05
Ge-Al2O3	Al2O3	24	5.0×10^6	100	100	7949 ± 89	1585 ± 40	1303 ± 36	282 ± 17	66.24 ± 0.74	13.21 ± 0.33	10.86 ± 0.3	2.35 ± 0.14
Ge-Al2O3	Top+Bottom	24	5.0×10^6	100	100	7949 ± 89	1585 ± 40	1303 ± 36	282 ± 17	66.24 ± 0.74	13.21 ± 0.33	10.86 ± 0.3	2.35 ± 0.14
Ge-Al2O3	Middle	96	5.0×10^6	30	30	23125 ± 152	1804 ± 42	1267 ± 36	537 ± 23	48.18 ± 0.32	3.76 ± 0.09	2.64 ± 0.07	1.12 ± 0.05
Ge-Al2O3	Total	120	5.0×10^6	-10	-10	31074 ± 176	3389 ± 58	2570 ± 51	819 ± 29	51.79 ± 0.29	5.65 ± 0.1	4.28 ± 0.08	1.36 ± 0.05
Simulation	Detector	Num. of Det.	Initial Neutrons	Thresh. (keV)	Coinc. Thresh. (keV)	Events Total	Events Threshold	Events Uncoinc	Events Coinc	Rate per Detector Total	Rate per Detector Threshold	Rate per Detector Uncoinc	Rate per Detector Coinc
Ge-LiF	Ge	96	5.0×10^6	30	30	23351 ± 153	1817 ± 43	1241 ± 35	576 ± 24	48.65 ± 0.32	3.79 ± 0.09	2.59 ± 0.07	1.2 ± 0.05
Ge-LiF	LiF	24	5.0×10^6	100	100	6798 ± 82	1313 ± 36	1076 ± 33	237 ± 15	56.65 ± 0.69	10.94 ± 0.3	8.97 ± 0.27	1.97 ± 0.13
Ge-LiF	Top+Bottom	24	5.0×10^6	100	100	6798 ± 82	1313 ± 36	1076 ± 33	237 ± 15	56.65 ± 0.69	10.94 ± 0.3	8.97 ± 0.27	1.97 ± 0.13
Ge-LiF	Middle	96	5.0×10^6	30	30	23351 ± 153	1817 ± 43	1241 ± 35	576 ± 24	48.65 ± 0.32	3.79 ± 0.09	2.59 ± 0.07	1.2 ± 0.05
Ge-LiF	Total	120	5.0×10^6	-10	-10	30149 ± 174	3130 ± 56	2317 ± 48	813 ± 29	50.25 ± 0.29	5.22 ± 0.09	3.86 ± 0.08	1.36 ± 0.05

TABLE VIII: Same as Tab. V, but with discrimination and coincidence thresholds for Ge and Si set to 30 keV, and those for Al_2O_3 and LiF set to 100 keV.

Top+Bottom Detector	Threshold (keV)	Threshold Coincident (keV)	Rate Total (Ge)	Rate Threshold (Ge)	Rate Uncoinc (Ge)	Rate Coinc (Ge)	Mass Rate Threshold (Ge)
Ge	10	10	1 ± 0.02	1 ± 0.03	1 ± 0.04	1 ± 0.05	1 ± 0.03
Si	10	10	0.72 ± 0.02	1.45 ± 0.04	1.36 ± 0.05	1.56 ± 0.06	3.35 ± 0.09
Al2O3	10	10	1.38 ± 0.02	3.04 ± 0.07	2.75 ± 0.08	3.39 ± 0.11	4.02 ± 0.09
LiF	10	10	1.18 ± 0.02	2.43 ± 0.06	2.44 ± 0.08	2.42 ± 0.08	4.96 ± 0.11
Top+Bottom Detector	Threshold (keV)	Threshold Coincident (keV)	Rate Total (Ge)	Rate Threshold (Ge)	Rate Uncoinc (Ge)	Rate Coinc (Ge)	Mass Rate Threshold (Ge)
Ge	10	5	1 ± 0.02	1 ± 0.03	1 ± 0.05	1 ± 0.04	1 ± 0.03
Si	10	5	0.72 ± 0.02	1.45 ± 0.04	1.35 ± 0.05	1.55 ± 0.05	3.35 ± 0.09
Al2O3	40	1	1.38 ± 0.02	1.8 ± 0.04	1.63 ± 0.06	1.94 ± 0.06	2.38 ± 0.06
LiF	40	1	1.18 ± 0.02	1.36 ± 0.04	1.29 ± 0.05	1.42 ± 0.05	2.77 ± 0.07

TABLE IX: Simulation numbers relative to Ge (Cross_Analysis_EDII.java — Reduced_Neutron_Analysis.tex); ie hits in top and bottom detector (per detector) divided by hits in Ge top and bottom detectors. Numbers calculated from Tab. V

Setup	Detector Type	Number of Detect.	Thresh. (keV)	Thresh. Coinc. (keV)	Rate Total all Det	Rate Threshold all Det	Rate Uncoinc all Det	Rate Coinc all Det	Rate Threshold per Det	Rate Uncoinc per Det	Rate Coinc per Det
Ge	Ge	120	10	10	5748 ± 34	2008 ± 20	886 ± 13	1121 ± 15	16.73 ± 0.17	7.39 ± 0.11	9.34 ± 0.12
Ge-Si	Ge	96	10	10	4718 ± 31	1623 ± 18	622 ± 11	1001 ± 14	16.91 ± 0.19	6.48 ± 0.12	10.42 ± 0.15
Ge-Si	Si	24	10	10	829 ± 13	583 ± 11	301 ± 8	282 ± 8	24.28 ± 0.45	12.53 ± 0.32	11.75 ± 0.31
Ge-Al2O3	Ge	96	10	10	4625 ± 30	1544 ± 18	519 ± 10	1025 ± 14	16.08 ± 0.18	5.4 ± 0.11	10.68 ± 0.15
Ge-Al2O3	Al2O3	24	10	10	1590 ± 18	1218 ± 16	606 ± 11	612 ± 11	50.73 ± 0.65	25.24 ± 0.46	25.49 ± 0.46
Ge-LiF	Ge	96	10	10	4670 ± 31	1497 ± 17	555 ± 11	942 ± 14	15.59 ± 0.18	5.78 ± 0.11	9.81 ± 0.14
Ge-LiF	LiF	24	10	10	1360 ± 16	976 ± 14	539 ± 10	438 ± 9	40.68 ± 0.58	22.44 ± 0.43	18.23 ± 0.39
Setup	Detector Type	Number of Detect.	Thresh. (keV)	Thresh. Coinc. (keV)	Rate Total all Det	Rate Threshold all Det	Rate Uncoinc all Det	Rate Coinc all Det	Rate Threshold per Det	Rate Uncoinc per Det	Rate Coinc per Det
Ge	Ge	120	30	30	5748 ± 34	476 ± 10	364 ± 9	113 ± 5	3.97 ± 0.08	3.03 ± 0.07	0.94 ± 0.04
Ge-Si	Ge	96	30	30	4718 ± 31	392 ± 9	265 ± 7	127 ± 5	4.09 ± 0.09	2.76 ± 0.08	1.33 ± 0.05
Ge-Si	Si	24	30	30	829 ± 13	342 ± 8	265 ± 7	77 ± 4	14.25 ± 0.34	11.02 ± 0.3	3.22 ± 0.16
Ge-Al2O3	Ge	96	30	30	4625 ± 30	361 ± 8	223 ± 7	137 ± 5	3.76 ± 0.09	2.33 ± 0.07	1.43 ± 0.05
Ge-Al2O3	Al2O3	24	30	30	1590 ± 18	841 ± 13	592 ± 11	249 ± 7	35.03 ± 0.54	24.65 ± 0.45	10.38 ± 0.29
Ge-LiF	Ge	96	30	30	4670 ± 31	363 ± 9	223 ± 7	141 ± 5	3.79 ± 0.09	2.32 ± 0.07	1.47 ± 0.06
Ge-LiF	LiF	24	30	30	1360 ± 16	638 ± 11	478 ± 10	160 ± 6	26.58 ± 0.47	19.91 ± 0.41	6.68 ± 0.24
Setup	Detector Type	Number of Detect.	Thresh. (keV)	Thresh. Coinc. (keV)	Rate Total all Det	Rate Threshold all Det	Rate Uncoinc all Det	Rate Coinc all Det	Rate Threshold per Det	Rate Uncoinc per Det	Rate Coinc per Det
Ge	Ge	120	30	10	5748 ± 34	476 ± 10	226 ± 7	251 ± 7	3.97 ± 0.08	1.88 ± 0.06	2.09 ± 0.06
Ge-Si	Ge	96	30	10	4718 ± 31	392 ± 9	164 ± 6	228 ± 7	4.09 ± 0.09	1.71 ± 0.06	2.37 ± 0.07
Ge-Si	Si	24	30	10	829 ± 13	342 ± 8	175 ± 6	167 ± 6	14.25 ± 0.34	7.3 ± 0.25	6.95 ± 0.24
Ge-Al2O3	Ge	96	30	10	4625 ± 30	361 ± 8	140 ± 5	221 ± 7	3.76 ± 0.09	1.46 ± 0.06	2.3 ± 0.07
Ge-Al2O3	Al2O3	24	30	10	1590 ± 18	841 ± 13	413 ± 9	428 ± 9	35.03 ± 0.54	17.21 ± 0.38	17.82 ± 0.39
Ge-LiF	Ge	96	30	10	4670 ± 31	363 ± 9	143 ± 5	221 ± 7	3.79 ± 0.09	1.49 ± 0.06	2.3 ± 0.07
Ge-LiF	LiF	24	30	10	1360 ± 16	638 ± 11	343 ± 8	295 ± 8	26.58 ± 0.47	14.28 ± 0.34	12.31 ± 0.32
Setup	Detector Type	Number of Detect.	Thresh. (keV)	Thresh. Coinc. (keV)	Rate Total all Det	Rate Threshold all Det	Rate Uncoinc all Det	Rate Coinc all Det	Rate Threshold per Det	Rate Uncoinc per Det	Rate Coinc per Det
Ge	Ge	120	30	30	5748 ± 34	476 ± 10	364 ± 9	113 ± 5	3.97 ± 0.08	3.03 ± 0.07	0.94 ± 0.04
Ge-Si	Ge	96	30	30	4718 ± 31	392 ± 9	265 ± 7	127 ± 5	4.09 ± 0.09	2.76 ± 0.08	1.33 ± 0.05
Ge-Si	Si	24	30	30	829 ± 13	342 ± 8	265 ± 7	77 ± 4	14.25 ± 0.34	11.02 ± 0.3	3.22 ± 0.16
Ge-Al2O3	Ge	96	30	30	4625 ± 30	361 ± 8	253 ± 7	107 ± 5	3.76 ± 0.09	2.64 ± 0.07	1.12 ± 0.05
Ge-Al2O3	Al2O3	24	100	100	1590 ± 18	317 ± 8	261 ± 7	56 ± 3	13.21 ± 0.33	10.86 ± 0.3	2.35 ± 0.14
Ge-LiF	Ge	96	30	30	4670 ± 31	363 ± 9	248 ± 7	115 ± 5	3.79 ± 0.09	2.59 ± 0.07	1.2 ± 0.05
Ge-LiF	LiF	24	100	100	1360 ± 16	263 ± 7	215 ± 7	47 ± 3	10.94 ± 0.3	8.97 ± 0.27	1.97 ± 0.13

TABLE X: Simulation numbers normalized to incident flux of neutrons (Cross_Analysis_EDII.java — Compare_Sims.tex). Numbers are for the sum of all detectors of a given type.

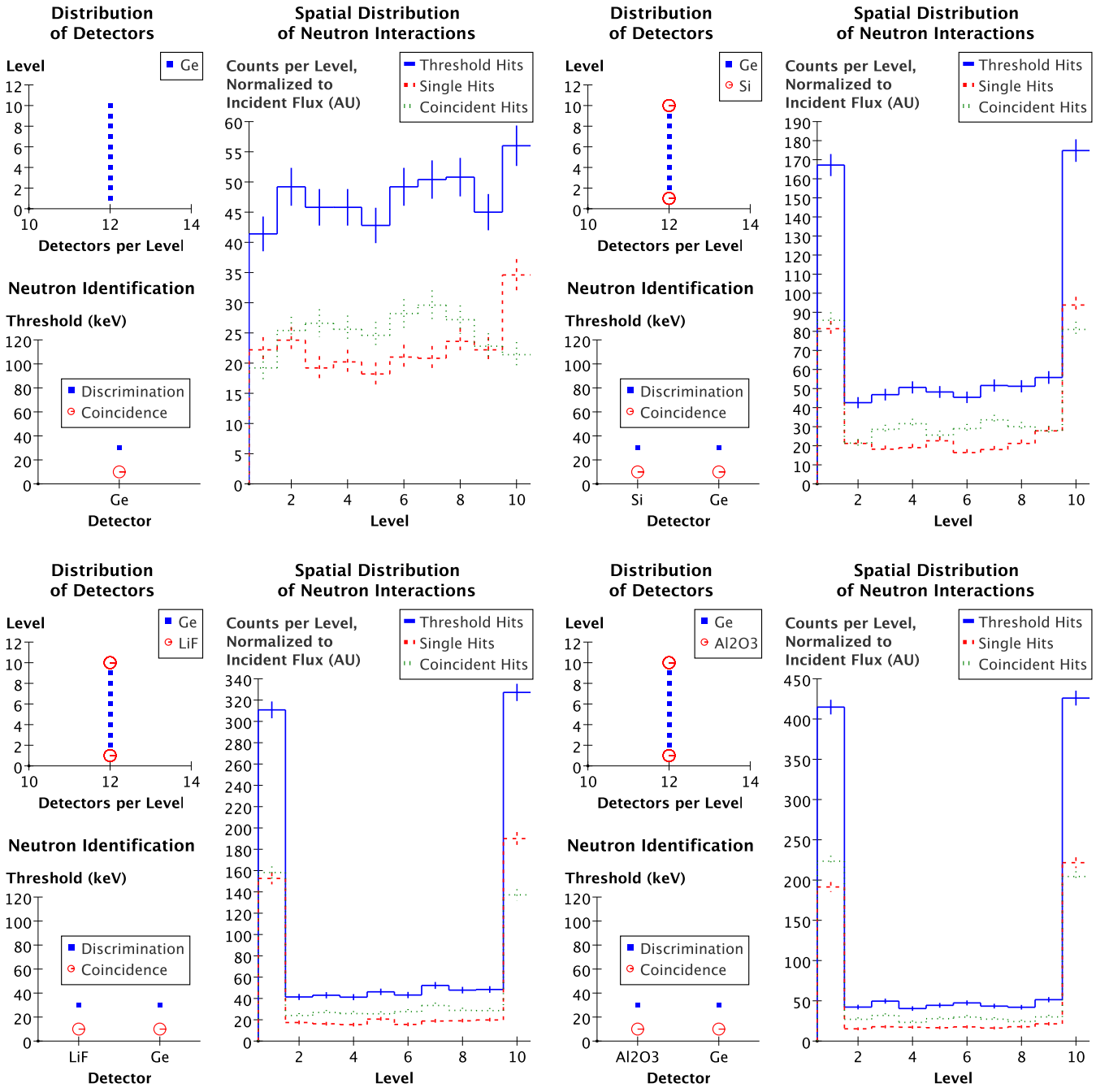

FIG. 3: Spatial distribution of neutron interactions for various detector configurations. Il all cases, single hits make up roughly one half of the totla number of interactions. Though a slight gradient is visible in the pure-Ge setup, statistically it will be hard to distinguish from the flat distribution expected for WIMPs. Replacing the top and bottom layers by Al_2O_3, or LiF or Si, results in a characteristic U shape.

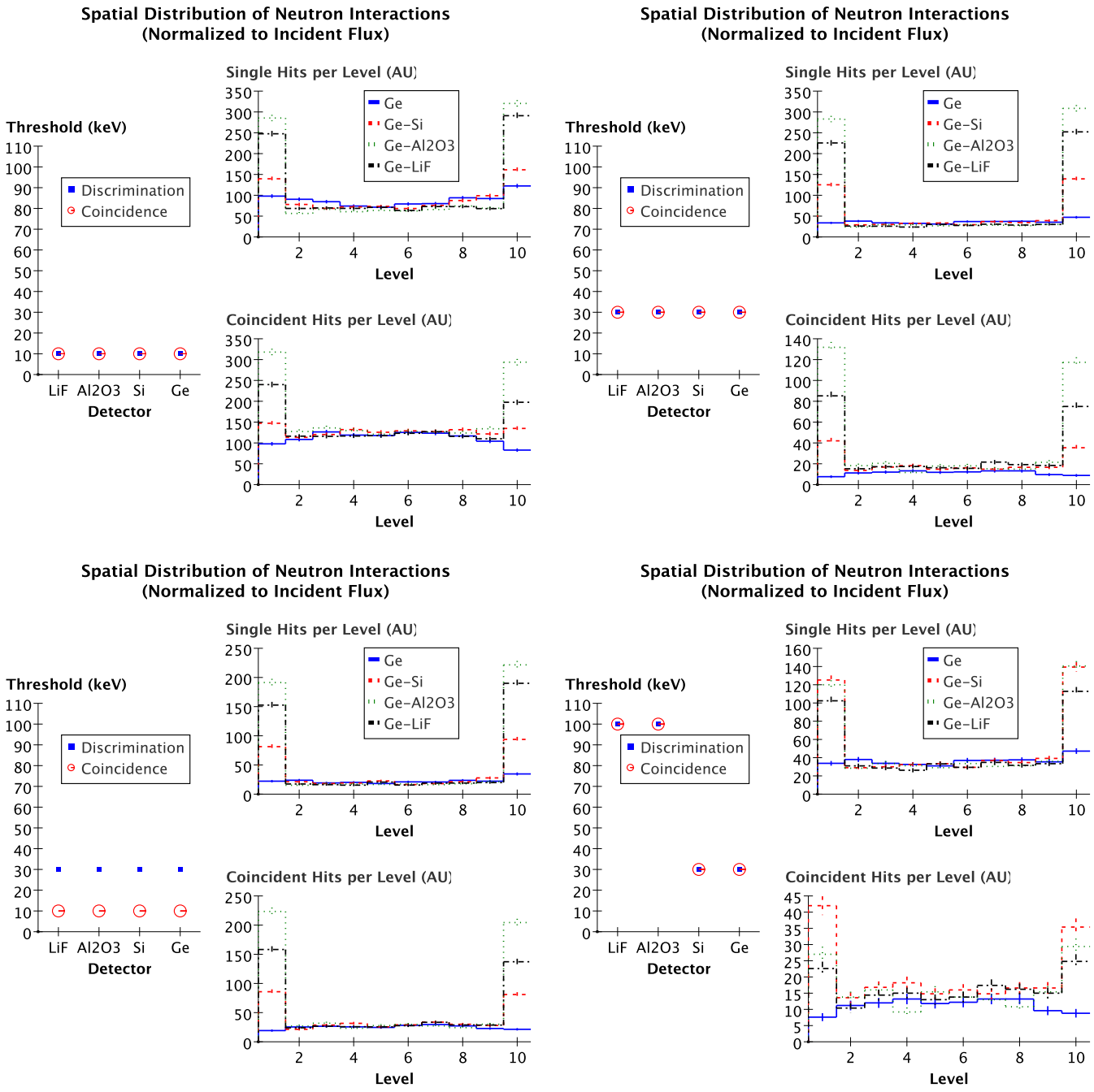

FIG. 4: Effect of detector thresholds on spatial distribution of neutron interactions.

II. WIMP INTERACTIONS

A. WIMP interactions

1. Spin-independent WIMP signal

The full spin-independent cross-section of a WIMP with mass $\mathcal{M}$ on a nucleus of mass number A and mass M, for a null momentum transfer, is [2]:

$$\sigma = \frac{4}{\pi}\mu^2 A^2 {f_{nucleon}}^2,$$

It depends mainly on one unknown parameter, $f_{nucleon}$, the effective coupling to a nucleon. The reduced mass of the system is $\mu = \frac{M\,\mathcal{M}}{M+\mathcal{M}}$. The coupling to the nucleon disappears from the ratio of cross sections of two elements; for instance with Ge:

$$\frac{\sigma}{\sigma_{\mathrm{Ge}}} = \left(\frac{\mu}{\mu_{\mathrm{Ge}}}\frac{A}{A_{\mathrm{Ge}}}\right)^2$$

For a given WIMP mass, the reduced mass increases with the target mass; if the WIMP is much heavier than the target, the reduced mass behaves like the target mass. Therefore, for WIMPs much heavier than the targets ($m \gg 100$ GeV), the ratio of cross-sections should behave like the fourth power of the ratio of atomic numbers. The cross-sections involved LiF and Al_2O_3 are thus much smaller than those in Ge; in particular for WIMPs heavier than 50 GeV, the cross-sections in LiF are less than 2 % those in Ge, and those in Al_2O_3 are less than 5 %. Therefore a WIMP is far less likely to interact in a spin-independent fashion with LiF than with Ge, and to a lesser extent with Si.

Also of interest is the interaction probability per unit length of WIMPs in matter. This is the sum of the products of cross-sections by target densities, $\Sigma\delta\times\sigma$. Since the target densities are similar in all materials studied here (Tab. I), the interaction probability is essentially dominated by the element with the largest cross-section, hence Si and Al_2O_3 have very similar values. LiF also has a longer mean free path than Si. At 50 GeV and above, interaction probabilities relative to Ge are less than 2 % for LiF and less than 6 % for Al_2O_3 and Si.

The spectrum of recoil energies left by WIMPs in a detector per unit mass and time is obtained by folding in the astrophysical parameters (the galactic velocity distribution and local mass densities of WIMPs, galactic speed of earthbound detector) with the particle physics parameters (the cross section σ and nuclear form factor F) and the elastic scattering kinematics, as described for instance in [3]. The spectrum falls off roughly like an exponential and can be expressed as:

$$\frac{dR}{dE} = \frac{1}{\sqrt{\pi}}\frac{\sigma n_0}{v_0\mu^2}F^2(E)\int_{v_{min}}^{v_{max}}\frac{f(v)}{v}dv \tag{1}$$

where $v_{min} = \sqrt{\frac{EM}{2\mu^2}}$ is the minimum WIMP speed that can deposit an energy E, and v_{max} is the maximum WIMP velocity given galactic evaporation. We assume a local dark matter density of $\rho_0 = \mathcal{M}n_0 = 0.3$ GeV/c^2, a Maxwellian WIMP galactic velocity distribution with a typical speed of 220 km/s and an escape velocity of 650 km/s, a speed of the Earth in the galaxy of 235 km/s, and a Helm type nuclear form factor with the parameters suggested in Sec. 4 of Ref. [3]. For the spin-independent interaction, the form factor describes the loss of coherence from a value of 1 at zero momentum transfer as the wavelength of the WIMP decreases compared to the typical size of the target. The form-factor thus somewhat reduces the advantage heavy targets (Ge) have over their lighter counterparts (Li and O). The slope of the spectrum depends on the WIMP mass; its shape may be hard to distinguish from that of the spectrum caused by the neutron background especially for low statistics (Fig. 4).

In Fig. 5, we numerically integrate Formula 1 over recoil energies to obtain interaction rates R^{SI} per unit mass and time in the detectors above a given threshold. Ge is the most effective WIMP detector considered except for the lightest WIMPs when LiF, Al_2O_3 and Si have a low enough threshold. For heavier WIMPs, LiF and Al_2O_3 are at least an order of magnitude less sensitive than Ge; Si is about a factor five less sensitive than Ge.

2. Spin-dependent WIMP coupling

The study of spin-dependent WIMP couplings is more complicated than the previous case, because the cross section depends on two parameters, the spin-dependent coupling to neutrons (a_n) and the spin-dependent coupling to protons

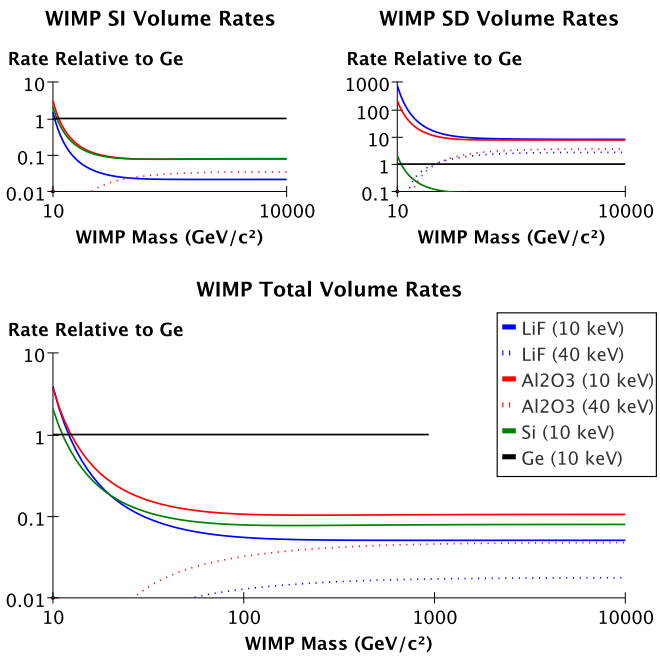

FIG. 5: Interaction rates of WIMPs per unit volume of various detectors as a function of WIMP mass, for 10 keV and 40 keV thresholds, relative to Ge (10 keV threshold). Top left: spin-independent rates. Cross section proportional to A^2 ensures Ge dominates other materials by at least an order of magnitude. Top right: spin dependent rates. LiF and Al_2O_3 dominate thanks to their abundance of spin-rich isotopes. Si is very disfavored because its rare isotope with spin has very little of it. Bottom: the spin-independent contribution dominates the combination of both interactions in typical supersymmetric scenarios.

(a_p). At zero momentum transfer, the cross section is [2] :

$$\sigma = \frac{32}{\pi} {G_F}^2 \mu^2 \left(a_p < S_p > + a_n < S_n >\right)^2 \frac{J+1}{J}$$

$< S_p >$ and $< S_n >$ are the expectations of the spin content of the proton and neutron groups in the nucleus, tabulated in Tab. XI. ^{7}Li, ^{19}F and ^{27}Al have unpaired protons, whereas ^{29}Si and ^{73}Ge have unpaired neutrons and ^{6}Li has both. We are not aware of any calculations of $< S_p >$ and $< S_n >$ for ^{6}Li and therefore assume that, as both the odd proton and the odd neutron are in p3/2 orbitals, both values are close to 1/2. The above properties give Ge and Si on the one hand (odd-neutron type nuclei), and Al_2O_3 and LiF on the other (odd-proton type nuclei), orthogonal SD reponses in terms of a_p and a_n. For a given a_n and a_p, there remains a dependence on the mass number of the target because of the reduced-mass term.

We next make the simplifying assumption, approximately true in many supersymmetric models [4], that the cross section with protons is similar to that with neutrons, and we further assume both couplings have the same sign: $a_p \approx a_n$. Because of its large reduced mass, ^{73}Ge has greater cross sections than the other isotopes except for the lightest WIMPs. However, because of the dearth of ^{73}Ge in natural Ge (Tab. II), the interaction probability is greater in LiF and Al_2O_3 than in Ge. Si has the smallest interaction probability by far, because ^{29}Si has little spin content and is rare in natural Si. We note that in the case of destructive coupling $a_n = -a_p$, the cross section on ^{6}Li vanishes; that on ^{19}F increases by 50 %; those on ^{27}Al and ^{73}Ge diminish by roughly 16 %, and those on ^{7}Li and ^{29}Si change by 2-3 %. These changes are independent of the WIMP mass.

Spin-dependent interaction rates per unit mass and time, R^{SD}, are computed as in the spin-independent case (Eq. 1), using the SD cross sections just calculated and the approximate form factor given in Eq. 4.5 of Ref. [3]. Results are in Fig. 5. In a destructive coupling scenario, the rate on LiF increases by 30-40 % depending on the WIMP mass; the rates on Al_2O_3 and Ge decrease by about 17 %; and the rate on Si increases by 3 %.

Isotope	J	$< S_p >$	$< S_n >$	Ref.
^{6}Li	1	0.5	0.5	—
^{7}Li	3/2	0.497	0.004	[5]
^{19}F	1/2	0.441	-0.109	[5]
^{27}Al	3/2	0.343	0.030	[6]
^{29}Si	1/2	-0.002	0.130	[7]
^{73}Ge	9/2	0.030	0.378	[8]

TABLE XI: Spin dependent contributions to cross-sections on various nuclei. J is the nuclear spin; $< S_p >$ and $< S_n >$ are the spin expectation values of the proton and neutron groups. Values reflect the classification of isotopes as odd proton (^{7}Li, ^{19}F and ^{27}Al), odd neutron (^{29}Si and ^{73}Ge) or both (^{6}Li). In the case of ^{6}Li, we have set both values to 0.5 since the odd neutron and the odd proton are each in p3/2 orbitals.

3. Total WIMP coupling

While recognizing that WIMPs are not necessarily MSSM — or even SUSY for that matter — we now place ourselves in a such a typical scenario to compare the SI and SD couplings. WIMPs in typical CMSSM benchmarks have spin-dependent couplings on protons about a thousand times stronger than the spin-independent couplings on protons [4]. For light isotopes such as ^{6}Li and ^{7}Li, the SI interaction can be neglected compared to the SD. For the medium-weight isotope ^{19}F, the SD interaction is slightly larger than the SI one. For ^{27}Al and ^{29}Si, the SI interaction is about an order of magnitude greater than SD; and for the heavy-weight ^{73}Ge, the SD is negligible.

In terms of interaction rates, in LiF, SD is a slightly larger contributor than SI. For Al_2O_3, SI contributes significantly more than SD. For Si and Ge, the SD contribution is negligible. Total interaction rates are compared to those of Ge in Fig. 5. Over the range of WIMP masses, the interaction rates in LiF and Al_2O_3 are less than 6 % of those in Ge. In Si however, the rates are at least 20 % those in Ge and can in fact be higher than those in Ge for light WIMPs.

The effect of destructive coupling ($a_n = -a_p$) is to increase the total rate on LiF by 20-30 % depending on the WIMP mass, and to decrease it by 3-4 % on Al_2O_3. The effect is negligeable on Si and Ge because the spin-independent interaction dominates.

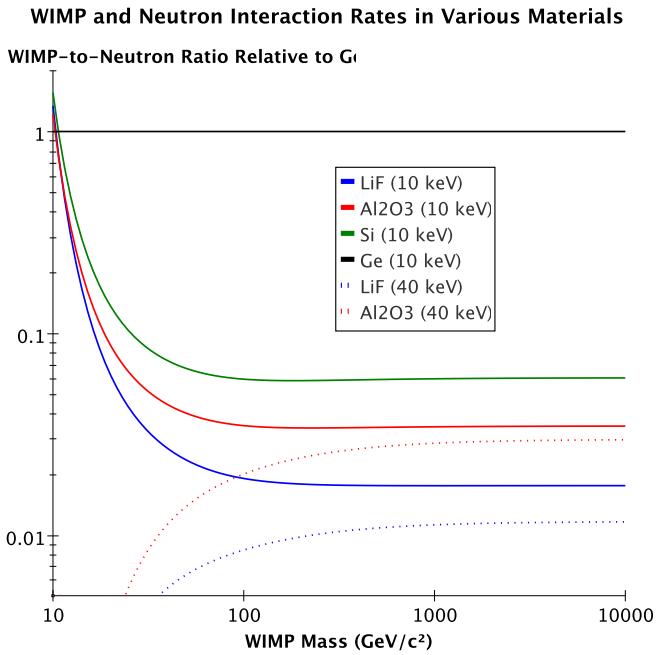

FIG. 6: Ratio of ratios.

III. NEUTRON BACKGROUND REDUCTION

Even if neutrons slip into the experiment, ways remain to identify them. This can be done by a combination of exploiting coincidences between detectors and relative rates between different types of detectors. We place ourselves in the typical supersymmetric scenario described in the previous section to set the relative SD and SI couplings. For the WIMPs, we leave as the single free parameter the SI coupling to the nucleon, or in other words the SI+SD rate on any given target. For the neutrons, since the ratios of rates in other detectors over that in Ge does not depend very much on the precise shape of the initial neutron spectrum, we leave as a free parameter the intensity of the background. We consider the case of germanium and Z, another type of detector (LiF, Al_2O_3 or Si). We assume these detectors have perfect rejection of highly ionizing particles down to threshold, and that apart from WIMPs and neutrons there are no other types of interactions that can create or mimic nuclear recoils.

A. Vetoing coincidences in a segmented detector to set an upper limit on WIMPs

The mean free path of 0.4–4 MeV neutrons in matter is of the order of a few cm; that of WIMPs is at least several light years. A closely packed, segmented, experiment with units of typical size a few cm would therefore see coincidences between detectors when a neutron passes through, but should only see single interactions from WIMPs. The simplest approach here is to use this to veto those neutrons. Simulations (Tab. X) show that in the EDELWEISS II geometry completely filled with Ge detectors of threshold 10 keV, only about 44% of all interacting neutrons are expected to escape a coincident cut. This number can be lowered to 41% by considering the top and bottom Ge layers just as a veto around the middle detectors, though this comes with a loss of 20% of fiducial volume for WIMPs. Replacing the top and bottom layers of detectors by Si, Al_2O_3 and LiF, the ratio of uncoincident to coincident neutrons in the middle Ge layers falls to respectively 38%, 34% and 37%.

In practice, sacrificing 20% of the fiducial volume means that reaching a 23% better identification of neutrons is more difficult from a statistical standpoint. We consider the scenario were the goal is to establish an upper limit on WIMPs, and all events seen in the detectors are prudently considered WIMPs. We compare two experimental configurations of EDELWEISS II type, both exposed for a duration T. In the first, all 120 detectors are Ge, and the total exposure of Ge is MT. The number of uncoincident events is:

$$n^{single}{}_{Ge} = n^{neutron\ single} + n^{\chi} = \mathcal{P}\left(MT(R^{n\ single}{}_{Ge} + R^{\chi})\right)$$

where $\mathcal{P}(x)$ is a realization of a Poisson distribution of expectation x. In the second configuration, the 96 detectors in the middle are Ge with an exposure of $0.8MT$, and the 24 top and bottom level detectors, called Z below, are Ge or Al_2O_3 or LiF or Si, and are considered a coincidence veto. After rejection of coincident events, the remaining experimental counts in Ge are in each case:

$$\begin{aligned} n^{single}{}_{Ge-Z} &= \mathcal{P}\left(0.8MT(R^{n\ single}{}_{Ge-Z} + R^{\chi})\right) \\ &= \mathcal{P}\left(0.8MT(\frac{R^{n\ single}{}_{Ge-Z}}{R^{n\ single}{}_{Ge}} R^{n\ single}{}_{Ge} + R^{\chi})\right) \end{aligned}$$

where $R^{n\ single}{}_{Ge}$ is the uncoincident neutron rate per unit mass of Ge in the 120 detector Ge setup, $R^{n\ single}{}_{Ge-Z}$ is the uncoincident neutron rate per unit mass of Ge in the Ge-Z setup, and R^{χ} is the WIMP rate per unit mass of Ge in both setups. The quantity $\frac{R^{n\ single}{}_{Ge-Z}}{R^{n\ single}{}_{Ge}}$ is determined through simulations (Tab. X); $R^{n\ single}{}_{Ge}$ and R^{χ} are unknown physical quantities. In each case the upper limit will be:

$$\begin{aligned} \left\{R^{\chi}\mathrm{Ge}\right\}^{UL} = \frac{\left\{n^{single}\right\}^{UL}}{MT} &= \frac{\left\{\mathcal{P}\left(MT\left(R^{n\ single}{}_{Ge} + R^{\chi}\right)\right)\right\}^{UL}}{MT} \\ \left\{R^{\chi}\mathrm{Ge}_{-Z}\right\}^{UL} = \frac{\left\{n^{single}{}_{Ge-Z}\right\}^{UL}}{0.8MT} &= \frac{\left\{\mathcal{P}\left(0.8MT\left(\frac{R^{n\ single}{}_{Ge-Z}}{R^{n\ single}{}_{Ge}} R^{n\ single}{}_{Ge} + R^{\chi}\right)\right)\right\}^{UL}}{0.8MT} \end{aligned}$$

If the WIMP rate is null, if the expected number of counts are oberved and if there are enough counts so that the

upper limit is approximately the number of counts:

$$\left\{R^{\chi}\mathrm{Ge}\right\}^{UL} = \frac{\left\{MT\left(R^{n\ single}{}_{Ge}\right)\right\}^{UL}}{MT} \approx R^{n\ single}{}_{Ge}$$

$$\left\{R^{\chi}\mathrm{Ge}{-}Z\right\}^{UL} = \frac{\left\{0.8MT\left(\frac{R^{n\ single}{}_{Ge-Z}}{R^{n\ single}{}_{Ge}}R^{n\ single}{}_{Ge}\right)\right\}^{UL}}{0.8MT} \approx \frac{R^{n\ single}{}_{Ge-Z}}{R^{n\ single}{}_{Ge}}R^{n\ single}{}_{Ge}$$

Figure 7 shows random generations of $\frac{\left\{R^{\chi}{}_{Ge-Z}\right\}^{UL}}{\left\{R^{\chi}{}_{Ge}\right\}^{UL}}$ as a function of $R^{n\ single}{}_{Ge}$ for the four configurations considered, assuming a null WIMP rate $R^{\chi}=0$. For each value of $R^{n\ single}{}_{Ge}$, a thousand realizations are drawn following a Poisson law of expectation $R^{n\ single}{}_{Ge}$. For each realization, the upper limit for a 90% confidence level is determined, and the plot shows the average of these upper limits as a function of $R^{n\ single}{}_{Ge}$. In the case where neither WIMPs nor uncoincident neutrons are observed, the Poisson upper limit on the observed counts will be 2.31 (for a 90 % confidence level) and sacrificing any Ge detectors to make place for Si (or Al_2O_3 or LiF) is marginally detrimental to the upper limit on the WIMP rate since $\frac{2.31}{MT} < \frac{2.31}{0.8MT} = 1.25 \times \frac{2.31}{MT}$. Indeed in any case where there are no neutrons, and hence no coincidences to exploit, reducing the Ge exposure in favor of some other detector type will always deteriorate the upper limit since the relative statistical error decreases as exposure increases. When there are enough neutrons, the ratio tends towards the ratio of single rates, $\frac{R^{n\ single}{}_{Ge-Z}}{R^{n\ single}{}_{Ge}}$. The break-even point is attained fairly quickly, after only 2–3 single events in Ge.

We note that from a standpoint of neutron coincidences, the EDELWEISS II setup is not optimized. Detectors have a characteristic length of 7 cm, comparable to the mean free path of neutrons (Fig. IV), and they are arranged in a fairly compact honeycomb geometry, twelve to a layer. However, it is not possible to use the outer detectors on each layer as a veto because the fiducial volume would suffer significantly: there would be three inner fiducial detectors compared to nine outer ones, ie a fiducial fraction of 1/4. In a future, larger experiment, one could consider adding some rings of detectors around the current twelve. The nth ring of detectors would have $3(2n-1)$ units; the total number of detectors in rings 1 to n would be $3n^2$, and the fiducial volume would be $(1-1/n)^2$. This increases steadily, reaching 56% for four layers.

B. Using coincidences and multiple targets to subtract neutron background

1. *Subtraction based on coincidences*

Rather than merely vetoing coincident events, we can use the number of coincident events to get an idea of how many uncoincident neutrons there are. In other words, given a number of coincidences, that can only be due to neutrons, and given a number of uncoincident events, due to neutrons and/or WIMPs, what is the rate of WIMPs and the error on it ? To start, we assume an all-Ge setup. The number of uncoincident events and coincident events are respectively:

$$n^{single}{}_{Ge} = n^{neutron\ single} + n^{\chi} = \mathcal{P}\left(MT(R^{n\ single}{}_{Ge} + R^{\chi}_{Ge})\right)$$
$$n^{coinc}{}_{Ge} = n^{neutron\ coinc} = \mathcal{P}\left(MTR^{n\ coinc}{}_{Ge}\right)$$

It follows from these two equations that the estimator of the WIMP rate in Ge is:

$$R^{\chi}{}_{Ge} = \frac{1}{MT}\left\{n^{single}{}_{Ge} - \frac{R^{n\ single}{}_{Ge}}{R^{n\ coinc}{}_{Ge}}n^{coinc}{}_{Ge}\right\}$$

Calculating a value for the WIMP rate is easy with this formula; error bars are more complicated because the weighted difference of two Poisson distributions is involved. If both the observed number of events $n^{single}{}_{Ge}$ and $n^{coinc}{}_{Ge}$ are large and therefore behave like normal variables, with values equal to their variance, then the standard deviation is easily interpreted in terms of confidence intervals:

$$R^{\chi}{}_{Ge} = \frac{1}{MT}\left\{n^{single}{}_{Ge} - \frac{R^{n\ single}{}_{Ge}}{R^{n\ coinc}{}_{Ge}}n^{coinc}{}_{Ge}\right\} \pm \frac{1}{MT}\sqrt{n^{single}{}_{Ge} + \left(\frac{R^{n\ single}{}_{Ge}}{R^{n\ coinc}{}_{Ge}}\right)^2 n^{coinc}{}_{Ge}}$$

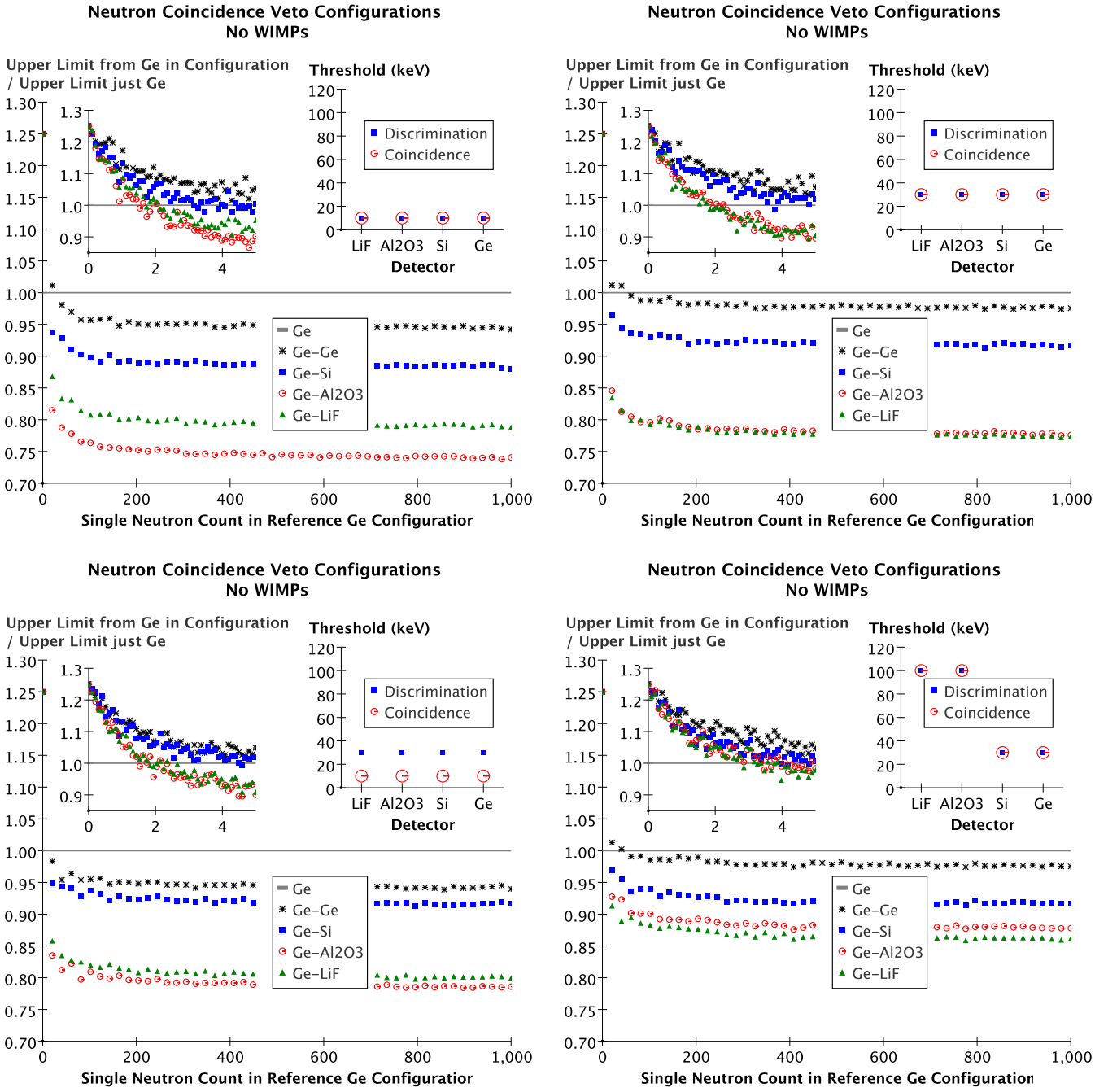

FIG. 7: Simulations showing effect of vetoing the neutron background on the upper limit that can be placed assuming a null WIMP signal. Each figure is for a different set of detector thresholds. The reference scenario is that all detectors are Ge; in this case, only 44% of interactions from neutrons are singles (in the case where all thresholds are 10 keV). Using the top and bottom layers of detectors as neutron coincidence vetos yields a relative gain in the upper limit of 5% given sufficient statistics. Replacing top and bottom layers by Si, LiF or Al_2O_3 yields an improvement in the upper limit on the WIMP rate of up to the ratio of single rates, $\frac{R^{n\ single}_{Ge-Z}}{R^{n\ single}_{Ge}}$ (about 25 % for Al_2O_3, 20 % for LiF and 10 % for Si). Sacrificing 20% of Ge fiducial volume costs at most 25% of the limit, however, the break-even point is reached quickly, after only 2 single neutrons in Ge for most Ge-Al_2O_3 scenarios.

If the expected number of events is seen, the statistical error becomes:

$$\sigma_{Ge} = \sqrt{\frac{1}{MT}\left[{R^{\chi}}_{Ge} + {R^{n\ single}}_{Ge}\left(1 + \frac{{R^{n\ single}}_{Ge}}{{R^{n\ coinc}}_{Ge}}\right)\right]} \tag{2}$$

We can carry out the same reasoning in a Ge-Z setup. The number of uncoincident and coincident events in the middle layers of Ge is:

$$\begin{aligned} {n^{single}}_{Ge-Z} &= n^{neutron\ single} + n^{\chi} = \mathcal{P}\left(0.8MT({R^{n\ single}}_{Ge-Z} + R^{\chi}_{Ge})\right) \\ {n^{coinc}}_{Ge-Z} &= n^{neutron\ coinc} = \mathcal{P}\left(0.8MT{R^{n\ coinc}}_{Ge-Z}\right) \end{aligned}$$

The estimator of the WIMP rate in Ge is now:

$${R^{\chi}}_{Ge} = \frac{1}{0.8MT}\left\{{n^{single}}_{Ge-Z} - \frac{{R^{n\ single}}_{Ge-Z}}{{R^{n\ coinc}}_{Ge-Z}}{n^{coinc}}_{Ge-Z}\right\}$$

If the expected number of events is observed and is large, the statistical error becomes:

$$\sigma_{\mathrm{Ge}-Z} = \sqrt{\frac{1}{0.8MT}\left[{R^{\chi}}_{Ge} + {R^{n\ single}}_{Ge}\frac{{R^{n\ single}}_{Ge-Z}}{{R^{n\ single}}_{Ge}}\left(1 + \frac{{R^{n\ single}}_{Ge-Z}}{{R^{n\ coinc}}_{Ge-Z}}\right)\right]} \tag{3}$$

The ratio of statistical errors from Eq. 2 and 3 is therefore:

$$\frac{\sigma_{Ge-Z}}{\sigma_{Ge}} = \frac{1}{\sqrt{0.8}}\sqrt{\frac{1 + \frac{{R^{n\ single}}_{Ge}}{{R^{\chi}}_{Ge}}\frac{{R^{n\ single}}_{Ge-Z}}{{R^{n\ single}}_{Ge}}\left(1 + \frac{{R^{n\ single}}_{Ge-Z}}{{R^{n\ coinc}}_{Ge-Z}}\right)}{1 + \frac{{R^{n\ single}}_{Ge}}{{R^{\chi}}_{Ge}}\left(1 + \frac{{R^{n\ single}}_{Ge}}{{R^{n\ coinc}}_{Ge}}\right)}}$$

$$\frac{{R^{n\ single}}_{Ge}}{{R^{\chi}}_{Ge}} \underset{\approx}{\to} 0 \quad \frac{1}{\sqrt{0.8}} > 1$$

$$\frac{{R^{n\ single}}_{Ge}}{{R^{\chi}}_{Ge}} \underset{\approx}{\to} \infty \quad \frac{1}{\sqrt{0.8}}\sqrt{\frac{\frac{{R^{n\ single}}_{Ge-Z}}{{R^{n\ single}}_{Ge}}\left(1 + \frac{{R^{n\ single}}_{Ge-Z}}{{R^{n\ coinc}}_{Ge-Z}}\right)}{\left(1 + \frac{{R^{n\ single}}_{Ge}}{{R^{n\ coinc}}_{Ge}}\right)}}$$

This ratio of errors on the WIMP rate is plotted in Fig. 8 as a function of the ratio of uncoincident-neutrons-to-WIMP rate. The ratio decreases from ≈ 1.1 (a loss, if there are far fewer neutrons that WIMPs), to ≈ 0.75 (an improvement, if there are far more neutrons than WIMPs).

2. Subtraction based on multiple target materials

A second approach is to compare the number of events in Ge to those in Z. The experimentally observed rates in Ge and Z are then the sum of the WIMP (SI and SD) and the neutron contributions :

$$\begin{aligned} n_{Ge} &= \mathcal{P}\left(0.8MT\left({R^{\chi}}_{Ge} + {R^{n}}_{Ge}\right)\right) \\ n_{Z} &= \mathcal{P}\left(0.2MT\frac{\rho_Z}{\rho_{Ge}}\left({R^{\chi}}_{Z} + {R^{n}}_{Z}\right)\right) \\ &= \mathcal{P}\left(0.2MT\frac{\rho_Z}{\rho_{Ge}}\left(\frac{{R^{\chi}}_{Z}}{{R^{\chi}}_{Ge}}{R^{\chi}}_{Ge} + \frac{{R^{n}}_{Z}}{{R^{n}}_{Ge}}{R^{n}}_{Ge}\right)\right) \end{aligned}$$

The left hand side of the equations is measured experimentally. The two fractions in the right hand side of the equations are determined in the previous section. Estimators of the WIMP and neutron rates in Ge can be extracted from the previous system of two equations, yielding:

$$\begin{aligned} {R^{\chi}}_{Ge} &= \frac{1}{1-\eta_Z}\left(\frac{n_{Ge}}{0.8MT} - \frac{{R^{n}}_{Ge}}{{R^{n}}_{Z}}\frac{n_Z}{0.2MT\frac{\rho_Z}{\rho_{Ge}}}\right) \\ {R^{n}}_{Ge} &= \frac{1}{1-\eta_Z}\left(-\eta_Z\frac{n_{Ge}}{0.8MT} + \frac{{R^{n}}_{Ge}}{{R^{\chi}}_{Z}}\frac{n_Z}{0.2MT\frac{\rho_Z}{\rho_{Ge}}}\right) \end{aligned}$$

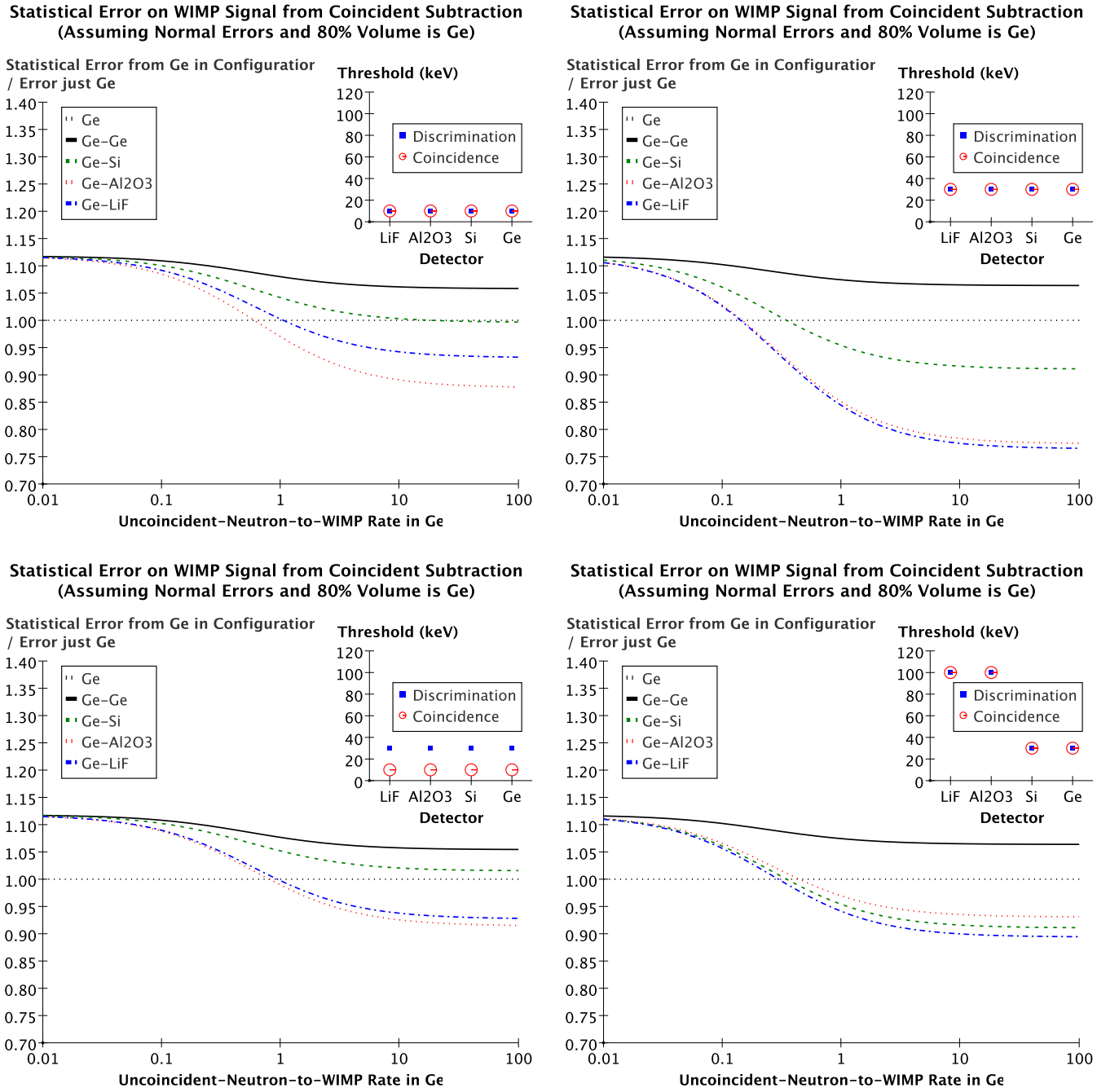

FIG. 8: Statistical error on a WIMP signal obtained by subtracting neutron background inferred from coincidences, as a function of uncoincident-neutron to WIMP rate, for various setups. Plot assumes a sufficient number of WIMPs and neutrons observed for their statistical errors to be normal. Errors are relative to those in the pure Ge setup. Each plot is for a set of thresholds. This methods allows to reduce the error on a WIMP signal by up to 25%.

where $1-\eta_Z$ is the determinant of the system and $\eta_Z = \frac{R^{\chi}{}_Z/R^{\chi}{}_{Ge}}{R^n{}_Z/R^n{}_{Ge}}$ can also be considered as the signal (WIMPs) to noise (neutrons) ratio of a Z divided by that of Ge. The ratio η is plotted as a function of the WIMP mass in Fig. 6. In the detectors we have studied, the neutron response does not depend much on the target mass number, whereas the WIMP cross-section does. Therefore, except for the lightest WIMPs, $\frac{R^{\chi}{}_Z}{R^{\chi}{}_{Ge}} \ll \frac{R^n{}_Z}{R^n{}_{Ge}} \approx 1$, and $\eta \ll 1$. This remains true even if the threshold of LiF and Al_2O_3 is 40 keV rather than 10 keV.

Assuming enough counts are observed in both types of detectors for the errors to be normal, the error on the WIMP

rate becomes:

$$\sigma_{Ge-Z} = \frac{1}{1-\eta_Z}\sqrt{\frac{{R^n}_{Ge} + {R^\chi}_{Ge}}{0.8MT} + \left(\frac{{R^n}_{Ge}}{{R^\chi}_Z}\right)^2 \frac{\frac{{R^n}_Z}{{R^n}_{Ge}}{R^n}_{Ge} + \frac{{R^\chi}_Z}{{R^\chi}_{Ge}}{R^\chi}_{Ge}}{0.2MT\frac{\rho_Z}{\rho_{Ge}}}} \tag{4}$$

The ratio of this error to that obtained by coincident subtraction in the pure Ge case (Eq. 3) is:

$$\frac{\sigma_{Ge-Z}}{\sigma_{Ge}} = \frac{1}{1-\eta_Z}\frac{1}{\sqrt{0.8}}\sqrt{\frac{1 + 4\frac{\rho_{Ge}}{\rho_Z}\frac{{R^\chi}_Z}{{R^\chi}_{Ge}} + \frac{{R^n}_{Ge}}{{R^\chi}_{Ge}}\left[1 + 4\frac{\rho_{Ge}}{\rho_Z}\frac{{R^n}_{Ge}}{{R^n}_Z}\right]}{1 + \frac{{R^{n\ single}}_{Ge}}{{R^{n\ coinc}}_{Ge}}\frac{{R^n}_{Ge}}{{R^\chi}_{Ge}}}}$$

$$\frac{{R^n}_{Ge}}{{R^\chi}_{Ge}} \overset{\approx}{\to} 0 \quad \frac{1}{1-\eta_Z}\ \frac{1}{\sqrt{0.8}}\sqrt{1 + 4\frac{\rho_{Ge}}{\rho_Z}\frac{{R^\chi}_Z}{{R^\chi}_{Ge}}} > 1$$

$$\frac{{R^n}_{Ge}}{{R^\chi}_{Ge}} \overset{\approx}{\to} \infty \quad \frac{1}{1-\eta_Z}\ \frac{1}{\sqrt{0.8}}\sqrt{\frac{{R^{n\ coinc}}_{Ge}}{{R^{n\ single}}_{Ge}}\left[1 + 4\frac{\rho_{Ge}}{\rho_Z}\frac{{R^n}_{Ge}}{{R^n}_Z}\right]}$$

3. Combining coincidences and multiple targets

Two unknowns (${R^\chi}_{Ge}$ and ${R^n}_{Ge}$), from which ${R^\chi}_Z$, ${R^{n\ coinc}}_{Ge}$ and ${R^{n\ single}}_{Ge}$ can be deduced; three measurement (${n^{single}}_{Ge}$, ${n^{coinc}}_{Ge}$ and n_Z). Each set of $({R^\chi}_{Ge}, {R^n}_{Ge})$ values generates three values $({\hat{n^{single}}}_{Ge}, {\hat{n^{coinc}}}_{Ge}, \hat{n}_Z)$. Define a distance $\Delta({R^\chi}_{Ge}, {R^n}_{Ge})$ between measurement and generated values, and minimize for $({R^\chi}_{Ge}, {R^n}_{Ge})$. A similar method appears to have been used by the CDMS experiment to analyze data coming from the shallow Stanford site [9]. This scenario and others are still under study.

4. Spatial distribution of neutrons and WIMPs

Another possibility may be to use the spatial distribution of single-neutron events and of WIMP events. In the all-Ge configuration, both distributions are roughly flat, whereas in Ge+other configurations, the neutron distribution is clearly concave whereas the WIMP one is clearly convex (Fig. 9).

---

[1] P. De Bièvre and P. D. P. Taylor. Table of the isotopic compositions of the elements. *International Journal of Mass Spectrometry and Ion Processes*, 123:149–166, 1993.

[2] Gerard Jungman, Marc Kamionkowski, and Kim Griest. Supersymmetric dark matter. *Physics Reports*, 267(5&6):195–376, March 1996.

[3] J. D. Lewin and P. F. Smith. Review of mathematics, numerical factors, and corrections for dark matter experiments based on elastic nuclear recoil. *Astroparticle Physics*, 6:87–112, 1996.

[4] John Ellis, Jonathan L. Feng, Andrew Ferstl, Konstantin T. Matchev, and Keith A Olive. Prospects for detecting supersymmetric dark matter at post-LEP benchmark points. *European Physical Journal C*, 24:311–322, 2002. astro-ph/0110225.

[5] A. F. Pacheco and D. Strottman. Nuclear-structure corrections to estimates of the spin-depdendent WIMP-nucleus cross section. *Physical Review D*, 40(6):2131–2133, September 1989.

[6] J. Engel, M. T. Ressell, I. S. Towner, and W. E. Ormand. Response of mica to weakly interacting massive particles. *Physical Review C*, 52(4):2216–2221, 1995.

[7] M. Ted Ressell, Maurice B. Aufderheide, Stewart D. Bloom, Kim Griest, Grant J. Matthews, and David A. Resler. Nuclear shell model calculations of neutralino-nucleus cross sections for ^{29}Si and ^{73}Ge. *Physical Review D*, 48(12):5519–5535, December 1993.

[8] V. I. Dimitrov, J. Engel, and S. Pittel. Scattering of weakly interacting massive particles from ^{73}Ge. *Physical Review D*, 51(2):R291–R295, January 1995.

[9] D. Abrams et al. Exclusion limits on the WIMP-nucleon cross-section from the Cryogenic Dark Matter Search. *Physical Review D*, 66:122003, 2002. http://www.arxiv.org/abs/astro-ph/0203500.

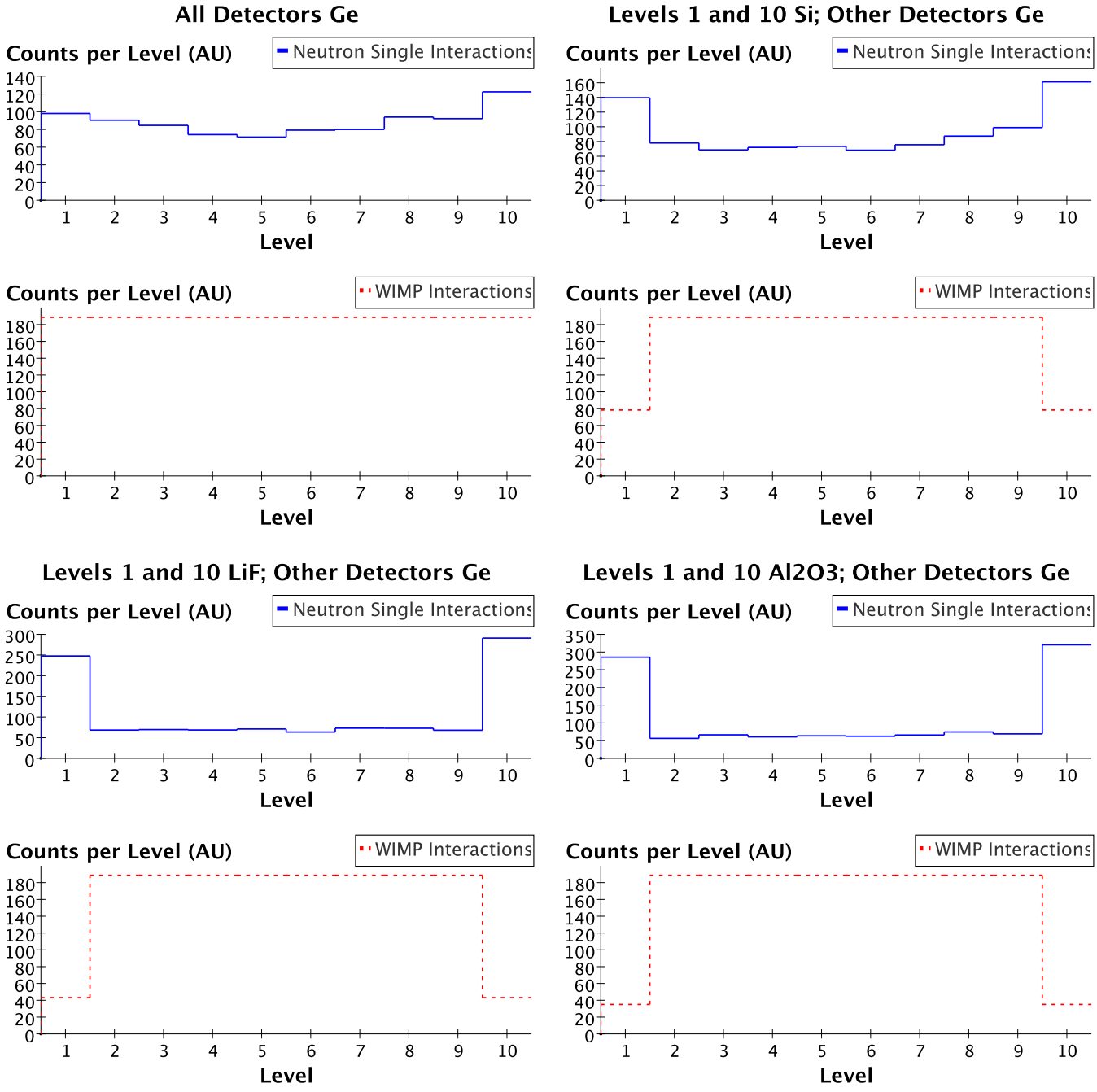

FIG. 9: Spatial distributions of single-neutron and WIMP interactions in various detector configurations. WIMPs are more easily distinguished from neutrons in the mixed configurations than in the pure-Ge one. All thresholds are set to 10 keV here.

Chapter 4

Cryogenic Scintillation

Germanium ionization-phonon cryogenic detectors are among the most sensitive for dark matter [40, 39] because of their ability to reject the dominant, highly-ionizing radioactive background. Understanding other backgrounds (e.g. from neutrons), confirming a discovery and studying various couplings will require a wider choice of target nuclei than the few semiconductors (germanium and silicon) available for the ionization-phonon technique. Moreover, the sensitivity of the ionization-phonon technique could ultimately be limited by mis-collected surface events [71], though there are many schemes to provide better identification of the surface events [61]. Scintillation-phonon detectors, in which the dominant radioactive background is rejected thanks to the simulatenous measurement of phonons and scintillation could provide a wider choice of target nuclei and do not seem to suffer from surface events [52]. Indeed, scintillation-phonon experiments using $CaWO_4$ [41, 72] are starting to obtain competitive sensitivities.

4.1 Cryogenic light detectors and scintillators

The scintillation-phonon detector is in fact made up of two calorimeters. In the principal one, a particle interacts in the absorber, creating phonons then read by an NTD or TES. This is often referred to as the phonon channel. If the absorber also happens to be a scintillator, the particle interaction creates scintillation photons that can escape the absorber and be measured in a second, smaller calorimeter, providing the light signal. Most of the energy deposited in the scintillator is converted into the phonon signal, either directly or through reabsorption of scintillation photons. A fraction of the energy deposited is converted to scintillation photons that are seen in the light detector, and a fraction of the energy is lost, for instance in the light collector surrounding the device. The typical ratio of detected to deposited energy is of the order of 1% [73]. However, based on anti-correlation in the phonon and scintillation signals, it has been argued that the fraction of energy initially converted to light is in fact much higher, up to 13% in Al_2O_3 [74].

The small amount of light seen in the light detector and the need for low rejection thresholds mean that the light detector must be optimized. The approach I followed in my third year as a postdoc at MPP in collaboration with PhD student T. Frank was to increase the light absorption of the silicon detector by using the texturing technique standard in photovoltaics [73] (Sec. 4.3A). We succeeded in increasing light absorption by a factor 1.7, in line with the effective surface area, but at the expense of a degradation in the homogeneity of detector response because of extra phonon scattering on the larger surface. More recent approaches include reducing the threshold of the light detector by using phonon-collector pads, and using silicon-on-sapphire substrates.

Establishing the ratio of detected-to-deposited energy required calibrating the light detector with direct hits from an ^{55}Fe source. In addition, this source provided the reponse function of the light detector to single particles. Comparing this response to the response to scintillation photons from $CaWO_4$ provided an estimate of the scintillation time constants of $CaWO_4$ at 20 mK. At least two time constants were found, one at 0.3 ± 0.1 ms making up 70% of the scintillation energy, and a slow one at 2.5 ± 1 ms. We note that a similar time structure has been confirmed independently

by another group in the same temperature range using a different light detector (Ir/Au TES rather than W) and other $CaWO_4$ crystals [75]. Yet another group, working with crystals at 9 K and photomultipliers at room temperature, finds a single decay time of 0.39 ± 0.02 ms [76]. It is not yet clear what explains this difference. Possible factors include actual differences in the scintillation between 9 K and 20 mK, variations between crystals, or detector-specific effects.

4.2 Cryogenic Scintillation of Sapphire

To identify cryogenic scintillators that could be employed in the future, I have started the SciCryo (Scintillation Cryogénique) project that brings together colleagues from CRESST (MPP Munich), ROSEBUD (IAS Orsay) and EDELWEISS (IPN Lyon) as well as scintillation experts (LPCML Lyon). This project is funded by the French national research agency *Agence Nationale de la Recherche* (ANR-05-BLAN-0031). Three students have made important contributions to this work: S. Chermati, during a TERE internship in 2003, M. Luca during an M2 internship and a PhD she completed under my co-supervision July 2007, and M.-A. Verdier, during an M2 internship and now a PhD, also under my co-supervision. The status of the project was reported at the LTD12 *Low Temperature Detectors* conference in Paris during the summer of 2007 (Sec. 4.4A [77]).

4.2.1 Scintillation and trace analysis

Sapphire is well-established as a cryogenic phonon-type detector [78, 51]. Moreover, low-temperature scintillation of Al_2O_3 has been reported in nominally pure and doped samples [79, 80, 74], making it feasible for a scintillation-phonon detector. We have therefore tested the X-ray luminescence of several dozen sapphire samples. All, including the nominally pure ones, show scintillation from Ti^{3+} and/or Cr^{3+}(Fig. 4.1).[1] We have carried out some tests at ≈ 10 mK to establish the ratio of detected to deposited energy; the results, along with those of some previous experiments are in Tab. 1 of Ref. [77] (Sec. 4.4A). They show that though there is a wide spread in the collected light yield of Al_2O_3, some samples scintillate at least as much as the $CaWO_4$ already used in cryogenic dark matter searches [41].

X-ray luminescence is very efficient at detecting the presence of impurities, but not at quantifying them, which would be useful to establish their optimal concentration. We have therefore considered various methods of trace analysis. Two commercial methods, laser-ablation inductively-coupled mass spectrometry (LAMS) and glow-discharge mass spectrometry (GDMS) reach sensitivities of a few parts per million (ppm). However, they are both destructive, as the laser of LAMS leaves small holes in the sample and GDMS destroys the whole sample. Moreover, neither method is sensitive to the oxydation state of the impurities. We have therefore used two optical methods. In the optical absorption method, the transmission of light at various wavelengths passing through the sample is measured; the absorption coefficient is deduced and is proportional to the concentration of optically active impurities. For the typical sample size used (a few mm), this technique is sensitive down to a few hundred ppm of Ti^{3+}as seen in Fig. 4.1.

In the fluorescence method, we directly excite a given type of impurity by illuminating it in its absorption band, and measure the luminescence. For Ti^{3+}, this is possible with an excitation at 470 nm, as long as there is no Cr^{3+} since the two absorption bands overlap. The absorption, and hence the luminescence, is proportional to the concentration of the impurity if the concentration is not too great. Various samples can be compared if they have identical geometries and surface polishing.

Absorption and fluorescence have been tested on a set of samples obtained from the Institute for Single Crystals in Kharkov. These samples have nominal titanium concentrations of 10, 50, 100, 500 and 1000 ppm respectively. Results, along with those from LAMS, are shown in Fig. 4.2. This shows that LAMS is a better estimator of titanium concentration than the nominal values. Moreover, fluorescence does indeed turn out to be more sensitive than absorption at low concentrations.

[1] As in the Tour de France, performance seems linked to doping.

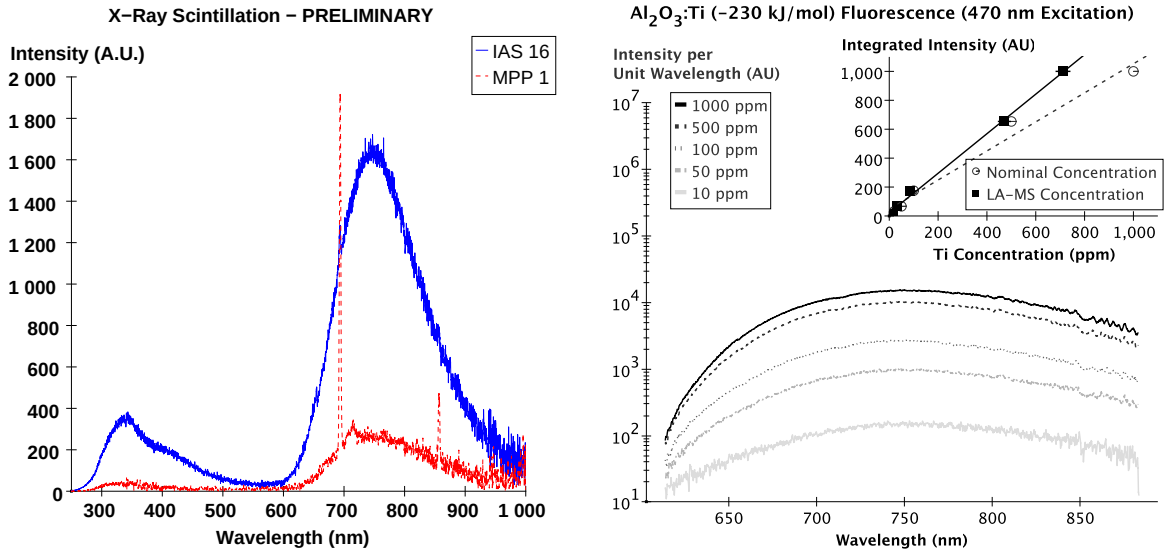

Figure 4.1: Left: X-ray scintillation spectra of nominally-pure crystals in identical conditions showing factor ≈ 6 difference in light yield. Spectra also show Ti^{3+} (750 nm band), Cr^{3+} (693 nm line) and probably colored centers (lower wavelengths). Right: Fluorescence of ISC samples used to verify Ti^{3+} content. Method is sensitive down to low concentrations and shows that laser ablation is a better indicator of concentration than nominal value is.

4.2.2 Tests from room temperature to 10 K

We have tested the ISC crystals at room temperature using an ^{241}Am α source. This required finding an appropriate light detector, sensitive to the red light coming from Ti^{3+}. Initial tests with avalanche photo-diodes were inconclusive, so we adopted a photomultiplier with a multialkili photocathode. With the α source, the PM response varies by close to a factor of six between crystals, with the most light coming at 500 ppm (Fig. 4.2). This result differs from that obtained during measurement of spectra under a strong flux of X-rays, where only a 30% variation is observed between crystals. This discrepancy is under study, and may well be due to the high dose used during the spectra measurements, of the order of 0.1 Gy per measurement. Red-sensitive photodetectors must be sensitive to smaller energy quanta than their blue-sensitive counterparts; they are therefore more sensitive to thermal noise. We are considering cooling our PMs to lower their threshold and study response from low-energy γ sources.

The ISC crystals have been cooled in an optical cryostat down to 10 K under X-ray flux. During this, we have monitored the response using the PM and/or measured the spectra. For all crystals, both methods show a roughly similar increase in light yield of just under two as the crystal is cooled (Fig. 4.2). A new optical cryostat will be commissioned at IPNL by the end of 2007; it will enable similar measurements with α and γ sources. Moreover, a series of tests is being planned with our partners at MPP and IAS to study the ISC crystals at 10 mK, with Si and Ge calorimetric light detectors.

4.2.3 A scintillation-phonon detector in EDELWEISS II

We have carried out an integration test of an IAS 50 g Al_2O_3 scintillation-phonon detector in EDELWEISS II. Performances of the detectors had already been studied by IAS at surface level [79]. Before even considering building it into the LSM cryostat, we screened the detector for radioactive background and found compatible with the strict standards of EDELWEISS II. Next, the mechanical compatibility had to be resolved; as the IAS detector is narrower and taller than standard EDELWEISS detectors, it pokes through two levels of detectors. Since the detector is optimized for

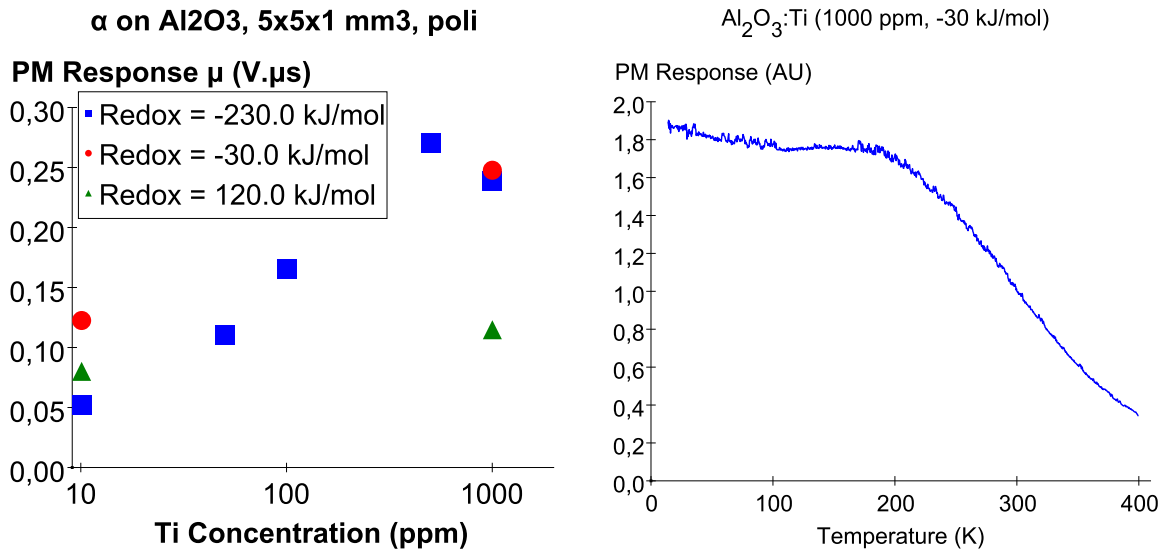

Figure 4.2: Left: PM response of ISC crystals under α particles. Spread is greater than that obtained under strong X-ray flux. Right: PM response as a crystal is cooled under X-rays.

a higher operation temperature than the standard Ge detectors, it is decoupled thermally by some NbTi washers and can be heated by a 20 kΩ resistor. From the standpoint of readout, the detector has two phonon channels but no ionization and therefore uses two EDELWEISS electronic boxes on which the ionization channel has been grounded. Moreover, the pulses are faster than the standard ones, so events are recorded at 100 kHz instead of being demodulated in the standard manner to 1 kHz; a custom off-line routine developped by J. Gascon is then used to remove the modulation. In initial runs, the phonon channel was noisy but comparable to those of the Ge detectors, whereas the scintillation channel of the very light 195 mg calorimeter suffered tremendously from microphonics. The cryostat was modified to reduce vibrations by decoupling the motors of the pulse tubes. All channels benefited from this, the phonon channel, like that of the Ge detectors reaching 3 keV FWHM of baseline noise, and the scintillation channel reaching a threshold of 70 keV ee. As there is no internal source to calibrate the light detector, its absolute performance is not known; however, based on the 1.3% light yield observed at ground-level [79] it would have an absolute threshold of 910 eV. While there remains room for improvement of the scintillation channel, it has already started to yield results during AmBe neutron calibrations. Because of its favorable elastic scattering kinematics, the Al_2O_3 detector with a 100 keV threshold sees ≈ 4 times as many neutrons as the Ge detectors with 30 keV thresholds, close to what is expected from neutrons simulations (Sec. 3.2.1). Moreover, Fig. 4.3 shows that the neutron quenching factor has been measured over the 500–1000 keV range to be 20 ± 2, in excellent agreement with the ground-level value [79].

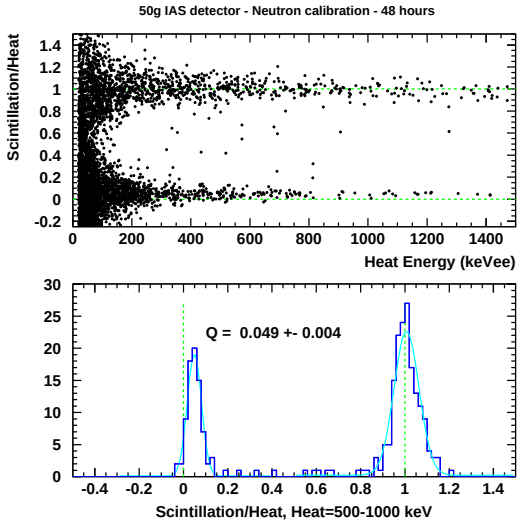

Figure 4.3: A 50 g Al_2O_3 scintillation-phonon cryogenic detector provided by IAS and tested in EDELWEISS II, here with a neutron source. Top: light yield as a function of heat signal (approximately recoil energy). Threshold is relatively high because of noisy light channel. Bottom: quenching factor averaged over the 500–1000 keV range.

4.3A Optimization of light detectors

Ref. [73].

Textured silicon calorimetric light detector

P. C. F. Di Stefano,[a] T. Frank, G. Angloher, M. Bruckmayer, C. Cozzini, D. Hauff, F. Pröbst, S. Rutzinger, W. Seidel, and L. Stodolsky
Max-Planck-Institut für Physik, Föhringer Ring 6, D-80805 Munich, Germany

J. Schmidt
Institut für Solarenergieforschung Hameln/Emmerthal, Am Ohrberg 1, D-31860 Emmerthal, Germany

(Received 15 May 2003; accepted 21 August 2003)

We apply the standard photovoltaic technique of texturing to reduce the reflectivity of silicon cryogenic calorimetric light detectors. In the case of photons with random incidence angles, absorption is compatible with the increase in surface area. For the geometrically thin detectors studied, energy resolution from athermal phonons, dominated by position dependence, is proportional to the surface-to-volume ratio. With the $CaWO_4$ scintillating crystal used as light source, the time constants of the calorimeter should be adapted to the relatively slow light-emission times. © *2003 American Institute of Physics.* [DOI: 10.1063/1.1619196]

I. INTRODUCTION

Cryogenic calorimeters, in which the phonons created by incoming particles are read out, now rival longer-established techniques of particle detection such as ionization in semiconductors and scintillation. They boast excellent thresholds and resolutions which can be enhanced by measuring athermal phonons in addition to the thermal ones. Another of their advantages, exploited by rare-event searches for which radioactive background is an issue, is the ability to distinguish between particles interacting with electrons in matter (e.g., photons and electrons) and those interacting with nuclei (e.g., neutrons and putative dark matter particles). This has been achieved mainly through a simultaneous measurement of charge in semiconducting calorimeters.[1–3] Another technique is a simultaneous measurement of scintillation, with a principal calorimeter made out of a scintillating material which emits photons read in a secondary calorimeter[4,5] (or some other light sensitive device[6]). For instance, the next phase of the Cryogenic Rare Event Search with Superconducting Thermometers (CRESST) dark-matter search will deploy up to 33 such modules with $CaWO_4$ as the main calorimeter.[7] The challenge is that the emitted light is but a small fraction of the deposited energy, and not all of it necessarily reaches the secondary calorimeter. We report on optimization of these light detectors.

In the case of main calorimeters like $CaWO_4$ emitting light in the visible spectrum, and for optical sources in general, silicon would appear well suited as an absorber for the light-detection calorimeter, because of its band gap around 1 μm (1.17 eV at mK temperatures). Moreover, Si has already been successfully used as an absorber in cryogenic calorimeters (e.g., Ref. 8). Its advantages include a high speed of sound ($\approx$5760 m/s) which gives good phonon properties, and a high melting point ($\approx$1690 K) which facilitates deposition of thin films made from materials with high melting temperatures, such as tungsten, when they are chosen as thermometers. However, polished silicon has a high visible reflectivity. A similar problem has been encountered in the field of photovoltaics, and solved by a combination of texturing the surface of the silicon and coating it with antireflective layers.[9] The texturing squares the reflectivity for normal incident photons by providing them with two chances to be absorbed. We first describe preparation of our textured light detectors before discussing experimental results obtained.

II. PREPARATION OF THE LIGHT DETECTORS

Two 4 in. diameter, 525 ± 35 μm thick, float-zone p-type silicon wafers with a resistivity of between 10 200 and 71 030 Ωm were used. Orientation of both wafers was (100) for the purpose of texturing. One side of each wafer was polished, the other lapped and etched. A natural silicon oxide layer is assumed to have been present on all Si surfaces. A 150 nm thick SiN_x layer was deposited by plasma-enhanced chemical vapor deposition through an Al mask into 5 mm diameter disks on the polished surface of one of the wafers. This wafer was then etched in a KOH-isopropanol mix at 75 °C in order to texture the exposed Si into a random pyramid structure.[10] Typical height of the pyramids is 2–5 μm, while the pyramid angle of 70.5° given by the crystalline structure of Si means that the textured surface area is about 1.74 times greater than the original, planar, surface area. The SiN_x remained unaffected by the texturing.

Samples of size 20×20 and 30×30 mm^2 were cut from both wafers. Tungsten transition-edge sensors of the type depicted in Fig. 1 were next deposited onto the samples using a standard procedure developed by the CRESST collaboration:[11] tungsten films about 300 nm thick were evaporated at 550 °C under 10^{-10} mbar onto the samples; the W was structured by photolithography and a KH_2PO_4–KOH–$K_3Fe(CN)_6$–H_2O solution to sizes of 2×2 mm^2 or 2×3 mm^2. Electrical contact pads made of 200 nm thick aluminum were then sputtered onto the tungsten for

[a]Permanent address: Institut de Physique Nucléaire de Lyon, 4 rue Enrico Fermi, F-69622 Villeurbanne Cedex, France; electronic mail: distefano@ipnl.in2p3.fr

 © 2003 American Institute of Physics

Downloaded 31 Jul 2007 to 134.158.137.155. Redistribution subject to AIP license or copyright, see http://jap.aip.org/jap/copyright.jsp

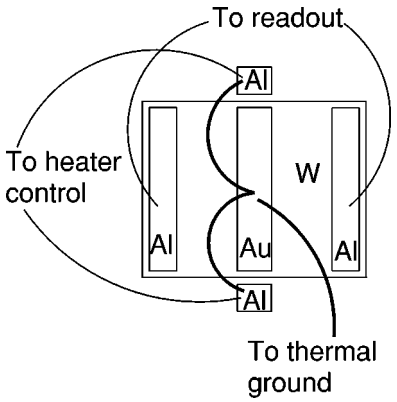

FIG. 1. Schematic of thermometers deposited on the Si cryogenic detectors. Typical dimension of tungsten film is 2 mm. Thick lines are Au wire, used for thermal contacts and resistive heaters; thin lines are Al wire, used as electrical contacts.

the readout, as was a 200 nm thick gold thermal contact. Similar aluminum pads were deposited as contacts for a film heater used to stabilize the operating temperature of the thermometer and to send periodic heat pulses to monitor the stability of the detector response. Gold or aluminum wires of 25 μm diameter were ultrasonically bonded to the pads to provide the thermal or electrical links. The W films were placed near the center of the Si absorbers, and on the SiN_x in the case of the textured samples. On silicon, the tungsten reliably gave superconducting transitions near 20 mK, once it was realized this transition appears to depend on the natural oxide on which the W is deposited: when the W was evaporated onto samples which had been etched in HF just before mounting in the deposition chamber, the transition temperature was of the order of 1 K; when the time lapse between HF bath and W deposition was of the order of a week the transition was at about 60 mK. This is presumably linked to some chemical interaction between Si and W which is inhibited by the presence of natural oxide. Such interactions also appear to have been blocked by the SiN_x layer in the case of the textured absorber, as a transition temperature near 20 mK was obtained.

Three detectors were selected for testing: 20×20 and 30×30 mm^2 planar Si absorbers, and a 20×20 mm^2 textured Si one. Their characteristics are summarized in Table I.

III. EXPERIMENTAL SETUP AND RESULTS

A. Preliminary tests and setup

All three light detectors were first cooled in a standard copper holder inside a dilution fridge and exposed to a collimated ^{55}Fe source (5.9 keV photons) to estimate their intrinsic energy resolution. Resolution, estimated as the full width at half the maximum (FWHM) of the 5.9 keV line, was 350 eV for the textured detector and 180 eV for the smooth ones. However, detector responses in terms of pulse height varied with the position of the collimated spot. It is quite likely that these resolutions, especially that of the textured detector, contain a contribution from the finite size of the collimated hole.

TABLE I. Silicon light detectors. $\mathcal{S}$ is the total surface area of both faces of the light detectors. Effective surface $\mathcal{S}_{\text{eff}}$ encompasses effect of texturing. Volume is $\mathcal{V}$. All devices were 0.5 mm thick.

Type	Size (mm^2)	$\mathcal{S}$ (mm^2)	$\mathcal{S}_{\text{eff}}$ (mm^2)	$\mathcal{V}$ (mm^3)
Planar–small	20×20	800	800	200
Planar–big	30×30	1800	1800	450
Textured	20×20	800	1377	200

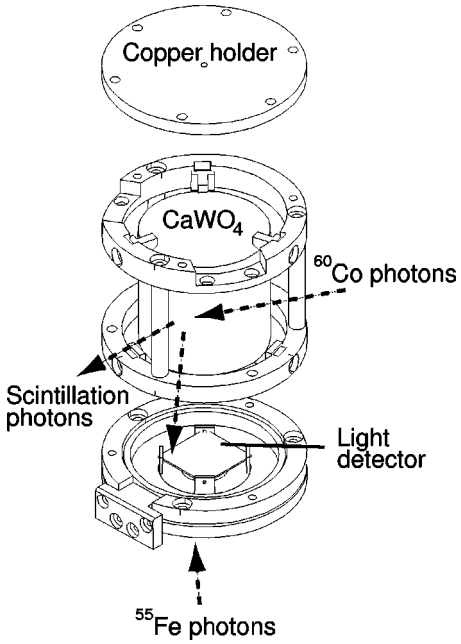

FIG. 2. Exploded view of copper holder, scintillator, and light detector (adapted from Ref. 12). Holder is lined with reflective foil, omitted here for clarity. Light detector is exposed to direct photon hits coming from a ^{55}Fe source and from scintillation photons coming from the $CaWO_4$ excited by cosmic rays and a ^{60}Co source. The combination of direct and scintillating events makes it possible to measure the absolute amount of light detected for a given setup.

Next, the three detectors were each placed in a setup inside the fridge to measure their light absorption. The setup (Fig. 2), described in detail elsewhere,[12,13] consisted of a $CaWO_4$ scintillating crystal of cylindrical shape (35 mm high with a 40 mm diameter) placed in a concentric 50 mm diameter light collector lined with a polymer reflective foil.[14] The $CaWO_4$ crystal had a non-functioning 5×6 mm^2 W film on it. Both ends of the light collector were lined with the same foil; however one of the ends had four Teflon pegs to hold the light detector. In this manner, both sides of the light detector should have been exposed to any available scintillating light. Care was taken to minimize thermal leaks between the calorimeters and their environment while avoiding spurious light traps in the setup. To provide an absolute energy reference, a ^{55}Fe source illuminated the light detector from outside the light collector foil, through a hole in the light collector's Cu structure behind the light detector (for mechanical reasons, the whole large light detector was exposed to the source, whereas the small detectors were illuminated through a 14 mm diameter hole). An external ^{60}Co source (main photon lines at 1.17 and 1.33 MeV) was used to

Downloaded 31 Jul 2007 to 134.158.137.155. Redistribution subject to AIP license or copyright, see http://jap.aip.org/jap/copyright.jsp

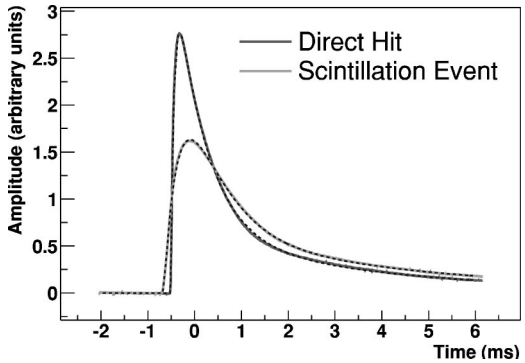

FIG. 3. Examples of averaged direct and scintillation-induced pulses from a detector (continuous lines) along with their fits (dashed lines). Pulses here have been averaged over some thirty events. Fits have been performed leaving all parameters free in both cases and assume a single scintillation time constant. The common, calorimetric parameters, are found to be compatible. When the fit parameters from the direct fit are imposed on the scintillation fit, the result is degraded. This indicates there is in fact more than one scintillation time constant.

stimulate scintillating light from the $CaWO_4$ [peak of emission $\approx$440 nm, FWHM$\approx$100 nm (Ref. 15)].

The detectors were operated in their superconducting transition by stabilizing their baseline temperature through the film heaters. This proved a challenge at ground level because the high rate of cosmic-ray-induced background interacting in the 266 g scintillator led to pileup in the light detector, especially in the large one. Pileup, a nuisance in itself, can also degrade the temperature stabilization of transition-edge sensors. The large device was therefore operated with active thermal feedback[16] to shorten pulse times in some runs. Stability of the small detectors was monitored with a pulser.

B. Pulse shapes in light detector

Two classes of light detector events were recognizable from their time constants (Fig. 3). Fast pulses were caused by direct hits in the light detector (mainly due to the ^{55}Fe source). Slower pulses were events of scintillating light (due to interaction in the $CaWO_4$ of the cosmic background and ^{60}Co when present). That the slow pulses originate in the scintillator was previously verified by the coincidences between the light detector and an instrumented $CaWO_4$ calorimeter.

The direct events in the detectors have been fitted with a model assuming an exponential rise (collection and thermalization of athermal phonons in the thermometer), a fast exponential decay (relaxation of thermal phonons in the thermometer through its heat sink, referred to as the athermal signal), and a slower exponential decay (relaxation of the entire detector, referred to as the thermal signal):[8]

$$R(t)=H(t)[A_{ath}(e^{-t/\tau_{ath}}-e^{-t/\tau_{\rm rise}}) + A_{th}(e^{-t/\tau_{th}}-e^{-t/\tau_{\rm rise}})], \quad (1)$$

where $H(t<0)=0$ and $H(t\geqslant 0)=1$ and, to simplify, the pulses are assumed to start at $t=0$. Direct 5.9 keV hits gave typical rise times of $\tau_{\rm rise}\approx 60$ μs with a FWHM of 15 μs for the distribution of these events. Both the athermal ($\tau_{ath}\approx$0.7 ms) and thermal ($\tau_{th}\approx$6 ms) components were clearly present, with the athermal component making up between 40% and 90% of the total pulse amplitude. All these parameters depended on the detector and to a certain extent the operating temperature.

Scintillation-induced hits with similar energy deposits in the light detector had typical rise times of 250 μs with a FWHM of 50 μs for the distribution. This slow rise time is interpreted as indicative of a relatively slow scintillation component in $CaWO_4$. The athermal component of the scintillating pulses was suppressed. Thus the light detectors appear to have been too fast for the scintillator, and were not quite in a calorimetric mode where they would fully integrate the energy of the individual photons emitted by an event in the scintillator.[8] Light detector response was therefore not optimal. To understand the scintillation pulse shapes, an exponential decay with time constant $\tau_{\rm scint}$ of the light emitted from the $CaWO_4$ scintillator has been assumed:

$$E(t)=H(t)\left(\frac{e^{-t/\tau_{\rm scint}}}{\tau_{\rm scint}}\right). \quad (2)$$

In this form, $\int_0^\infty E(t)\,dt$, the total energy emitted in scintillation, is normalized to unity whatever the time constant. Convolution with the response of the light detector for direct hits yields the expected shape of the scintillation-induced pulses:

$$\begin{aligned} S(t)=&\int_0^\infty E(u)R(t-u)du=H(t)\\ &\times\left\{A_{ath}\left[\frac{\tau_{ath}}{\tau_{\rm scint}-\tau_{ath}}(e^{-t/\tau_{\rm scint}}-e^{-t/\tau_{ath}})\right.\right.\\ &\left.\left.-\frac{\tau_{\rm rise}}{\tau_{\rm scint}-\tau_{\rm rise}}(e^{-t/\tau_{\rm scint}}-e^{-t/\tau_{\rm rise}})\right]\right\}+H(t)\\ &\times\left\{A_{th}\left[\frac{\tau_{th}}{\tau_{\rm scint}-\tau_{th}}(e^{-t/\tau_{\rm scint}}-e^{-t/\tau_{th}})\right.\right.\\ &\left.\left.-\frac{\tau_{\rm rise}}{\tau_{\rm scint}-\tau_{\rm rise}}(e^{-t/\tau_{\rm scint}}-e^{-t/\tau_{\rm rise}})\right]\right\}. \end{aligned} \quad (3)$$

Should the scintillation time constant be equal to one of the phonon time constants τ, the relevant term would become $t/\tau e^{-t/\tau}$. Should $\tau_{\rm scint}$ be much smaller than all the phonon time constants, Eq. (3) would simplify to Eq. (1): $S=R$. Fits have been performed independently on the direct hits using Eq. (1) and on the scintillation events using Eq. (3). For each detector, the common calorimetric parameters are found to be compatible within the error bars of both sets of fits. The resulting scintillation time constant is $\tau_{\rm scint}=0.4\overset{\rm sys}{\pm}0.1$ ms, where the error quoted is systematic. When the parameters of the direct fit are imposed on the scintillation fit, the result is degraded. This indicates that there may in fact be several scintillation time constants. The scintillation emission written in Eq. (2) can be generalized to two or more scintillation constants, for instance

$$H(t)\left[\alpha\frac{e^{-t/\tau_{\rm scint}}}{\tau_{\rm scint}}+(1-\alpha)\frac{e^{-t/\tau'_{\rm scint}}}{\tau'_{\rm scint}}\right].$$

Downloaded 31 Jul 2007 to 134.158.137.155. Redistribution subject to AIP license or copyright, see http://jap.aip.org/jap/copyright.jsp

TABLE II. Resolutions of detectors for direct ^{55}Fe and scintillating ^{60}Co calibrations, and baseline noise. ^{55}Fe resolution is mainly due to inhomogeneous response of light detector. This is exacerbated in the case of the textured detector, which has a lower volume-to-effective-surface ratio. ^{60}Co resolutions, expressed in units of energy deposited in the scintillator, are comparable for the three detectors, and probably dominated by inhomogeneous response of the scintillator. Baseline noise, an indicator of threshold, is also comparable in all detectors.

Detector	$\mathrm{FWHM_{Fe}}$ (keV)	$\mathrm{FWHM_{Co}}$ (MeV ee)	$5\sigma_{\mathrm{noise}}$ (eV)	$\mathrm{FWHM_{Fe}}\times\mathcal{V}/\mathcal{S}_{\mathrm{eff}}$ (keV mm)
Planar–small	0.65	0.26	68	0.16
Planar–big	0.61	0.30	73	0.15
Textured	1.25	0.28	39	0.18

Generalization of Eq. (3) is linear. With the direct-fit parameters set, fits yield a fast time constant of $0.3\overset{\mathrm{sys}}{\pm}0.1$ ms making up $\alpha=(70\overset{\mathrm{sys}}{\pm}15)\%$ of the emitted scintillation energy, and a slow constant of $2.5\overset{\mathrm{sys}}{\pm}1$ ms. More complicated emission time structures are possible but have not been investigated.

We note also that because the light detectors are not fully calorimetric for the scintillating light, pulse height is a biased estimator of the actual energy of the scintillation-induced pulses. Compared to the energy scales provided by the direct hits [Eq. (1)], the energy of the scintillation pulses [Eq. (3)] may be greatly underestimated. To correct for this, pulse parameters are obtained from the fit with a single scintillation time constant and all parameters left free. These parameters are used to build a numerical pulse model based on Eq. (3). The correction factor is defined as the ratio of the amplitude of this model pulse, assuming a scintillation time constant much shorter than the other time constants (i.e., $S_{\tau_{\mathrm{scint}}\to 0}=R$, ideal calorimetric response), divided by the amplitude of the model pulse with the fitted time constant (i.e., $S_{\tau_{\mathrm{scint}}}$, actual response). Because each detector has its own phonon time constants, the correction factor varies from one detector to the next. The correction factors are $1.45\overset{\mathrm{sys}}{\pm}0.15$ for the textured detector, $1.7\overset{\mathrm{sys}}{\pm}0.2$ for the small planar detector, and $1.2\overset{\mathrm{sys}}{\pm}0.1$ for the large planar detector. The main errors are systematic and come from the estimation of the scintillation time. Most of the loss in amplitude comes from the athermal component, because of its shorter time constant. For the three detectors, the athermal correction factors are, respectively, $1.55\overset{\mathrm{sys}}{\pm}0.15$, $2.1\overset{\mathrm{sys}}{\pm}0.3$, and $1.4\overset{\mathrm{sys}}{\pm}0.1$, whereas they are only $1.17\overset{\mathrm{sys}}{\pm}0.05$, $1.45\overset{\mathrm{sys}}{\pm}0.1$, and $1.12\overset{\mathrm{sys}}{\pm}0.03$ for the slower thermal component. One way to improve the detector design might be to slow down the relaxation time of the athermal component, with a weaker coupling of the thermometer to the heat bath.

C. Detector resolutions

Resolutions for the direct ^{55}Fe hits and the scintillating ^{60}Co hits are given in Table II. These ^{55}Fe resolutions are worse than the spot resolutions, confirming that the response of the light detector depends on the position of the interaction in it. This is because in the thin absorber crystal used, to reach the thermometer, phonons created far from it must bounce off the crystal surfaces and thus risk decay more often than phonons created near it. Moreover, in the case of the nontextured silicon detectors, which have similar volume-to-surface ratios (0.25 mm), the resolutions are close to one another (about 0.62 keV FWHM). The resolution of the textured detector, however, is noticeably worse. We attribute this to the lower volume-to-effective-surface ratio (0.15 mm) of the light detector, which causes extra scattering of the athermal phonons on the crystal surface before they are absorbed in the thin film.[8]

^{60}Co resolution is comparable in all three detectors. Given an energy of $\approx$2.8 eV per scintillating photon, this resolution is not compatible with simple Poisson photon statistics. Rather, it appears to result from fluctuations in the light escaping the crystal depending on the position of the interaction in the scintillator because of flaws in the latter. This effect may be more or less pronounced from one $CaWO_4$ crystal to another.

Last, the 5σ baseline noise, also reported in Table II, varies between 40 and 70 eV. This gives an indication of detector threshold, though the high background from cosmic rays interacting in the scintillator has thwarted attempts to verify it directly.

D. Light absorption properties

Thanks to the combined use of the ^{55}Fe and ^{60}Co sources, it was possible to measure the absolute amount of light detected by each silicon calorimeter in this particular setup. The energy deposited by a photon in the $CaWO_4$ scintillator can go into three channels:

$$E_{\mathrm{dep}}=E_{\mathrm{phonon}}+E_{\mathrm{scint}}+E_{\mathrm{lost}}, \tag{4}$$

where E_{phonon} is transferred to phonons in $CaWO_4$ (either directly or by absorption of some scintillation photons). E_{scint} represents the energy of scintillation photons that are eventually seen in the light detector. It can be measured absolutely thanks to the ^{55}Fe calibration of the light detector. E_{lost} is energy lost, probably mainly in the form of scintillation photons escaping or absorbed in the light collector. E_{dep} itself is known in the case of a photon source like ^{60}Co by identification of the photon lines. This method does not provide a means of estimating E_{phonon} and E_{lost}, though the former is thought to represent the majority of the deposited energy.

Results for the three detectors are summarized in Table III in terms of $\varepsilon=E_{\mathrm{scint}}/E_{\mathrm{dep}}$, the fraction of the energy deposited by a photon in the scintillator that is converted to light and eventually seen in the light detector. The main uncertainty, discussed previously, is of a systematic nature and comes from the difficulty of estimating the true pulse energy because the response of the light detector is rather fast for the scintillating time structure. A smaller systematic effect comes from possible nonlinearities in detector response due to irregular transition curves. An upper limit on this effect has been estimated using the film pulser in the case of the small detectors, and different operating points on all detectors. The

Downloaded 31 Jul 2007 to 134.158.137.155. Redistribution subject to AIP license or copyright, see http://jap.aip.org/jap/copyright.jsp

TABLE III. Light absorption properties of Si light detectors. ε is the fraction of energy deposited by ^{60}Co photons in the scintillator and eventually detected in the light detector. Nontextured silicon detectors exhibit comparable absorption per unit area. This indicates that total light absorption could still be improved by a larger surface area in this particular setup. Textured light detector has greater absorption per unit area. Taking into account effective area brings results into line, though estimating $\mathcal{S}_{\text{eff}}$ precisely is not straightforward. Errors are systematic and come mainly from the estimate of the scintillation energy, based on pulse amplitude, which depends on knowledge of the scintillation time structure.

Detector	$10^3\times\varepsilon$	$\varepsilon/\mathcal{S}$ (m^{-2})	$\varepsilon/\mathcal{S}_{\text{eff}}$ (m^{-2})
Planar–small	3.0 ± 0.3	3.8 ± 0.4	3.8 ± 0.4
Planar–big	7.8 ± 0.8	4.3 ± 0.5	4.3 ± 0.5
Textured	5.4 ± 0.5	6.7 ± 0.7	3.9 ± 0.4

effect was also reduced in the case of the large detector through the active thermal feedback[16] for some runs.

The nontextured silicon detectors absorb comparable amounts of light per unit area. This indicates that detector size could still be increased before the quantity of absorbed light reaches a limit for this combination of light collector and scintillator. The textured detector has a significantly better light absorption per unit area. Light absorption of the textured detector is in line with its effective surface area, though the estimation of $\mathcal{S}_{\text{eff}}$ is rough and assumes that light falls uniformly on both faces of the detector, and that the small SiN_x and W structures on the front face of the detector have reflectivities similar to Si.

Last, we note that the absolute amount of light seen in the light detector depends on the efficiency of the light collector, and also on the quality of the scintillator. Indeed, significant variations have been observed between $CaWO_4$ crystals leading to values of ε of up to about 1.3% for configurations similar to those described here.[12]

IV. CONCLUSION

The absorptivity in the visible wavelengths of cryogenic silicon calorimeters with a given size has been enhanced through the standard photovoltaic technique of texturing. The increase is compatible with the extra surface created by the texturing (a factor of 1.74), as expected for photons with random incidence angles. We presume that for normal-incident photons, the gain would be greater due to photons having two chances to be absorbed between surface pyramids as is the case for solar cells.

Response of the cryogenic light detector has been corrected for the misadaptation between its time constants and the scintillation time structure of the $CaWO_4$ crystal used as light source at 20 mK. The latter is estimated to contain at least a fast ($\approx$0.3 ms) component and a slow ($\approx$2.5 ms) one. A slower light detector than the one used here would allow a better estimation of the scintillation energies. Conversely, a faster one might provide more insight into the time structure of the scintillator, and, at energies high enough to yield a statistically significant number of photons, could make it possible to check if the time structure depends on the nature of the interaction in the scintillator. Indeed differences have already been observed between the time constants of alpha particles and those of gammas interacting in $CaWO_4$ at 20 mK.[13]

Energy resolution for a monochromatic source, which in the case of two-dimensional athermal silicon devices is dominated by the correlation between response and position of the interaction, is degraded by the decrease in volume-to-surface ratio caused by texturing, which induces extra phonon scattering. It may be possible to improve the sensitivity of the light detector through the use of smaller thermometers with phonon collector pads.[17] Another option might be to exploit the Neganov–Luke effect,[18,19] the semiconducting analog of resistive heating, which can amplify the phonon signal.

Finally, for low-radioactivity applications, contaminations from the naturally occurring unstable isotope ^{40}K should be avoided. The tungsten thermometer etch used here would therefore be replaced by a potassium-free one such as HF or H_2O_2. It may also be possible to replace the KOH texturing bath with NaOH or an organic one.[20]

ACKNOWLEDGMENTS

This work was funded by the European TMR Network for Cryogenic Detectors ERB-FMRX-CT98-0167, and is dedicated to the memory of Marie Folkart.

[1] N. J. Spooner, A. Bewick, G. Homer, P. Smith, and J. Lewin, Phys. Lett. B **273**, 333 (1991).
[2] T. Shutt *et al.*, Phys. Rev. Lett. **69**, 3425 (1992).
[3] L. Bergé *et al.*, Nucl. Phys. B (Proc. Suppl.) **70**, 69 (1999), astro-ph/9801199.
[4] C. Bobin, I. Berkes, J. P. Hadjout, N. Coron, J. Leblanc, and P. de Marcillac, Nucl. Instrum. Methods Phys. Res. A **386**, 453 (1997).
[5] P. Meunier *et al.*, Appl. Phys. Lett. **75**, 1335 (1999).
[6] A. Alessandrello *et al.*, Phys. Lett. B **420**, 109 (1998).
[7] C. Bucci *et al.* (2001), MPI-PhE/2001-02 http://www.vms.mppmu.mpg.de/cresst/proposal_01.zip.
[8] F. Pröbst, M. Frank, S. Cooper, P. Colling, D. Dummer, P. Ferger, G. Forster, A. Nucciotti, W. Seidel, and L. Stodolsky, J. Low Temp. Phys. **100**, 69 (1995).
[9] R. A. Arndt, J. F. Allison, J. G. Haynos, and A. Meulenberg, Jr., in 11th IEEE Photovoltaic Specialists Conference (Scottsdale, AZ) (1975), pp. 40–43.
[10] J. B. Price, in *Semiconductor Silicon Symposium* (The Electrochemical Society Series, Pennington, NJ, 1973), pp. 339–353.
[11] P. Colling, A. Nucciotti, C. Bucci, S. Cooper, P. Ferger, M. Frank, U. Nagel, F. Pröbst, and W. Seidel, Nucl. Instrum. Methods Phys. Res. A **354**, 408 (1995).
[12] T. Frank, M. Bruckmayer, C. Cozzini, P. Di Stefano, D. Hauff, F. Pröbst, W. Seidel, G. Angloher, and J. Schmidt, in *Seventh International Conference Advanced Technology and Particle Physics* (Villa Olmo, Como, Italy) (2001).
[13] T. Frank, Ph.D. thesis, Technische Universität München and Max-Planck-Institut für Physik, Werner-Heisenberg-Institut, Munich, 2002, http://tumb1.biblio.tumuenchen.de/publ/diss/ph/2002/frank.pdf.
[14] M. F. Weber, C. A. Stover, L. R. Gilbert, T. J. Nevitt, and A. J. Ouderkirk, Science **287**, 2451 (2000).
[15] M. J. Treadaway and R. C. Powell, J. Chem. Phys. **61**, 4003 (1974).
[16] O. Meier *et al.*, Nucl. Instrum. Methods Phys. Res. A **444**, 350 (2000).
[17] M. Loidl, S. Cooper, O. Meier, F. Pröbst, G. Sáfrán, W. Seidel, M. Sisti, L. Stodolsky, and S. Uchaikin, Nucl. Instrum. Methods Phys. Res. A **465**, 440 (2001).
[18] B. S. Neganov, V. N. Trofimov, and V. Stepankin, J. Low Temp. Phys. **93**, 417 (1993).
[19] P. Luke, J. Beeman, F. S. Goulding, S. E. Labov, and E. H. Silver, Nucl. Instrum. Methods Phys. Res. A **289**, 406 (1990).
[20] J. S. You, D. Kim, J. Y. Huh, H. J. Park, J. J. Pak, and C. S. Kan, Sol. Energy Mater. Sol. Cells **66**, 37 (2001).

Downloaded 31 Jul 2007 to 134.158.137.155. Redistribution subject to AIP license or copyright, see http://jap.aip.org/jap/copyright.jsp

4.4A The SciCryo project

Ref. [77].

Journal of Low Temperature Physics manuscript No.
(will be inserted by the editor)

**P.C.F. Di Stefano[⋆◇], N. Coron[+], P. de Marcillac[+],
C. Dujardin[○], M. Luca[⋆], F. Petricca[•],
F. Proebst[•], S. Vanzetto[⋆], M.-A. Verdier[⋆]
and the EDELWEISS collaboration[1]**

The SciCryo project and cryogenic scintillation of Al_2O_3 for dark matter

October 2, 2007

Keywords Scintillation, cryogenics, sapphire, dark matter

Abstract We discuss cryogenic scintillation of Al_2O_3. Room-temperature measurements with α particles are first carried out to study effect of Ti concentration on response. Measurements under X-rays between room temperature and 10 K confirm a doubling of light output. The integration of a scintillation-phonon detector into an ionization-phonon dark matter search is underway, and the quenching factor for neutrons has been verified.

PACS numbers: 29.40.Mc, 07.20.Mc, 95.35.+d ,91.67.Pq

1 Introduction

Cryogenic experiments using ionization-phonon [1,2] or scintillation-phonon [3,4] detectors are among the most sensitive dark-matter searches thanks to their excellent rejection of the dominant, highly-ionizing background. Understanding other backgrounds, such as that produced by fast neutrons, searching for various WIMP couplings [5], and confirming evidence for detection will require a variety of target nuclei. The SciCryo project (IPN Lyon, IAS Orsay, MPP Munich and LPCML Lyon) is therefore investigating materials that could make suitable cryogenic scintillation-phonon detectors. Sapphire, for instance, is attractive because scattering kinematics and cross section make it a good detector to control the fast neutron background. Moreover, it is well-established as a cryogenic phonon detector for dark

⋆ Institut de Physique Nucléaire de Lyon, IPNL, UMR5822, CNRS-IN2P3, Université Claude Bernard Lyon 1, Université de Lyon, F-69622 Villeurbanne, France.
+ Institut d'Astrophysique Spatiale, CNRS & Université Paris Sud, Bât. 121, Orsay, Cedex 91405, France.
○ Laboratoire de Physico-Chimie des Matériaux Luminescents - UMR 5620, Université Claude Bernard Lyon 1, F-69622 Villeurbanne, France.
• Max-Planck-Institut für Physik, Föhringer Ring 6, D-80805 München, Germany.
◇ E-mail: distefano@ipnl.in2p3.fr

Sample	CLY (%)	Light detector	[Ti] (ppm)	[Cr] (ppm)
MPP-3	1.4	Si	68.4–72.5 (LA)	1.38–2.85 (LA)
MPP-4	1.4	Si	70.2–79.4 (LA)	1.43–1.9 (LA)
IAS-B213[8]	1.3	Ge		
IAS-A104			5.11–6.98 (LA) 5.8 (GD)	0.27–0.44 (LA) 0.22 (GD)
IAS-A080[8]	1.27	Ge	800–1200 (N)	
IPNL-1.3	0.8	Ge		
IPNL-1.2			<0.83–1.79 (LA) 1.1 (GD)	0.76–2.57 (LA) 0.34 (GD)
IAS-A107	0.25	Si		
IAS-A109			1.16–3.66 (LA)	0.55–1.74 (LA)

Table 1 Cryogenic γ scintillation collected-light yield (CLY, see text for definition) of various sapphire crystals. Crystals are grouped by supplier, a weak indication of composition. Concentrations of Ti and Cr are either nominal (N), or determined by laser-ablation-ICPMS (LA) or by glow-discharge-MS (GD) (for LA, range is spread of results over 5 measurement points; for GD, nominal error is ± 20 % of value). Yields vary by ≈ 6. For a given type of crystal, differences may arise from size, geometry and polish of samples, light collection efficiency and light detector. However, collected-light yields comparable to those of standard dark-matter detectors ($\approx 1.3\%$) are possible, both with Ge and Si light detectors.

matter[6,7], and certain samples have already been shown to scintillate at low temperature[8,9,10].

2 Crystals, doping and X-ray scintillation spectra

We have compiled the results of previous cryogenic experiments and performed some new ones to study the collected-light yield of various sapphire crystals. Collected-light yield here is understood as the fraction of energy that is deposited in a scintillator, transformed into light and detected by a calorimetric light detector[11]. It is not an absolute value, since a fraction of the light may be lost depending on the efficiency of the light detector and the setup. Results in Tab. 1 show a wide spread. However, several samples show a light yield comparable or better than the 1.3%[11] of the $CaWO_4$ already in use by some dark matter experiments[3].

We have recorded the scintillation spectra of many nominally pure sapphire crystals at room temperature under a strong flux of X-rays (for example, Fig. 1). These spectra are indicative of scintillation efficiency. Moreover, all spectra exhibit the presence of Ti^{3+} (wide band around 750 nm) and/or Cr^{3+} (line at 698 nm), dopants commonly used for sapphire laser rods. Though X-ray scintillation is very sensitive to small levels of impurities, it does not allow the quantification of the concentrations of dopants necessary to optimize light yield. In addition to their sensitivity, techniques to quantify traces in crystals have several different aspects: surface or bulk, destructive or non-destructive, sensitive to oxydation states or not. For sapphire, two commercially available methods, laser-ablation mass-spectrometry (LAMS) and glow-discharge mass-spectrometry (GDMS) are sensitive down to ppm levels. However, they are destructive, and do not distinguish between oxydation states such as Ti^{3+} and Ti^{4+}. We have therefore used two non-destructive optical methods sensitive to oxydation state: absorption and fluorescence. To carry out a systematic study of doping, a set of crystals has been obtained from ISC Kharkov scanning two parameters, the nominal concentration

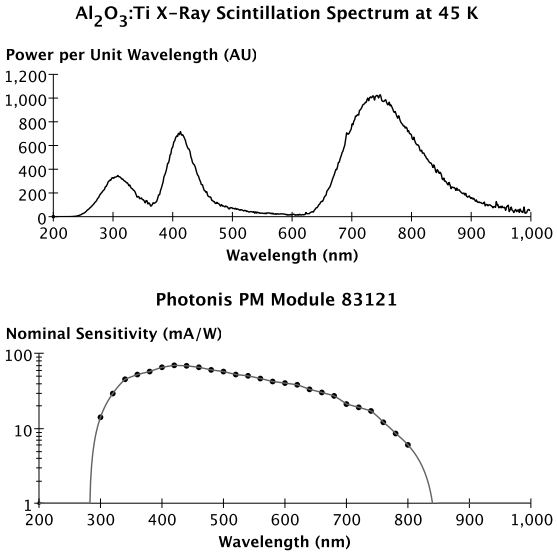

Fig. 1 Top: scintillation spectrum of an Al_2O_3:Ti sample at 45 K, measured under continuous X-ray stimulation with a monochromator and a CCD. Spectrum has been converted from intensity to power. Height of each band depends on doping of sample as well as redox potential. Bottom: sensitivity of PM used in subsequent tests with α particles and X-rays.

of Ti (10, 50, 100, 500 or 1000 ppm), and the redox potential under which the crystal is treated (-230 kJ/mol, -30 kJ/mol or 120 kJ/mol), affecting the fraction of Ti in the Ti^{3+} oxydation state. LAMS tests show the samples have at most 2 ppm of Cr; moreover, whatever Cr there is has a negligible contribution to their spectra (Fig. 1). Absorption and fluorescence properties of the samples, as well as X-ray scintillation spectra down to 50 K, will be described in a future publication [12].

3 Room-temperature α scintillation

The room-temperature response of several crystals to α particles has been tested using a Photonis 83121 photomultiplier module. Unlike standard photomultipliers, the one in this module has a multialkali photocathode which is fairly sensitive to the red light from Al_2O_3:Ti (Fig. 1). The module has a built-in high-voltage supply and 10 MHz amplifier. Moreover, the photocathode is transmission-type and deposited on the window of the PM, providing it with good geometrical efficiency. Crystals are pressed against the PM window by a white Delrin endcap. This allows comparison of the light yield of crystals of same geometry.

Tests have been performed using a ^{241}Am α source and several $5 \times 5 \times 1$ mm^3 samples. The particles hit the crystal on its large face opposite the window of the PM. Typical FWHM resolution on the α line is 10–15%. Responses of several samples are compared in Fig. 2. We note that the results have not been corrected for PM sensitivity (Fig. 1) which differs from that of a Si or Ge calorimetric light

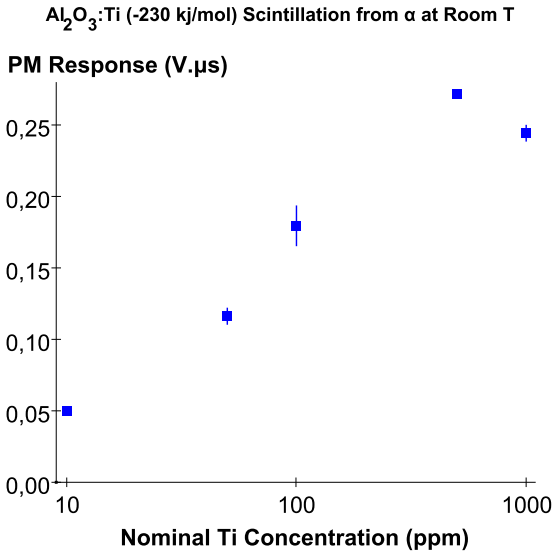

Fig. 2 Room-temperature response of various $5 \times 5 \times 1$ mm^3 Al_2O_3:Ti samples (230 kJ/mol) to α particles from a ^{241}Am source, as measured with the PM described in Fig. 1. Response is defined here as integral of PM pulse. Each measurement has been carried out twice.

detector or a CCD. Results may also differ under continous bombardment of other types of particles. Future work includes studying response to photons [12] and neutrons.

4 X-ray scintillation down to 10 K

The luminescence under X-ray bombardment of some samples has been measured down to 10 K using an optical cryostat. In this setup, X-rays from a tube operating at 35 mA current and 40 kV voltage enter the cryostat through an aluminium window and excite the $5 \times 5 \times 1$ mm^3 sample. Light escapes the cryostat through quartz windows and reaches the 83121 module outside, at room temperature. The module records the light emitted as the temperature of the sample changes. Temperature sweeps are carried out at 10 K/minute. During cooling, only luminescence is in play, whereas during warming, thermoluminescence can also be a factor. Results from a sample, measured without and with a 600 nm high pass filter, are shown in Fig. 3. The results show an increase of the light yield of about a factor two as the crystal is cooled to 10 K. This is in agreement with previous work [9]. Comparing the data with and without filter, and extrapolating to lower temperatures provides a hint that there may be a greater increase in store and that it may come from the short-wavelength component of the scintillation spectrum. Similar tests on other samples are in preparation.

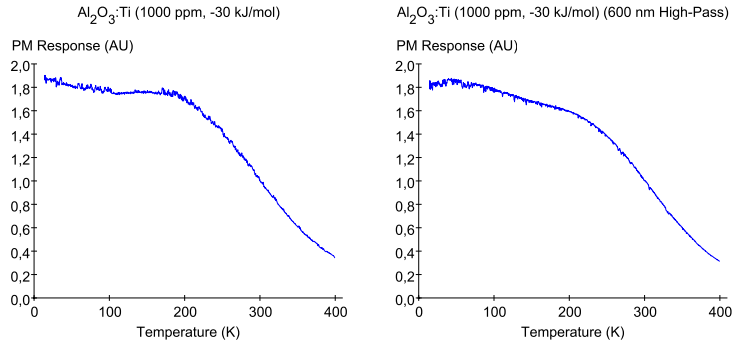

Fig. 3 PM response as a Al_2O_3:Ti (1000 ppm, -30 kJ/mol) sample is cooled under X-rays, with no filter (left) and with a 600 nm high-pass filter (right). Curves are normalized to a value of 1 at 300 K. Both show a gain of ≈ 2 at low temperature. A similar evolution is found for -230 kJ/mol crystals.

5 Integration of a detector into a dark matter experiment

We have integrated a scintillation-phonon detector into an ionization-phonon environment. This test is relevant for future large-scale cryogenic dark matter experiments such as EURECA [13] that may combine both technologies. The scintillation-phonon detector is a 50 g Al_2O_3 device previously characterized at surface level [8]. It has been installed in the low-background cryostat of the EDELWEISS II experiment at the Modane Underground Laboratory [14], after having been screened for radioactive background. Issues such as the mechanical, thermal and electrical compatibilities have been resolved. Performance of the phonon channel is on a par with that of the Ge ionization-phonon devices in the cryostat, with a baseline noise of 3 keV. The scintillation channel suffers from excess noise however, some of it coming from microphonics in the very small (195 mg) light detector, itself a calorimeter. Further work is necessary for the scintillation channel, as the overall background rejection threshold remains high (about 70 keV). Despite this, neutrons from calibrations with an AmBe source are clearly visible, thanks to the elastic scattering kinematics that favor Al_2O_3 over Ge. This amounts to ≈ 4 times more neutrons per unit volume visible in Al_2O_3 (100 keV threshold) than in Ge (30 keV threshold). The quenching factor for neutrons has been measured over the 500–1000 keV range to be 20 ± 2, compatible with the ground level value [8].

6 Conclusions

Systematic tests of the cryogenic scintillation properties of sapphire are underway with crystals of different Ti^{3+} concentrations. First results confirm that response to X-rays doubles when temperature goes down to 10 K. Tests at low temperature are necessary to establish a relationship between cryogenic light yield and doping concentrations. An integration test of a small cryogenic scintillation-phonon device into the ionization-phonon EDELWEISS experiment is progressing. It shows

that sapphire can be useful to monitor the neutron background close to the germanium detectors.

Acknowledgements Funding for this project has been provided by Agence Nationale de la Recherche (ANR) grant SciCryo ANR-05-BLAN-0031. We thank Photonis for lending us the 83121 module. Prof. L. A. Lytvynov of ISC Kharkov has provided useful discussions on Al_2O_3. This paper is dedicated to our late colleague J. Mugnier of UCBL.

References

1. V. Sanglard et al., Phys. Rev. D **71**, 122002 (2005).
2. D. S. Akerib et al., Phys. Rev. D **72**, 052009 (2005).
3. G. Angloher et al., Astropart. Phys. **23**, 325 (2005).
4. S. Cebriàn et al., Nucl. Phys. B (Proc. Suppl.) **138**, 519 (2005).
5. A. Benoit et al., Phys. Lett. B **616**, 25 (2005).
6. A. de Bellefon et al., Astropart. Phys. **6**, 35 (1996).
7. G. Angloher et al., Astropart. Phys. **18**, 43 (2002).
8. N. Coron et al., Nucl. Instrum. Methods A **520**, 159 (2003).
9. V. B. Mikhailik et al., Nucl. Instrum. Methods A **546**, 523 (2005).
10. J. Amaré et al., Appl. Phys. Lett. **87**, 264102 (2005).
11. P. C. F. Di Stefano et al., J. Appl. Phys. **94**, 6887 (2003).
12. M. Luca et al., in preparation.
13. H. Kraus et al., J. Phys.: Conf. Ser. **39**, 139 (2006), TAUP 2005, Proc. Ninth Int. Work. Topics Astroparticle Underground Phys., Zaragoza, Spain, 10–14 Sept. 2005.
14. S. Marnieros et al., Nucl. Instrum. Methods A **520**, 101 (2004).

Chapter 5

Calorimetric Detection of Fracture

Hergé, Les sept boules de cristal [81]

5.1 The curious cracking cryogenic crystal

Physics sometimes holds surprises for us, as I found out during my post-doc on the CRESST experiment. The experiment deployed four 262 g sapphire phonon-only calorimeters in a low-background cryostat at the Gran Sasso underground laboratories. Each cubic crystal was read by a tungsten superconducting transition-edge sensor (TES). Before I joined the experiment in the autumn of 1998, much effort had been put into developing heat-pulser technology to linearize the response of the detectors and rigorously establish the energy scales. This demonstrated that the detectors reached a threshold of 350 eV [82]. Shortly after my arrival, we installed the detectors underground and calibrated them before launching a WIMP search. To our dismay, the rate of background events was much higher than expected; indeed it surpassed our expectations by three orders of magnitude (Fig. 5.1). While the pulse shape of the individual events was consistent with that obtained from ^{57}Co calibrations, there were no lines or structure to be observed in the background spectrum, the waiting time distribution between events did not follow a Poisson law, and the distribution of differences in event times in the various detectors was not peaked, as one would expect for particle coincidences, but flat, as if the events were uncorrelated. All of this indicated that the background was not of radioactive origin. We first considered vibrations as the

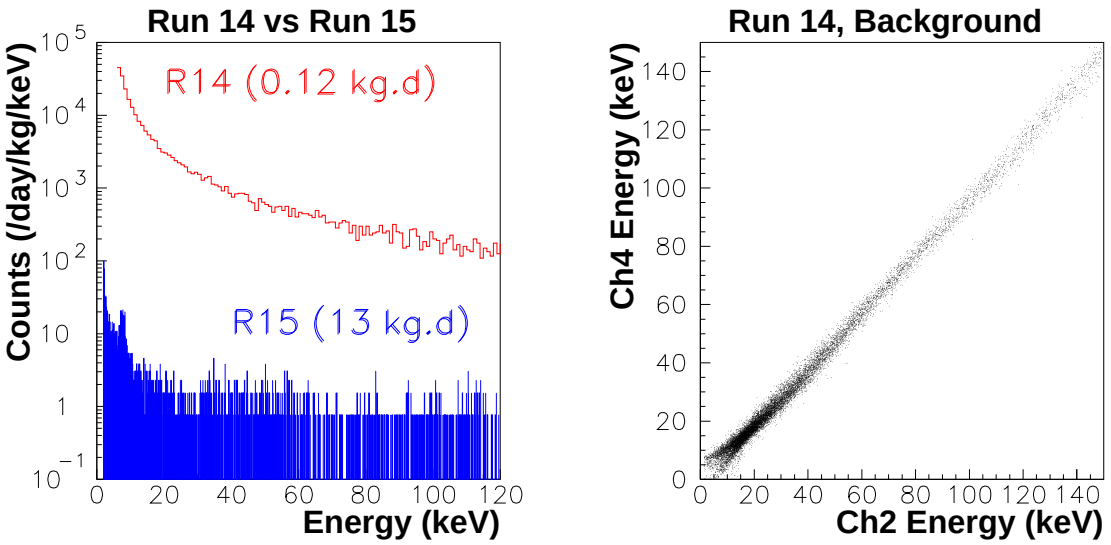

Figure 5.1: Left: CRESST background, before and after modification of how crystal was held. Modifications reduced background by three orders of magnitude. Right: CRESST background before modifications in a crystal with two TES, demonstrating the background comes from the crystal rather than the TES.

source of the problem, and in the next run installed a device allowing us to pump the liquid nitrogen bath to keep it from boiling; this had no effect. I next designed and installed a set of springs with a low-pass cutoff close to 1 Hz to isolate the detectors mechanically from the cryostat; this did not improve the situation either. We then investigated electrical perturbations as the source of our noise. Colleagues suggested there might be a *common mode* problem stemming from an asymmetry in the current sources used to bias the superconducting films, and causing current to run through the gold thermal bond wire, thereby heating the detectors. To counter this, I first built a primitive electrical low-pass (several loops of copper wire wound around a Delrin core) for the link to the thermal bath. As this did not improve things, I electrically isolated the thermal heat sink using copper-Kapton-copper pieces that had enough surface area to conduct heat but were electrically isolating thanks to the Kapton. This was also to no avail. Colleagues and I had now spent many tedious months toiling in a tunnel in Italy. On one of his field trips to the LNGS, an elderly director of the Max-Planck inquired with a straight face why we did not work underground over the Christmas break. Things were looking bleak during the winter of 1999–2000.

At that point, the millenium changed[1] and with it our fortunes. One of the PhD students back in Munich managed to manufacture a detector identical to the others but with two TES on it; this was not a given as the two films needed matching transition temperatures. We installed this new detector at LNGS. All the events were coincident in the two sensors. This demonstrated that the background did not originate in the electronics or the TES, but in the sapphire crystal itself. We dismantled and inspected the crystal and found that it was slightly scratched at its contact points. To avoid microphonics, the crystal had to be held very firmly; however to minimize heat leaks, the contact area had to be as small as possible. Mechanical contact was therefore made using twelve 2 mm diameter sapphire bearings pressed against the sapphire crystal. The bearings were at the end of thin copper rods held in place by Delrin bridges. During detector assembly, the copper rods were firmly screwed into place; however, as the cryostat cooled, the Delrin contracted by more than a percent [83] creating a large force on a very small contact area of the crystal, hence the cracks (Fig. 5.2). We promptly modified the way our crystals were held, replacing the sapphire bearings

[1] More precisely, the decimal notation for the year passed a psychologically significant value.

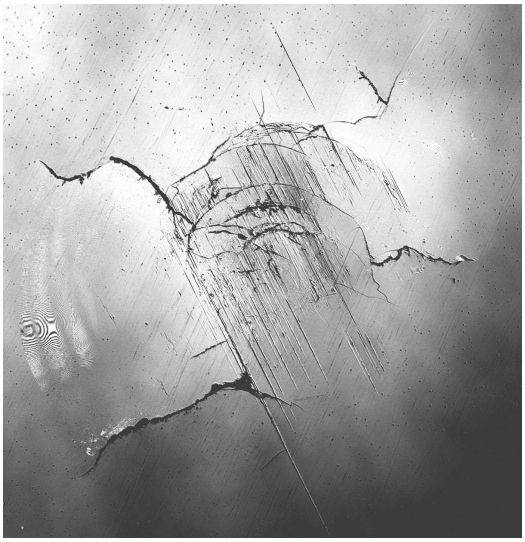

Figure 5.2: Fractures from our serendipitous indentation experiment of a 2 mm diameter sapphire bearing on a sapphire crystal.

by blunt Delrin stubs, and to our great relief the background shrunk by three orders of magnitude (Fig. 5.1). We were thus able to set new limits on WIMPs lighter than 5 GeV thanks to our low threshold [51]. As our goal was to seek WIMPs, we moved on quickly from our newly-vanquished background without giving it too much thought. However, in the back of my mind I hoped there would be payback for the trouble it had caused us.

5.2 Brittle fracture and earthquakes

A few years later, Finnish colleagues pointed out to us the silver lining in our data: we had inadvertantly obtained the first calorimetric measurement of brittle fracture [84, 85]. The sapphire bearings meant to hold the sapphire calorimeter were pressed against the crystal with such force that they indented the crystal, fracturing it. The small contact surfaces generated stress fields vanishing quickly with distance, and ensured stability of the fractures [86]. Each fracture released phonons that looked just like those from a particle when collected in the transition-edge sensor. This yielded a direct measurement of the energy of each fracture event, as opposed to an indirect measurement via the acoustic chanel as is common in the acoustic emission technique. Another advantage of this calorimetric technique is its great sensivity, in our case femto-Joules. In fact, the thermodynamics involved are not totally straightforward. Breaking a bond consumes, rather than releases, energy, yet calorimetry — like acoustic emission — measures an energy release. Presumably, the answer lies with the formation of the cracks. Elastic energy in the crystal is transferred to break bonds, and during this transfer, part of the elastic energy may be converted to phonons. Calorimetry has an advantage over acoustic emission here, because the former measures all the phonons whereas the latter measures only an unknown fraction of them. The rich and complete event catalogues obtained, of many thousand femto-fractures each, contain the arrival time and energy of each event, and show several statistical similarities to other results in brittle fracture and earthquakes, despite the many orders of magnitude difference in the energy ranges [87].

One very striking similarity is that the probability distribution of fracture-energy release is a power law with an exponent close to that of the Gutenberg-Richter law. Charles Frances Richter and Beno Gutenberg worked at the Pasadena Seismology Lab initially managed by the Carnegie Institute; a historical curiosity is that this lab was located from its inception in 1921 until 1927,

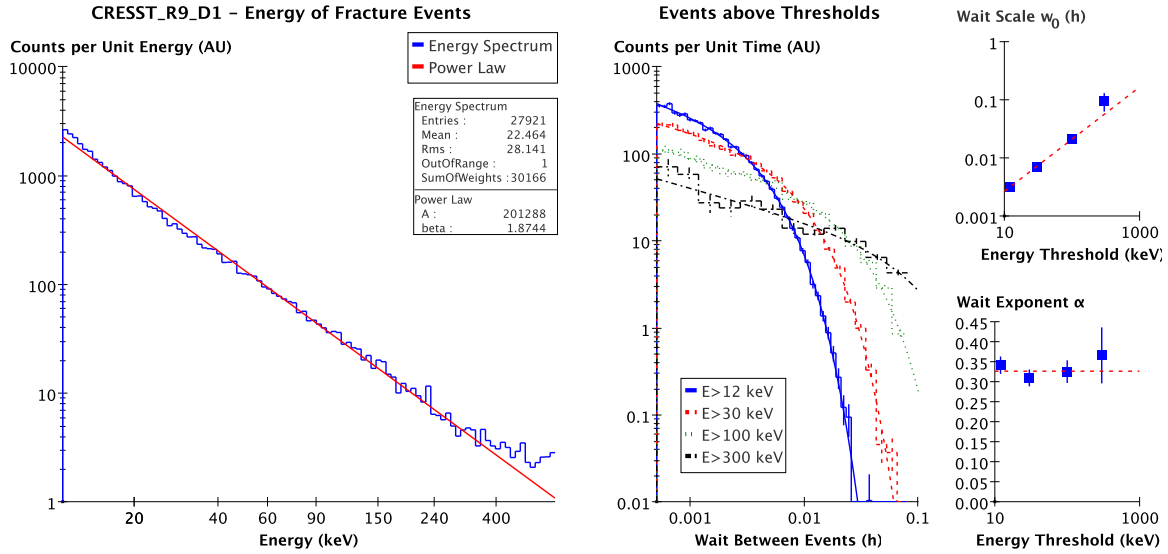

Figure 5.3: Left: energy spectrum of fracture events. Distribution follows a Gutenberg-Richter inverse-power law $E^{-\beta}$ with an exponent of $\beta \approx 1.9$. Right: distribution of waiting times w between consecutive events, for various energy thresholds. Distributions are not of Poisson type, as there is an excess of short wait times. Distributions are fitted by $w^{-\alpha} \exp -w/w_0$. As expected from the energy distribution, the wait scale w_0 depends on energy threshold like $E^{\beta-1}$. The power law exponent α shows little dependance on energy.

the year Richter was hired [88], in offices of the Mount Wilson observatory — the very observatory Fritz Zwicky would have frequented around that period. As Fig. 5.3 shows, the differential energy distribution of the events follows $dN/dE \propto E^{-\beta}$, with $\beta \approx 1.9$. The Gutenberg-Richter law giving the number of earthquakes of moment greater than M is $N(\geq M) \propto M^{-B}$, with $B \approx 2/3$ [89]; thus the differential distribution is $dN/dM \propto M^{-B-1}$. Since earthquake moment is homogeneous to energy, $M \propto E$, and it follows that for earthquakes $dN/dE \propto E^{-5/3}$ with an exponent of $5/3 \approx 1.7$ close to that we have found for fractures. An interesting feature of this distribution is that it is scaleless: replacing E with $E' = \gamma E$ yields exactly the same law, $dN/dE' \propto E'^{-\beta}$. This is unlike other distributions in this work, such as the recoil energy spectrum of WIMPs (Sec. 1.3). Moreover, the power involved, -1.9, is non-integer; this is characteristic of fractals. This inverse power law and its integral diverge at low energies, perhaps an indication that there is in fact a lower energy scale somewhere.

Another similarity with earthquakes is the waiting-time distribution, also shown in Fig. 5.3. The waiting time w between consecutive events does not follow an exponential distribution as it would for a Poisson process, but instead a law of the form $dN/dW \propto w^{-\alpha} \exp -w/w_0$. This expression contains a wait scale w_0 which must be proportional to the average wait $\overline{w}$; integration by parts yields $\overline{w} = (1-\alpha)w_0$. There is also an inverse-power law term, with exponent $\alpha \approx 0.33$. The average wait time between events above a given threshold is inversely proportional to the number of events above said threshold given by the integral of the Gutenberg-Richter law: $\overline{w} \propto E^{1-\beta}$. This means that the wait scale w_0 must depend on the energy threshold and indeed must scale like $w_0 \propto E^{1-\beta}$, whereas the power law term α must not depend on the energy. Both points are verified in Fig. 5.3. This behavior and the value obtained for the power exponent α are very close to those obtained for earthquakes [87] and are also compatible with those for acoustic emission of fractures in rocks [90].

Among the other similarities are the time correlation in the data and the clustering. The self-correlation function of the binned data is close to a hyperbola, demonstrating long-term correlations in the data. Moreover, the event rate, and the energy rate, increase before and after each event, as demonstrated in Fig. 5.4. Though evident for events of all sizes, the surge is greater for larger

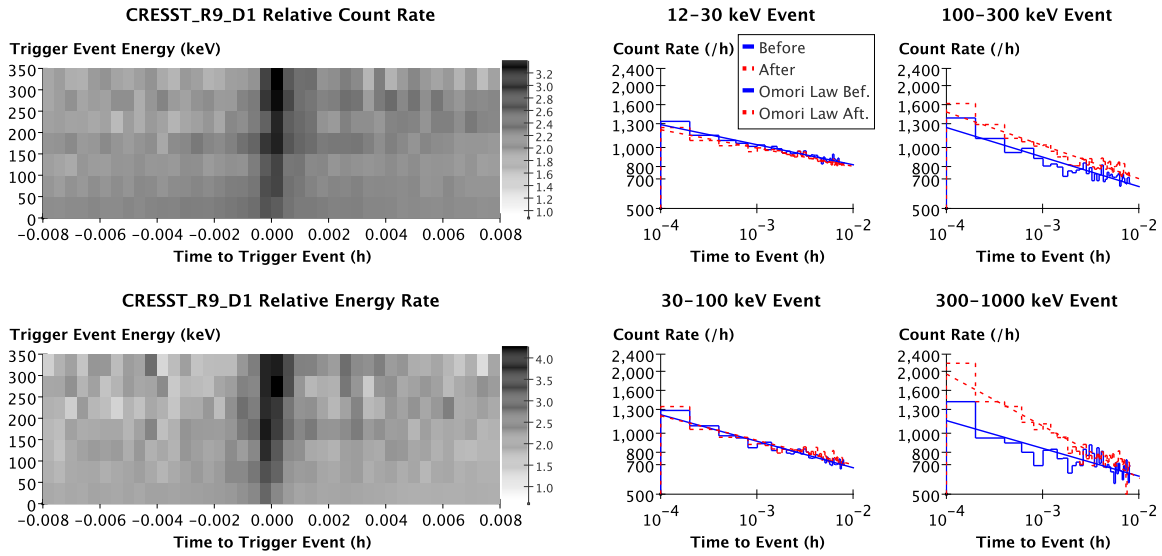

Figure 5.4: Left: distribution of count rate (top) and energy rate (bottom) as a function of time to a given trigger event and the energy of that event. Rates are normalized to average of run. There is a clustering effect as the rates rise around each event. Moreover, the increase becomes more pronounced with event size. Right: count rate around events of different energies. In addition to the increase in rate around events that becomes more pronounced with larger events, an asymmetry in rates before and after events is also visible. Fits are of Omori type, using inverse-power laws.

events. This phenomenon is similar to the foreshocks and aftershocks of earthquakes. F. Omori noted in Equation b of his 1894 paper [91] that the time distribution of aftershocks of earthquakes followed a hyperbola. We find in Fig. 5.4 that the fore- and aftershocks follow a generalization of Omori's expression to inverse power laws [92]. We lastly note an asymmetry, in that the aftershocks are more pronounced than the foreshocks.

5.3 Towards detection of single-bond fractures

It is quite remarkable that the Gutenberg-Richter distribution holds all the way from major earthquakes down to keV energies. Intuitively, one would expect it to break down at energies of the order of the bonds in material, in other words the eV scale. The binding energy in sapphire has been calculated as 7 eV per atom [93]. Reaching such a sensitivity in a $\approx$ cm^2 detector seems a relatively sure extrapolation of the current performances of CRESST-type detectors, and we propose to carry out such an experiment [94] (Sec. 5.5A). The challenge will be stiffer however if the energy going to phonons is much smaller than that used to break bonds, in other words if elementary fractures release energies much smaller than a few eV. Though energies of the order of eVs are routinely reached by microcalorimeters, the typical size of these devices is a few 100 μm, and not necessarily suitable to the indentation-type setup considered here.

An advantage of using a small, $\approx$ cm^2 device for this measurement is that it could be operated at ground level, rather than in the ultra-clean but cumbersome underground setups of CRESST or EDELWEISS, since radioactive background decreases when detector mass decreases, and the expected fracture spectrum rises faster at low energies than the extrapolation of radioactive background does (Fig. 5.5). Other issues that can be investigated include:

- whether or not the rate of fractures depends on the force applied to the indenter, and if there exists a transition-stress regime where the waiting-time distribution becomes a pure inverse-power law with no characteristic scale;

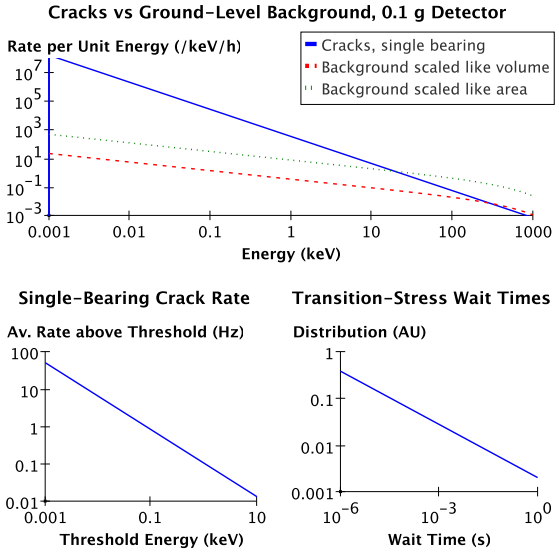

Figure 5.5: Towards single bond measurements. Top: extrapolation of fracture rate and radioactive background at surface level down to bond energies. Fractures should dominate background in a small enough crystal. Bottom left: average rate of fractures should be compatible with calorimetric time constants. Bottom right: distribution of waiting times in putative transition stress limit, where average energy release vanishes. Pile-up will be inevitable, because of inverse power-law type distribution.

- cryogenic fracture in other materials such as the Ge of EDELWEISS or the $CaWO_4$ of CRESST;
- if any predictability is possible in very simple fracture systems;
- if there is any fracto-emission of photons or other particles [95] that could ultimately hamper the background rejection capabilities of ionization-phonon or scintillation-phonon type detectors.

Overall, these cryogenic measurements could provide new insight into brittle fracture, despite being harder to carry out than conventional, room-temperature, acoustic-emission measurements.

5.4A Cryogenic fracture

Ref. [85].

Available online at www.sciencedirect.com
SCIENCE DIRECT
Physics Letters A 356 (2006) 262–266
PHYSICS LETTERS A
www.elsevier.com/locate/pla

Fracture processes observed with a cryogenic detector

J. Åström [f], P.C.F. Di Stefano [a,h], F. Pröbst [a], L. Stodolsky [a,*], J. Timonen [g], C. Bucci [d], S. Cooper [c], C. Cozzini [a], F.v. Feilitzsch [b], H. Kraus [c], J. Marchese [c], O. Meier [a], U. Nagel [b,i], Y. Ramachers [j], W. Seidel [a], M. Sisti [a], S. Uchaikin [a,e], L. Zerle [a]

[a] *Max-Planck-Institut für Physik, Föhringer Ring 6, D-80805 Munich, Germany*
[b] *Technische Universität München, Physik Department, D-85747 Munich, Germany*
[c] *University of Oxford, Physics Department, Oxford OX1 3RH, UK*
[d] *Laboratori Nazionali del Gran Sasso, I-67010 Assergi, Italy*
[e] *Joint Institute for Nuclear Research, Dubna 141980, Russia*
[f] *CSC–IT Center for Science, P.O. Box 405, FIN-02101 Esbo, Finland*
[g] *Department of Physics, P.O. Box 35 (YFL), FIN-40014 University of Jyväskylä, Finland*
[h] *Institut de Physique Nucléaire de Lyon, Université Claude Bernard Lyon I, 4 rue Enrico Fermi, 69622 Villeurbanne cedex, France*
[i] *Institute of Chemical Physics and Biophysics, EE-0026 Tallinn, Estonia*
[j] *University of Warwick, Department of Physics, Coventry CV4 7AL, UK*

Received 19 December 2005; received in revised form 22 March 2006; accepted 25 March 2006

Available online 3 April 2006

Communicated by R. Wu

Abstract

In the early stages of running of the CRESST dark matter search using sapphire detectors at very low temperature, an unexpectedly high rate of signal pulses appeared. Their origin was finally traced to fracture events in the sapphire due to the very tight clamping of the detectors. During extensive runs the energy and time of each event was recorded, providing large data sets for such phenomena. We believe this is the first time the energy release in fracture has been directly and accurately measured on a microscopic event-by-event basis. The energy threshold corresponds to the breaking of only a few hundred covalent bonds, a sensitivity some orders of magnitude greater than that of previous technique. We report some features of the data, including energy distributions, waiting time distributions, autocorrelations and the Hurst exponent. The energy distribution appear to follow a power law, $dN/dE \propto E^{-\beta}$, similar to the power law for earthquake magnitudes, and after appropriate translation, with a similar exponent. In the time domain, the waiting time w or gap distribution between events has a power law behavior at small w and an exponential fall-off at large w, and can be fit $\propto w^{-\alpha} e^{-w/w_0}$. The autocorrelation function shows time correlations lasting for substantial parts of an hour. An asymmetry is found around large events, with higher count rates after, as opposed to before, the large event.
© 2006 Elsevier B.V. All rights reserved.

1. Introduction

In the spring of 1999 preliminary runs of the CRESST dark matter search [1] were carried out at the Gran Sasso Laboratory (LNGS), a deep underground laboratory for low background physics located in the Apennines. In these first runs of CRESST a phenomenon was observed which we believe may be of interest for the study of crack and fracture formation in brittle materials. CRESST is a cryogenic detector, working in the vicinity of 10 milli-Kelvin [2]. In addition to being deep underground for shielding against cosmic rays, it is carefully designed to minimize effects of radioactive background. The detector elements were large (262 gram) high quality single crystals of sapphire, with a strip of superconductor (W) evaporated on one surface to serve as a sensitive thermometer. This system, as shown by tests with gamma ray sources, detects single events in the sapphire with energies in the range from about 1 keV to several hundred keV with good energy resolution (0.5 keV) and good time resolution (40 or 100 μs for the onset of a pulse).

* Corresponding author.
E-mail address: les@mppmu.mpg.de (L. Stodolsky).

0375-9601/$ – see front matter © 2006 Elsevier B.V. All rights reserved.
doi:10.1016/j.physleta.2006.03.059

In order to reach these low temperatures it is important to eliminate the effects of any vibrations ("microphonics") that might deliver energy to the crystal. Thus in addition to special suspensions to isolate the apparatus, the crystals are held very tightly in their holders to prevent any even microscopic frictional effects. In the data to be discussed here this was effected by small sapphire balls held against the sapphire crystal by a plastic clamp. The plastic of the clamp, Delrin, is known to contract substantially at low temperature, thus providing additional "tight holding". An unanticipated result of the small contact area of the hard sapphire balls and the great force of the clamp turned out to be a cracking or fracturing of the sapphire. This was observed as follows.

When the system was first brought into operation, an unexpectedly high rate of signal pulses was observed. Initial fears that this might be due to an unexpected radioactive contamination were relieved by the observation that even an unknown radioactive contamination must be Poisson distributed in time, while the unexpected pulses appeared rather to come in "bursts" or "avalanches". Examination of the time distributions showed that they were indeed non-Poissonian.

Pulse formation and fractures. The pulses themselves resembled those seen from good particle events. However, this is a rather unspecific criterion, due to the operating characteristics of the detector. There are essentially three steps in the production of a signal pulse (1) a relatively localized energy release within a short time; (2) a rapid degradation of this energy into a uniform "hot" (~ 10 K) gas of phonons produced through phonon–phonon interaction and decay, as well as interaction with the crystal surface; (3) absorption of the phonons in the thermometer strip. This leads to a heating with an increase of electrical resistance for the superconductor, which is finally read out by SQUID electronics. The resulting pulse shape is well described by a model employing the various thermal and electrical parameters of the system [3]. As may be seen from this brief description, the pulse shape is essentially determined by the thermal responses of the system and not by the initiating event, as long as it is "fast". Hence any release of a given energy in the crystal in a short time (μ seconds) leads to the same pulse shape and so examination of the pulses does not lead to an identification of their origin. An extensive search for the origin of the pulses was finally successful when it was noticed that there appeared to be markings or scratches on the crystal at the contact points with the sapphire balls. When the sapphire balls were replaced by plastic stubs, which are evidently much softer, the event rate immediately dropped from some thousands per hour to the expected few per hour.

These observations strongly suggest that the pulses were due to some kind of cracking or micro-fracturing phenomena in the sapphire crystal and/or its support balls. Indeed, examination under a microscope revealed a small crater with radiating irregular fissures extending sideways and down into the crystal. Damage to the sapphire balls was also observed. Since the reduction in rate after the exchange of the sapphire balls was so large, we believe the data taken with the sapphire balls are essentially all fracture events. If we accept this crack or fracture hypothesis, our data then represent a large sample of well measured fracture events, under low background conditions, and with good time and energy determination.

Calibration runs. In order to calibrate the energy scale regular calibration runs were carried out. In these runs the system is left undisturbed and a radioactive source supplying 120 keV photons (which can penetrate to the detectors) is inserted in an external plug in the shielding. These photon-induced events can be selected by using the resulting 120 keV peak in the data. Since a radioactive source produces statistically independent events, that is Poisson statistics, these events provide a useful comparison when studying statistical properties of the data.

2. Energy distributions

We believe this is the first time that the energy release in microfracture has been accurately measured on a microscopic event-by-event basis.

It is to be emphasized that the cryogenic method provides an *absolute* measurement of the *total* energy release in the fracture. This is to be contrasted with the study of acoustic emission in materials or seismic measurements of earthquakes. There the energy determination is necessarily indirect since there are various assumptions and uncertainties concerning production, propagation, and detection involved in translating the observed signals into the true energy of the event. On the other hand, the cryogenic method, essentially calorimetric in character, is a direct measurement of the full energy. The energy scale is fixed by the calibration with known sources and the resulting accuracy of the CRESST energy determination is on the order of a few percent [1].

In addition to the directness of the energy measurement an important feature of the cryogenic method is its great sensitivity. The closest previous technique appears to be the study of acoustic emission in materials [4,5]. There the smallest emitting region considered is on the order of a square micron.[1] This will correspond to the breaking of $\sim 10^7$ bonds in the crystal. On the other hand, our energy threshold is typically some keV (Fig. 1). This corresponds to the breaking of only a few hundred or thousand bonds. Thus the cryogenic method appears to be many orders of magnitude more sensitive than previous technique. Small cryogenic devices can even be sensitive to energies in the eV range [2] and it is possible that studies of this type involving stress release of only a few atoms are feasible [6].

In Fig. 1 we show the differential distribution dN/dE for the number of events N per unit energy, for four data sets with two detectors from run 9. The straight line is the result of a power law fit

$$\frac{dN}{dE} \propto E^{-\beta} \tag{1}$$

to the lowest curve, which yields $\beta \approx 1.9$. Similar results are found from fits to other data sets. From a total of seven sets ex-

[1] L.M. Rogers, Ref. [5] defines magnitude zero—the smallest event—as a microfracture of size 1 μm^2. The use of the square dimension stems from the slip-plane picture of the fracture.

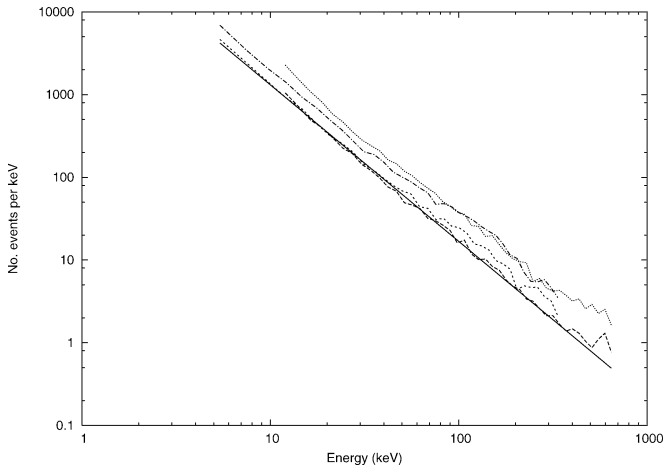

Fig. 1. Energy spectra from four data sets of run 9, with 53 hr for the upper pair of curves and 28 hr for the lower. The straight line shows a fit to the lowest curve $\propto E^{-\beta}$, yielding $\beta \approx 1.9$.

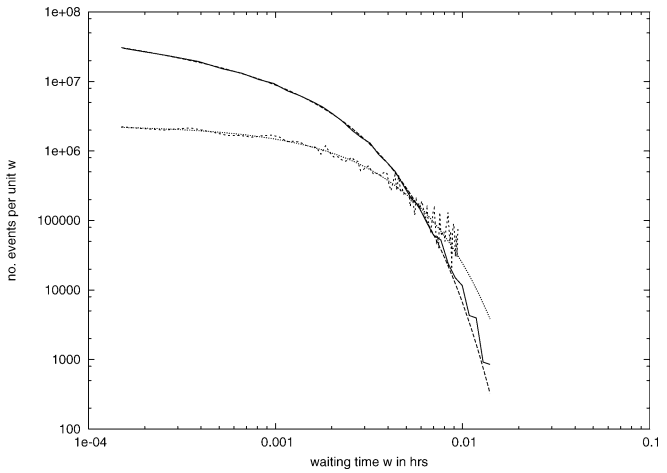

Fig. 2. Waiting time distributions. Upper curve: fractures, fit to $\propto w^{-\alpha}e^{-w/w_0}$. Lower curve: photon-induced events from a calibration run, fit to $\propto e^{-w/w_0}$.

amined (from runs 9, 10 and 11) β ranged between 1.7 and 2.0. An interesting point is that the rates do not appear to differ greatly from one data set to another, despite the fact that different crystals and mountings are often involved. At 21 keV for example, the rates over the various data sets vary between 4 and 11 pulses/keV h.

A power law of this type, called the Gutenberg–Richter law [7], is well known for the "magnitudes" of earthquakes. Unfortunately the "magnitude" is a seismic amplitude and not a direct measurement of the energy of an earthquake. Thus a simple comparison is not possible. However if one takes the prescription that the seismic amplitude to approximately the 3/2 power [7,8] represents the energy, and uses the power ≈ 1.0 found for the *integral* distribution of earthquake magnitudes [8], it corresponds to $\beta \approx 1 + \frac{2}{3} \approx 1.7$, not far from our $\beta \approx 1.7$–2.0. Of course, the six orders of magnitude range available for seismic data is much greater than the one or two orders of magnitude available here.

It should also be noted that such power law, that is scale free, distributions appear in many phenomena, often related to an underlying fractal process [9]. In the acoustic emission recordings of microfracture events in brittle materials, for example, such a distribution typically appears, with a somewhat lower exponent, $\beta \approx 1.5$ [4].

3. Time series

Waiting time distributions. A useful quantity in the study of intermittent data such as the present is the "waiting time" w. To each event i we assign w_i, the time interval till the next event, and study the distribution of these intervals. Fig. 2 shows the waiting time distribution for detector 2 in a 28 hr data set of run 9. The distribution has power law behavior at small w and an exponential fall off at large w, and an accurate fit is obtained with $dN/dw \propto w^{-\alpha}e^{-w/w_0}$, with $\alpha = 0.33$. Similar results are found for other data sets with α in the range 0.25–0.5. The parameter w_0 determines the location of the crossover from power law to exponential and is essentially the inverse rate or average waiting time, with $\bar{w} = (1-\alpha)w_0$. Qualitatively similar results, with α near to or somewhat less than one, have been reported for earthquakes in California [10].

For the simple case of Poisson statistics, one expects a waiting time distribution $\propto e^{-w/w_0}$, where $1/w_0$ is the average count rate. The lower curve of Fig. 2 shows the waiting time distribution for the photon-induced events of a calibration run, with a fit to $\propto e^{-w/w_0}$. As expected there is a good fit, and with $1/w_0$ in agreement with the event rate.

An interesting point concerns the behavior of w_0 for fracture events as the energy threshold for the sample is raised. It appears that the form $w^{-\alpha}e^{-w/w_0}$ is preserved, with α varying little. Since the count rate is reduced however, the value of w_0 increases and so the crossover between power law and exponential behavior moves to larger w. Indeed, taking a given data set (run 9-d2, 100 μs), repeatedly raising the energy threshold and fitting for w_0, we find a linear relation between the inverse count rate, that is $\bar{w}$, and the fitted w_0. The slope and the relation $\bar{w} = (1-\alpha)w_0$ then gives a global determination $\alpha \approx 0.26$.

The power law behavior for the waiting times at small w, as well as the power law for the energy distribution in the previous section, is suggestive of an underlying scale-free processes without any intrinsic dimensional parameter, as is common in fractal processes [9]. However, this cannot be entirely true here since w_0 is a time and has dimensions. Since e^{-w/w_0} corresponds in fact to a Poisson distribution, this may suggest an interpretation in terms of some basic scale free processes where several such processes are occurring independently and simultaneously and so are overlapping in the data. This arises trivially if the signals originate from more than one of the support points of the crystal, of which there were several; but one can also imagine independent crack systems beneath one support point.

The increase of w_0 as the count rate goes down suggests that the limit of zero count rate is a kind of critical point: the waiting time becomes infinite as the distribution becomes non-integrable and completely scale free, while $1/w_0$ appears as a diverging correlation length. Understanding w_0 is an interesting point for further study.

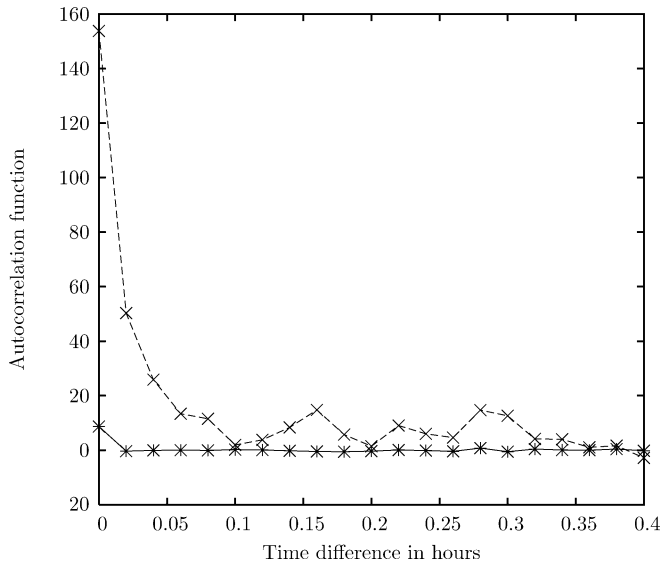

Fig. 3. Autocorrelation function C for the event rate from calibration data of run 10. The lower curve is for photon-induced events (events in the 120 keV peak), and the upper curve is for fractures plus some admixture of Compton scatters (events below the peak). For the photons the data is consistent with $C = 0$ for $(t - t') \neq 0$ as expected for Poisson statistics, with $C(0) = \text{Variance} = \bar{R}$.

Correlations in time. We expect the existence of correlations in time, corresponding to the "bursts" or "avalanches". We use the event rate R_t of a calibration run to construct the autocorrelation function

$$C(t - t') = \overline{(R_t - \bar{R})(R_{t'} - \bar{R})} \tag{2}$$

and compare C for photon-induced events and fractures in Fig. 3. While for photons we have $C = 0$ as expected, for the microfractures there are correlations lasting for substantial fractions of an hour. These long-term correlations are found for the fracture events of all data sets. The physical origin of the correlations may be in stress relaxation phenomena where a slow "diffusion" of strain [11] can trigger new microfractures when meeting other weak spots in the crystal.

Hurst exponent. The autocorrelations as in Fig. 3 can be approximately fit to power laws $\propto (t - t')^{-p}$. As noted above, this is suggestive of the scale free, self-similar behavior associated with fractal statistics. A way of characterizing such behavior is in terms of what is called the Hurst exponent H; and we can check the plausibility of such a description by comparing the consistency of H found in different ways. Table 1 shows H found in three ways for various data sets. First the autocorrelation exponent p is fitted to find $H = 1 - p/2$. The next column shows H determined by the "growth of the standard deviation", a characterization of the fluctuations in the event rate $\sim t^H$, where $t^{0.5}$ would be the classical Gaussian or random walk behavior with finite range correlations. Finally, the last column gives H found from the "Shannon entropy", related to the probability of the number of events over a time interval t [12]. Although the fits were not all excellent and there is considerable fluctuation in the results, the overall rough consistency of the three determinations supports the picture of a scale free, self-similar process. We do not necessarily expect the same H for different data sets since these involve different energy thresholds and sensitivities.

Table 1
Exponent H found by different methods. d1 and d2 refer to the two detectors in operation, and 40, 100 μs to different digitization windows used in data taking in run 9

Data set	Autocorr.	Stnd. dvtn.	Sh. entropy
Run 9 d1 100 μs	0.77	0.70	0.69
Run 9 d2 100 μs	0.80	0.80	0.80
Run 9 d1 40 μs	0.73	0.70	0.67
Run 9 d2 40 μs	0.69	0.70	0.65
Run 10 d2	0.59	0.63	0.59
Run 11 d1	0.60	0.64	0.53
Run 11 d2	0.69	0.66	0.62

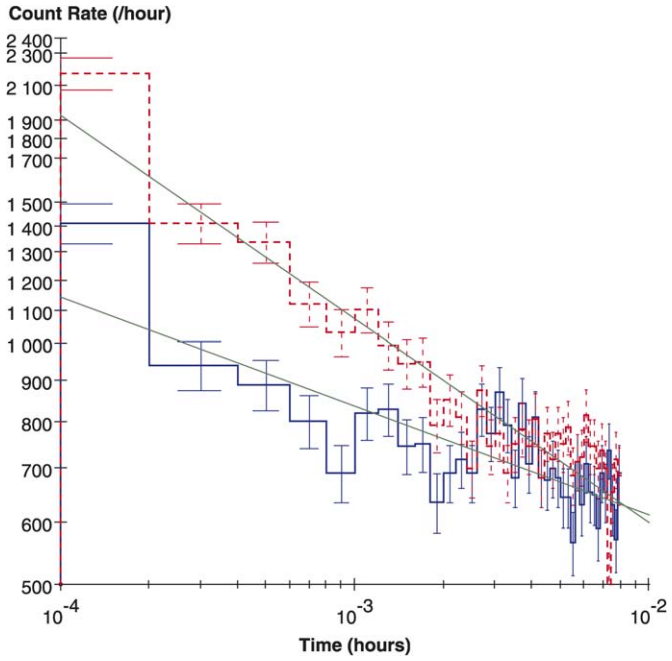

Fig. 4. Count rates in the vicinity of "big events", showing a time asymmetry "before" and "after" the "big events". From a 53 hr data set of run 9, plotted in 0.72 s bins. The upper (dotted, red) histogram is for times following the "big event" and the lower (solid, blue) histogram for times preceding the "big event". The straight lines are power law fits, yielding a power 0.13 ± 0.01 "before" and a power 0.25 ± 0.01 "after". There were 1082 "big events", defined as a single pulse with $E > 300$ keV. The average rate in the run was 526/h. (For interpretation of the references to colour in this figure legend, the reader is referred to the web version of this Letter.)

4. Clusters

A frequently used concept in the earthquake literature is the "Omori cluster": a "big shock" followed by "aftershocks". As Fig. 1 shows, and as is also the case for earthquakes, there is no separate class of high energy events—no distinctive "big shocks". Naturally, as should be expected from the "avalanches" or correlations, given any event, there is a general increase in rate at nearby times. Although this increase is quite substantial (a factor four with one second bins, see Fig. 4) this simply

reflects the "bursts" or "avalanches" and is not specific to "big events".

More specific to "big events", however, we find a time asymmetry with respect to "before" and "after". That is, there is on average more activity after, as opposed to before, "big events". Fig. 4 shows the count rate from a data set of run 9, for times close to "big events", with "after" (upper histogram) and "before" (lower histogram) plotted separately. "Big" was defined as a pulse with $E > 300$ keV. The bin size is 2.0×10^{-4} h = 0.72 s. One notes a significantly higher rate in the first bin "after" relative to that in the first bin "before". There is a reasonable fit to a power law for the decline in the rate toward the average value, and a significantly steeper power "after" relative to that "before" is found. Similar results are obtained for other data sets.

An asymmetry of this type appears to exist in seismic data and certain models [13] and seems to indicate that the "big events" tend to occur early in the "bursts".

5. Crack propagation and material properties

Our material is a single crystal of high purity.[2] In crack propagation models the growing stress enhancement at the crack tip implies that a "hard spot" is necessary to limit the propagation of a crack; thus when a homogeneous stress is applied to a defect-free material there is nothing to stop a propagating crack. Presumably the microfractures here were limited by the random, non-homogeneous stress and defect field which quickly arises as fractures form in the pure material. This may have been assisted by the damage to the small sapphire balls, leading to an irregular application of the stress. Although we speak of "cracks", it should be kept in mind that from our simple observation of pulses we cannot infer the exact nature of the microfracture. Finally, with respect to materials it should be noted that our system is of course quite opposite to those in the geological context, where one has highly heterogeneous systems, while here we have a very pure material.

6. Development of the technology

It is interesting to contemplate the extension of this method in the study of fracture phenomena. The superconducting thermometer, and perhaps other cryosensors [2], can be applied to many materials. The very low temperature and large crystals of the dark matter search would not always be needed, and indeed it might be possible to follow the crack development in time with a smaller and thus faster system. However, low background conditions may still be necessary to avoid contamination of the data by non-fracture events. In the present data the crystal was contacted by several of the small sapphire balls, and we are unable to determine where an event originates. Such effects lead to a dilution of correlations, which thus may be intrinsically much stronger than appear here. In an apparatus especially designed for such studies one could arrange to have only one "hard" contact and with a known force. Finally, since the energy range available is relatively small compared to that for earthquakes it would be useful to consider techniques for increasing the dynamic range.

[2] The crystals were high quality single crystals, optically defect free. One was supplied by the Hemex company, the other by BEC Breznikar.

References

[1] For recent CRESST results on dark matter see: G. Angloher, et al., Astropart. Phys. 23 (2005) 325, astro-ph/0408006;
For the apparatus as it was in operation here, see: M. Sisti, et al., Nucl. Instrum. Methods A 466 (2001) 499.
[2] For a general introduction to cryogenic detectors see L. Stodolsky, Phys. Today (August 1991);
Or see N. Booth, B. Cabrera, E. Fiorini, Annu. Rev. Nucl. Part. Sci. 46 (1996) 471.
[3] F. Pröbst, et al., J. Low Temp. Phys. 100 (1995) 69.
[4] P. Diodati, F. Marchesoni, S. Piazza, Phys. Rev. Lett. 67 (1991) 2239;
G. Caldarelli, F.D. Di Tolla, A. Petri, Phys. Rev. Lett. 77 (1996) 2503;
A. Garcimartín, A. Guarino, L. Bellon, S. Ciliberto, Phys. Rev. Lett. 79 (1997) 3202;
C. Maes, A. Van Moffaert, H. Frederix, H. Strauven, Phys. Rev. B 57 (1998) 4987.
[5] A useful overview of acoustic emission is given by L.M. Rogers, in: Structural and Engineering Monitoring by Acoustic Emission Methods—Fundamentals and Applications, Lloyd's Register, 2001.
[6] It is conceivable that such events have been detected as "excess noise" in certain cryodetectors. See the remarks by L. Stodolsky, in: Proceedings LTD-11, Tokyo 2005, Nucl. Instrum. Methods, in press.
[7] B. Gutenberg, C.F. Richter, Seismicity of the Earth, Hafner, 1965.
[8] K. Christenson, L. Danon, T. Scalon, P. Bak, Proc. Natl. Acad. Sci. 99 (1) (2002) 2509.
[9] A general review of such concepts may be found in B.J. West, M. Bologna, P. Grigolini, Physics of Fractal Operators, Springer-Verlag, 2003.
[10] N. Scafetta, B.J. West, Phys. Rev. Lett. 92 (2004) 138501.
[11] M.S. Mega, et al., Phys. Rev. Lett. 90 (2003) 188501.
[12] N. Scafetta, P. Grigolini, Phys. Rev. E 66 (2002) 036130;
For these issues in the geological context see J. Kruhl (Ed.), Fractals and Dynamic Systems in Geoscience, Springer-Verlag, 1994.
[13] A. Helmstetter, S. Hergarten, D. Sornette, Phys. Rev. E 70 (2004) 046120.

5.5A Towards single bonds

Ref. [94]

LYCEN 2007-14

Brittle fracture down to femto-Joules — and below

J. Åström[2], P.C.F. Di Stefano[1*], F. Pröbst[4], L. Stodolsky[4], J. Timonen[3]

[1] *Institut de Physique Nucléaire de Lyon, IPNL,*

UMR5822, CNRS-IN2P3; Université de Lyon,

Université Claude Bernard Lyon 1, F-69622 Villeurbanne, France;

[2] *CSC - IT Center for Science, P.O.Box 405, FIN-02101 Esbo, Finland;*

[3] *Department of Physics, P.O. Box 35 (YFL),*

FIN-40014 University of Jyväskylä, Finland;

[4] *Max-Planck-Institut für Physik, Föhringer Ring 6, D-80805 Munich, Germany;*

[*] *Corresponding author, email address: distefano@ipnl.in2p3.fr.*

(Dated: September 24, 2007)

arXiv:0708.4315v2 [cond-mat.mtrl-sci] 21 Sep 2007

Abstract

We analyze large sets of energy-release data created by stress-induced brittle fracture in a pure sapphire crystal at close to zero temperature where stochastic fluctuations are minimal. The waiting-time distribution follows that observed for fracture in rock and for earthquakes. Despite strong time correlations of the events and the presence of large-event precursors, simple prediction algorithms only succeed in a very weak probabilistic sense. We also discuss prospects for further cryogenic experiments reaching close to single-bond sensitivity and able to investigate the existence of a transition-stress regime.

PACS numbers: 62.20.Mk,91.30.Px,07.20.Mc

We have recently described a serendipitous and novel measurement of brittle fracture using cryogenic calorimetry[1]. In a 260 g pure sapphire crystal cooled to 20 mK, cracks formed under pressure from sapphire bearings in what amounts to a sharp indentation experiment (Fig. 1, 2). The small contact surfaces generated stress fields vanishing quickly with distance, and ensured stability of the fractures[2]. The calorimetric measurement provided a direct measurement of the energy of the phonons from fracture events, and great sensitivity, of the order of a few femto-Joules. The rich and complete event catalogues, of many thousand femto-fractures each, contain the arrival time and energy of each event, and show several statistical similarities to earthquakes, despite the many orders of magnitude difference in the energy ranges[3]. The similarities include: (*i*) the probability distribution of fracture-energy release is a power law with an exponent close to that of the differential Gutenberg-Richter relation expressed for seismic moment (which is proportional to earthquake energy)[4], (*ii*) fracture events are long-range correlated in time with a power-law waiting-time distribution for short times, (*iii*) the fracture time series has the characteristics of fractal Gaussian intermittant noise, and (*iv*) there is an elevated event rate right after large events and a power-law event rate decay. More generally, the absence of trends in the data indicate that this represents a new example of steady-state slow brittle fracture, in an ordered system. Up to now, such fracture has been linked to the disorder inherent in self-organized-criticality[5,6,7].

In the following, we show that the waiting-time distribution follows a general power-law exponential form observed in earthquakes and rock fracture, with the same power. We demonstrate further correlations in the data and attempt to use them as predictors of the large, catastrophic fractures that should eventually occur. Lastly, we discuss a dedicated cryogenic experiment to study these phenomena, down to energies close to those of single bonds in the crystal. Such an experiment could also probe putative stress-dependent variations of the fracture rate, and investigate the existence of a transition-stress regime where the average energy release would vanish.

I. WAITING TIMES AND CLUSTERING

We have shown[1,8] that the distribution of the waiting time between consecutive events above threshold, w, follows a power law at short times with an exponential fall-off at large waits: $dN/dw \propto w^{-\alpha} \exp -w/w_0$. The form of this waiting-time distribution is identical

to that observed for earthquakes and rock fracture, further extending its validity[9]. Similar forms may be derived from the Gutenberg-Richter and Omori laws[10]. The average wait must be proportional to the scale term w_0; integration by parts yields: $\overline{w} = (1-\alpha)w_0$. On the other hand, the distribution of events as a function of energy follows a power law: $dN/dE \propto E^{-\beta}$, with $\beta \approx 1.9$[1]. By integration, the number of events above a given energy therefore also follows a power law: $N(\geq E) \propto E^{-\beta+1}$. This is inversely proportional to the average waiting time for events above a threshold: $\overline{w(\geq E)} = (1-\alpha)w_0(\geq E) \propto E^{\beta-1}$. Fig. 3 shows that, as threshold energy increases, the distribution of waiting times retains the form $w^{-\alpha}\exp\left(-w/w_0(\geq E)\right)$, where the power α has little dependence on the threshold energy and w_0 scales like $E^{\beta-1}$. A fit of the wait power yields $\alpha = 0.33 \pm 0.01$. With the notations from Ref.[9], we find $B = \frac{1}{1-\alpha} = 1.49 \pm 0.02$ and $\gamma = 1-\alpha = 0.67 \pm 0.01$. These values are strikingly close to those obtained for earthquakes[3] and are also compatible with those for acoustic emission of fractures in rocks[9].

If the energy distribution can be extrapolated to values large enough to cause a catastrophic destruction of the detector itself, then such a catastrophic event would arrive in a long, perhaps, but finite, time. If E_{cat} is the energy released as the crystal breaks, then, in this setup, it would be expected after $\overline{w_{cat}} = w_0(\geq E)\left[E_{cat}/E\right]^{\beta-1} \approx (0.003\text{ h}) \times \left[E_{cat}/(10\text{ keV})\right]^{0.9}$. This scales slightly slower than a linear relation. To obtain an order of magnitude of the timescales involved, we assume the fracture surface energy of sapphire is an upper limit on the energy that would be released by a crack. For instance, taking a value of 7.3 J/m^2 $\approx 4.5 \times 10^{12}$ keV/cm^2 for the surface energy of the $\{\bar{1}012\}$ plane[11], and defining a catastrophic crack size as 1 cm^2 in the $4 \times 4 \times 4$ cm^3 cubic crystal, this translates to an upper bound of $E_{cat} \leq 4.5 \times 10^{12}$ keV. The weak upper limit on the expected wait for such a catastrophic event is therefore several millenia.

The distribution of time intervals between all, rather than consecutive, events above various energies is shown in Fig. 4. As energies increase, the distribution becomes more and more peaked at low time intervals. This is further indication that the large events cluster[1]. As a control, the same analysis is applied to a random shuffle of the arrival times in the data. In the shuffle, there is no energy-dependent effect.

II. WEAK PREDICTABILITY

Some examples of event-energy time series from a 50 h run containing $\approx$ 30000 events above a threshold of 12 keV are shown in Fig. 5. Various cases are visible, including a large event with a precursor ($t \approx 16.154$ h), a relatively isolated large event ($t \approx 22.915$ h), and a lull before a large event followed by aftershocks ($t \approx 22.93$ h). In Figures 6 A and A', we plot the average value of the waiting time before each of the $\approx$ 14000 small events (12–30 keV) and $\approx$ 1100 large events (300-1000 keV). The waiting times for small (respectively large) events are here defined as the wait between a small (resp. large) event and the preceeding event regardless of its size. On average, there is less wait before large events (0.0013 h) than before small events (0.002 h). To check if this a statistical fluctuation, we generate 100 shuffles of the data set, by randomly permuting the arrival times of the events, then do the same analysis as on the original data. The distribution of the average values of the shuffles does not cover the spread of the real values, confirming that in the actual data, the wait is shorter before large events than before small ones. This appears to be another manifestation of the increase in rate which is particularly evident around large events[1].

These and the numerous other correlations present in the data provide motivation to attempt prediction of large events, a challenge of relevance for other phenomena, ranging from avalanches in snow[12] to earthquakes[4]. Fig. 6 B compares the distribution of waiting times before small and large events. The significant correlations present on average are much harder to exploit on an event-per-event basis, as the distribution for large events does not differ greatly from that for small events.

We also attempt to predict the arrival of large events using the distribution of events in a given time window (Fig. 6 C). Window duration is 0.002 h, corresponding to the average waiting time in the run. For comparison, we generate 5000 random intervals. The difference between the distribution of counts in the random intervals and in the intervals preceeding small or large events is slim, while the difference between intervals preceeding small and large events is slighter yet. With these simple methods, predictability of individual large events is therefore poor.

While the weak predictability we have described here could perhaps be enhanced by more sophisticated algorithms, it might also be either a general conclusion for brittle fracture, or indicate that, in our particular setup, the combination of several crack systems propagating

independently masks any individual patterns and predictability.

III. PROSPECTS FOR FURTHER STUDY

Further study would benefit from a dedicated cryogenic detector with only a single bearing creating the cracks. It could allow investigation of fractures down to low energies. Additionally, if fracture rate is found to depend on applied stress, it might allow investigation of low rates close to a possible transition stress at which fractures just appear. If such a regime exists, the waiting-time distribution would be a pure power-law, and the whole system could be in a critical transition at which the average energy release rate vanishes.

One option would be to carry on in a low-background, deep-underground setup, such as that of the CRESST II experiment[13]. An existing detector holder could be modified to include a single bearing pressing against one end of the cylindrical crystal of 40 mm height and 40 mm diameter. In itself, this will require some ingenuity as the crystal itself must not move because of the bearing but cannot, for thermal reasons, be held firmly by large contact areas. One of the currently standard $CaWO_4$ crystals could be used, or a new Al_2O_3 one could be manufactured. In either case, it would be interesting to retain the light detector of the CRESST II setup to see if crack formation is accompanied by light emission, since fracto-emission of photons and electrons has been reported in other crystals[14]. Adjusting the tightness of the spring pressing the bearing to probe an effect on crack rate, and to reach transition stress if it exists, would have to be done between cryogenic cycles and would require some trial and error. As in the original work, energy calibration would be obtained by an external, removable, ^{57}Co source, providing 122 keV photons. Lower-energy calibration would be obtained via heater pulses. It should be possible to lower the phonon threshold down to around 1 keV compared to the $\approx$ 10 keV in this work, though this gain would probably not be significant from the standpoint of brittle fracture. Another underground setup that could be of interest is that of the EDELWEISS experiment which uses germanium ionization-phonon detectors[15]. In this case, there would be a simultaneous measurement of the phonons created by the cracks as well as of whatever ionization the cracks create[14].

Though the original work was carried out in a special low-background environment underground, it would be simpler if in the future it could be done in a standard cryostat on the surface. For this, the rate of crack events must be much larger than the rate of other events;

this means that though a low-threshold experiment may be feasible, a transition-stress one will be difficult. The rate of crack events may depend on the force pressing the bearing against the crystal but does not depend on the mass of the crystal itself. We assume that in a dedicated experiment, there would be only a single bearing rather than a dozen as in the original work, and therefore divide the original rate by 12. The competing backgrounds, mainly cosmic-ray-induced particles and radioactivity of the detector and its surroundings, both increase with detector mass. As illustration, we extract a rough estimate of the sum of these backgrounds from previously published data for a partially shielded 1 kg sapphire detector at the Earth's surface[16]. Between the threshold of 50 keV and $\approx$ 1 MeV, the background follows the product of an inverse power law, with an exponent of 0.6, and a decaying exponential, with a typical energy of $\approx$ 600 keV, high above the range relevant here. In Fig. 7, we compare the scaled rate of cracks to the backgrounds in an 0.1 g sapphire detector for two different scaling laws of the background as a function of detector mass m: scaling proportional to mass (i.e. volume, $\propto m$), and scaling proportional to surface area ($\propto m^{2/3}$). In both cases, we assume that the background power-law holds below 50 keV. A significant background proportional to the surface area comes from cosmic muons of which there are $\approx$ 1 cm^{-2} min^{-1} depositing $\approx$ 500 keV per mm of Al_2O_3 passed through[17]. Working at ground-level will require some combination of small crystals, low threshold, and, if possible, increased crack rate, though this last point is incompatible with a reduction in stress to the level at which fractures may nearly vanish. Energy calibration of a small crystal requires a low-energy radioactive source such as ^{55}Fe; the source must be placed within the cryostat for calibration, though it may be possible to remove it or block it during data-taking for fractures. Such a small crystal could have a threshold of less than a few hundred eV, and as energy decreases, the crack rate ($\propto E^{-1.9}$) rises faster than the extrapolated background ($\propto E^{-0.6}$).

In addition, an energy threshold below a few eV could make the device sensitive to the rupture of single sapphire bonds. A binding energy of 7.34 eV per atom has been reported for Al_2O_3[18], though it is not apparent to us what phonon energy accompanies rupture of a bond. A 10 eV threshold is achievable given current, $\approx$ cm^2, cryogenic detector development. For instance, the CRESST experiment has developed thin silicon calorimeters, of surface area several cm^2 and thickness about 0.5 mm, with thresholds better than 40 eV[19,20]. These detectors are optimized for light detection rather than for a low threshold per se. A smaller,

parallelipiped-shaped, Al_2O_3 device, measuring $5 \times 5 \times 1$ mm^3 (m=0.1 g), with an optimized thermometer, should be able to reach lower thresholds, while remaining large enough for a pressure-bearing 1 mm diameter sapphire or diamond ball. The device could be mounted ≈ 1 mm from a CRESST-type light detector of similar size, to see any light produced by the fractures[14]. We note that to obtain an absolute energy calibration at 6 keV from ^{55}Fe and to have a threshold of 10 eV will require a dynamic range of about three orders of magnitude which may be difficult to obtain with a transition-edge sensor. Another challenge will come from the rate of cracks. Detectors of size $3 \times 3 \times 0.5$ mm^3, optimized for speed rather than threshold, reach rise times of ≈ 1 μs[21] (smaller devices in which the transition-edge sensor itself is the absorber can be an order of magnitude faster[22]). Though this may be compatible with the average rate of cracks, pileup will be inevitable, even for an arbitrarily fast detector, since the distribution of waiting times contains an inverse-power-law term (Fig. 7).

The calorimetric technique is readily applicable to many other dielectric materials, such as $CaWO_4$, Ge and Si already mentioned. As we have stated, we are not however aware of a clear relationship between the elastic energy used to break bonds and the elastic energy left over in phonons which we measure. Nonetheless, the partition of energy is simpler than in the case of acoustic emission, where only a fraction of phonons are measured. The calorimetric technique could therefore provide new insight into the mechanics of fracture.

IV. CONCLUSION

The distribution of waiting times between brittle fracture events observed in a cryogenic detector contains a power-law term which is independent of energy threshold and an exponential scale that depends on it. This form matches that previously observed by acoustic emission in rock and that observed for earthquakes. If the energy distribution holds for events large enough to shatter the detector, then such an event is expected in a very long, but finite amount of time. Though we have shown additional correlations in the data, predicting such large, catastrophic, fractures is not straightforward. To see if this is due to the multiple sources of cracks in this data, we propose a dedicated experiment with a single pressure point. With typical fracture rates observed heretofore, such an experiment is feasible at ground level with a smaller cryogenic detector if extrapolation of background holds to low energies and masses. However, searching for vanishing fracture rates requires at least

a shallow underground site. In either case, the lower threshold associated with a smaller, optimized, detector would enable it to probe brittle fracture down close to the energy of single bonds in the crystal. The calorimetric technique could provide additional insight into the partition of elastic energy into permanent dislocations and phonons.

V. ACKNOWLEDGMENTS

P. Di Stefano acknowledges discussions with M. P. Marder on the physics of brittle fracture. I. Maasilta has provided helpful comments on low-threshold detectors. The Java implementation of the Abstract Interface for Data Analysis (`http://java.freehep.org`) has been used for data analysis and figure preparation.

---

[1] J. Åström et al., Phys. Lett. A **356**, 262 (2006), URL `www.arxiv.org/abs/physics/0504151`.

[2] B. Lawn, *Fracture of Brittle Solids, Second Edition* (Cambridge Univ. Pr., 1993), chap. 8.

[3] Á. Corral, Phys. Rev. Lett. **92**, 108501 (2004), URL `www.arxiv.org/abs/cond-mat/0310215`.

[4] C. H. Scholz, *The Mechanics of Earthquakes and Faulting, 2nd edition* (Cambridge Univ. Pr., 2002).

[5] S. Zapperi et al., Nature **388**, 658 (1997).

[6] A. Garcimartín et al., Phys. Rev. Lett. **79**, 3202 (1997).

[7] L. I. Salminen et al., Phys. Rev. Lett. **89**, 185503 (2002).

[8] J. Åström et al. (2006), URL `www.arxiv.org/abs/physics/0612081`.

[9] J. Davidsen et al., Phys. Rev. Lett. **98**, 125502 (2007), URL `www.arxiv.org/abs/cond-mat/0610720`.

[10] A. Saichev and D. Sornette, Phys. Rev. Lett. **97**, 078501 (2006), URL `www.arxiv.org/abs/physics/0604018`.

[11] S. M. Wiederhorn, J. Am. Ceram. Soc. **52**, 485 (1969).

[12] J. A. Åström and J. Timonen, Phys. Rev. E **64**, 011305 (2001).

[13] G. Angloher et al., Astropart. Phys. **23**, 325 (2005), URL `www.arxiv.org/abs/astro-ph/0408006`.

[14] S. C. Langford et al., J. Appl. Phys. **62**, 1437 (1987).

[15] P. Di Stefano et al., Astropart. Phys. **14**, 329 (2001), URL www.arxiv.org/abs/astro-ph/0004308.

[16] S. Pécourt et al., Nucl. Instrum. Methods A **438**, 333 (1999).

[17] W.-M. Yao et al., J. Phys. G: Nucl. Part. Phys. **33**, 1+ (2006), URL pdg.lbl.gov.

[18] H.-M. Hong et al., Phys. Rev. B **72**, 205435 (2005).

[19] F. Petricca et al., Nucl. Instrum. Methods A **520**, 193 (2004).

[20] P. C. F. Di Stefano et al., J. Appl. Phys. **94**, 6887 (2003), URL www.arxiv.org/abs/physics/0307042.

[21] S. Rutzinger et al., Nucl. Instrum. Methods A **520**, 325 (2004).

[22] B. Cabrera et al., Phys. B: Cond. Mat. **280**, 509 (2000).

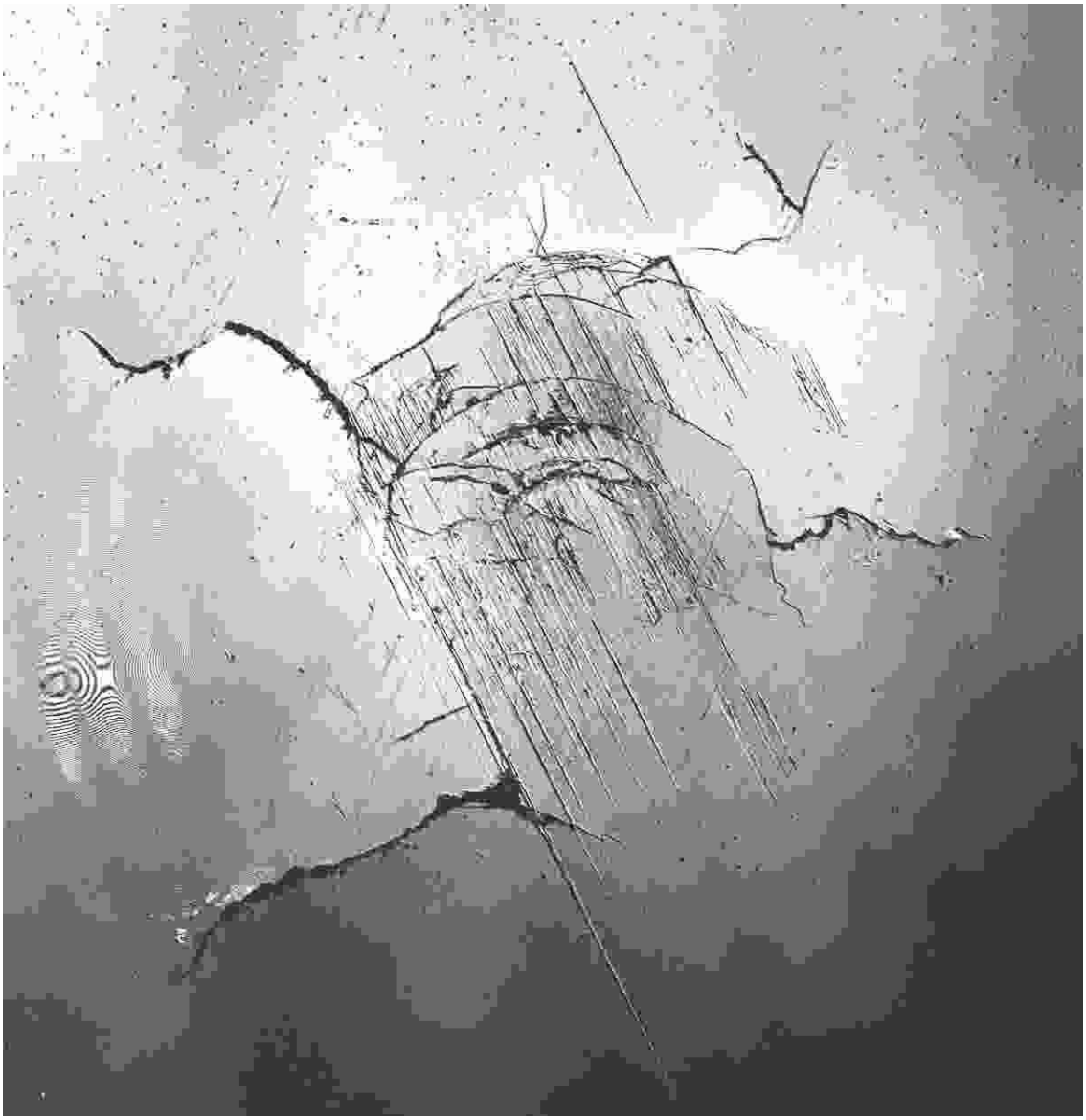

FIG. 1: Confocal microscopy picture of sapphire crystal fractured by sapphire bearing. Diameter of affected area is ≈ 2 mm. Slide marks are visible, as are irregular fractures of radial and circumferential type.

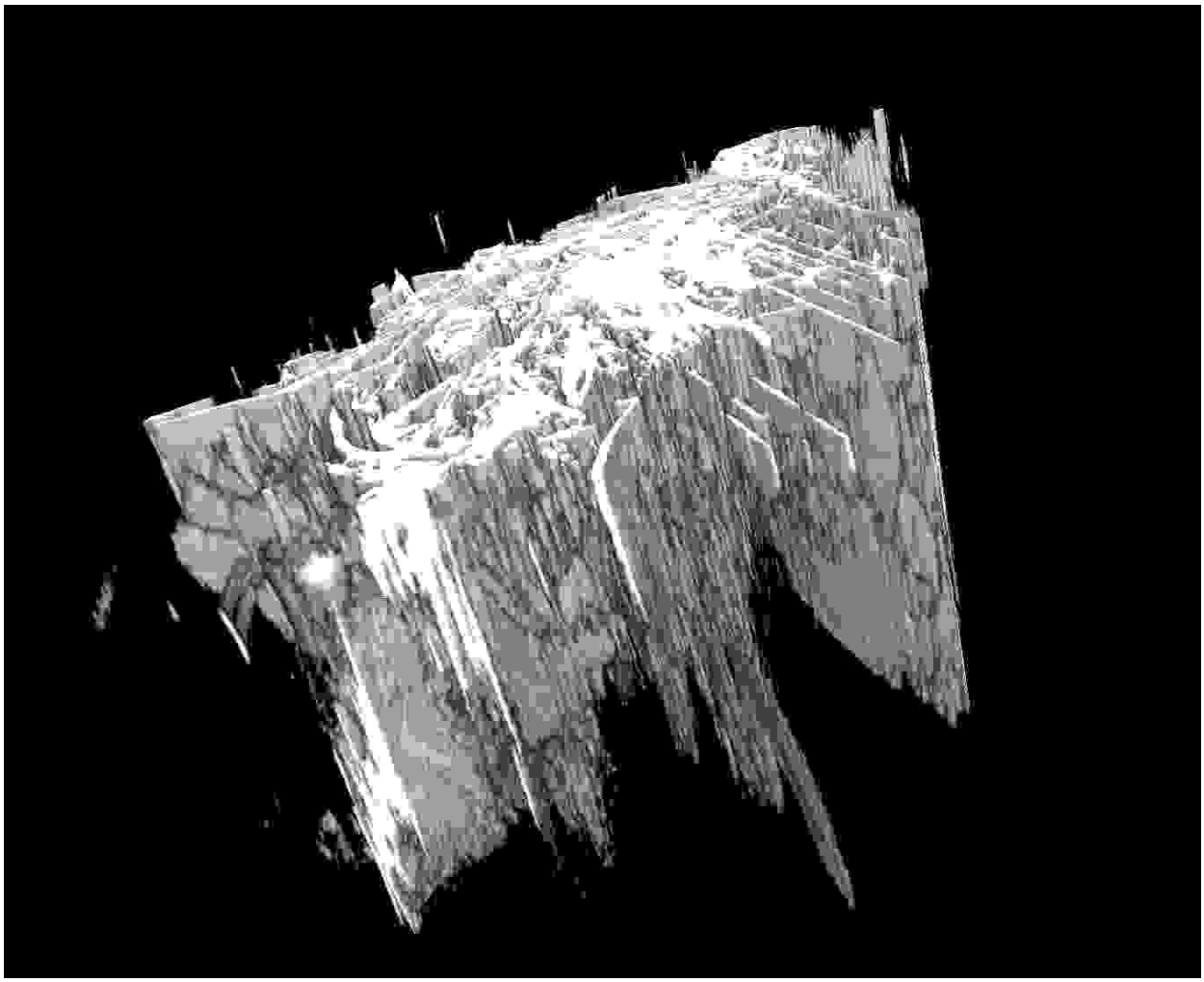

FIG. 2: Fractured area of the crystal scanned by confocal microscopy to a depth of about 150 μm. Features visible at the sapphire surface are openings of two-dimensional cracks that extend fairly deep into the crystal. Their depth could not be measured accurately with the present method. This three-dimensional image was made by volume rendering of the cracks only, i.e. the solid material is not shown here.

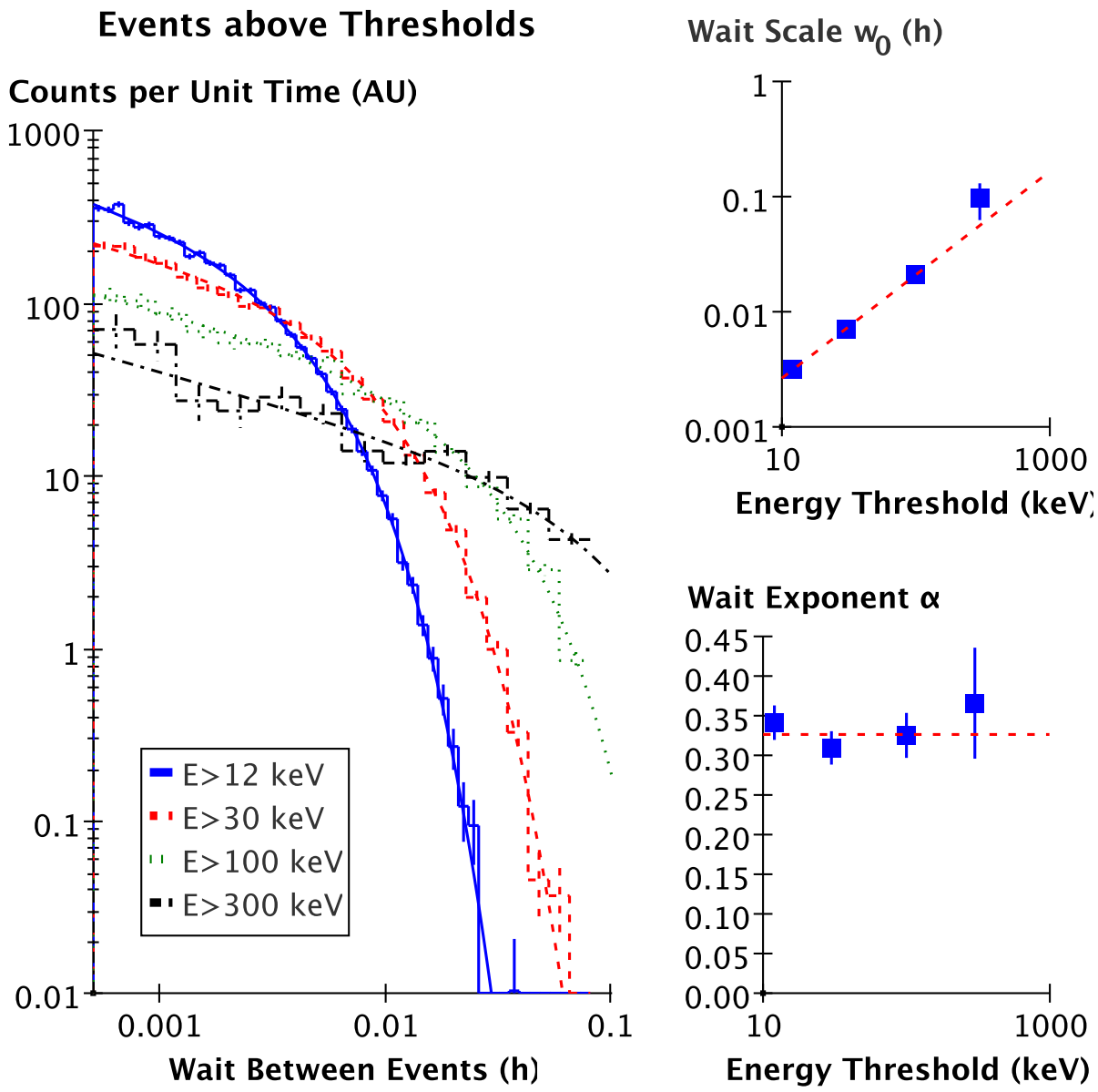

FIG. 3: Left: distributions of waiting times w between consecutive events above various energy thresholds. Error bars are the square root of each bin content. Data are well fitted by the product of an inverse power law and an exponential decay ($\propto \; w^{-\alpha} \exp -w/w_0$). Top right: the wait distribution scale term, $w_0(\geq E)$, obtained from fits of the wait distribution (error bars are from fit) is compatible with fit by $\propto \; E^{\beta-1}$ (dashed red line), where $\beta = 1.9$ is obtained from the fit of the energy distribution[1]. Bottom right: wait exponent α obtained from fits, as a function of threshold energy (error bars are fit errors). Data are fitted by constant function yielding $\alpha = 0.33 \pm 0.01$. These figures demonstrate that at least up to the highest energies, the wait scale term does indeed scale like $w_0(\geq E) \propto E^{\beta-1}$, whereas the wait power term does not depend strongly on the energy threshold.

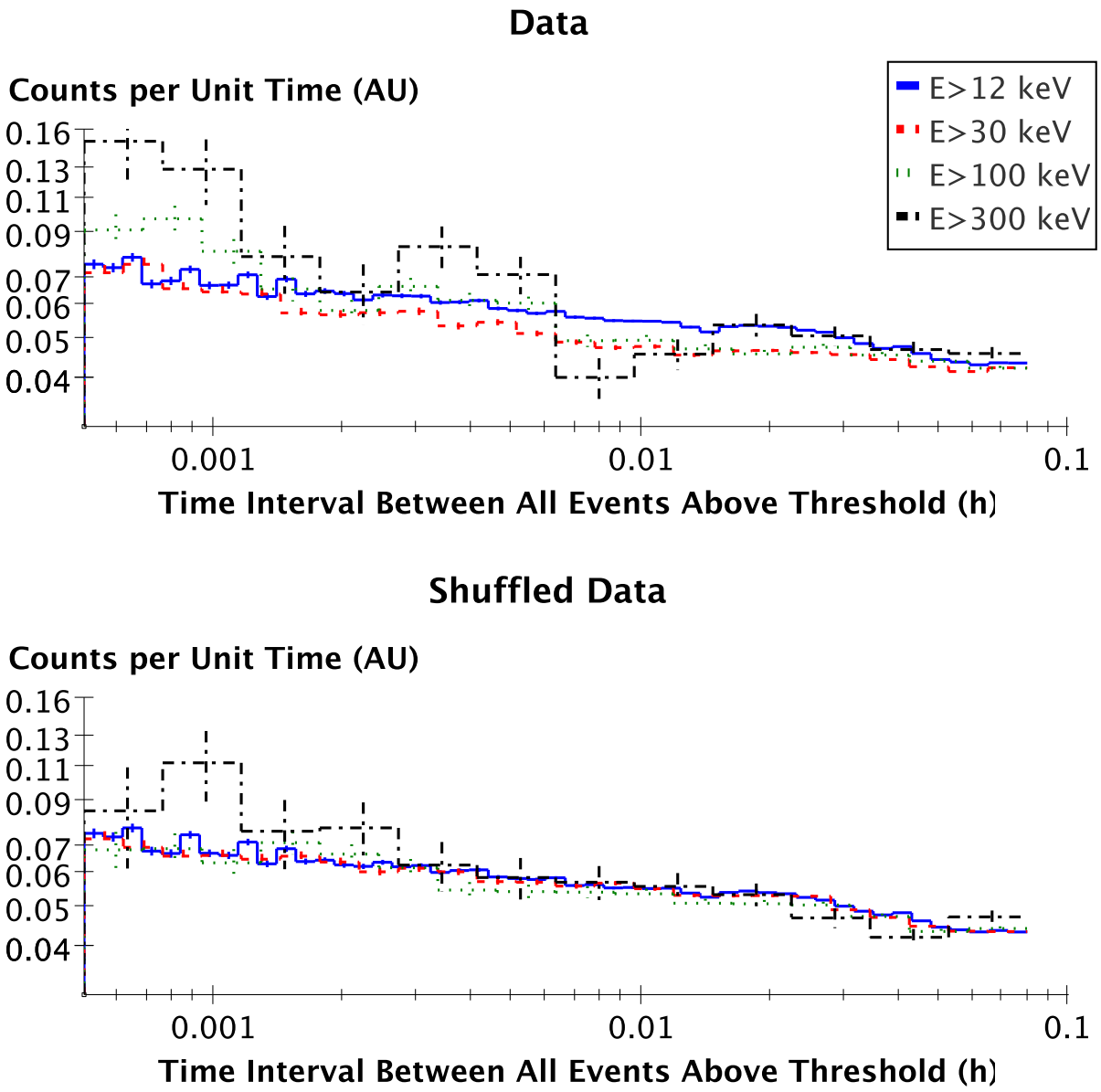

FIG. 4: Distribution of times between all (as opposed to consecutive) events in various energy ranges (note that binning varies between ranges). Top: in the data, the distribution becomes peaked at low times as the event size increases. This is an indicator of clustering for large events. Bottom: in a random shuffle of the data, the distributions differ less for all event sizes.

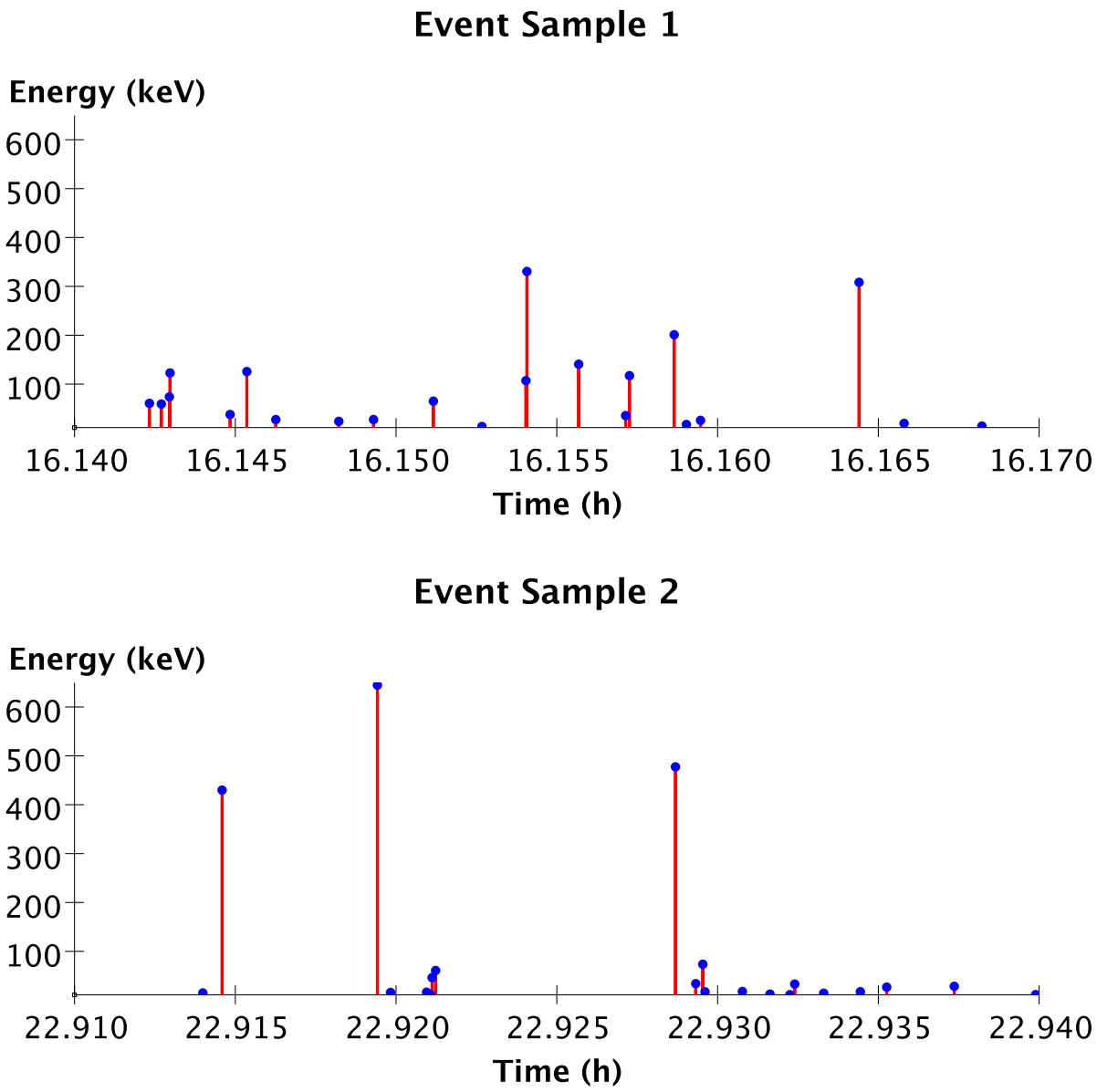

FIG. 5: Examples of event energies as a function of time. Some large events ($E > 300$ keV) appear after relatively quiet periods (for instance just before 22.92 h) whereas others have some precursors (for instance just before 16.155 h) and others display aftershocks (around 22.93 h)

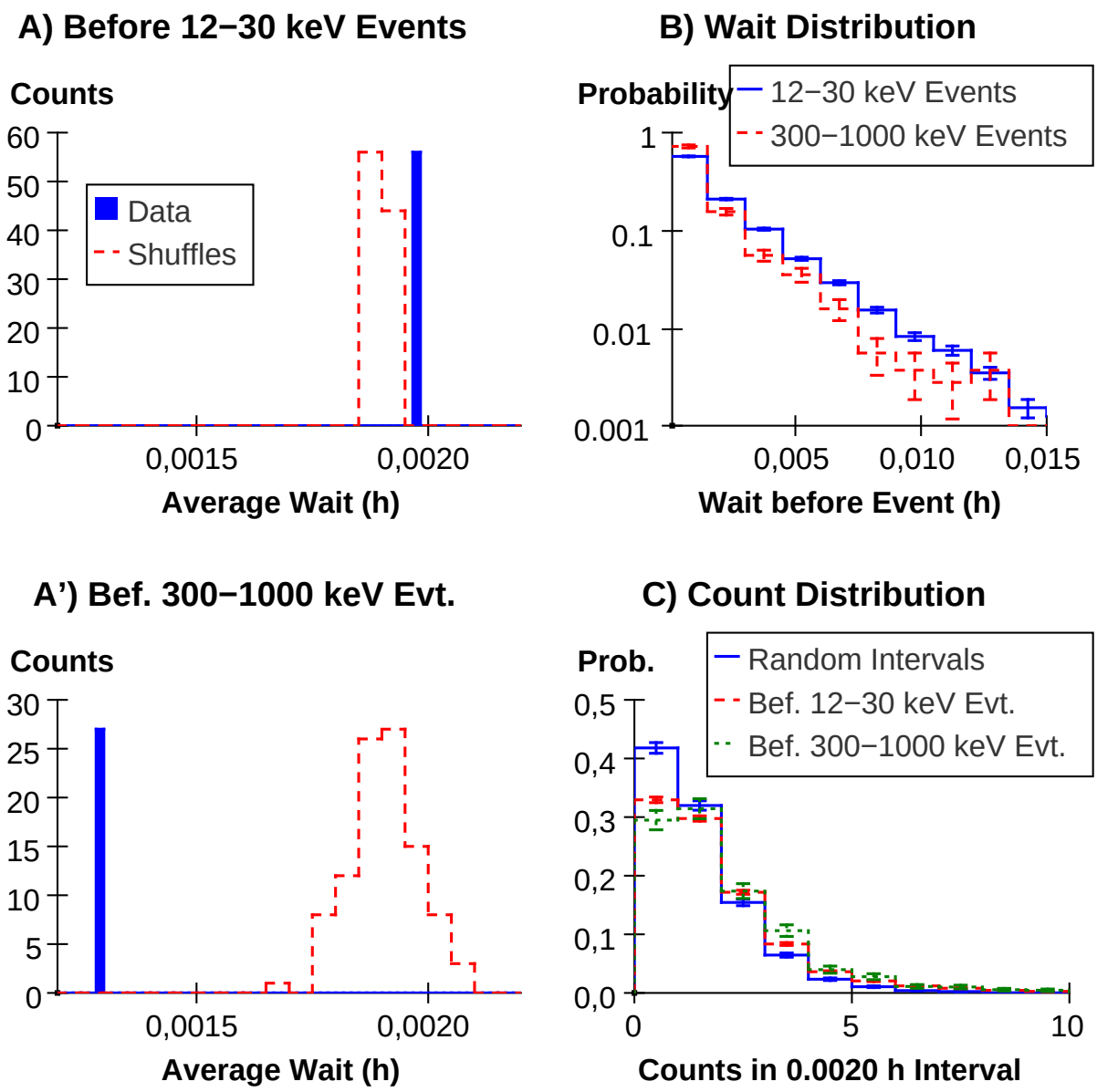

FIG. 6: Fig. A shows the average wait between a small (12–30 keV) event and the event of any size preceeding it (solid blue bar), and the distribution of this average wait before small events in 100 shuffles of data (dashed red histogram). Fig. A' shows the same but for large events (300–1000 keV). Fig. A and A' demonstrate that there is significantly less wait on average before a large event than before a small one. However, Fig. B illustrates that though the averages differ, the distribution of waiting times before small and large events are quite similar and will not provide strong discrimination between individual small and large events. Fig. C shows the distribution of counts in random intervals (solid blue line), in intervals before small events (dashed red) and in intervals before large events (dotted green). The distributions do not show a strong distinction between small and large events, and indeed little difference between random intervals and intervals preceeding events.

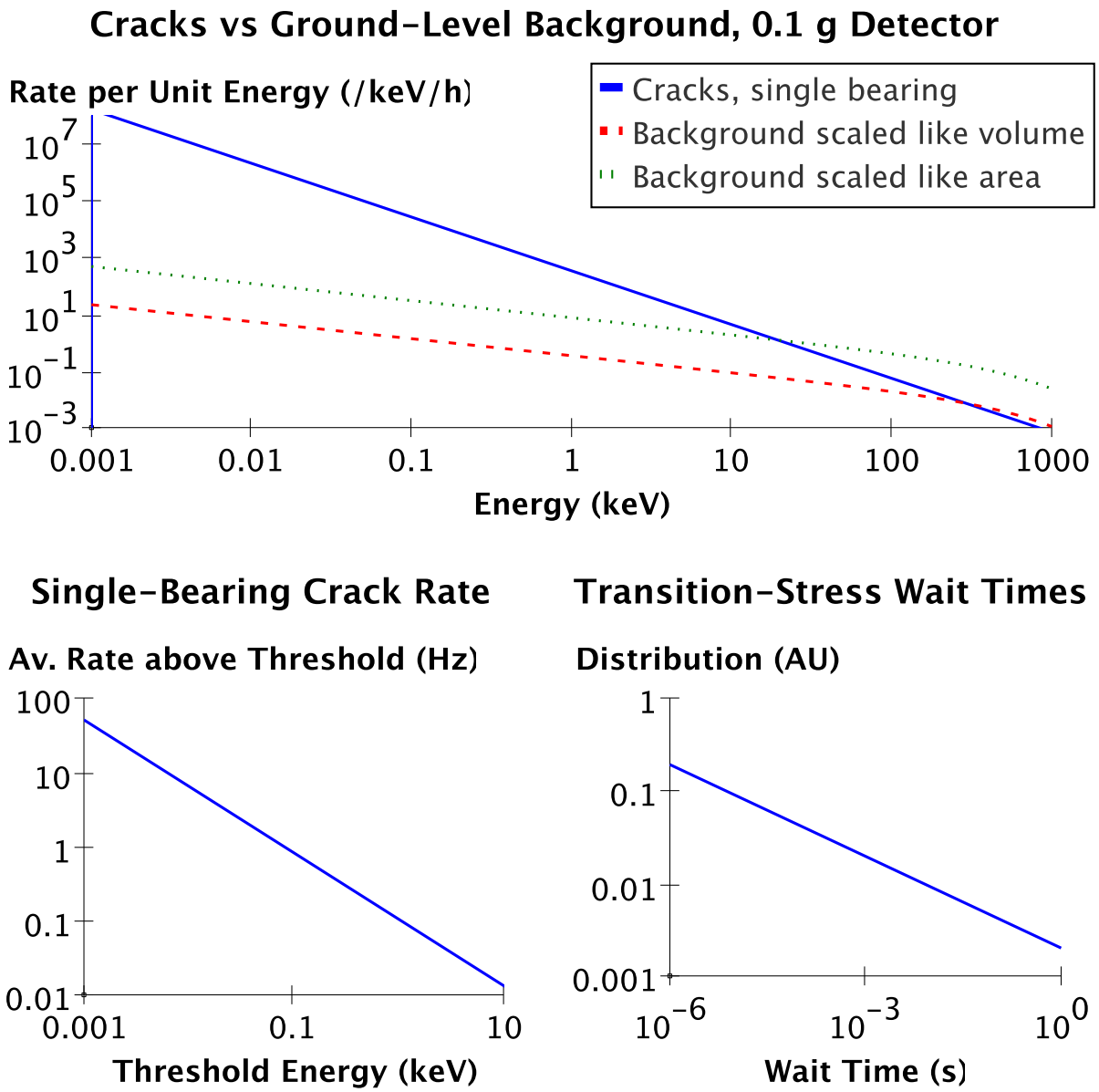

FIG. 7: Top: crack rate compared to backgrounds in hypothetical 0.1 g detector in the case of a background scaling like detector mass and in the case of one scaling like detector area. Rate of cracks is scaled to a single pressure point, though in a new experiment this rate could perhaps be fine-tuned between cryogenic runs by altering the force applied on the bearing. Backgrounds are natural radioactivity and cosmic-induced at ground level, and are extrapolated from Fig. 2 of Ref.[16] to low energies and to low detector masses. Being able to observe the cracks at ground level will require a small crystal and perhaps an increased rate of cracks. Bottom left: the crack rate integrated above even a low threshold remains, on average, compatible with typical thermal time constants of cryogenic detectors and typical acquisition rates. Bottom right: the distribution of waiting times, here in the $\propto w^{-\alpha}$ transition-stress limit with $\alpha = 0.33$, shows that the abundance of short waiting times makes pile-up inevitable.

Chapter 6

Summary and outlook

The mystery of dark matter — most of the matter in the universe is observed only through its gravitational effects — persists after more than seventy years. New particles may provide the answer. Small cryogenic detectors of ionization-phonon or scintillation-phonon type are now among the most sensitive in the search for such particles. Current experiments are operating tens of kilograms of detectors in specially shielded cryostats underground. Experiments deploying several hundred kilograms of crystals are being planned. A challenge for these experiments comes from the fast neutron background, indistinguishable from the expected signal using the standard ionization-phonon or scintillation-phonon discrimination technique. This background may be reduced to low, but ultimately significant, levels through shielding and identification of the muons generating part of it. Dealing with the remaining part will require solutions such as segmented arrays of detectors were neutron coincidences can be exploited. Mixing light targets such as Al_2O_3 with the main Ge detectors can also provide information.

Developping scintillating calorimeters out of Al_2O_3 is therefore an important task. There is a wide spread in collected light yields of sapphire at cryogenic temperatures, and systematic work is ongoing to understand how to reproduce, and eventually mass-produce, the high values.

Lastly, we have serendipitously found that cryogenic detectors can also provide insight into the fracture of brittle materials. Though more complex to operate than the standard room-temperature technique of acoustic emission, cryogenic calorimetry provides a full measurement of the phonon channel, is much more sensitive and is more precisely calibrated. Cryogenic calorimetry may therefore be considered a complement to acoustic emission in this field.

Bibliography

[1] M. Proust, *A la recherche du temps perdu IV. Sodome et Gomorrhe*, Folio Classique, Gallimard, Paris, 1988.

[2] E. P. Hubble, The Observatory **48**, 139 (1925), Observed some cepheids that must be outside Milky Way.

[3] E. P. Hubble, The Astrophysical Journal **62**, 409 (1925), Describes a system, "far outside the limits of the galactic system".

[4] E. P. Hubble, Proceedings of the National Academy of Sciences **15**, 168 (1929), Demonstrates redshift-distance correlation implying expansion of Universe, and gives first estimate of what is now called Hubble's constant : 500 km/s/Mpc. Landmark result, despite large systematics in distance scale, and though redshifts not properly attributed, as discussed elsewhere [5].

[5] R. P. Kirshner, Proceedings of the National Academy of Sciences **101**, 8 (2004), Historical review of Hubble's 1929 paper. Discusses its importance, and shortcomings like source of velocities not being cited and the presence of large systematic in distance scale.

[6] D. E. Osterbrock, *Walter Baade: A Life in Astrophysics*, Princeton University Press, Princeton, New Jersey, 2001.

[7] R. P. Kirshner, *The Extravagant Universe: Exploding Stars, Dark Energy, and the Accelerating Cosmos*, Princeton University Press, Princeton, New Jersey, 2004.

[8] W. Baade and F. Zwicky, Proceedings of the National Academy of Sciences **20**, 254 (1934), Popularizes the fact that supernovae are distinct from ordinary novae.

[9] W. Baade and F. Zwicky, Proceedings of the National Academy of Sciences **20**, 259 (1934), Proposes the gravitational collapse to a neutron star as the mechanism for supernaovae.

[10] F. Zwicky, Physical Review **51**, 290 (1937).

[11] F. Zwicky, Proceedings of the National Academy of Sciences **15**, 773 (1929), Suggests that redshifts and Hubble's recent redshift-distance correlation [4] are not due to expansion but to the fact that light loses energy as it interacts gravitationally with matter.

[12] F. Zwicky, Helvetica Physica Acta **6**, 110 (1933).

[13] S. Smith, The Astrophysical Journal **83**, 23 (1936).

[14] S. van den Bergh, The Astrophysical Journal **131**, 558 (1960), First independant citation of Zwicky 1933. Mentions that 95% of matter in Coma is not observable, and that Zwicky suggested intergalactic matter.

[15] V. C. Rubin, Constraints on the dark matter from optical rotation curves, in *Dark matter in the universe*, edited by J. Kormendy and G. R. Knapp, volume 117 of *IAU Symposium*, pages 51–62, 1987.

[16] D. Clowe et al., The Astrophysical Journal **648**, L109 (2006).

[17] P. Tisserand et al., Astronomy & Astrophysics **469**, 387 (2007).

[18] E. W. Kolb and M. S. Turner, *The Early Universe*, chapter 9.5, Frontiers in Physics, Addison-Wesley, Reading, Massachusetts, 1990.

[19] Diogenes Laertius, The lives and opinions of eminent philosophers, Translated by C.D. Yonge, http://classicpersuasion.org/pw/diogenes/dlempedocles.htm.

[20] W.-M. Yao et al., Journal of Physics G: Nuclear and Particle Physics **33**, 1+ (2006).

[21] P. W. Higgs, Physical Review **145**, 1156 (1966).

[22] H. Pagels and J. R. Primack, Physical Review Letters **48**, 223 (1982).

[23] G. Jungman, M. Kamionkowski, and K. Griest, Physics Reports **267**, 195 (1996).

[24] J. Ellis, J. L. Feng, A. Ferstl, K. T. Matchev, and K. A. Olive, European Physical Journal C **24**, 311 (2002), astro-ph/0110225.

[25] G. Taubes, *Nobel Dreams*, Microsoft Press, 1988.

[26] E. Zavattini et al., Physical Review Letters **96**, 110406 (2006).

[27] W. de Boer, C. Sander, V. Zhukov, A. V. Gladyshev, and D. I. Kazakov, Physics Letters B **636**, 13 (2006).

[28] C. Boehm, D. Hooper, J. Silk, M. Casse, and J. Paul, Physical Review Letters **92**, 101301 (2004).

[29] A. Drukier and L. Stodolsky, Physical Review D **30**, 2295 (1984), MPI-PAE/PTh 26/82.

[30] M. W. Goodman and E. Witten, Physical Review D **31**, 3059 (1985).

[31] J. Diemand, B. Moore, and J. Stadel, Nature **433**, 389 (2005).

[32] P. Smith and J. Lewin, Physics Reports **187**, 203 (1990).

[33] J. D. Lewin and P. F. Smith, Astroparticle Physics **6**, 87 (1996).

[34] S. Ahlen et al., Physics Letters B **195**, 603 (1987).

[35] D. O. Caldwell et al., Physical Review Letters **61**, 510 (1988).

[36] M. Beck et al., Physics Letters B **336**, 141 (1994).

[37] R. Bernabei et al., Physics Letters B **389**, 757 (1996).

[38] G. Gerbier et al., Astroparticle Physics **11**, 287 (1999).

[39] D. S. Akerib et al., Physical Review D **72**, 052009 (2005).

[40] V. Sanglard et al., Physical Review D **71**, 122002 (2005).

[41] G. Angloher et al., Astroparticle Physics **23**, 325 (2005).

[42] J. E. Angle et al., Physical Review Letters (2007).

[43] M. Barnabé-Heider et al., Physics Letters B **624**, 186 (2005), http://www.arxiv.org/abs/hep-ex/0502028.

[44] P. C. Di Stefano, Journal of Physics G: Nuclear and Particle Physics **27**, 1959 (2001).

[45] R. J. Gaitskell et al., http://dmtools.brown.edu.

[46] D. S. Akerib et al., Physical Review D **72**, 052009 (2005), http://www.arxiv.org/abs/astro-ph/0507190.

[47] V. Sanglard et al., Physical Review D **71**, 122002 (2005), http://www.arxiv.org/abs/astro-ph/0503265.

[48] E. A. Baltz and P. Gondolo, Physical Review D **67**, 063503 (2003).

[49] A. Benoit et al., Physics Letters B **545**, 43 (2002), http://www.arxiv.org/abs/astro-ph/0206271.

[50] O. Meier et al., Nuclear Instruments and Methods in Physics Research A **444**, 350 (2000).

[51] G. Angloher et al., Astroparticle Physics **18**, 43 (2002).

[52] P. Meunier et al., Applied Physics Letters **75**, 1335 (1999), http://physics/9906017.

[53] P. Di Stefano, *Recherche de matière sombre non-baryonique au moyen d'un bolomètre à ionisation dans le cadre de l'expérience* EDELWEISS, PhD thesis, Université Paris XI Orsay, 1998.

[54] P. Di Stefano et al., Astroparticle Physics **14**, 329 (2001).

[55] P. N. Luke et al., IEEE Transactions on Nuclear Science **41**, 976 (1994).

[56] T. Shutt et al., Nuclear Instruments and Methods in Physics Research A **444**, 340 (2000).

[57] A. Benoit et al., Physics Letters B **513**, 15 (2001), http://www.arxiv.org/abs/astro-ph/0106094.

[58] R. Abusaidi et al., Physical Review Letters **84**, 5699 (2000), http://www.arxiv.org/abs/astro-ph/0002471.

[59] P. C. F. Di Stefano et al., New Astronomy Reviews **49**, 251 (2005), Proceedings of the 6th UCLA Symposium on Sources and Detection of Dark Matter and Dark Energy in the Universe, February 18-20, 2004, Marina del Rey, California.

[60] A. Juillard et al., Nuclear Instruments and Methods in Physics Research A **559**, 393 (2006).

[61] A. Broniatowski et al., Nuclear Instruments and Methods in Physics Research A **559** (2006).

[62] H. Kraus et al., Journal of Physics: Conference Series **39**, 139 (2006), TAUP 2005, Proceedings of the Ninth International Workshop on Topics in Astroparticle and Underground Physics, Zaragoza, Spain, 10–14 September 2005.

[63] P. L. Brink et al., Proc. Texas Symposium Relativistic Astroph., Stanford, Dec. 2004 (2005), http://www.arxiv.org/abs/astro-ph/0503583.

[64] V. Chazal et al., Astroparticle Physics **9**, 163 (1998).

[65] G. Chardin et al., in *Proceedings of IDM 2002*, page 470, World Scientific, 2003.

[66] http://www.kopos.cz.

[67] L. Chabert, *Etude du bruit de fond neutron induit par les muons dans l'expérience EDELWEISS II*, PhD thesis, Université Claude Bernard Lyon I, 2004.

[68] G. Drexlin et al., Nuclear Instruments and Methods in Physics Research A **289**, 490 (1990).

[69] C. Berger et al., Nuclear Instruments and Methods in Physics Research A **262**, 463 (1987).

[70] P. C. F. Di Stefano, EDELWEISS II, neutrons, wimps and light targets, EDELWEISS internal note.

[71] A. Benoit et al., Physics Letters B **479**, 8 (2000), http://www.arxiv.org/abs/astro-ph/0002462.

[72] S. Cebriàn et al., Nuclear Physics B (Proceedings Supplements) **138**, 519 (2005).

[73] P. C. F. Di Stefano et al., Journal of Applied Physics **94**, 6887 (2003).

[74] J. Amaré et al., Applied Physics Letters **87**, 264102 (2005).

[75] W. Westphal et al., Nuclear Instruments and Methods in Physics Research A **559**, 372 (2006).

[76] H. Kraus et al., Nuclear Instruments and Methods in Physics Research A **553**, 522 (2005).

[77] P. C. F. Di Stefano et al., Journal of Low Temperature Physics (2007), submitted.

[78] A. de Bellefon et al., Astroparticle Physics **6**, 35 (1996).

[79] N. Coron et al., Nuclear Instruments and Methods in Physics Research A **520**, 159 (2003).

[80] V. B. Mikhailik et al., Applied Physics Letters **86**, 101909 (2005).

[81] Hergé, *Les sept boules de cristal*, Casterman, 1948.

[82] M. Sisti et al., Nuclear Instruments and Methods in Physics Research A **466**, 499 (2001).

[83] F. Pobell, *Matter and Methods at Low Temperatures, Second Edition*, Springer-Verlag, Berlin, 1996.

[84] J. Åström et al., Nuclear Instruments and Methods in Physics Research A **559**, 754 (2006).

[85] J. Åström et al., Physics Letters A **356**, 262 (2006).

[86] B. Lawn, *Fracture of Brittle Solids, Second Edition*, chapter 8, Cambridge University Press, Cambridge, 1993.

[87] Á. Corral, Physical Review Letters **92**, 108501 (2004).

[88] S. E. Hough, *Richter's Scale: Measure of an Earthquake, Measure of a Man*, Princeton University Press, Princeton, New Jersey, 2007.

[89] C. H. Scholz, *The Mechanics of Earthquakes and Faulting,* 2nd *edition*, chapter 4.3.2, Cambridge University Press, Cambridge, 2002.

[90] J. Davidsen et al., Physical Review Letters **98**, 125502 (2007).

[91] F. Omori, Journal of the College of Science of the Imperial University of Tokyo **7**, 111 (1894).

[92] T. Utsu et al., Journal of Physics of the Earth **43**, 1 (1994).

[93] H.-M. Hong et al., Physical Review B **72**, 205435 (2005).

[94] J. Åström, P. C. F. Di Stefano, F. Pröbst, L. Stodolsky, and J. Timmonen, Physical Review E (2007), submitted.

[95] S. C. Langford et al., Journal of Applied Physics **62**, 1437 (1987).